Non-linear lattices of granular aluminium resonators

Mathieu Féchant

université
PARIS-SACLAY

Non-linear Lattices of Granular Aluminium Resonator

Réseaux Non Linéaires de Résonateurs en Aluminium Granulaire

Thèse de doctorat de l'université Paris-Saclay

École doctorale n° 564, Physique de L'Ile de France (PIF)
Spécialité de doctorat: Physique
Unité de recherche: Université Paris-Saclay, CNRS, Laboratoire de Physique des Solides, 91405, Orsay, France
Référent: Faculté des sciences d'Orsay

Thèse présentée et soutenue à Paris-Saclay, le 4 mai 2021, par

Mathieu FECHANT

Composition du jury:

Pascal Simon Professeur, Laboratoire de Physique des Solides, Université Paris-Saclay	Président
Claude Chapelier Directeur de Recherche, Laboratoire de Transport Electronique Quantique et Supraconductivité	Rapporteur & Examinateur
Martin Weides Professeur,James Watt School of Engineering, University of Glasgow	Rapporteur & Examinateur
Wiebke Hasch Professeur, Université Grenoble-Alpes, Grenoble	Examinatrice
Florence Levy-Bertrand Chargé de recherche, CNRS, Institut Néel, Grenoble	Examinatrice

Direction de la thèse

Marco Aprili Directeur de Recherche,CNRS, Laboratoire de Physique des Solides, Université Paris-Saclay	Directeur de thèse
Jérôme Estève Chargé de recherche,CNRS, Laboratoire de Physique des Solides, Université Paris-Saclay	Co-encadrant de thèse

Thèse de doctorat

NNT: 2021UPASP034

Contents

Introduction

This thesis is part of a long-term project that aims to implement a quantum simulator for interacting bosons in a lattice using superconducting circuits, more specifically superconducting resonators in the microwave domain. The principle of a quantum simulator, developed almost 40 years ago by R. Feymann [1], is based on the idea of using a well-controlled quantum experiment to enable simulation of complex systems. It has been a focus in varied research fields [2]. Superconducting circuits are one of the promising platforms to realize quantum simulators in large and well controlled systems. The building blocks of these circuits are high quality factor resonators (Q$\approx 10^5$) in the GHz range, and non-linear resonators based on Josephson junctions, which play the role of artificial atoms or qubits [3, 4]. Circuits made of these two elements allow the manipulation of the quantum state of the electromagnetic field with sufficient precision and low decoherence to open the way to quantum information processing [5–7]. The same tools also allow for quantum simulations in the strongly interacting regime to probe many-body effects and create synthetic materials[8–11]. Experiments have been performed in few qubit systems in the single photon regime [12, 13] and also in larger yet more disordered systems [14–16]. Other types of superconducting circuits, such as 2D Josephson junction arrays, have also been used to probe quantum transitions and many-body effects [17–21].

Within this framework, this thesis is in the continuity of previous work in our group [22], where we have studied large lattices consisting of hundreds of linear superconducting resonators. Similar works in this direction have been pursued with coplanar waveguide resonators in the Houck group. [23, 24]. In this thesis, we aim at creating lattices with a large number of resonators in a non-linearity regime where non-linear phenomena appear in a mean-field regime corresponding to a number of photons per lattice site on the order of a few thousands. In order to create the non-linearity, we focus on the use of high kinetic inductance wires made of granular aluminium (GrAl). Departing from transmission line resonators, we use transmon like resonators following a basic transmon design consisting of two pads connected together by a high kinetic inductance superconducting (HKIS) GrAl wire as shown below.

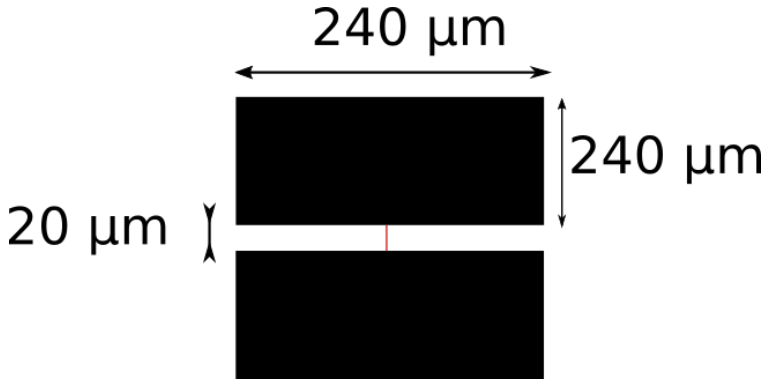

High inductance elements, such as GrAl wires, are an interesting building block for quantum superconducting circuits. They offer the possibility to bypass the need for geometrical

inductance thus reducing cross talk and the size of the circuit. They can also be used to create resonators or waveguides with a characteristic impedance larger than the quantum of resistance, which can be useful to increase the coherence in quantum information setups [7, 25]. Josephson junction chains have enabled creation of such superinductors but another way to create high inductances is to use a disordered superconductor. The principle of kinetic inductances has been used for example in detectors for astronomy [26, 27]. Granular aluminium, studied for the past 50 years [28] has been recently used to realize superinductors [29–32]. The structure of granular aluminium consists of aluminum grains separated by aluminum oxide barriers. By controlling the oxygen pressure during the deposition of aluminium, one can control the resistivity of the material. When the resistivity increases, the critical temperature for the superconducting transition first increases up to 2.2 K or 3 K, depending on the size of the grains, before decreasing again. If the resistivity is too large, the material becomes insulating at low temperature. On the superconducting side of this superconducting to insulator transition, kinetic inductances up to a few nH/□ may be obtained, which can be used to create non-linear resonators with a single photon non-linearity in the MHz range [33].

In this thesis, we have designed and fabricated lattices of transmons made with HKIS GrAl wires as shown below

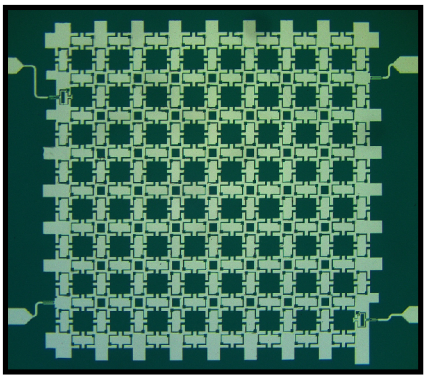

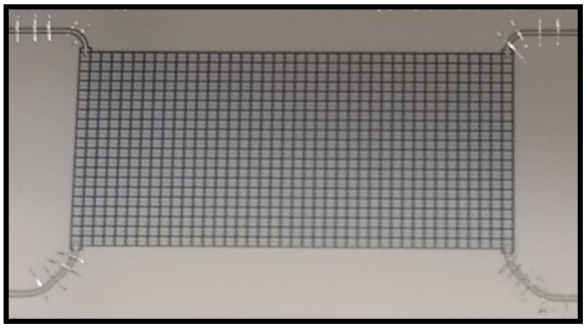

The sample on the right realizes a Lieb lattice, which has the particularity to have a band structure with a flat band. Flat band systems [34] exhibit a dispersion less band in which transport vanishes and in which other parameters such as non-linearity become the leading perturbation. The sample on the left is a square lattice with a non linearity on the order of 10 kHz per photon and per site. Because the non-linearity is small compared to the coupling between the resonators, we expect that the physics of these lattices is well described by non-linear classical waves. The study of non-linear classical waves is a vast field of research that encompasses various situations [35]. An interesting regime is the one corresponding to the so-called weak turbulent regime, where the energy redistributes between the different modes following scaling laws. Many different experimental studies in optics [36, 37], with water waves [38], magnon gas in YIG [39], or photo-refractive crystals [40] have successfully used the framework of weak turbulence. This thermalization process leads toward an equilibrium over the modes with a classical Rayleigh Jeans distribution of the photon numbers n_i for each mode i defined by the parameters T and μ :

$$\overline{n}_i = \frac{T}{e_i - \mu} \tag{0.0.1}$$

where e_i is the energy of the mode i. In analogy to the Bose-Einstein condensation, the Rayleigh-Jeans distribution function can also undergo condensation, where a macroscopic population accumulates in a single mode of the system [41].

Chapter 1 focuses on the theory and design of lattices of transmon like resonators. We first present the parameters of non-linear microwave resonators using high kinetic inductance wire. We will compare the parameters with resonators using a Josephson junction as their source of non-linearity and show the impact of the inductive material used as well as the dimension of the inductive wire. We then show how to predict the parameters of lattices made of such resonators using simulation of the capacitance matrix of the lattice. Finally, we give the design details of the two lattices fabricated in this PhD: a square lattice with a quadratic dispersion of the frequency at the top of the band structure and a lattice similar to Lieb lattice

Chapter 2 will focus on the characterization of the granular aluminium inductances used in the non-linear resonators. We first present the theory around the kinetic inductance of superconductors as well as its non-linear characteristics. The second part of this chapter is dedicated to showing the fabrication techniques. We show the evaporation process, in situ measurements of the resistivity as well as measurements of the width, O_2 pressure on the resistivity and its dispersion. The third part focuses on the theory and measurement of the resonance of single non-linear parameters.

Chapter 3 introduces the expected results of the wave turbulence theory on the square sample. Firstly, we show the condensation process and the paramaters of the Rayleigh-Jeans distribution in the context of our square lattice. We then explain the issues of finite size linked with the thermalization and phase matching of the modes. Finally, we present the numerical simulation we used based on the parameters of the experiment and compare its results with expectations.

Chapter 4 will present the experimental results of both the Lieb and square lattice. We present first the linear parameter associated with both samples. We compare the resonance pattern of transmission to the frequencies and loss rate expected from measurements of the resistance for each sample. We then measure the non-linear parameter between each mode by measuring the self-Kerr, cross-Kerr and Four Wave mixing term between four phase-matching modes. We also present measurements of frequency combs which are characteristic of non-linearity in our lattices. Finally, we present preliminary results on thermalization of amplitude between the modes and dynamical aspects of the non-linear lattice. We explain the microwave setup that enabled us to create pulsed frequency combs necessary to drive the lattice. We then show the evolution of the measured mode amplitudes for varied initial conditions and expand on limitation of this technique due to lack of information.

Introduction (Français)

Cette thèse s'inscrit dans un projet à long terme qui vise à mettre en oeuvre un simulateur quantique de bosons en interaction dans un réseau utilisant des circuits supraconducteurs, plus particulièrement des résonateurs supraconducteurs dans le domaine des micro-ondes. Le principe d'un simulateur quantique, développé il y a près de 40 ans par R.Feymann [1], est basé sur l'idée d'utiliser une expérience quantique bien contrôlée pour permettre la simulation de systèmes complexes. Il a été au centre de divers domaines de recherche [2].

Les circuits supraconducteurs sont l'une des plates-formes prometteuses pour réaliser des simulateurs quantiques de systèmes de grandes tailles avec un grand contrôle. Les éléments constitutifs de ces circuits sont des résonateurs à haut facteurs de qualité ($Q \approx 10^5$) dans la gamme GHz, et des résonateurs non linéaires basés sur des jonctions Josephson, qui jouent le rôle d'atomes artificiels ou qubits [3, 4]. Des circuits constitués de ces deux éléments permettent la manipulation de l'état quantique du champ électromagnétique avec une précision et décohérence suffisante pour ouvrir la voie au traitement de l'information quantique [5–7]. Les mêmes outils permettent également des simulations quantiques dans le régime d'interactions fortes pour sonder les effets à N corps et créer des matériaux synthétiques [8–11]. Des expériences ont été effectuées dans quelques systèmes de qubit dans le régime de photon unique [12, 13] et aussi dans des systèmes plus grands mais plus désordonnés [14–16]. D'autres types de circuits supraconducteurs, tels que les chaines de jonction Josephson 2D, ont également été utilisés pour sonder les transitions quantiques et les effets à plusieurs corps [17–21].

Cette thèse s'inscrit dans la continuité des travaux antérieurs de notre groupe [22], où nous avons étudié de grands réseaux constitués de centaines de résonateurs supraconducteurs linéaires. Des travaux similaires dans ce sens ont été poursuivis avec des résonateurs à guide d'ondes coplanaires dans le groupe de Houck. [23, 24]. Dans cette thèse, nous cherchons à créer des réseaux avec un grand nombre de résonateurs non-linéaires où des phénomènes non linéaires apparaissent dans un régime de champ moyen correspondant à un nombre de photons par site de réseau de l'ordre de quelques milliers. Afin d'implémenter cette non-linéarité, nous nous concentrons sur l'utilisation de fils à haute inductance cinétique en aluminium granulaire (GrAl). A la place des résonateurs en ligne de transmission, nous utilisons des résonateurs de type transmon suivant une conception composée de deux plots reliés entre eux par un fil GrAl supraconducteur à haute inductance cinétique (HKIS) comme indiqué ci-dessous.

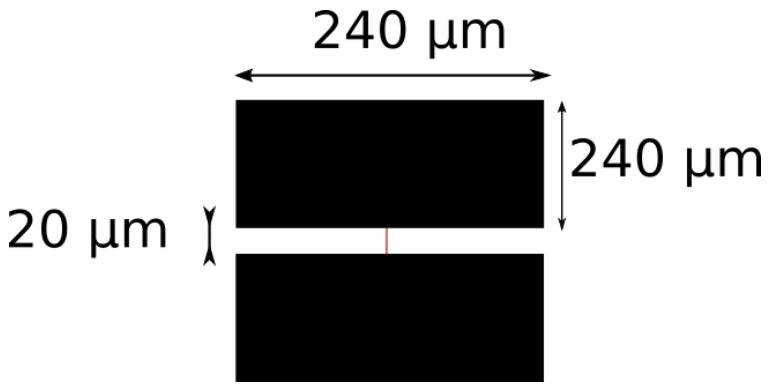

Les éléments à haute inductance, tels que les fils GrAl, sont des éléments de base intéressants pour les circuits supraconducteurs quantiques. Ils offrent la possibilité de contourner le besoin d'inductance géométrique réduisant ainsi les couplages inductifs et la taille du circuit. Ils peuvent également être utilisés pour créer des résonateurs ou des guides d'ondes avec une impédance caractéristique supérieure au quantum de résistance, ce qui peut être utile pour augmenter la cohérence dans les configurations d'informations quantiques [7, 25]. Les chaînes de jonction Josephson ont permis la création de tels superinducteurs, mais une autre façon de créer des inductances élevées consiste à utiliser un supraconducteur désordonné. Le principe des inductances cinétiques a été utilisé par exemple dans les détecteurs pour l'astronomie [26, 27]. L'aluminium granulaire, étudié depuis 50 ans [28] a été récemment utilisé pour réaliser des superinducteurs [29–32]. La structure de l'aluminium granulaire est constituée de grains d'aluminium séparés par des barrières en oxyde d'aluminium. En contrôlant la pression d'oxygène lors du dépôt d'aluminium, il est possible de contrôler la résistivité du matériau. Lorsque la résistivité augmente, la température critique pour la transition supraconductrice augmente d'abord jusqu'à 2,2 K ou 3 K, selon la taille des grains, avant de redescendre. Si la résistivité est trop importante, le matériau devient isolant à basse température. Du côté supraconducteur de cette transition supraconductrice vers isolant, on peut obtenir des inductances cinétiques allant jusqu'à quelques nH / □, qui peuvent être utilisées pour créer des résonateurs non linéaires avec une non-linéarité de photon unique dans la gamme MHz [33].

Dans cette thèse, nous avons conçu et fabriqué des réseaux de transmons fabriqués avec des fils HKIS GrAl comme indiqué ci-dessous

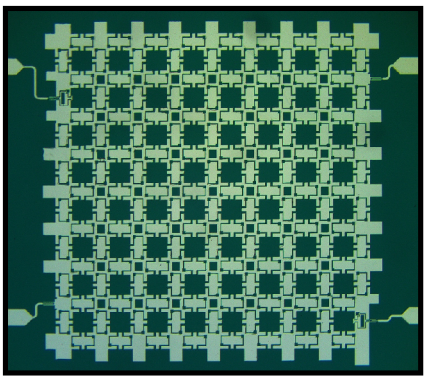

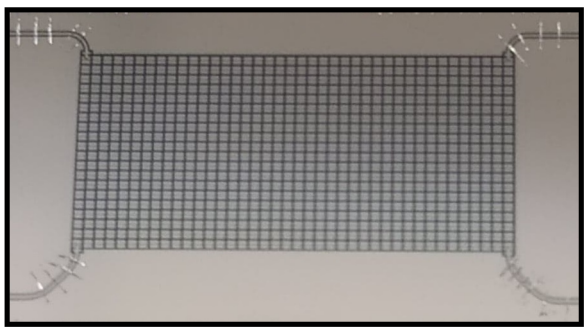

L'échantillon de droite réalise un reseaux Lieb, qui a la particularité d'avoir une structure de bande contenant une bande plate. Les systèmes à bande plate [34] présentent une bande dans laquelle le transport s'annule et dans laquelle d'autres paramètres tels que la non-linéarité passent au premier ordre. L'échantillon de gauche est un réseau carré avec une non linéarité de l'ordre de 10 kHz par photon et par site. Comme la non-linéarité est faible par rapport au

couplage entre les résonateurs, nous nous attendons à ce que la physique de ces réseaux soit bien décrite par les ondes classiques non linéaires. L'étude des ondes classiques non linéaires est un vaste champ de recherche qui englobe diverses situations [35]. Un régime intéressant est celui correspondant au régime turbulent dit faible, où l'énergie se redistribue entre les différents modes suivant des lois d'échelles. De nombreuses études expérimentales en optique [36, 37], avec des vagues d'eau [38], du gaz magnon dans YIG [39], ou des cristaux photo-réfractifs [40] ont utilisé avec succès ce cadre. Ce processus de thermalisation conduit vers un équilibre sur les modes avec une distribution classique de Rayleigh Jeans des nombres de photons n_i pour chaque mode i défini par les paramètres T et μ:

$$\overline{n}_i = \frac{T}{e_i - \mu} \tag{0.0.2}$$

où e_i est l'énergie du mode i. Par analogie avec la condensation de Bose-Einstein, la fonction de distribution de Rayleigh-Jeans peut également subir une condensation, où une population macroscopique s'accumule dans un seul mode du système [41].

Le chapitre **??** se concentre sur la théorie et la conception de réseaux de transmons comme des résonateurs. Nous présentons d'abord les paramètres des résonateurs hyperfréquences non linéaires utilisant un fil à inductance cinétique élevée. Nous comparerons les paramètres avec des résonateurs utilisant une jonction Josephson comme source de non-linéarité et montrerons l'impact du matériau inductif utilisé ainsi que la dimension du fil inductif. Nous montrons ensuite comment prédire les paramètres de réseaux constitués de tels résonateurs en utilisant la simulation de la matrice capacitive du réseau. Enfin, nous donnons les détails de conception des deux réseaux fabriqués dans cette thèse: un réseau carré avec une dispersion quadratique de la fréquence au sommet de la structure de bande et un réseau similaire au réseau de Lieb

Le chapitre **??** se concentrera sur la caractérisation des inductances granulaires d'aluminium utilisées dans les résonateurs non linéaires. Nous présentons d'abord la théorie autour de l'inductance cinétique des supraconducteurs ainsi que ses caractéristiques non linéaires. La deuxième partie de ce chapitre est consacrée à la présentation des techniques de fabrication. Nous montrons le processus d'évaporation, des mesures in situ de la résistivité ainsi que des mesures de la largeur, O_2 pression sur la résistivité et sa dispersion. La troisième partie se concentre sur la théorie et la mesure de la résonance de paramètres non linéaires uniques.

Le chapitre **??** présente les résultats attendus de la 'weak wave' théorie sur l'échantillon carré. Tout d'abord, nous montrons le processus de condensation et les paramètres de la distribution Rayleigh-Jeans dans le contexte de notre réseau carré. Nous expliquons ensuite les problèmes de taille finie liés à la thermalisation et à l'adaptation de phase des modes. Enfin, nous présentons la simulation numérique que nous avons utilisée en fonction des paramètres de l'expérience et comparons ses résultats avec les attentes.

Le chapitre **??** présentera les résultats expérimentaux des reseaux de Lieb et carré. Nous présentons d'abord les paramètres linéaires associé aux deux échantillons. Nous comparons les fréquences mesurées en transmission aux fréquences et taux de perte attendus des mesures de la résistance pour chaque échantillon. Nous mesurons ensuite le paramètre non linéaire entre chaque mode en mesurant le terme de mélange self-Kerr, cross-Kerr et Four Wave entre quatre modes d'adaptation de phase. Nous présentons également des mesures de peignes de fréquences caractéristiques de la non-linéarité dans nos réseaux. Enfin, nous présentons des résultats préliminaires sur la thermalisation d'amplitude entre les modes et les aspects dynamiques du réseau non linéaire. Nous expliquons la configuration des micro-ondes qui nous a permis de créer des peignes de fréquences pulsées nécessaires pour piloter le réseau. Nous montrons ensuite l'évolution des amplitudes des modes mesurés pour des conditions initiales variées et développons sur les limitation de cette technique liées au manque d'information.

Chapter 1

Designing lattices of superconducting transmon like resonators

Contents

In this chapter, we first present how non-linear microwave resonators can be obtained using a high kinetic inductance superconducting wire (HKIS) as a non-linear inductive element. We compare this non-linearity to the one that is obtained when the non-linear element is a Josephson junction. Interestingly, the same design of resonator with a planar capacitance formed by two large pads, having a size of a few hundred by a few hundred microns, which are connected either with a HKIS wire or a Josephson junction, may be used to obtain resonators with the same resonant frequency but very different non-linearities. In the case where the inductance is a Josephson junction, this design corresponds to the so-called "transmon" design, which is one of the main building block for superconducting quantum circuits. We use the same terminology to name our resonator even when the inductance is not a junction but a HKIS wire. We will show how the non-linearity of the HKIS transmon depends on the properties of the disordered superconductor and how it scales with the dimensions of the wire.

In the second part of the chapter, we present the formalism and the numerical simulation tools that we use to predict the properties of coupled transmon resonators arranged in a lattice. Because a transmon does not create any magnetic field, the coupling between neighboring resonators is purely capacitive. The numerical simulation thus reduces to the computation of the capacitance matrix between the different pads forming the resonators. We use the Sonnet software to perform this simulation. We then analytically compute the band structure of the lattice or numerically diagonalize the Hamiltonian to find the eigenmodes of finite size lattices. The fact that the coupling is purely capacitive considerably simplifies the simulation and the calculation in comparison to lattices with mixed capacitive and inductive coupling as previously studied in the group. Very accurate predictions can be made, even for large lattices, with a modest computational effort.

We conclude this chapter by discussing in details the design of the two lattices studied later in this thesis. The first one is a rectangular lattice with a band having a quadratic dispersion corresponding to a negative effective mass for the microwave photons. The second design is similar to a Lieb lattice, a well known tight-binding model with a flat band. We show how the equivalent circuit has a flat band and what may limit the flatness of the band. For each design, we discuss how to tune the resonators located on the edge of the lattice in order to minimize finite size effects. Finally, the coupling of the lattice to the measurement lines is considered, we show how to compute the coupling rate of the lattice modes to the lines and how it can be adjusted to the desired value.

1.1 Properties of transmon resonators

The transmon is an evolution of the Cooper pair box that was designed to have a non-linear spectrum, as the Cooper pair box, while being insensitive to charge noise, which is the main source of decoherence in the Cooper pair box [6, 42]. The corresponding circuit is shown in figure 1.1. It consists of two pads forming a capacitance, with a typical value of a few tens of fF, which are connected by a Josephson junction characterized by its Josephson energy E_J. The Hamiltonian of the circuit is [6]:

$$H = \frac{q^2}{2C} - E_J \cos\left(2\pi \frac{\phi}{\phi_0}\right) \tag{1.1.1}$$

where q is the charge difference between the two pads, ϕ is the conjugate variable corresponding to the magnetic flux, ϕ_0 is the flux quantum and $C = C_c + C_g/2$ is the total capacitance defining the charging energy $E_C = e^2/2C$. The transmon regime is reached when $E_J \gg E_C$, in this case, the spectrum of the system is slightly anharmonic as shown in figure 1.1. The resonance frequency ω_0 is obtained by approximating the Josephson cosine potential by

a quadratic potential $\phi^2/(2L_J)$, where the Josephson inductance is $L_J = (\phi_0/2\pi)^2/E_J$. In order to obtain a resonance frequency $\omega_0 = 1/\sqrt{L_J C}$ around $2\pi \times 6\,\mathrm{GHz}$ with $C = 30\,\mathrm{fF}$, an inductance of 20 nH is required. This corresponds to a Josephson energy of $30\,\mu\mathrm{eV}$ or a critical current $(\phi_0/2\pi)/L_J$ of 15 nA. The charging energy is $E_C = 2.7\,\mu\mathrm{eV}$ and the circuit is well inside the transmon regime.

Taking into account the next term in the Taylor expansion of the cosine potential, we obtain

$$-E_J \cos\left(2\pi\frac{\phi}{\phi_0}\right) \simeq -E_J + \frac{\phi^2}{2L_J} - \frac{\pi^2}{6L_J\phi_0^2}\phi^4 \tag{1.1.2}$$

The non-linearity U, which is defined as the difference between the transition frequencies of the first to second excited state and the ground to first excited state (see figure 1.1), can be calculated by transforming the quartic term into a Kerr term. The quantization of the circuit leads to $\phi = \sqrt{\hbar Z/2}(a + a^\dagger)$, where a is the operator destroying one photon in the resonator mode and $Z = \sqrt{L_J/C}$ is the characteristic impedance of the mode. The quartic term then becomes

$$-\frac{\pi^2}{6L_J\phi_0^2}\phi^4 = -\frac{e^2}{24C}(a + a^\dagger)^4 \tag{1.1.3}$$

This term introduces a quadratic dependence of the energy of the nth Fock state as $\hbar U n(n-1)/2$ with $U = -E_C/\hbar$ [6]. With the parameters considered here, the non-linearity U is about $2\pi \times -650\,\mathrm{MHz}$. In a mean-field approach, the resonance is shifted to the red when the amplitude in the resonator increases, which corresponds to a repulsive interaction for the photons. The non-linearity U is to be compared to the resonant frequency, which defines the following anharmonicity ratio

$$\frac{-U}{\omega_0} = \pi\frac{Z}{R_K} \tag{1.1.4}$$

where $R_K = h/e^2$ is the quantum of resistance.

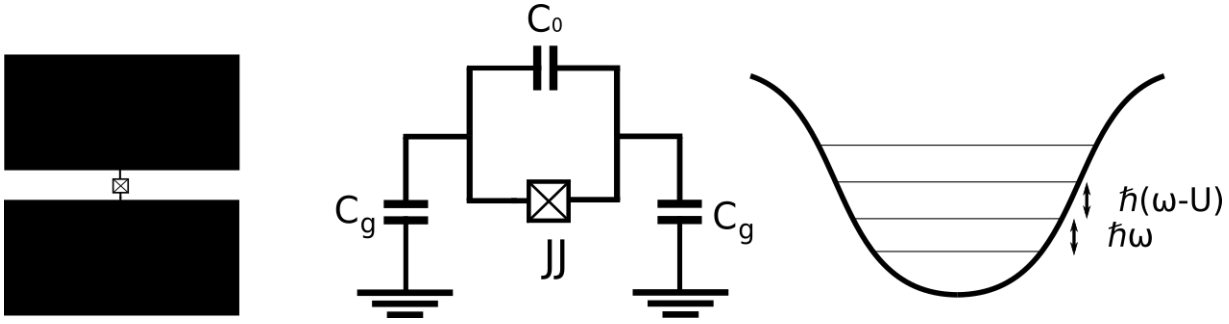

Figure 1.1: Schematics of a transmon resonator, which consists of two pads connected by a Josephson junction. The equivalent circuit is shown, including the capacitance to the ground, which cannot be neglected when the transmon is fabricated on a Si wafer with a metallic back plane, as this is the case in this thesis. In the transmon regime (see text), the spectrum is close to harmonic with an anharmonicity U, which is equal to the charging energy.

1.1.1 Transmon with a high kinetic inductance superconducting wire

The typical coupling energy between two neighboring transmons, which comes from the capacitive coupling between their pads, is approximately equal to the charging energy introduced above, if the transmons are placed closed to each other. If the distance between the transmons is increased and becomes significantly larger than the distance between the pads of the

transmon, the coupling energy can be reduced to a fraction of the charging energy. Therefore, lattices of transmons are naturally in the strongly interacting regime where the interaction energy per photon U is comparable to the hopping energy of the lattice. As motivated in the introduction, the goal of this thesis is to explore the mean-field regime where the interaction U is much smaller than the hopping energy. We will now show that, keeping the transmon design, but replacing the Josephson junction by a HKIS wire, leads to a significant reduction of U. An other approach to reduce U consists in replacing the single Josephson junction by a chain of junctions with a much larger critical current. We have started a collaboration with the group of N. Roch, W. Guichard and O. Buisson in Grenoble to explore this second route [43], but we have not succeeded so far to build a working lattice.

In a thin HKIS wire, the kinetic inductance of the wire is proportional to $l/(wt)$ where l is the wire length, w the width and t the thickness [44]. This allows one to define a sheet inductance, which is related to the sheet resistance of the wire in the normal state through

$$L_\square = R_\square \frac{\hbar}{\pi \Delta} \tag{1.1.5}$$

where Δ is the superconducting gap of the material. This formula is valid at very low temperature and very low frequency compared to the gap. We will give more details in chapter 2 about the origin of this kinetic inductance and show how this formula can be derived by considering the kinetic energy of the Cooper pairs carrying the microwave current or by using the Mattis-Bardeen formula to obtain a more quantitative approach.

For a material with a superconducting critical temperature around 2 K, the sheet inductance corresponds to 0.7 nH for a sheet resistance of 1 kΩ. Such values are typical of many materials including Nb_xSi_{1-x}, TiN, NbN_x or granular Aluminum (GrAl), which is the material used in this thesis. This value must be compared to the electromagnetic, or geometric, inductance, which for a thin wire ($w \ll t$), is approximately given by [45]:

$$L/\mathrm{nH} = 0.2\, l/\mathrm{mm} \left[\ln\left(\frac{2l}{w}\right) + \frac{1}{2} + \frac{w}{3l} \right] \tag{1.1.6}$$

For a GrAl wire with $R_\square = 1\,\mathrm{k}\Omega$, the number of squares to obtain an inductance of 20 nH, a typical value for a transmon, is about 30 squares. Considering a wire with $w = 1\,\mu$m and $l = 30\,\mu$m, the geometric inductance is 0.03 nH, which is negligible compared to the kinetic inductance. This confirms that a HKIS wire, as the Josephson junction, is in a regime where the inductive behavior is solely due to the energy stored in the superconducting material and not in the magnetic field created by the current in the resonator.

1.1.2 Scaling of the non-linearity for a HKIS transmon

The Josephson potential depends only on a single parameter, E_J. Therefore, once the resonant frequency and the characteristic impedance of the resonator are fixed, the anharmonicity of a Josephson transmon is also fixed as derived in (1.1.4). This is not the case for a HKIS transmon, because the non-linearity of the wire and its inductance can be tuned independently, very much like in the case of a chain of Josephson junctions.

The non-linearity of the kinetic inductance comes from the fact that, when the current increases in the wire, the gap reduces and the kinetic inductance increases. We will come back in more details on this effect in the next chapter. Taking this effect into account adds for small current a quartic term to the kinetic inductance of the pairs, which becomes

$$\frac{1}{2} L_0 \left(1 + \frac{I^2}{I_*^2}\right) I^2 = \frac{\phi^2}{2L_0} - \frac{\phi^4}{2L_0^3 I_*^2} \tag{1.1.7}$$

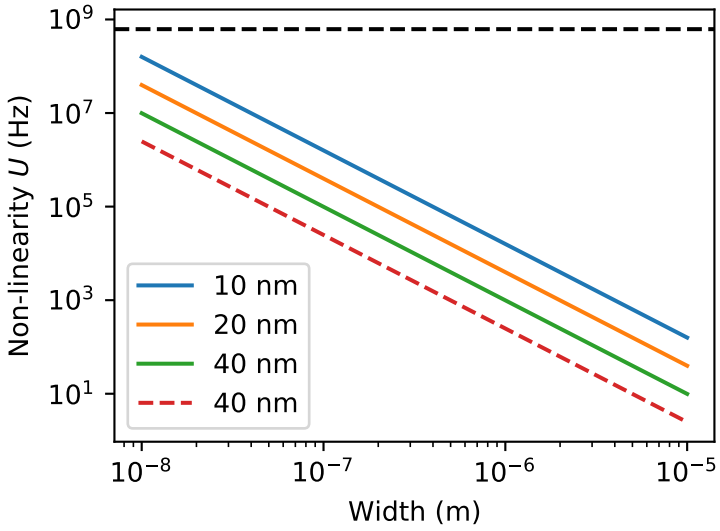

Figure 1.2: Variation of the non-linearity U for a HKIS transmon as a function of the width of the wire. The resonance frequency and the characteristic impedance are fixed to 6 GHz and 850 Ω, which are typical values for a Josephson transmon. The horizontal dashed line corresponds to the non-linearity of the Josephson transmon with these parameters. The different curves correspond to different wire thicknesses as indicated in the legend and to different critical current densities. Solid (dahsed) lines correspond to $j_* = 1$ (2) mA.μm^{-2}.

where L_0 is the kinetic inductance at zero current and I_* sets the scale for the non-linearity. We will show in the next chapter that I_* is proportional to the critical current I_c. We therefore define a current density $j_* = I_*/(wt)$, which is a material property of the disordered superconductor.

In order to convert the quartic term into a Kerr term, we follow the same approach as for the Josephson transmon and obtain

$$-\frac{\phi^4}{2L_0^3 I_*^2} = -\frac{\hbar^2 Z^2}{8L_0^3 I_*^2}(a + a^\dagger)^4 \tag{1.1.8}$$

The non-linearity U is then

$$U = -\frac{3\hbar\omega^2}{2L_0 I_*^2} = -\frac{3\hbar\omega^3}{2Z j_*^2 w^2 t^2} \tag{1.1.9}$$

In the last expression, we eliminate the length of the wire in order to obtain a scaling law for U as a function of the transverse dimensions of the wire. In figure 1.2, we plot the variation of U as a function of the wire width for different values of j_*, which are typical for GrAl, and different thicknesses. The resonant frequency is fixed to 6 GHz and the characteristic impedance to 850 Ω as for the Josephson transmon discussed above. The non-linearity spans several orders of magnitude, from the weakly interacting regime up to the strongly interacting regime, with a maximum non-linearity on the order of 100 MHz. This highly non-linear regime has not been reached yet in experiments and requires the fabrication of small wires with a section of $10 \times 10\,\text{nm}^2$, which is within the reach of state of the art e-beam lithography. To our knowledge, the largest non-linearity observed so far with a GrAl resonator is $U = 2\pi \times 30$ kHz [46].

If wanted, the non-linearity may be further increased by reducing the impedance of the transmon, which increases the size of the pads, or by reducing the critical current density. Here, we have chosen two values $j_* = 1$ (2) mA.μm^{-2}, which have been observed in our group, as we will show in the next chapter, and also in Karlsruhe and Grenoble [46]. The critical current density can be further decreased by increasing the resisitivity of the material as also discussed in the next chapter. The minimal value that can be reached is limited by the fact that

the material becomes insulating when ρ is increased above a critical value. A recent publication suggests that GrAl with $\rho = 10^5\,\mu\Omega$.cm is still superconducting [47]. This value is almost two orders of magnitude larger than in our group, suggesting that higher values of j_* are within reach. In conclusion, it seems reasonable to assume that HKIS transmons with a GrAl wire can be tuned to target any non-linearity between a few Hz and a few tens or even hundreds of MHz. This characteristic is very interesting to simulate the physics of bosons on a lattice in a wide range of interaction parameters, while keeping the same sample design for the capacitance pads and only changing the properties of the HKIS wire.

1.2 Normal modes and band structure of transmon lattices

In this section, we explain how we model two-dimensional lattices of transmon resonators. Figure 1.3 shows the example of a rectangular lattice, whose design is very close to the one that is experimentally measured in chapter 4. Here again, the term "transmon" designates a resonator where the inductive component is created by a superconducting element, either a Josephson junction or a HKIS wire. The important aspect is that the transmon does not create any magnetic field, so that the coupling between the resonators is purely capacitive. The equivalent circuit of the lattice is shown in figure 1.3. Each metallic pad is associated to a node i, each node has a capacitance to the ground, and two nodes may be connected by a capacitance $C_{c,ij}$, if they are sufficiently close, and by an inductance L_{ij}, if a HKIS wire or a junction connects the pads. With these definitions, the number of nodes is twice the number of transmons, and thus twice the number of independent degrees of freedom in the system. These non physical degrees of freedom have to be eliminated later.

With this approach, the finite element numerical simulation of the circuit is reduced to the calculation of the values of the capacitances to the ground and between the pads. We use the Sonnet software to obtain these values. For example, the lattice shown in figure 1.3 is sufficiently small to be fully simulated and we can obtain the coupling capacitances between any node of the circuit. For large systems, we use the fact that the lattice is periodic to obtain the capacitance values from the simulation of a smaller lattice and combine the results of different simulations to build the capacitance matrix of the full lattice, taking into account edge effects.

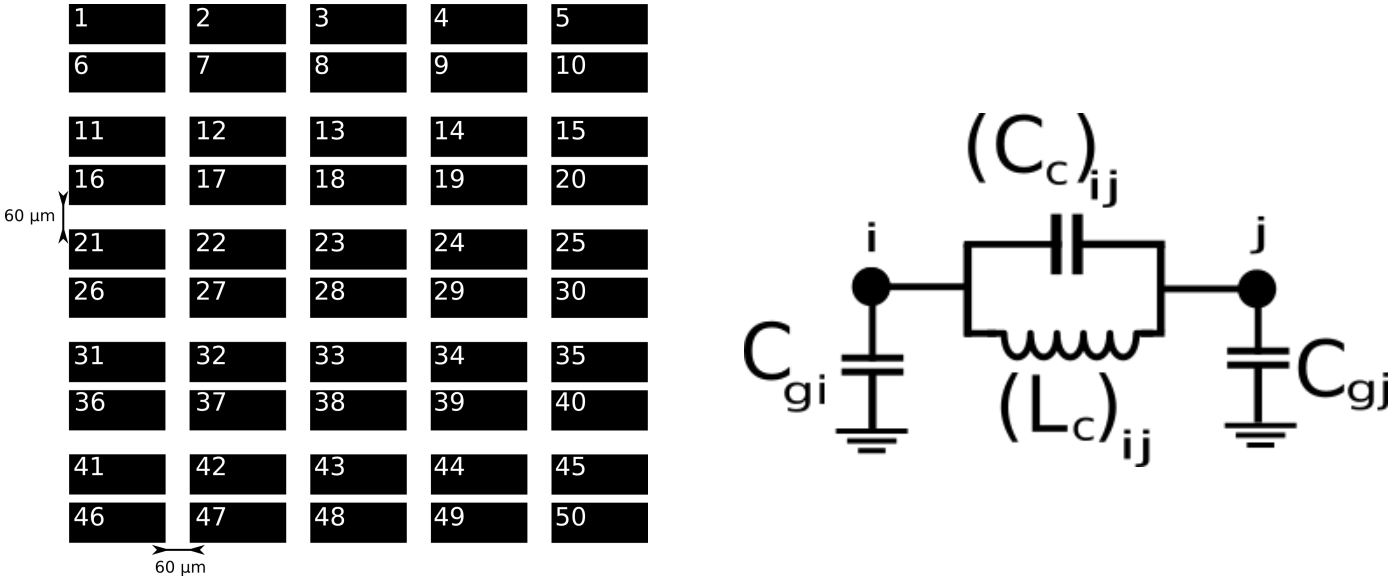

Figure 1.3: The left drawing shows an example of a rectangular lattice of transmons. Each transmon is made of two pads (for example 1&6 or 2&7) that are connected by a superconducting inductive element, such as a Josephson junction or a HKIS wire. Each pad is considered to be a node at a uniform potential. The nodes are connected by the equivalent circuit shown on the right.

1.2.1 Linear Hamiltonian and admittance matrix

Here, we are only interested in the linear behavior of the lattice in order to obtain its band structure, we therefore neglect the non-linearity of the inductive element. It will be included

in the Hamiltonian in the third chapter. Defining the capacitance matrix C as

$$C_{ij} = \begin{cases} -C_{c,ij} \text{ if i} \neq \text{j} \\ C_{g,i} + \sum_{k \neq i} C_{c,ik} \quad \text{if i} = \text{j} \end{cases} \tag{1.2.1}$$

and the stiffness matrix K as

$$K_{ij} = \begin{cases} -L_{ij}^{-1} \text{ if i} \neq \text{j} \\ \sum_{k \neq i} L_{ik}^{-1} \text{ if i} = \text{j} \end{cases} , \tag{1.2.2}$$

the Lagrangian of the circuit is

$$\mathcal{L} = \frac{1}{2}\dot{\phi}^T C \dot{\phi} - \frac{1}{2}\phi^T K \phi \tag{1.2.3}$$

where the element of the vector ϕ correspond to the magnetic flux at each node. The conjugate momenta to the fluxes ϕ are the charges at node i, which are defined as

$$q = \frac{\partial \mathcal{L}}{\partial \dot{\phi}} = C\dot{\phi} \tag{1.2.4}$$

The Hamiltonian of the circuit is then obtained from the usual Legendre transformation

$$H = \dot{\phi}^T q - \mathcal{L} = \frac{1}{2} q^T C^{-1} q + \frac{1}{2}\phi^T K \phi \tag{1.2.5}$$

We arrive at the standard quadratic Hamiltonian for a system of coupled harmonic oscillators. This Hamiltonian is a good approximation of the true Hamiltonian of the circuit, if the voltage is spatially uniform on the metal pads that define the nodes. This is the case if the pad dimensions are much smaller than the wavelength of the microwave signal at the considered frequency. At 6 GHz, the wavelength in a micro-strip line consisting of a 220 μm wide wire is 18 mm, which is 60 times larger than the typical size of a pad. The other assumption that we make is that the capacitive coupling between the HKIS wire and the pads can be neglected. We will see in the next chapter that this is not always the case, when the wire becomes too long and/or too wide. The validity of this assumption can be verified by considering a single transmon and compare the resonance frequency predicted by the equations above to a full finite element numerical solution of the transmon including the wire.

The equation of motion of the flux vector may be obtained from the Lagrangian, leading to

$$C\ddot{\phi} = -K\phi \tag{1.2.6}$$

If the circuit is excited at a frequency ω, the previous equation becomes

$$j\omega CV = -KV/(j\omega) \tag{1.2.7}$$

where $V = \dot{\phi}$ is the voltage at each node. Introducing the admittance matrix $Y[\omega] = j\omega C + K/(j\omega)$, we obtain

$$Y[\omega]V = 0 \tag{1.2.8}$$

In the following, we use either equation 1.2.5 or 1.2.8 to obtain the resonant modes of the lattice.

1.2.2 Normal modes of a finite size lattice

The standard way to obtain the modes of the quadratic Hamiltonian H is to define a canonical transformation $Q = T_q^{-1}q$ and $\Phi = T_\phi^{-1}\phi$ such that the Hamiltonian becomes

$$H = \frac{1}{2}Q^T\Omega Q + \frac{1}{2}\Phi^T\Omega\Phi \tag{1.2.9}$$

where Ω is the diagonal matrix containing the eigen frequencies of the system. An efficient way to obtain these different matrices is to first decompose the two matrices C^{-1} and K as

$$C^{-1} = YY^T \quad K = XX^T \tag{1.2.10}$$

This Cholesky decomposition is defined only if the matrix is positive, which is the case of C because of the capacitance to the ground but not of K. In the numerical code, we regularize K by adding a small constant term on the diagonal to make the matrix positive. We then consider the matrix Y^TX and compute its singular value decomposition

$$Y^TX = U\Omega V \tag{1.2.11}$$

The singular values correspond to the frequency of the normal modes and a straightforward calculation shows that the transformations

$$T_q = XV^T\Omega^{-1/2} \quad T_\phi = YU\Omega^{-1/2} \tag{1.2.12}$$

define the required canonical transformation. The matrices fulfill $T_q^TC^{-1}T_q = T_\phi^TKT_\phi = \Omega$ and $T_\phi^TT_q = 1$. One sees that the elements of T_q and T_ϕ respectively have the dimension of $1/\sqrt{Z}$ and $\sqrt{Z}$ where Z is an impedance. Introducing the mode amplitudes $\alpha = (\Phi + jQ)/\sqrt{2}$, the Hamiltonian can be rewritten

$$H = \alpha^\dagger\Omega\alpha \tag{1.2.13}$$

The α's are called the normal modes of the system. We use this method to numerically obtain the modes of finite size lattices as experimentally measured.

1.2.3 Band structure of an infinite lattice

We now look for the band structure of a transmon lattice circuit taking into account the lattice periodicity and neglecting any finite size effect. The Hamiltonian 1.2.5 can be rewritten

$$H = \frac{1}{2}\sum_{R_iR_j} q^T[R_i]C[R_i - R_j]q[R_j] + \frac{1}{2}\sum_{R_iR_j}\phi^T[R_i]K[R_i - R_j]\phi[R_j] \tag{1.2.14}$$

where we have rearranged the sum over the nodes to a sum over the lattice cells. The displacements R_i identify the position of the cell and belong to the Bravais lattice underlying the circuit, which, for the example considered here, is a rectangular lattice as shown in figure 1.4 with two primitive vectors a_1 and a_2. The vectors $q[R_i]$ and $\phi[R_i]$ correspond to the charge and flux of the nodes inside the cell at position R_i. For the lattice considered here, there are two nodes per cell and the capacitance matrix $C[R_j - R_i]$ is a 2×2 matrix that contains the capacitance couplings between the nodes at R_i and R_j, which only depends on the difference $R_i - R_j$. The matrix $C[0]$ contains the ground capacitances and the coupling between the two pads of the transmon that belong to the same cell. The same notation is used for the stiffness matrix. In the example considered here, $K[R_j - R_i]$ is zero unless $R_i = R_j$.

We now go to the reciprocal space and define

$$q[k] = \frac{1}{\sqrt{N}}\sum_{R_i} e^{jkR_i}q[R_i] \quad \phi[k] = \frac{1}{\sqrt{N}}\sum_{R_i} e^{jkR_i}\phi[R_i] \tag{1.2.15}$$

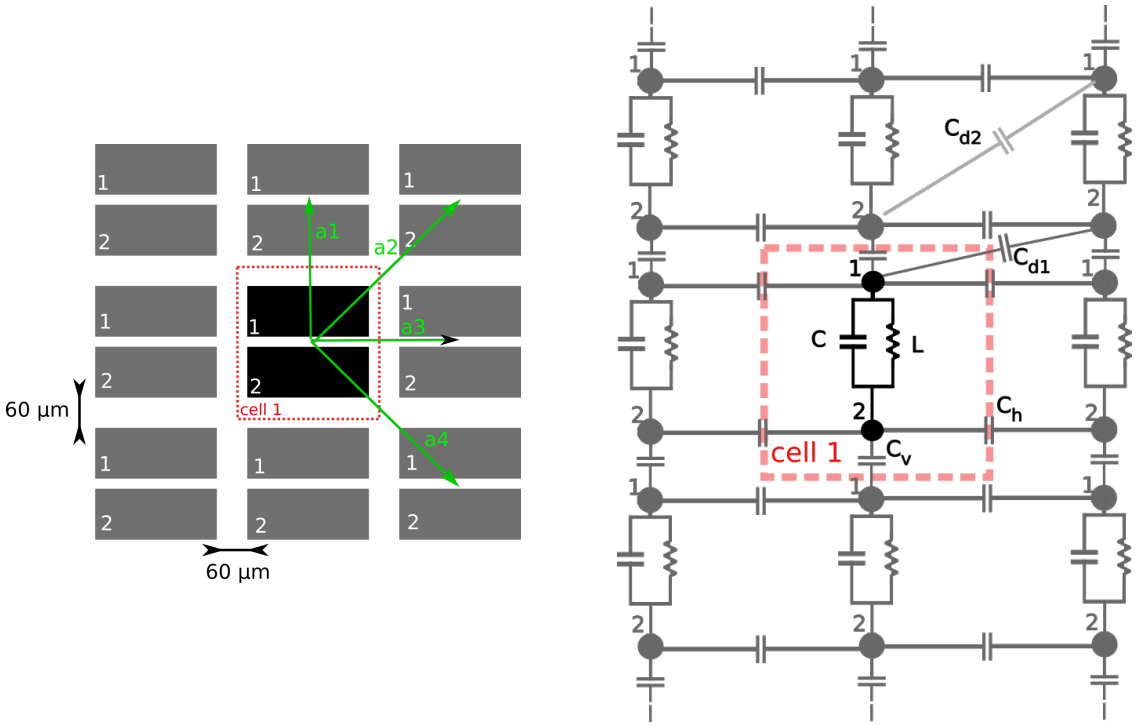

Figure 1.4: Primitive cell and its equivalent circuit of a rectangular lattice of transmons. The vectors a_1 and a_2 are the two primitive vectors of the lattice and the unit cell contains two nodes. The nodes in the cell R_i capacitively couple to the ones of the neighboring cells at position $R_i \pm a_j$, where a_j is one of the four vectors a_1, a_2, $a_3 = a_1 + a_2$, $a_4 = a_1 - a_2$. Capacitive couplings at larger distances are negligible. The values of the different capacitances are obtained from Sonnet simulations. We obtain $C_c = 17.8\,\mathrm{fF}$, $C_h = 6.5\,\mathrm{fF}$, $C_v = 16.8\,\mathrm{fF}$, $C_{d1} = 2.2\,\mathrm{fF}$ and $C_{d2} = 1.5\,\mathrm{fF}$ .The ground capacitance $C_g = 29\,\mathrm{fF}$ is the same for each pad and is not shown in the circuit.

where N is the number of cells. We suppose periodic boundary conditions, this constrains k to take N values inside a primitive cell of the reciprocal lattice, for example the first Brillouin zone. We also define the Fourier transform of the C and K matrices

$$C[k] = \sum_{R_i} e^{jkR_i} C[R_i] \qquad K[k] = \sum_{R_i} e^{jkR_i} K[R_i] \tag{1.2.16}$$

In the calculation of the Fourier transform of C and K, the sum is truncated to some range of nearest neighbor couplings. For example, in the simulation of the rectangular lattice considered here, it is sufficient to consider the couplings between one site and the eight neighboring sites that ate located immediately next to it, including diagonal sites. This leads to the following expression for $C[k]$

$$\begin{aligned} C[k] = \begin{bmatrix} C_t & -C_c \\ -C_c & C_t \end{bmatrix} + 2\begin{bmatrix} -C_h & -C_{d2} \\ -C_{d2} & -C_h \end{bmatrix} \cos ka_1 + \begin{bmatrix} 0 & -C_v e^{jka_2} \\ -C_v e^{-jka_2} & 0 \end{bmatrix} \\ + \begin{bmatrix} 0 & -C_{d1}(e^{jka_3} + e^{-jka_4}) \\ -C_{d1}(e^{-jka_3} + e^{jka_4}) & 0 \end{bmatrix} \end{aligned} \tag{1.2.17}$$

where $C_t = C_g + C_c + C_v + 2C_h + 2C_{d1} + 2C_{d2}$ and C_g is the capacitance to the ground of each pad. The $K[k]$ matrix is given by

$$K[k] = \begin{bmatrix} 1/L & -1/L \\ -1/L & 1/L \end{bmatrix} \tag{1.2.18}$$

where L is the inductance of the superconducting element constituting each transmon. Using the relation $\sum_{R_i} e^{j(k-q)R_i} = N\delta_{k,q}$, we obtain the Hamiltonian in the reciprocal space

$$H = \sum_k H[k] \quad \text{with} \quad \mathrm{H[k]} = \frac{1}{2}\mathbf{q}^\dagger\mathrm{[k]C[k]}\mathbf{q}\mathrm{[k]} + \frac{1}{2}\phi^\dagger\mathrm{[k]K[k]}\phi\mathrm{[k]} \tag{1.2.19}$$

We can apply the same technique, as explained above for the finite size lattice, in order to obtain the normal modes of $H[k]$ and the band structure of the lattice $\Omega[k]$. We can also define a k dependent admittance matrix as

$$Y[\omega, k] = j\omega C[k] + \frac{1}{j\omega} K[k] \tag{1.2.20}$$

The band structure is then obtained by solving $\det Y[\omega, k] = 0$. This second approach is equivalent to finding the normal modes of $H[k]$. It is useful to obtain analytical expressions for the band structure. In the case of a lattice with two nodes per cell, $\det Y[\omega, k] = 0$ leads to a second order polynomial equation in $x = \omega^2$ that is easily solved analytically.

For the lattice considered here as an example, solving $\det Y[\omega, k] = 0$ leads to one non trivial solution for ω^2, while the trivial null solution corresponds to the fact that the number of nodes is twice the number of degrees of freedom. Figure 1.5 shows the band in the first Brillouin zone for the values of the capacitances given in 1.4 and an inductance $L = 18\,\mathrm{nH}$.

The expression of ω as a function of k_x and k_y, including all the capacitive couplings is complicated. Here, we only give it in the case where $C_{d1} = C_{d2} = 0$, in which case it simplifies to

$$\omega = \sqrt{\frac{2(C_c - C_t + 2C_h \cos k_x a_x + C_v \cos k_y a_y)}{L(C_c^2 - 2C_h^2 - C_t^2 + C_v^2 + 4C_h C_t \cos k_x a_x - 2C_h^2 \cos 2k_x a_x + 2C_c C_v \cos k_y a_y)}} \tag{1.2.21}$$

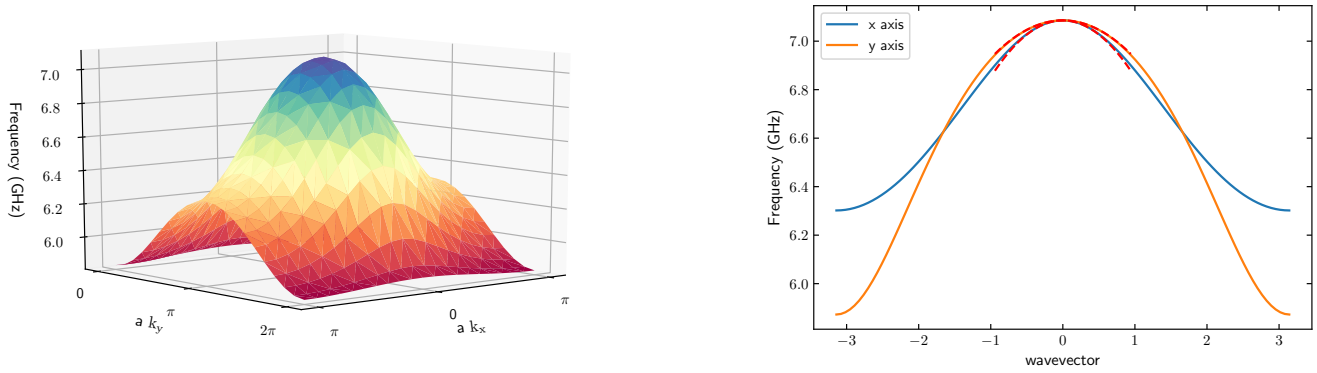

Figure 1.5: Band structure of the rectangular lattice shown in figure 1.4 and an inductance $L = 18\,\mathrm{nH}$. The right plot shows a cut through the horizontal and vertical directions. For the vertical cut, the origin of the wave-vector is shifted to π/a_y.

where a_x and a_y are the horizontal and vertical dimensions of the unit cell. Supposing that the transmons are weakly coupled, meaning that $C_h \ll C_c$ and $C_v \ll C_c$, we obtain

$$\omega \approx \omega_0 \left(1 + \frac{C_h}{C_c + C_t} \cos k_x a_x - \frac{C_v}{2(C_c + C_t)} \cos k_y a_y\right) \tag{1.2.22}$$

where $\omega_0 = \sqrt{2/L(C_t + C_c)}$ is the transmon resonance frequency. The band is quadratic around a maximum located at $k_x = 0$ and $k_y = \pm\pi/a_y$ with a negative effective mass, which is different in the x and y direction unless $C_v = 2C_h$. The $k_x = 0$ and $k_y = \pm\pi/a_y$ state corresponds to the state where each transmon is excited with the same amplitude and the sign of the potential difference between the two pads of the transmon alternates from one horizontal line to the other.Figure 1.5 shows the dispersion relation along the horizontal and vertical directions around the point $k_x = 0$ and $k_y = \pi/a_y$ without any approximation and including the values of C_{d1} and C_{d2}.

Other example of rectangular lattice Figure 1.6 shows a different rectangular lattice and the associated band structure. Here, the transmons couple to each other through the same pad, while in the previous design, the two pads were used to provide the coupling capacitances. This shifts the maximum of the band to the $k_x = k_y = 0$ point in the Brillouin zone.

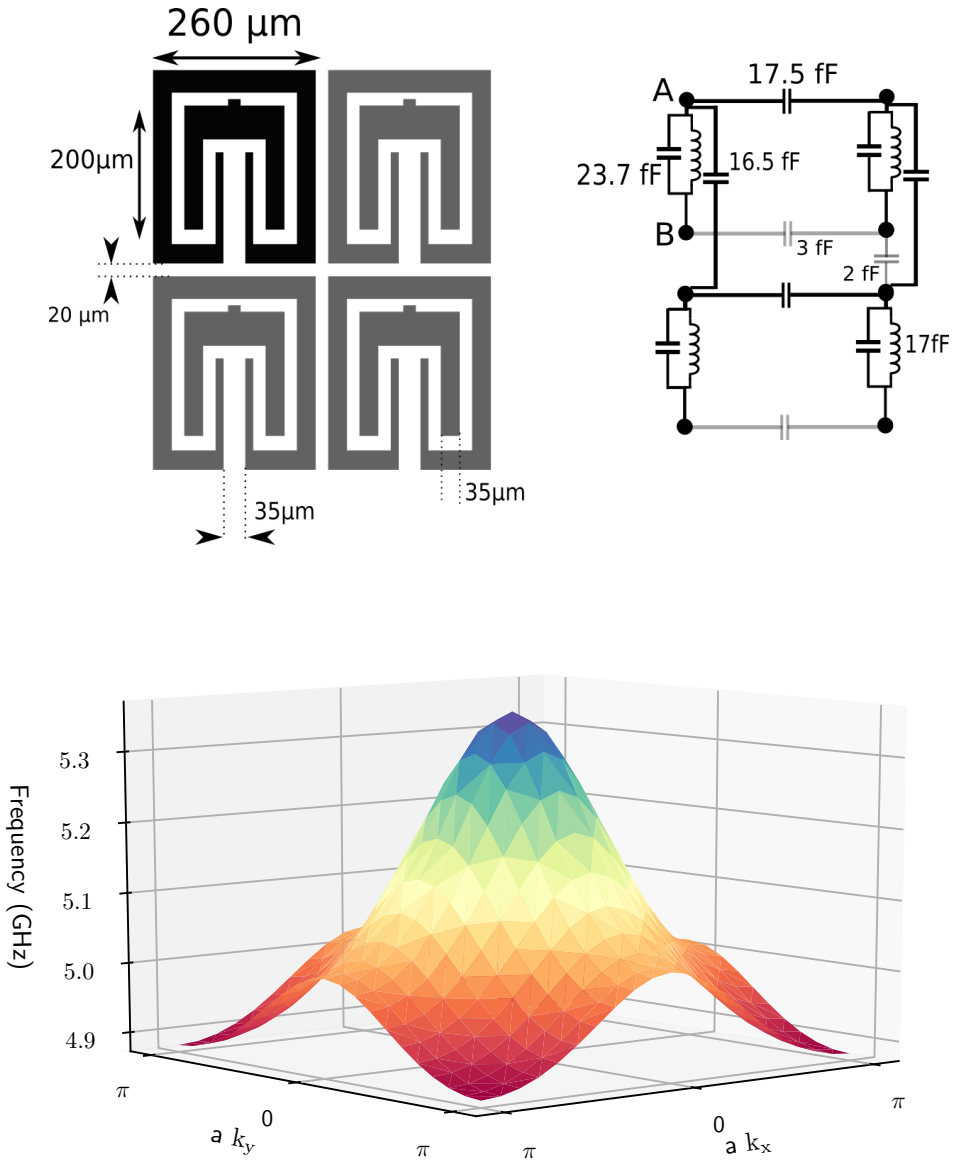

Figure 1.6: Rectangular lattice of transmons coupled through one pad. One of the pad surrounds the other and shields it. The coupling happens via the capacitance to the surrounding pad as shown by the equivalent circuit. The band structure is computed for an inductance $L = 18\,\mathrm{nH}$.

1.3 Input-output formalism for transmon lattices

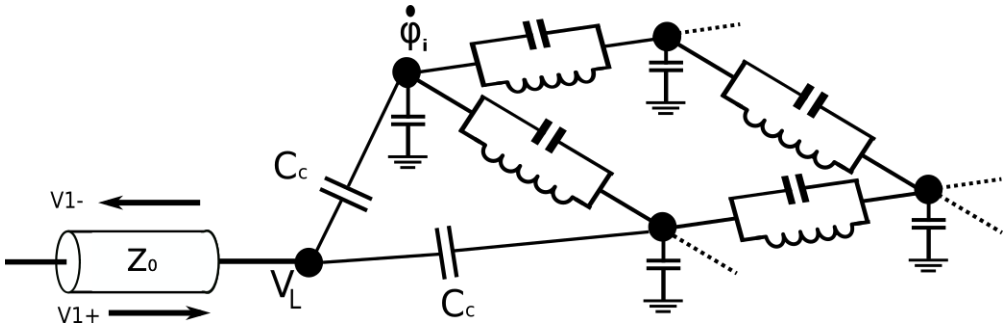

Figure 1.7: Equivalent circuit for the capacitive coupling of a microwave line to a transmon lattice. The line is coupled to the different nodes of the lattice through the vector of capacitance C_L. The voltage at the end of the line V_L is the sum of the ingoing and outgoing waves V_{in} and V_{out}.

In order to inject light into the lattice and retrieve a signal, we couple microwave guides to sites that are located on the edge of the lattice. In this section, we present the input-output formalism that allows us to compute the coupling constant of the normal modes to the measurement lines. Here, we follow a classical formulation but we use the same Born-Markov approximation as usually done in the quantum derivation of the input-output relations for a system coupled to transmission lines [48]. The final equations can therefore be used considering that the quantity α is a classical mode amplitude or a quantum bosonic operator.

We suppose that a line of impedance Z_0 is capacitively coupled to the lattice as shown in figure 1.7. The equation of motion for the lattice is modified to

$$C\ddot{\phi} + K\phi = C_L\dot{V}_L \tag{1.3.1}$$

where V_L is the voltage at the end of the line and the vector C_L contains the capacitance values between the end of the line and each node of the lattice. The diagonal terms of the capacitance matrix C are also modified to include the coupling capacitances C_L. The voltage at the end of the line is the sum of the ingoing and outgoing waves V_{in} and V_{out}. The equation of motion for the V_L is given by the conservation of the current at the end of the line

$$C_L^T(\dot{V}_L - \ddot{\phi}) = Z_0^{-1}(V_{\text{in}} - V_{\text{out}}) \tag{1.3.2}$$

We suppose that the coupling to the line is small at the considered frequency, such that $Z_0^{-1} \ll \omega \sum_i C_{L,i}$. Using $V_L = V_{\text{in}} + V_{\text{out}}$, the previous equation simplifies to

$$V_L \approx 2V_{\text{in}} + Z_0 C_L^T \ddot{\phi} \tag{1.3.3}$$

In the derivation of the input-output relations in quantum optics, this corresponds to the Born approximation. For a fixed V_{in}, the equations of motion for the lattice and the outgoing signal V_{out} are calculated by solving the equations of motion of the lattice

$$\dot{\phi} = C^{-1}q \tag{1.3.4}$$

$$\dot{q} = -K\phi + C_L(2\dot{V}_{\text{in}} + Z_0 C_L^T C^{-1}\ddot{q}) \tag{1.3.5}$$

and using the input-output relation

$$V_{\text{out}} - V_{\text{in}} = Z_0 C_L^T C^{-1}\dot{q} \tag{1.3.6}$$

In the normal mode basis, we obtain

$$\dot{\alpha} = -j\Omega\alpha + j\sqrt{2}T_\phi^T C_L \dot{V}_{\text{in}} + \frac{Z_0}{2} T_\phi^T C_L C_L^T C^{-1} T_q (\ddot{\alpha} - \ddot{\alpha}^*) \tag{1.3.7}$$

The second term is proportional to the amplitude of the ingoing wave and constitutes a source term. In order to put the last term in the usual form of a loss term, we suppose that $\ddot{\alpha} \approx -\Omega^2\alpha$ and we neglect the α^* term. These two approximations correspond to the Markov and the rotating wave approximation in the usual quantum optics derivation. We then arrive at the following equation of motion for the normal modes

$$\dot{\alpha} = -j\Omega\alpha + \eta - \kappa\alpha \tag{1.3.8}$$

with the pump η and the loss κ that are given by

$$\eta = j\sqrt{2}T_\phi^T C_L \dot{V}_{\text{in}} \tag{1.3.9}$$

$$\kappa = \frac{Z_0}{2} T_\phi^T C_L C_L^T T_\phi \Omega^3 \tag{1.3.10}$$

The last formula generalizes the formula for the loss of a LC resonator coupled to a line to the case of a lattice. We will see in the next chapter that it is given by

$$\kappa = \frac{Z Z_0 C_L^2 \omega^3}{2} \tag{1.3.11}$$

where $Z = \sqrt{L/C}$ and $\omega = 1/\sqrt{LC}$. If the line connects only to one node i_L through a capacitance C_L, as this is often the case in our designs, the loss rate of the mode μ simplifies too

$$\kappa_\mu = \frac{Z_0 C_L^2 \Omega_\mu^3}{2} T_{\phi, i_L \mu}^2 \tag{1.3.12}$$

With the same approximations, the input-output relation becomes

$$V_{\text{out}} - V_{\text{in}} = -\frac{Z_0}{\sqrt{2}} C_L^T T_\phi \Omega^2 \alpha \tag{1.3.13}$$

1.4 Design of the rectangular lattice sample

In this section, we present the detailed design of the rectangular lattice that is measured in chapter four. It corresponds to the sample labeled MF56. This lattice was taken as an example of band structure calculation in the section 1.2. Here, we show how we adjust the edges of the lattice and the coupling to the measurement lines in order to obtain the final design.

1.4.1 Edge and corner resonators

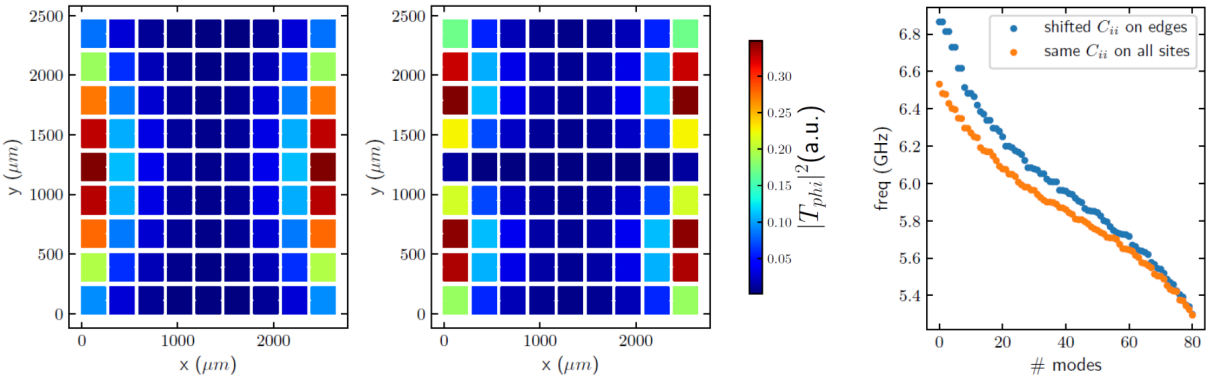

Figure 1.8: Spatial distribution of the two highest frequency modes of a 9 by 9 lattice without corrected self-capacitance. The modes are localized on the edges. The right plot shows the spectrum of the lattice in blue and compares it to the one of a lattice where all the pads have the same self-capacitance in orange.

The design of the bulk of the lattice is shown in figure 1.4. If the lattice is abruptly ended, the self-capacitance of the pads located on the edge is significantly smaller than for a pad in the bulk. Figure 1.8 shows the modes of a 9×9 lattice in this situation, we clearly see that modes localized at the edges appear. In order to recover the same self-capacitance for the pads on the edge and in the bulk, we add a ground plane around the lattice and adjust the distance between the edge resonators and the ground plane (see figure 1.9).

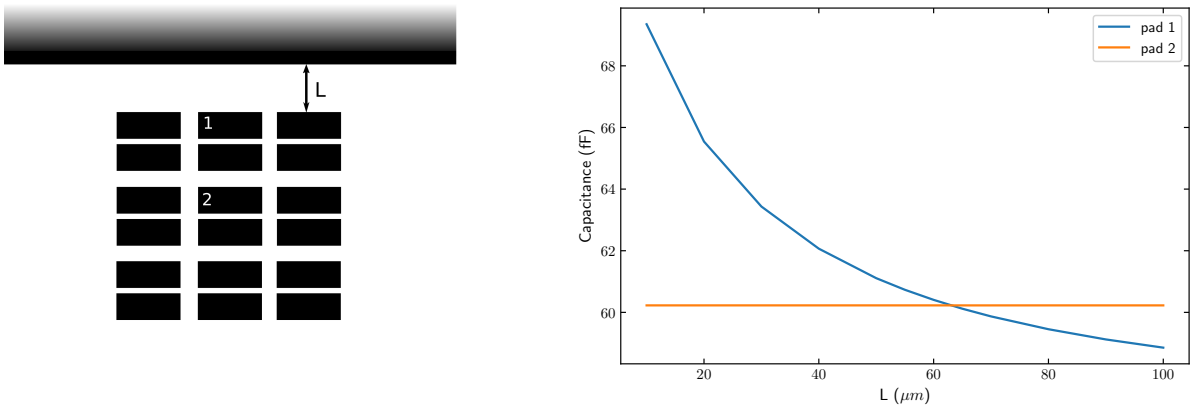

Figure 1.9: Left: simulated geometry to adjust the self-capacitance of pads located at the edge of the lattice. Right: Variation of the self-capacitance of the pads 1&2 as a function of L. In the final design, we choose L such that these two values are equal.

1.4.2 Coupling to the measurement lines

The design of the coupling to the measurement lines for the MF56 lattice is shown in 1.10. Four coplanar waveguides are capacitively coupled to one pad of the the transmon resonators located at each corner of the lattice. The penetration of the line inside the pad and the different distances have been adjusted in order keep the self-capacitance of the coupled node to its bulk value. The figure also shows the coupling κ_μ for the modes of a 40×20 lattice. We observe that the high frequency modes only weakly couple to the lines, because of their small weight on corner sites.

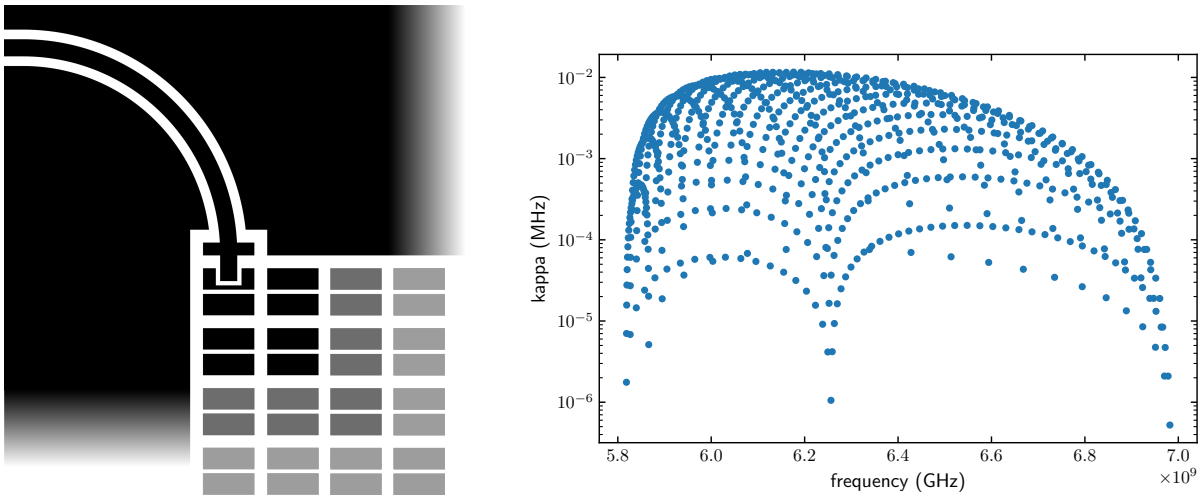

Figure 1.10: Left: Geometry used to couple a coplanar waveguide (CPW) to the transmon located in the corner of the MF56 lattice. The CPW line has a 50 Ω impedance with a central strip of 80 μm wide and two 45 μm wide slots. The coupling capacitance is $C_c = 20\,\mathrm{fF}$. Right: Coupling rates of the different modes of a 40 by 20 lattice corresponding to the coupling geometry shown on the left with $L = 18\,\mathrm{nH}$.

Because we want to be able to experimentally measure the amplitude of these modes, we adjust the frequency of the corner sites by changing the inductance of the transmon in order to increase the coupling. The corner resonators act as a filter between the lattice modes and the line. The figure 1.11 shows the variation of the frequency of the twenty highest frequency modes while increasing the frequency of one corner resonator. It also shows the variation of the coupling rates for the five highest frequency modes and the modes 50 & 100. As the frequency of the corner resonator increases and crosses the bulk modes, avoided crossings appear. Modes with a frequency close to the avoided crossing highly couple to the line. When the frequency of the corner site is above the band of the lattice, a localized corner mode appear. This new mode does not participate to the dynamics of the lattice, but enhances the coupling of the high frequency modes as desired.

Taking into account all the design decisions mentioned above, we converged to the MF56 design shown in 1.13. The number of sites is 20×40 for a total size of $5.6\,\mathrm{mm} \times 13.6\,\mathrm{mm}$. With a transmon inductance $L = 18\,\mathrm{nH}$ on bulk resonators and $L = 14.5\,\mathrm{nH}$ on the four corners, the simulated frequencies of the normal modes are shown in 1.12, where we also show the spatial dependence of two modes. The mode 5 shown at the top left is the highest frequency mode of the lattice after the four corner modes.

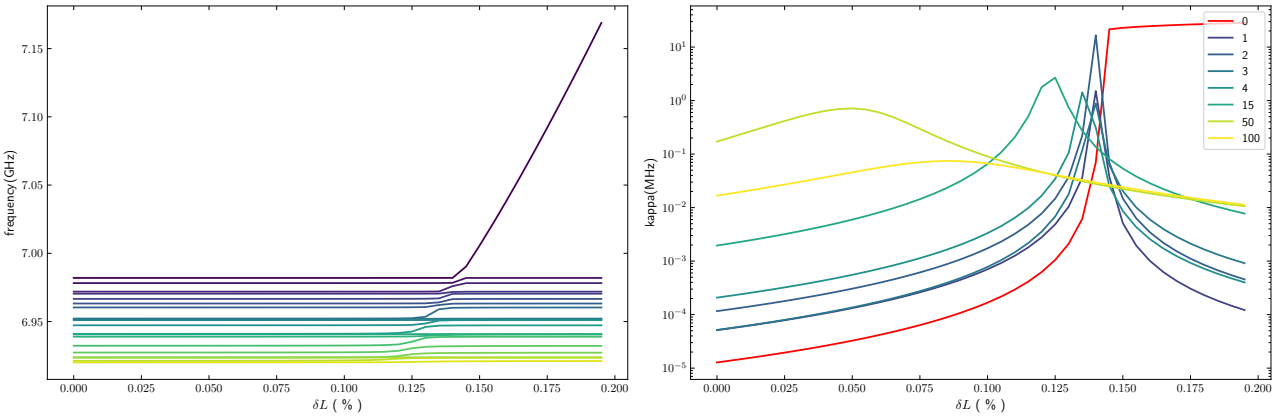

Figure 1.11: Left: Frequency of the 20 highest frequency modes as a function of the inductance of the corner resonators that are coupled to the measurement lines. Right: Evolution of the coupling rates of the five highest frequency modes and two bulk modes.

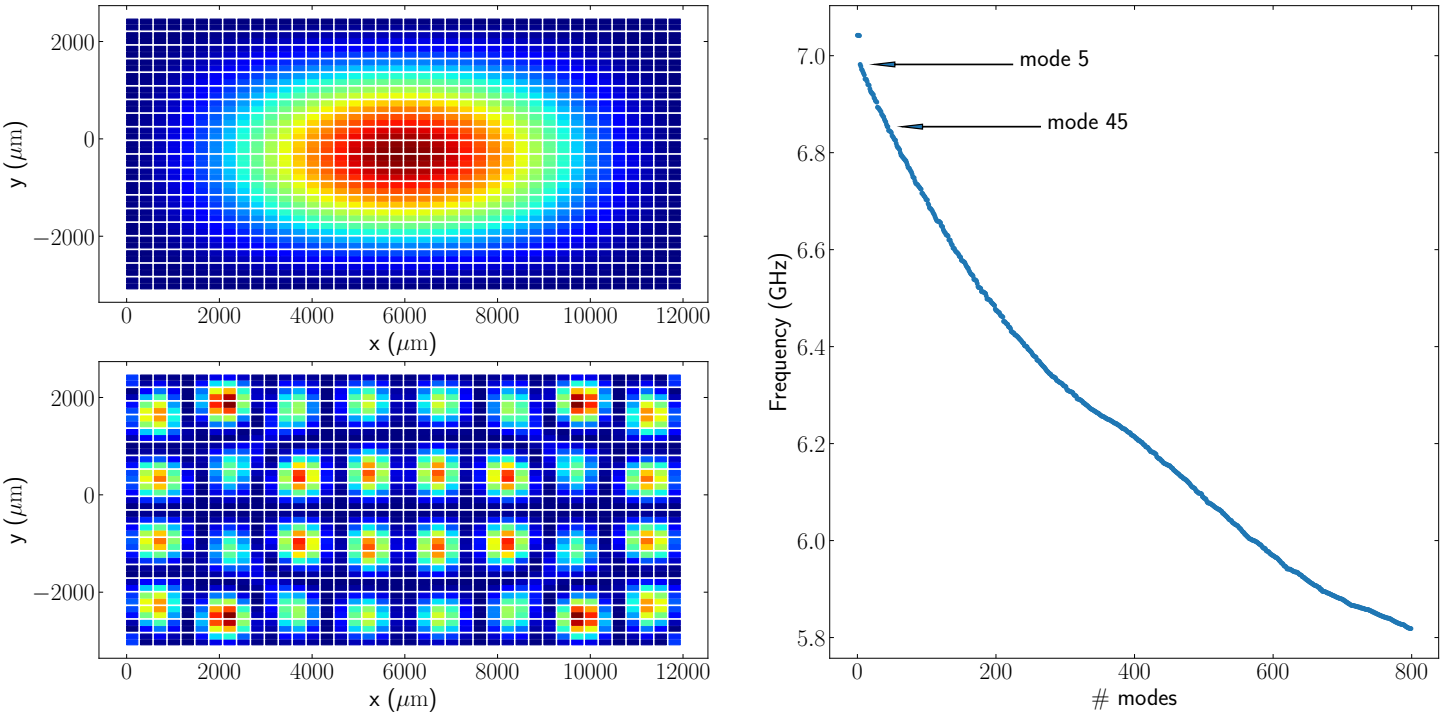

Figure 1.12: Normal modes of the MF56 design with a transmon inductance of $L = 18\,\mathrm{nH}$ on bulk resonators and $L = 14.5\,\mathrm{nH}$ on the four corners. The right plot shows the normal mode frequencies as a function of the mode index. The left plot shows the intensity of the frequency mode (mode 5) on the top and the mode with index 45 on the bottom.

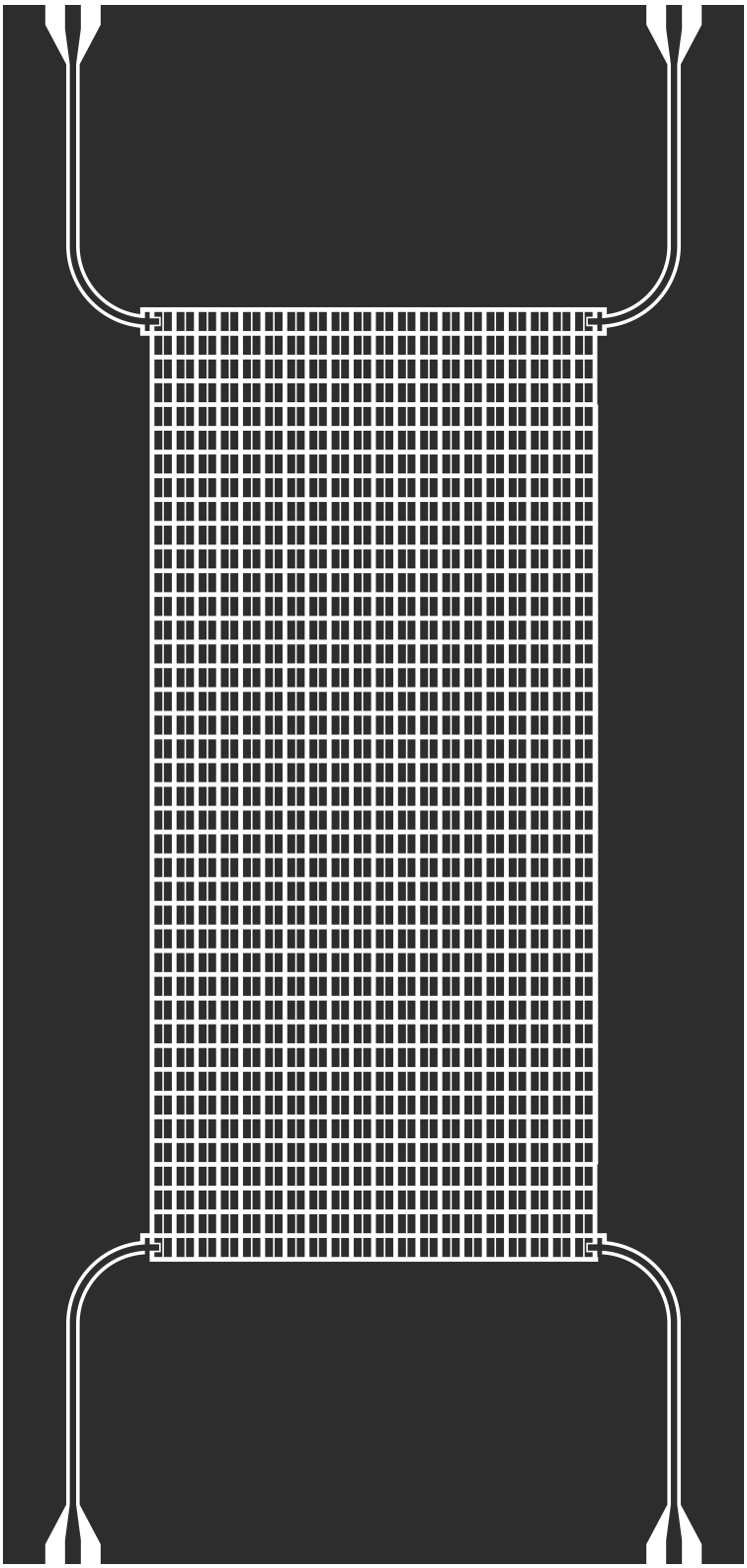

Figure 1.13: Design of the MF56 sample including the measurement lines. The lattice is a 20×40 rectangular lattice, the sample overall size is 10 mm × 20 mm.

1.5 Design of the Lieb lattice sample

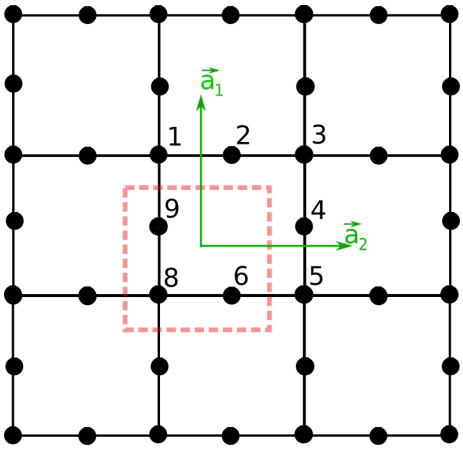

Figure 1.14: Geometry of the Lieb lattice. The unit cell is represented by the dotted red square. The two primitive lattice vectors a_1 and a_2 are represented in green. The eigenstates of the flat band are localized on the sites with two neighbors, for example the sites labeled 2,4,6 and 9.

The Lieb lattice is a tight-binding model with a band structure that includes a flat band, *i.e* a band with zero dispersion. The eigenstates of the flat band are localized plaquette states distributed on four sites. Such lattices are interesting, because the smallest perturbation such as disorder or non-linearity is hence the dominant energy scale [49–51].

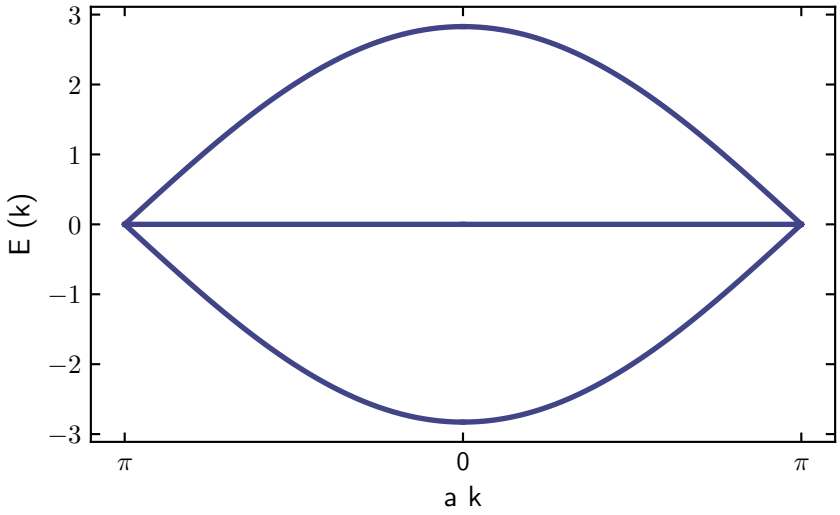

Figure 1.15: Band structure of a Lieb lattice with hopping $J = 1$.

Figure 1.14 shows the geometry of the Lieb lattice. The unit cell contains three sites and the underlying Bravais lattice is a square lattice with the primitive vectors a_1 and a_2. When all hopping terms are equal, the resulting band structure is shown in figure 1.15 with two dispersive bands and a flat band at zero energy. With the notation of figure 1.14, the flat band state localized in the central square is the combination

$$a_s = a_2 - a_4 + a_6 - a_9 \tag{1.5.1}$$

where the operator a_i corresponds to the amplitude on the i site.

1.5.1 Electric Lieb lattice

Figure 1.16 shows a circuit inspired from the Lieb lattice. The unit cell contains three nodes, as in the original Lieb lattice, but only two resonators. We therefore expect that the band structure only contains two bands.

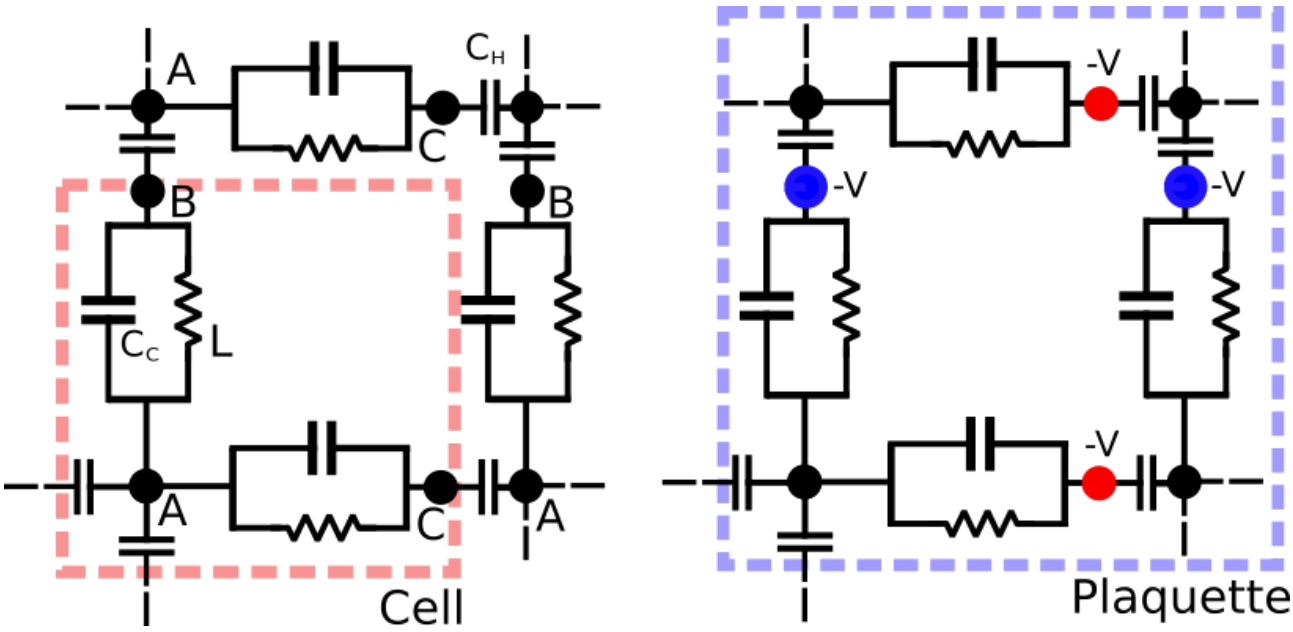

Figure 1.16: Lattice circuit based on the Lieb lattice. The unit cell shown in red on the left contains three nodes but only two independent degrees of freedom. Each node may also include a capacitance to the ground that is not shown. If the B and C nodes are not connected and if the circuit is symmetric by reflection along $a_1 + a_2$, then localized states as shown in the blue plaquette on the right may be solution of the circuit equations. They have zero amplitude on the A nodes and opposite amplitudes on the B and C nodes.

The admittance matrix in the Fourier space as defined in 1.2.20 is

$$Y[k,\omega] = \begin{pmatrix} Y_{AA}[k,\omega] & Y_{AB}[k,\omega] & Y_{AC}[k,\omega] \\ Y_{BA}[k,\omega] & Y_0[\omega] & 0 \\ Y_{CA}[k,\omega] & 0 & Y_0[\omega] \end{pmatrix} \tag{1.5.2}$$

where the Y_{BC} and Y_{CB} terms are zero because of the connectivity of the circuit. By construction Y_{BB} does not depend on k, because the B node is not connected to another B node in a neighboring cell. The same applies to the C node. If we suppose that the circuit has a symmetry such that $Y_{BB}[\omega] = Y_{CC}[\omega] \equiv Y_0[\omega]$, we arrive at the general form of admittance matrix written above. The resonant condition $\det Y(k,\omega) = 0$ then gives

$$Y_0[\omega](Y_{AA}[\omega,k]Y_0[\omega] - Y_{AB}[k,\omega]Y_{BA}[k,\omega] - Y_{AC}[k,\omega]Y_{CA}[k,\omega]) = 0 \tag{1.5.3}$$

which leads to a flat band defined by the resonant condition $Y_0[\omega] = 0$.

We now go back to real space and consider a mode localized in one square plaquette (with eight nodes) such that $V_A = 0$ on all A nodes as shown in figure 1.16. In order to be solution of the circuit equation 1.2.8, the voltages V_B and V_C must fulfill

$$Y_{AB}[\omega]V_B + Y_{AC}[\omega]V_C = 0 \tag{1.5.4}$$
$$Y_0[\omega]V_B = 0 \tag{1.5.5}$$
$$Y_0[\omega]V_C = 0 \tag{1.5.6}$$

At the frequency of the flat band, the last two equations are verified and the first equation fixes the ratio between V_B and V_C that define the localized flat band modes. Supposing that the lattice has a symmetry such that $Y_{AB}[\omega] = Y_{AC}[\omega]$, we obtain $V_B = -V_C$. All the flat band modes are obtained by considering one localized mode per square plaquette.

In the simple circuit considered in figure 1.16, the unit cell contains two LC resonators with inductance L and capacitance C_c coupled by hopping capacitances C_h. Each pad also has a capacitance to the ground C_g. The dispersion of the two bands are then given by

$$\omega_{\text{flat}} = \frac{1}{\sqrt{L(C_g + C_c + C_h)}} \tag{1.5.7}$$

$$\omega_{\text{dispersive}} = \frac{1}{\sqrt{L\left(C_c + \frac{C_g(C_g+3C_h)}{3C_g - 2C_h(\cos k_x a + \cos k_y a - 2)}\right)}} \tag{1.5.8}$$

The flat band is located below the dispersive band which has a minimum at $k_x = k_y = 0$. The dispersive band is quadratic around this minimum with a positive effective mass. It is interesting to note that we obtain an effective mass with the opposite sign compared to the rectangular lattice of the previous section.

1.5.2 Capacitance design of a Lieb lattice

Figure 1.17 shows a simple design to realize the circuit discussed above using metallic pads and superconducting inductive elements. The figure also shows the calculated band structure. The lower band is much flatter than the upper one, but it is not entirely flat because of the parasitic coupling between the B and C nodes.

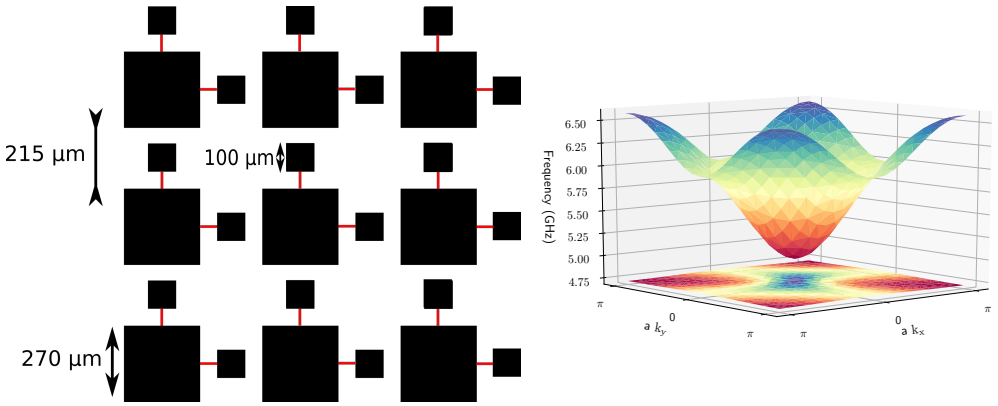

Figure 1.17: Simple design to realize the Lieb circuit shown in figure 1.16. The right plot shows the calculated band structure with an inductance (red wire) of 25 nH. One clearly sees the flat band below the dispersive band.

The design shown in figure 1.18 improves the band flatness by using the A pad to shield the B and C pads in order to minimize their coupling. The parasitic capacitance between B and C is reduced to 1.2 fF and must be compared to the 43 fF capacitance between A and B (or C).

1.5.3 Edge and corner resonators

For the Lieb lattice, we decided not to have a ground plane surrounding the lattice. Therefore, we have to change the design of the edge A pads in order to keep the value of the self-capacitance to the bulk value. Figure 1.19 shows the geometry simulated in Sonnet in order to obtain the correct self-capacitance.

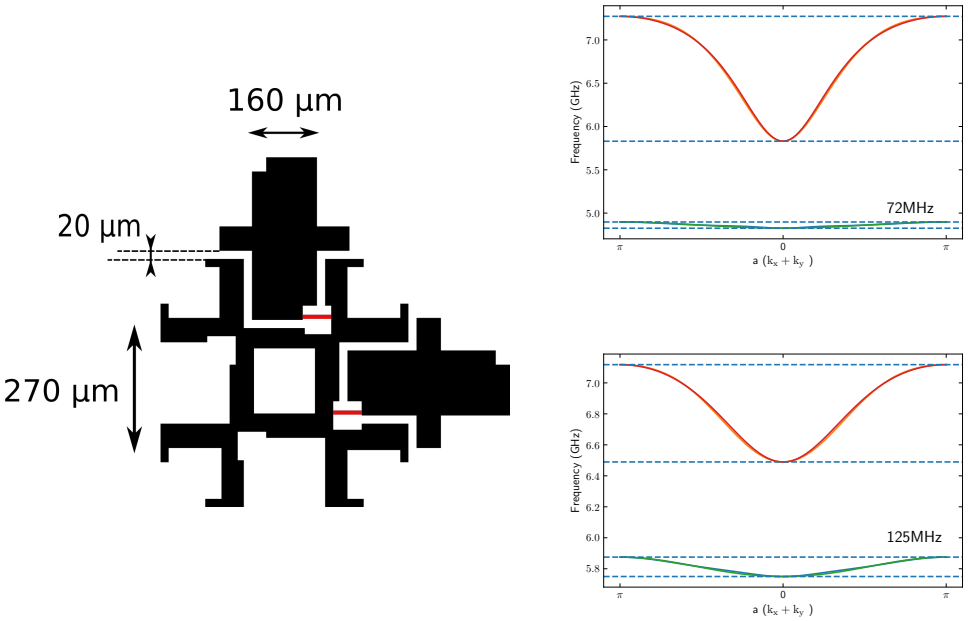

Figure 1.18: Improved design for the Lieb circuit. The A pad is used to shield the B and C pads so that they do not couple capacitively. The two right plots show a cut of the band structure in the $x+y$ direction. The upper (lower) plot corresponds to the improved (basic) design showing how the band flatness improves by a factor four. The inductance for the improved design is 10 nH.

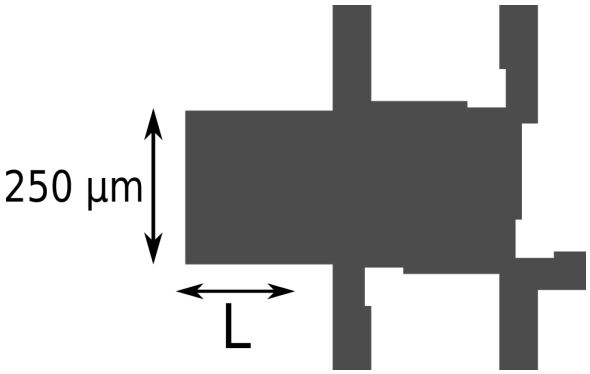

Figure 1.19: Simulated geometry for the A pads located at the circuit edges. The result of the simulation is that the self-capacitance of the edge pad is equal to the one in the bulk if $L = 210\,\mu$m.

1.5.4 Effect of disorder on the flat band

The main source of disorder in the architecture considered in this chapter comes from the dispersion of the inductive elements, which can either be Josephson junctions or HKIS wires. This is a well-known problem for Josephson junctions and a major issue to build large circuits with many transmon qubits [52]. At the time we started to work with HKIS wires, it was not known if they would disperse more or less than junctions. We have now learned that GrAl wires also experience disorder because of inhomogeneities in the material properties across the sample. We will give more details about this in chapter four. When designing the Lieb lattice, we decided to obtain a design where the gap between the flat and the dispersive band would not close including a 5% dispersion of the inductances.

The gap between the bands can be adjusted by varying the capacitance to the ground of the A node. We use the design of figure 1.18 and numerically compute the frequencies of the normal modes of 9 by 9 plaquette lattice for various ground capacitance of the A node as shown in figure 1.20. For a ground capacitance of 50 fF, we find that the gap is large enough such that a 4% disorder on the inductance does not close the gap as shown in the right plot of the figure.

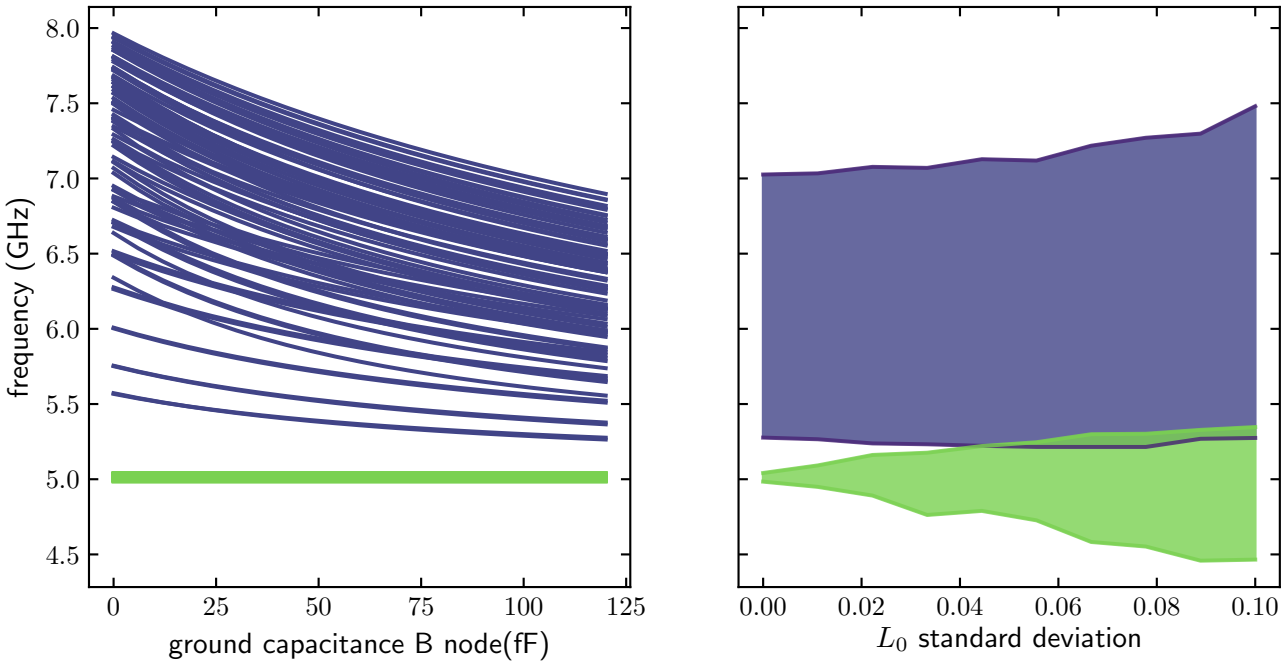

Figure 1.20: Left: Normal mode frequencies of a Lieb circuit based on the design of figure 1.18 except for the value of the ground capacitance of the A node that is varied. The gap closes when the capacitance increases. Right: Evolution of the band widths including gaussian fluctuations of the inductance for a ground capacitance of 50 fF. The gap closes when the standard deviation of L reaches 4.5%.

1.5.5 Coupling to the measurement lines

The final design for the Lieb lattice is shown in figure 1.21. It consists of a 8×8 square plaquettes with 144 resonances as shown in 1.24. The lattice is coupled to four measurement lines that capacitively couple to A and B nodes. Following the same reasoning as for the MF56

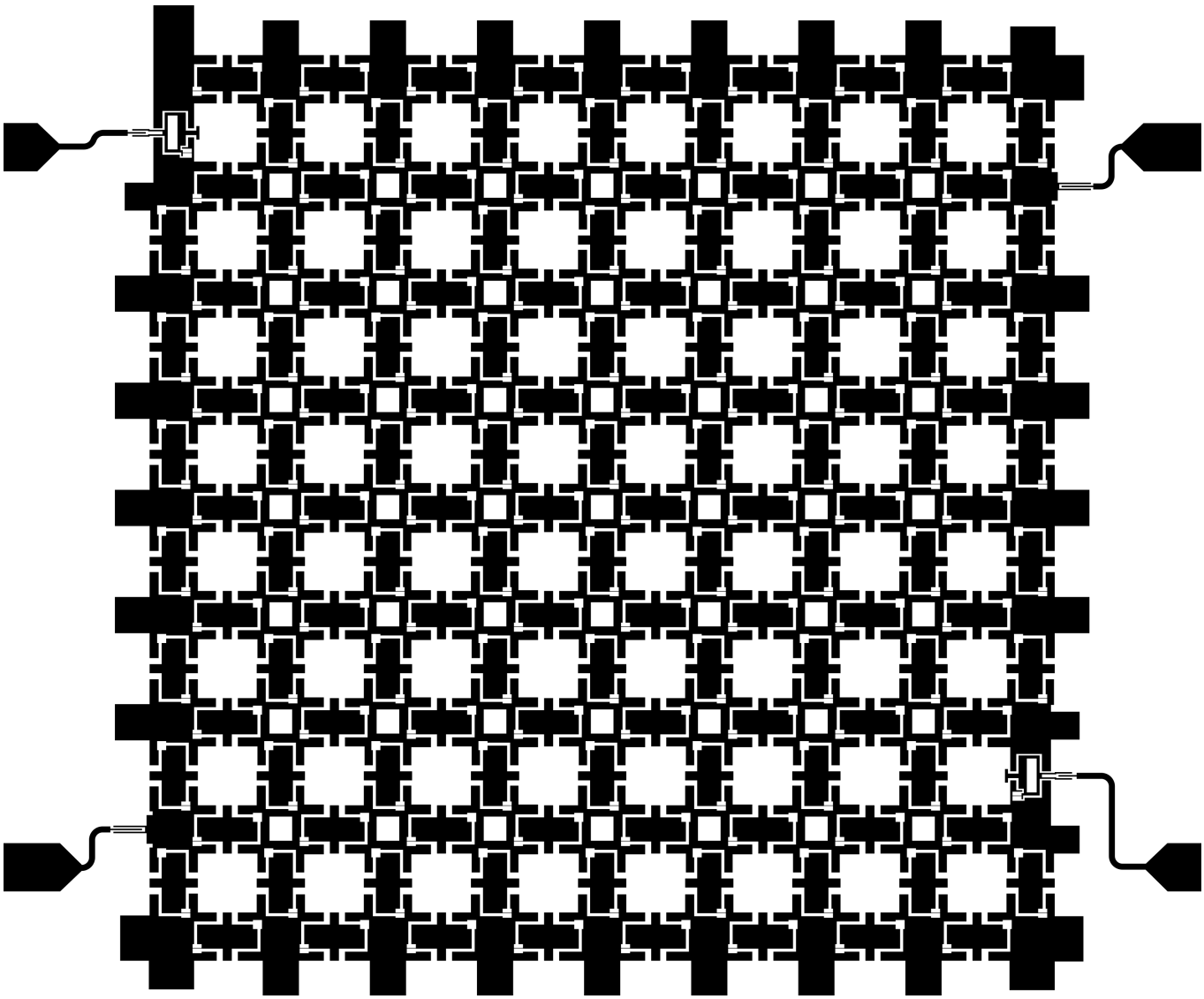

Figure 1.21: Design of the Lieb lattice sample including the measurement lines. The sample overall size is 8 mm×8 mm.

lattice, the pads corresponding to a coupled node are adjusted so that the capacitive coupling to the line does not change its self-capacitance. A close-up on the geometry of the coupled pads is shown in figure 1.22. The corresponding coupling rates are shown in figure 1.23.

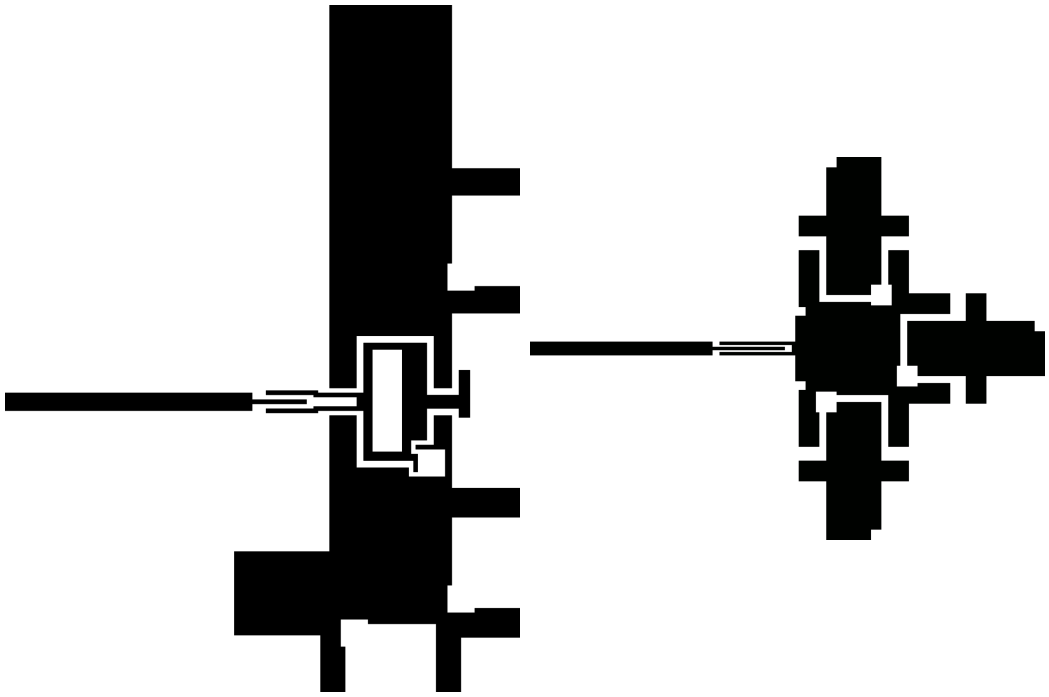

Figure 1.22: Left: Design for the coupling of a 50 Ω micro-strip line to a B node of the Lieb lattice. The coupling capacitance is 16 fF. Right: Same for a A node. The coupling capacitance is 3 fF.

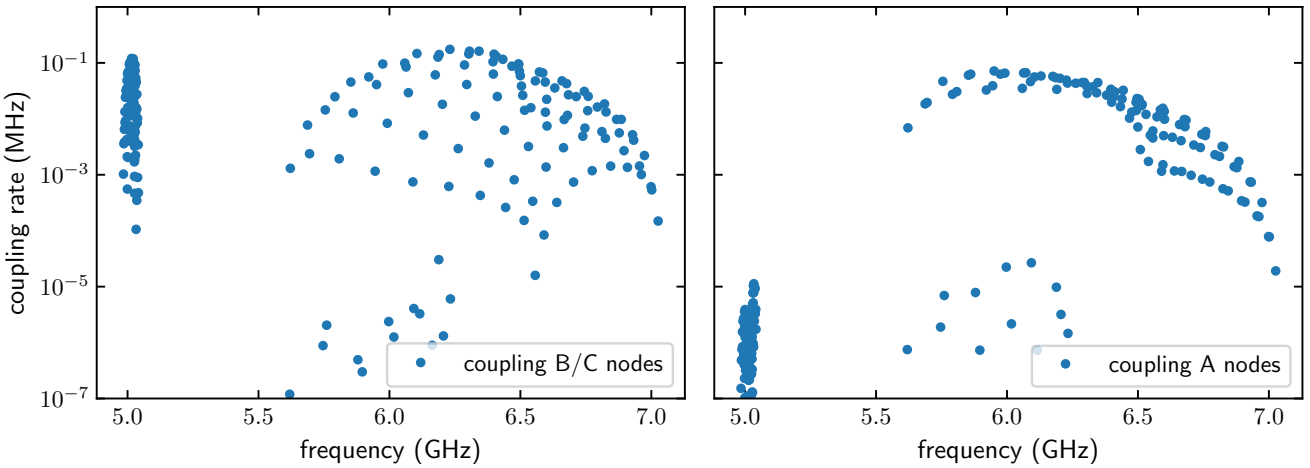

Figure 1.23: Coupling rates κ_μ of the normal modes of the lattice shown in figure 1.21 with an inductance of 7.5 nH. The left (right) plot corresponds to the coupling rates to a line coupled to a A (B) node. As expected, the line coupled to the A node only weakly couple to the flat band modes.

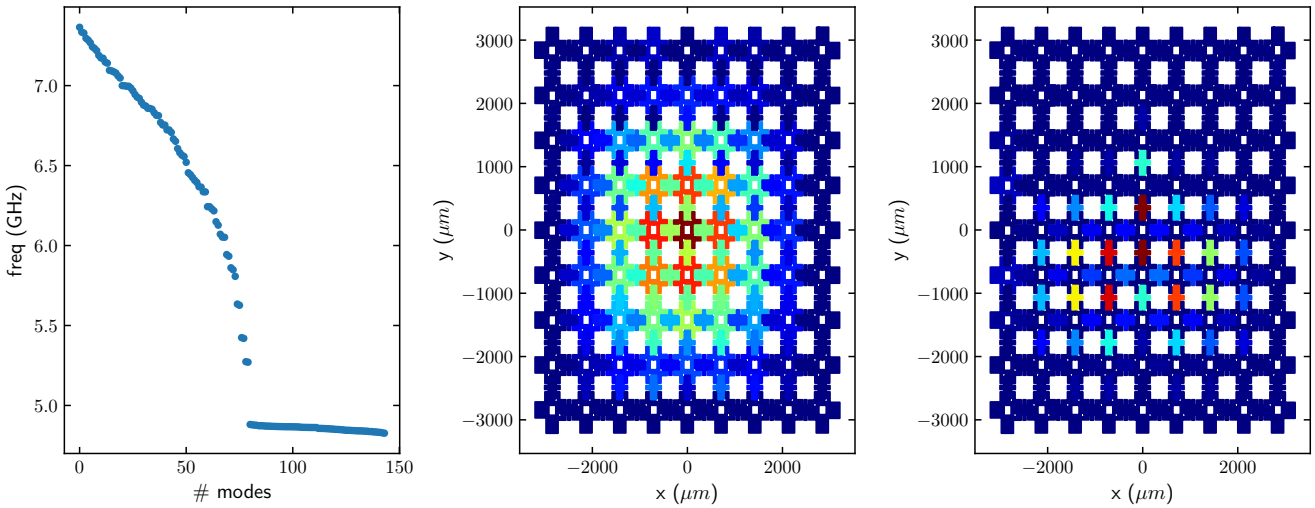

Figure 1.24: Normal modes frequencies of the Lieb sample shown in 1.21 with an inductance of 7.5 nH. The left plot shows the normal mode frequencies as a function of the mode index. The two right plots show the intensity of one mode of the dispersive band (center) and one mode of the flat band (most right).

Conclusion

In this chapter we presented non-linear microwave resonators using high kinetic inductance superconducting wires. We showed the difference in scaling between a Josephson junction transmon and a HKIS transmon resonator. We then presented a formalism for lattices of electrical nodes with purely capacitive coupling. We used this formalism in addition to simulation of electrical designs to compute the band structure of an infinite lattice, the eigenmodes of a finite version of it and input-output formalism for the coupling of the lattice to a microwave guide. We then applied these results to the full design of a rectangular lattice and Lieb lattice. We presented the parameters chosen for both lattice and the coupling to the microwave guides chosen in each case. We described the emergence of a flat band in the Lieb tight-binding lattice and showed its relationship with our electrical design.

Chapter 2

Characterization of a granular Aluminium Resonator

Contents

The implementation of kinetic inductances made by disordered superconductors as building blocks of circuit QED systems is still a relatively new technique and brings new possibilities in circuit design. More specifically Granular Aluminium (GrAl) as shown in recent experiments [26, 31, 46, 53, 54], is an interesting source of kinetic inductance as well as non-linearity because its intrinsic low losses. However, the choice of the more reliable deposition technique and the ultimate reproducibility of thin films are still in question. This is because the electronic properties of GrAl have been found to be very dependent on the deposition technique, lithography and design as well as the specific evaporation setup. Therefore, we wish to characterize our GrAl resonators and compare them to the existing literature. In the first part of this chapter we will address the expected theoretical relationships between the parameters of GrAl: the inductance, resistance per square, critical temperature, and non-linearity of the inductance. We will then illustrate the lithography and evaporation techniques used in this thesis. We will compute the non linearity of an LC resonator containing a non-linear inductance and present the measurement of 3 resonators whose inductance is made by a mesoscopic wire of GrAl. From the measure of the non linearity and resonant frequency, we will extract the critical current density and compare it to the expected value from DC experiments.

2.1 Granular aluminium wire as an inductance in a resonator

2.1.1 Kinetic energy and kinetic inductance of Cooper Pair

In the Drude theory of normal metals, the AC-conductivity is given by the expression :

$$\sigma(\omega) = \frac{\sigma_0}{1 + j\omega\tau} \tag{2.1.1}$$

with $\sigma_0 = ne^2\tau/m$ being the DC conductivity. The collision time τ is typically around 10^{-14} s in normal metals and thus the impedance mostly resistive in the GHz regime. However, for a superconductor where $\sigma_0 \to \infty$ and $\omega\tau \to \infty$ the superflow is characterized by a zero resistance at low frequency, but also an inductive response inversely proportional to the carrier density. Physically, the carriers have a mass and thus a kinetic energy associated to them. Following the Mattis-Bardeen theory it is possible to estimate the dissipative and inductive parts of the admittance of a superconducting thin film in the dirty limit from the BCS theory. The result for the complex conductivity $\sigma(\omega) = \sigma_1(\omega) - j\sigma_2(\omega)$, is :

$$\frac{\sigma_1(\omega)}{\sigma_0} = \frac{2}{\hbar\omega}\int_{\Delta}^{\infty} dE \frac{E^2 + \Delta^2 + \hbar\omega E}{\sqrt{E^2 - \Delta^2}\sqrt{(E+\hbar\omega)^2 - \Delta^2}} \left[f(E) - f(E+\hbar\omega)\right] \tag{2.1.2}$$

$$\frac{\sigma_2(\omega)}{\sigma_0} = \frac{1}{\hbar\omega}\int_{\Delta}^{\Delta+\hbar\omega} dE \frac{E^2 + \Delta^2 - \hbar\omega E}{\sqrt{E^2 - \Delta^2}\sqrt{\Delta^2 - (E-\hbar\omega)^2}} \left[1 - 2f(E)\right] \tag{2.1.3}$$

where Δ is the superconducting energy gap. For $T \ll T_c$ and $\hbar\omega \ll \Delta$, we find $\sigma_1 \to 0$ for $\omega \neq 0$ and :

$$\frac{\sigma_2(\omega)}{\sigma_0} = \frac{\pi\Delta}{\hbar\omega} \tag{2.1.4}$$

The critical temperature, T_c, of GrAl is about 2 K which is much higher than our working point of 10 mK and for typical frequency of about 6 GHz, the ratio $\hbar\omega/\Delta \approx 1\%$. Therefore a superconducting wire at this frequency and temperature is mainly an ideal inductor and dissipation can be neglected. This is a key result for applications of disordered superconductors

in quantum circuits. Using the definition of the normal sheet resistance, i.e. $\sigma_0 = (R_\square t)$, where t is the thickness of the wire, we can find the inductance per square $L_\square$, also called sheet inductance:

$$L_\square = \frac{1}{\omega\sigma_2 t} = \frac{\hbar R_\square}{\pi\Delta_0} \tag{2.1.5}$$

We can give an estimate of such an inductance. The value of the superconducting gap is given by the BCS relation $\Delta = 1.76K_BT_c$. As the elastic scattering time dominates the resistivity even at T=300K, the resistance doesn't change significantly lowering the temperature. We can then use the room temperature value of the sheet resistance $R_\square$. We find that for $R_\square$ of about 1000 $\Omega/\square$, the inductance per square is about 0.7 nH. As a comparison the geometrical inductance of the wire is in the order of 0.005 nH/$\square$

2.1.2 Non linear term for LC resonator with a kinetic inductance

We wish now to address the non-linearity in the inductive response of a superconducting wire to an electromagnetic excitation. We have shown in the previous paragraph that the sheet inductance is proportional to the sheet resistance and inversely proportional to the energy gap. The sheet resistance is fixed by material parameters and can not be changed by an electromagnetic excitation, but the same is not true for the energy gap. In fact, the energy gap depends on the supercurrent flowing through the wire. In particular, increasing the amplitude of the microwave current through the superconductor reduces its energy gap. Physically the reason is that the condensation energy of the superconductor is reduced by the kinetic energy of the supeflow. This effect provides a mechanism for non-linearity. More importantly it doesn't introduce any dissipation as the supercurrent weakens the superconducting gap without creating quasiparticles. Thus a disordered superconducting wire is a non-dissipative non-linear inductor. The exact dependance of the inductance on current is difficult to obtain analytically but, for disordered superconductors, the current induced gap changes can be calculated using the Usadel and self-consistent gap equations as reported in [55]. This system of equations can be solved numerically, however in the limit of a small drive current density, J, much smaller than the critical current density, J_c, a linear expansion gives an analytical expression for Δ which for a narrow wire is :

$$\Delta(\Gamma) = \Delta_0 - 0.75\Gamma \tag{2.1.6}$$

where Δ_0 is the energy gap at $J = 0$ and Γ is the depairing parameter due the current driven though the wire. It's interesting to note that this expression of Δ as a function of Γ is universal and it doesn't depend on the particular depairing mechanism at work. This is a consequence of a fundamental aspect of the BCS theory, namely that any time reversal breaking symmetry mechanism is pair-breaking as pointed out in [56]. In the same limit of low current, we get

$$\Gamma = 0.115\frac{J^2}{J_c^2}\Delta_0 \tag{2.1.7}$$

where $J_c = 0.75\Delta_0^{1.5}\sqrt{N_0\sigma_0/\hbar}$ and N_0 is the density of states at the Fermi level in the normal state. Therefore the energy gap goes as :

$$\frac{\Delta}{\Delta_0} = 1 - 0.09\frac{J^2}{J_c^2} \tag{2.1.8}$$

From this dependance of the gap and replacing it in the equation 2.1.5 we obtain the expected current dependance of the inductance at first order in I :

$$L = \frac{\hbar R_\square}{\pi\Delta(1 - 0.09\frac{I^2}{I_c^2})} \approx L_0(1 + \frac{I^2}{(I^*)^2}) \tag{2.1.9}$$

where $I^* = 3.3I_c$ and I_c is the critical current. We should remind here that this approach is valid at current amplitudes that are low compared to I_c.

Also following calculations from [44] using the BCS theory, it is possible to obtain the dependance of the inductance with the parameter $\zeta = Dk^2/2\Delta$, k being the current induced phase gradient and D the diffusion coefficient. The inductance is given by the expression :

$$L = L_0 \frac{1}{e^{-\pi\zeta/4}} \tag{2.1.10}$$

Moreover the ratio I/I_c is also a function of ζ:

$$\frac{I}{I_c} = 1.897e^{-3\pi\zeta/8}\sqrt{\zeta}(\frac{\pi}{2} - \frac{2\zeta}{3}) \tag{2.1.11}$$

The curve obtained by inverting 2.1.11 and introducing the result in 2.1.10 is shown in figure 2.1

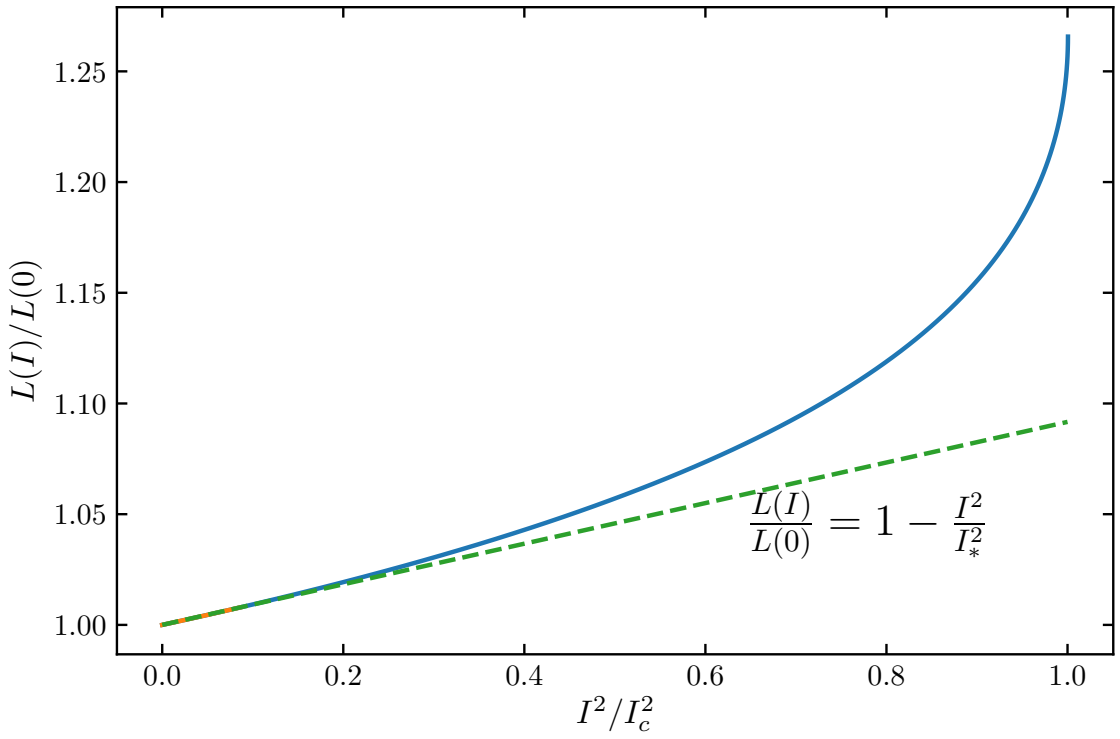

Figure 2.1: Variation of the inductance with square of the ratio of current over critical current.

At low current we get numerically the same value of the non-linear coefficient found above using the Usadel equations. Another equation using [57] writes a direct relationship between the kinetic inductance and critical current. we have yet to include and compare this result to the BCS equation showed previously.

Therefore a GrAl superconducting wire has a known inductance which can be reliably estimated from its critical temperature and its resistance at room temperature, and a non-linearity which can be estimate from its critical current. This makes it a perfect candidate as non-linear element in a quantum circuit.

2.1.3 Losses and TLS

Different loss mechanisms are present in superconducting circuits and precisely measuring the noise sources at the origin of these losses is an active research area [58, 59] Some of those mechanisms can be enhanced by the presence of a disordered material in the resonator. One possible way of explaining losses in our system is linked with the presence of Two Level Systems at the dielectric interfaces.

These Two-Level Systems (TLS) at the interfaces and in the insulator substrate couple to the superconducting electrons and induce decoherence. One interpretation of these TLS induced losses is their electric resonant coupling to the resonator [60]. In [61], the authors propose that the TLS around the kinetic inductance originate quantum fluctuations, δG, of its conductance G which at the end create a distribution of resonator's resonance frequency, f . The width of the distribution is δf such that

$$\frac{\delta f}{f} = \frac{\delta G}{G_N} \tag{2.1.12}$$

where the resonator's inductance is given by inductive granular wire.

As in the theory of quantum correction to the conductance, here the key parameter is the single electron coherence length, L_ϕ. If dephasing induced by the TLS is at work, the authors in [61] argue that the maximum quality factor $Q_{TLS}^{-1} = \delta f/2f$ where each conductance channel is maximally coupled to a TLS can be written :

$$Q_{TLS}^{-1} = \left(\frac{L_\phi}{l}\right)^{3/2} \frac{l}{w} G_k R_\square \tag{2.1.13}$$

where l and w are the length and width of the wire and $G_k = 1/R_k$ the quantum of conductance.

Reducing the wire width and thickness, reduces the number of channels, thus increasing the fluctuations of each channel. This effect would restrains the possibility of using narrow and thin wires of GrAl. In the subsequent experiment, we do see a qualitative decrease of the quality factor with a narrowing of the inductive wire but we won't be able to point to a specific approach that explains quantitatively the losses of our system.

Other research points to out-of-equilibrium quasi-particles as a possible explanation for the microwave losses [30] and gives a model of quasi-particle relaxation with photon number that also explains the power variation usually used as a smoking gun for TLS losses. Namely the saturation of the fluctuations at high microwave power. At the core of this model the authors argue that because the superconductor is disordered a portion of quasi-particules is localized. With the increase of power the ratio of mobile and localized quasi-particules changes and affects the coherence in a similar way as expected by TLS losses . In this picture, the fact that the resonator is not DC coupled prevents fast evacuation of quasi-particles in the environment. [62]. The main result from this work is that losses are mainly due to absorbed radiation and hence incoming radiation should be eliminated to reduce quasi-particle burst into the resonator.

The samples that we will show at the end of this chapter do not provide enough information to discriminate between these two mechanisms.

For the rest of this PhD we will analyze the variation of the losses using the model of the TLS shown in [59] that gives the the variation of the loss rate κ as an inverse of the quality factor with the input power.

$$\kappa(P) = \kappa TLS \frac{1}{\sqrt{1 + (P/P_s)^{\beta/2}}} + \kappa_0 \tag{2.1.14}$$

Where $\kappa_0 = 1/Q_0$ is the loss rate of the mode with saturated TLS and $\kappa_{TLS} + \kappa_0$ is the total loss rate at low power , P_s is a saturation power of the TLS and β is related to the geometry

of the sample.

2.2 Fabrication of high kinetic inductance GrAl wires

2.2.1 Lithography and Double angle evaporation

The Granular wires are the central part of the devices we made. We developed two lift-off techniques to make those wires. The first technique uses optical lithography which enables us to go down to patterns of 4.5 μm width . The second lithography technique uses an Electron Microscope to make wires down to 500 nm width with enough accuracy. Both technique principles are shown in figure 2.2 .

Fabrication with optical lithography Here, we use an optical masker to pattern the entire sample size. We apply a thick layer of optical resist AZ 9260 on a silicium wafer using a spin coater, and then place it inside an optical masker (DMO MicroWriter ML3). We can then pattern the design directly on the resist. We pay a special attention to avoid stitching of the fields of the writer at the position of the wires. Because of the maximum precision of the masker of 2 μm and the need to perform angle evaporation, we had to use a thick resist. This is why we choose the AZ 9260 which is 9 μ m thick. We develop the patterned resist with TMAH and water and then evaporate the sample. We lift the entire sample . The process and an example of the resulting wire are shown in figure 2.2

The main issue of this technique is the minimum size of the wire that we can fabricate. Because of the thickness of the resist the minimum wire width that we can pattern is 4.5 μm. Also the resist is rounded and creates no undercut. The GrAl layer is quite thin so it is very well attached to the substrate but having no undercut can make the lift off dangerous for the second layer of the evaporation which is a thicker normal aluminium layer. Moreover, the rounding of the resist prevents us from having well defined wire edges as can be seen on the picture of a wire in figure 2.2 . This creates an added dispersion of the resistance values from fluctuations in the wire width.

Fabrication with the Electron microscope Using electron beam lithography enables us to greatly increase the lateral resolution of the patterns and hence to achieve designs down to 10 nm precision. We first spin coat a trilayer of resin PMMA 450 A6 and 2 layers of PMMA 950 A6 onto a cleaned silicium substrate . The PMMA 450 A6 creates a small undercut as the length of polymers are shorter. We then insulate the resist with the electron microscope and reveal the pattern with 1 min in a solution of MIBK. As described above, we perform a double angle evaporation and make the lift-off in an acetone bath. The process is summarized in the bottom part of figure 2.2 . It is important to have as small undercut for the double angle technique so that the second evaporation of aluminium goes on the flanks of the resist.

The height of the resist is around 1.4 μm. With an angle of evaporation of a maximum of 45 $^\circ$ we can pattern wires up to 1.4μm wide. The wires have a reproducible size down to a width of 500 nm. Below this value the resist trench is not reliable and its width varies over multiple realizations.

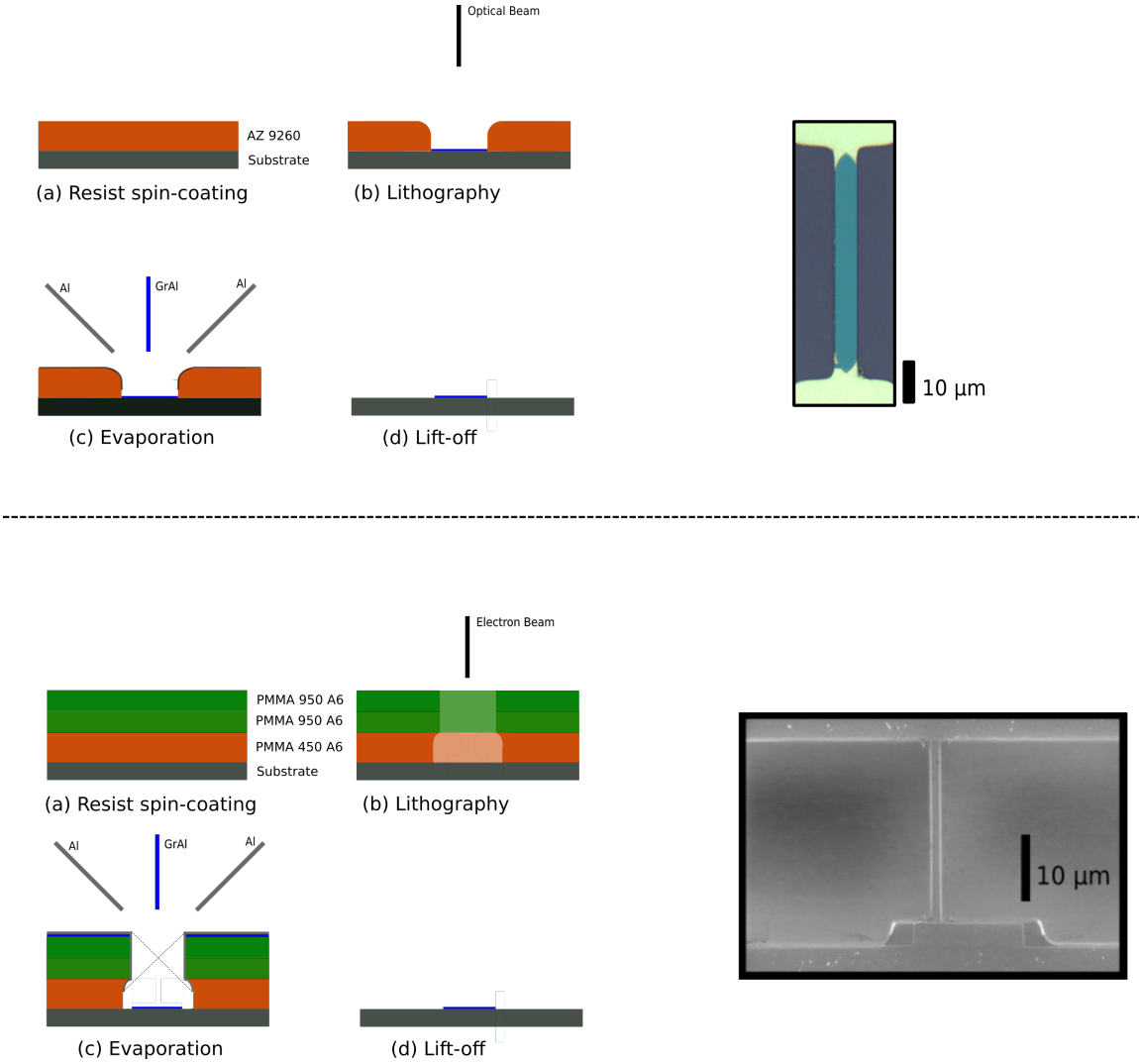

Figure 2.2: Lithography processed for the GrAl wires. The process

2.2.2 Evaporation

The evaporation is the most critical step of the fabrication. The precision of the evaporation parameters is crucial. First the GrAl resistivity varies fast with the oxygen partial pressure. Second the differential oxygen pressure between the evaporation chamber and the sample chamber is less that a factor 10, therefore Al is evaporated in presence of a quite high oxygen pressure about 2.0 $\cdot 10^{-6}$ which leads to partial oxidation of the target while evaporating. The resulting GrAl parameters vary between each evaporation. As will be shown in figure 2.6, the same evaporation parameters can still lead to variations up to half of the resistivity between samples. We will explain the evaporation process and then the different steps we implement to make it more reproducible.

Evaporation process We start with the GrAl layer. This layer is done by letting between 0.8 $\cdot 10^{-5}$ and 1.5 $\cdot 10^{-5}$ mbar of oxygen pressure in the evaporation chamber shown in figure 2.3 while evaporating at a rate of 1.5 Å/s. The ionic pump as well as a titanium sublimation pump are turned on in the evaporation chamber containing the target of aluminium to help preventing contamination during evaporation [63] . Preventing this oxidation is the reason why we clean and prepare the droplet and rise the rate of aluminium just before letting oxygen enter in the chamber. Doing so, the time where the droplet is hot and evaporates in an oxygen environment is reduced to a minimum.

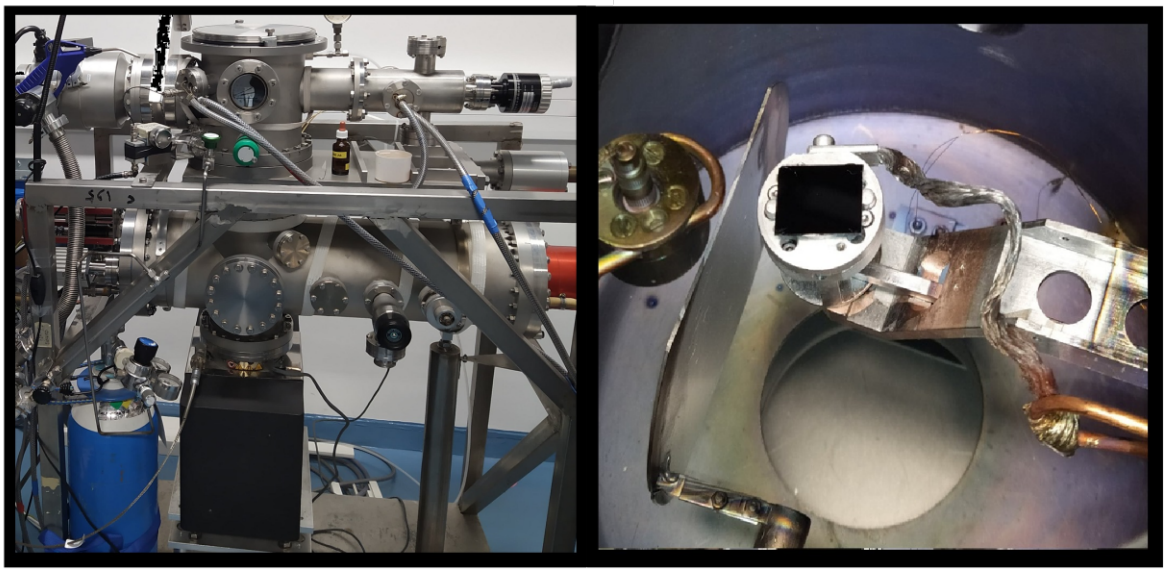

Figure 2.3: Photo of the evaporator on the left. The top chamber is the part of the evaporator that we open to air for every evaporation. It is pumped by a turbo pump able to bring down the pressure to 1 10^{-7} mbar. The bottom chamber is where the aluminium target is. It is pumped by an ionic pump that goes down to 1 10^{-8}mbar. There is also a titanium sublimation pump that we turn on during the GrAl evaporation.(right) Inside of the top chamber in which there is the sample holder and the shutter behind it, as well as the quartz that measure the deposition rate. (left

In Situ Resistance Measurement In order to enhance the reproducibility of our fabrication we decided to setup an in situ measurement of the resistance inside the evaporator and during the evaporation. Using a blank slab of silicium wafer with two connecting metal pads we were able to perform a continuous measurement of the resistance between the pads and deduce the resistance per square in real time as shown in figure 2.4

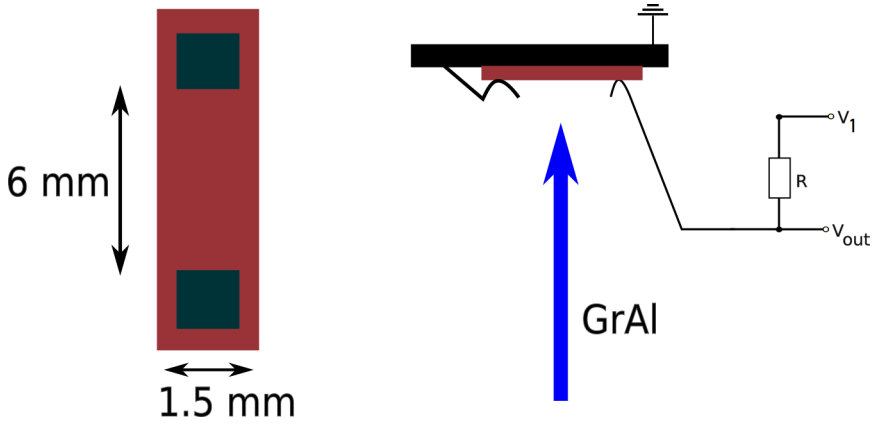

Figure 2.4: In situ measurement setup. The design of the slabs of silicium used for this experiment with two gold & aluminium metal squares of 10 nm thickness in total. One edge was connected to the sample holder and thus the ground. The other pad was connected to a wire used for a voltage measure.

We measured the voltage using a tension divider as shown in figure 2.4 with 10 kΩ resistor and voltage V_1 of 50 mV. By doing so we effectively put a limit on the maximum current carried in the thin film. This is especially important at the percolation threshold when the electrical continuity is established between the pads. A simple voltage bias through the wire would create a high current density at first contact and burn the wire. We show in figure 2.5 the resistance per square and the resistivity variation with thickness for one evaporation. This evaporation was done with a partial pressure of oxygen of 1 10^{-5} mbar and a rate of 1.5 Å/s.

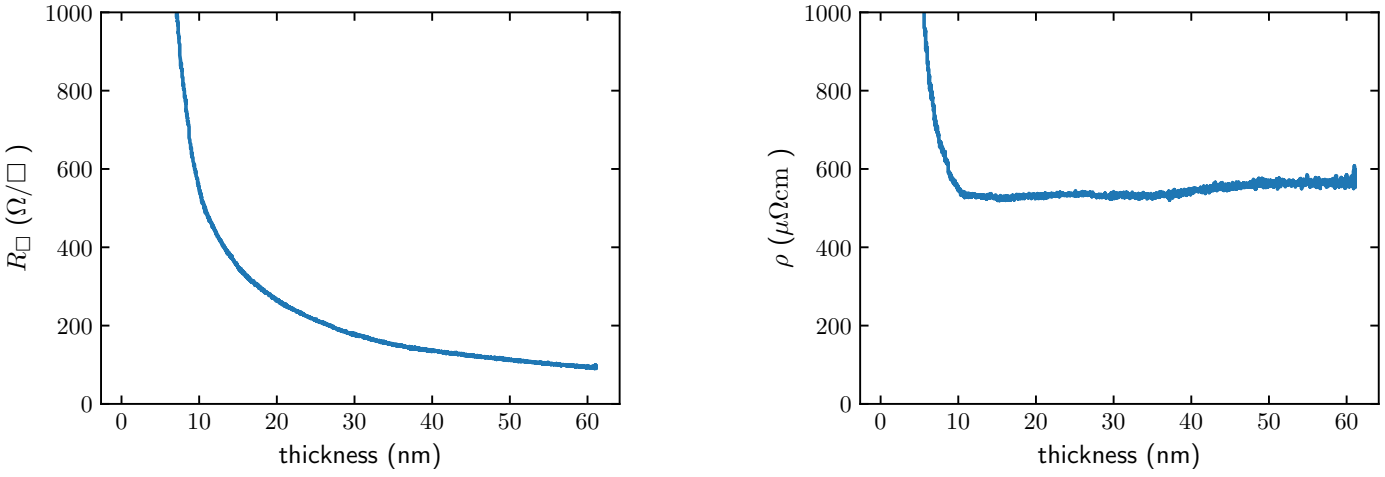

(a) (b)

Figure 2.5: In situ measurement of the resistance per square with thickness (left) and the resistivity with thickness

$R_\square$ decreases with thickness as expected and the resistivity stays constant above 10 nm giving a good estimate of the resistivity of the wire above this threshold. Below 10 nm the

resistivity and thus resistance per square are hindered by the contact resistance between the aluminium contact pads and the GrAl thin film rendering this measurement impractical below this thickness.

With this experiment, we showed that there was a way to make the GrAl thin films more reproducible for thicknesses above 10 nm. The samples used for the experiments shown in the last part of this section where 10 nm thick and thus not in the regime where this in-situ measurement of the GrAl resistance during evaporation was really useful.

Resistivity of the layer and SIT transition The evaporation is the most critical step of the fabrication process. There is a lack of reproducibility of the evaporation parameters which comes from different sources. The first problem that we encounter is the contamination of the target as mentioned in the previous paragraph. There is also a lack of precision of the O_2 throttle especially with respect to the fact that the resistivity varies rapidly with pressure. Moreover as the droplet of aluminium varies size we have seen changes of resistivity. A summary of all the evaporations for which the resistivity of the layer was measured is shown in 2.6.

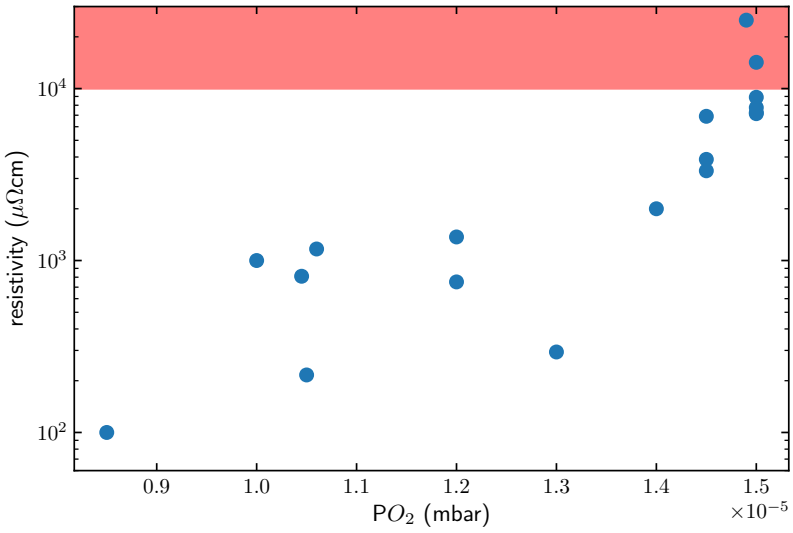

Figure 2.6: Resistivity of samples with measured pressure of the evaporation. The red bar show the expected superconductor to insulator transition.

Even if the scattering in the experimental data is high, we see a consistent change of the GrAl resistivity with the O_2 pressure. Note that the resistivity can change by two orders of magnitude be increasing the oxygen partial pressure from 0.9 10^{-5}mbar to 1.5 10^{-5}mbar, i.e. by less than a factor two.

Superconductor to insulator transition For a sufficiently high content of oxide, the grains are less coupled and , above a certain threshold, the material will turn into an insulator. This has been reported in the literature. We show the results of the work by [64]in figure 2.7 where is plotted the critical temperature as a function of the GrAl resistivity.

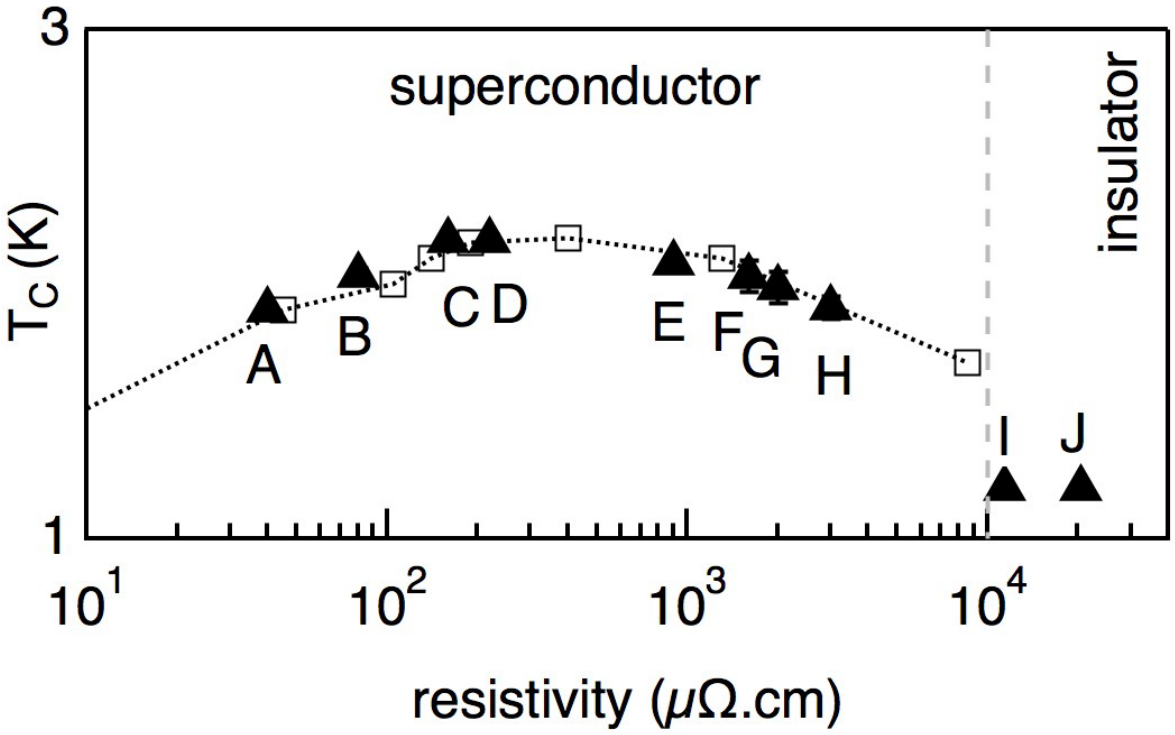

Figure 2.7: Critical temperature T_c with resistivity ρ taken from [64]

We have made resonators where the kinetic inductor is either a 10 nm or a 40 nm thick GrAl thin film. For 10 nm we went up to 10 kΩ/□ of square sheet resistance whereas for 40 nm we stayed below 2 kΩ/□ to stay below $10^4 \mu\Omega cm$. All of our sample lie in the region from 500 to 4000 Ω/□.

Geometrical Variation The resistivity is also very much impacted by the width of the patterned wire obtained by electron lithography. We think that this observation is related to local pressure of O_2 in the channel through its resist aspect ratio. We patterned a set of wires of width ranging from the smallest and widest pattern possible with our technique using an angle of 55 °. This wider angle allowed us to evaporate GrAl wires wider than the 1.5 μm. We measured the resistance per square for each of the wires as shown in figure 2.8.

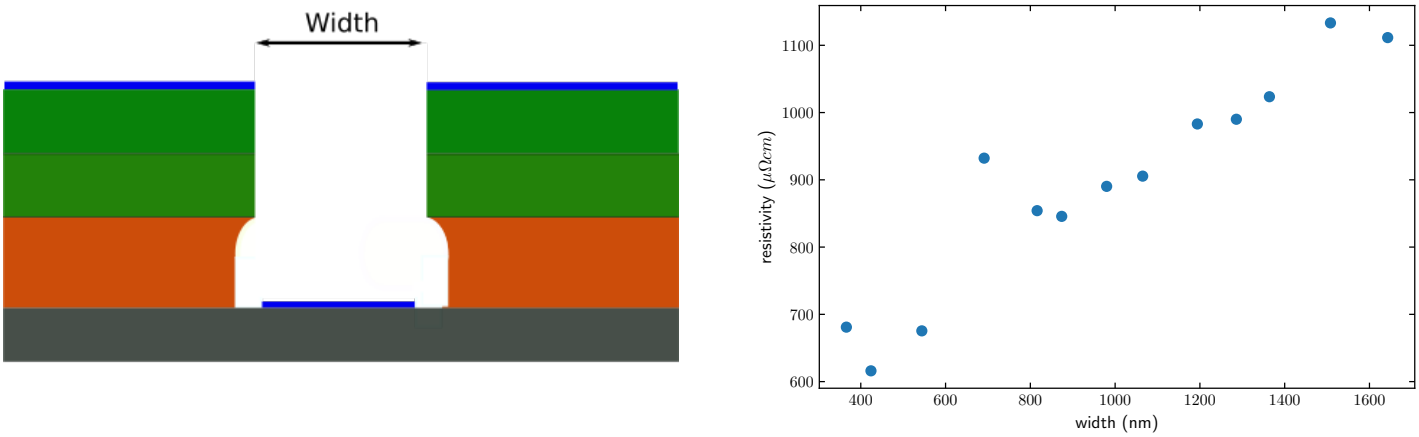

Figure 2.8: Geometrical shape surrounding the wire during evaporation leading to lowering of the O_2 pressure around the wire. (left) Variation of resistivity with width of the wire for a sample of 9nm of GrAl evaporated at 1.2 10^{-5}Å$/s$.(right)

The resistivity of GrAl decreases as the walls of PMMA resist tighten and the channel becomes narrower suggesting that the local O_2 pressure in the channel is also lower. This result indicates that the oxidation of the material occurs when the aluminium is already deposited on the substrate.

2.2.3 Measurement of the critical current

We measured the critical current and temperature of 3 wires of a 10 nm thick layer of GrAl of widths 366, 980 and 1340 nm and a fixed length of 9.8 μm. Because of the varying width, the three wires had different resistance per square of 616 , 854 and 990 $\Omega/\square$. We also measured their critical temperature during the cool down of our fridge which gave us a critical temperature of 2.1 $\pm$ 0.05 K in agreement with [64]. The critical current of the three wires is linear with the width of the wire and corresponds to a current density of 1.03 $\mu A/\mu m^2$.

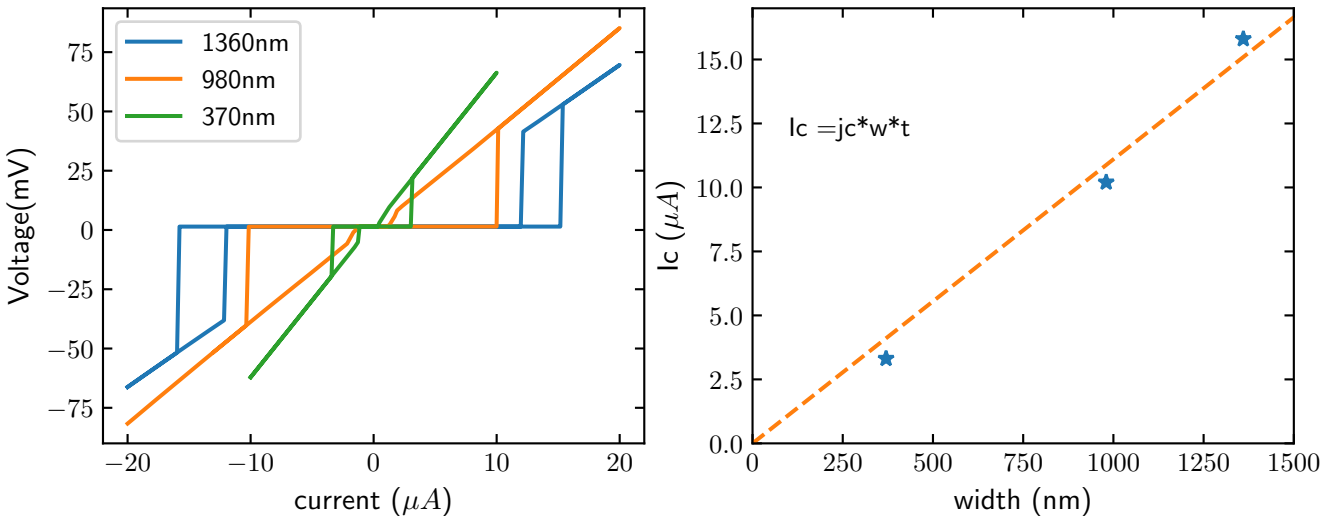

Figure 2.9: Critical current measurement of 3 of the wires fabricated with different width.

We have thus proved that it was possible to fabricate a wire of a given resistance per square and to control its parameters with the width, the oxygen pressure and thickness.

2.2.4 Automatic Resistance measurements

The last problem we observed with the evaporation is the dispersion of the resistivity with the position in the sample. We addressed this issue by measuring automatically a large number of wires evenly spaced on a substrate whose surface is up to 3 cm by 3 cm.

The resistance measurement at each lattice site where crucial to fabricate lattices with a large number of sites. By measuring automatically we could estimate the impact of pressure and geometry of the wires on the dispersion in the values of the resistances in less than an hour for 800 values. The resistance measurements have been done using a voltage divider with a 100 MΩ resistor in series to fix the current to a minimum value. This prevents possible annealing of the wire. We measured using the automatic probe shown in figure 2.10

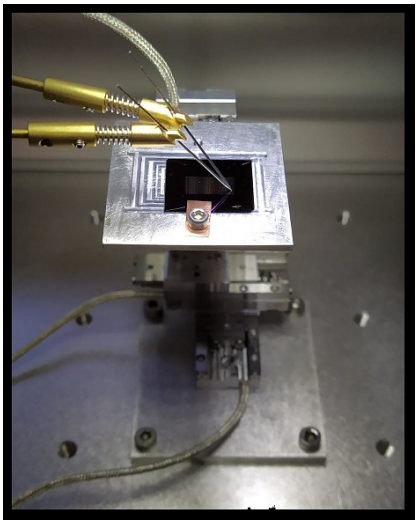

Figure 2.10: Picture of the automatic Probe. The probe is driven by piezo motors. The resistance is measured using the needles that we can see applied to a sample on the picture.

We show in figure 2.11 the variation of resistance of a sample made of 5 by 9 wires of 20 μm (long) by 1 μm (wide) each.

The spread is between 6 and 10 % even with optimal deposition. We succeeded in getting a sample of 5 % resistance deviation only by evaporating an entire wafer of 16 samples but this technique is difficult to use routinely so we decided to go towards thicker layers of aluminium in order to reduce the impact of thickness fluctuations on the wire resistance.

For thicker wires, we observe a gradient on the values of the resistances in one direction of the substrate but also a smaller spread with respect to thinner wires. This gradient may come from the position of the oxygen inlet line in the sample chamber. We measured this gradient precisely at 1.45 10^5 mbar on a sample of 625 wires over a distance of 5.1 cm by 3.1 cm shown in figure 2.12 .

For this sample we get a spread in the wire resistances on each line of only 3 % and a 6% per cm gradient throughout the sample.

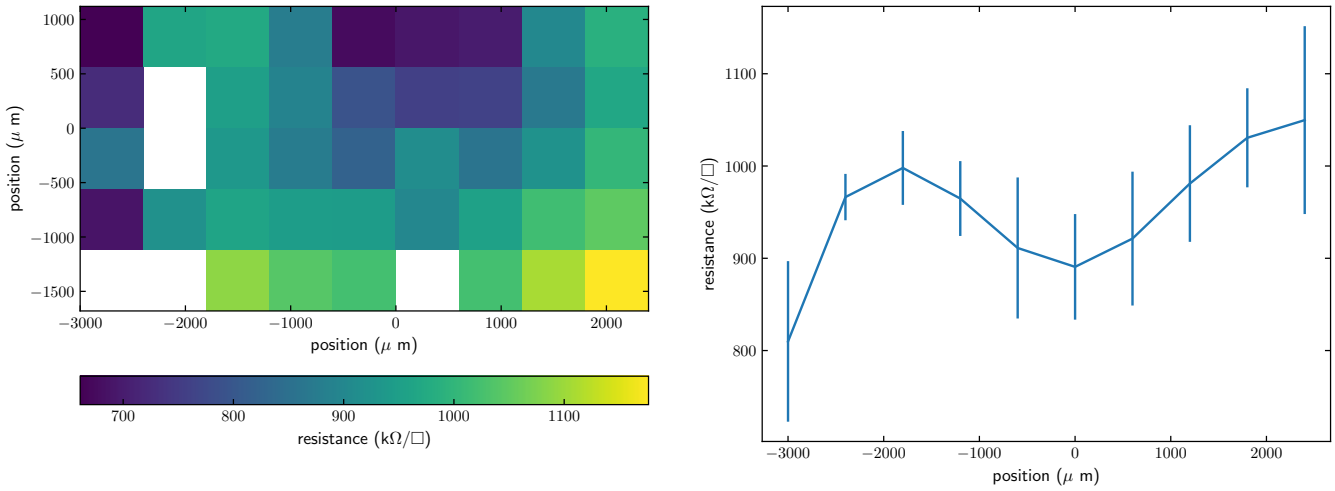

Figure 2.11: Measurement made using automatic probe on a 10 nm Granular aluminium sample consisting of 625 resonators over a 5.1 cm by 3.1 cm sample

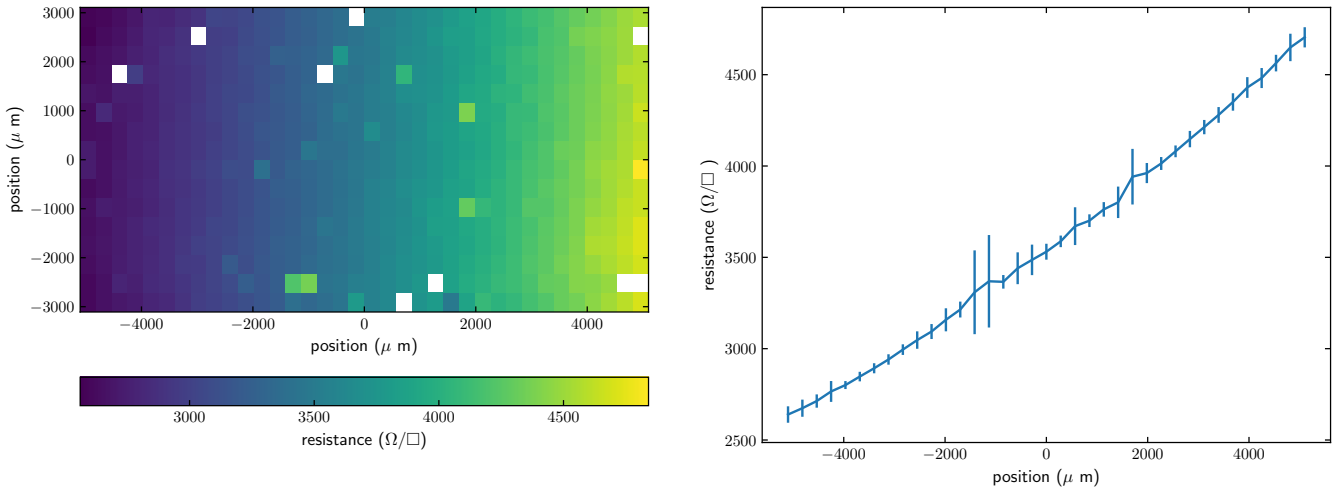

Figure 2.12: Measurement made using automatic probe on a 40 nm Granular aluminium sample consisting of 625 resonators over a 5.1 cm by 3.1 cm sample

2.3 Spectroscopy of granular aluminium transmon-like-resonators

The goal behind the use of the Granular Aluminium was to use the non-linearity of its inductance.As shown in the previous sections, we expect a direct link between the resistance at room temperature, the value of inductance and the non-linearity, given by the value of a nonlinear current parameter j_* expected at 3.3 j_c. We will measure those three parameters for 3 different sample and show that those parameters match with the critical current density measured in DC.

2.3.1 Model of hanger resonator

Linear part of the resonator The hanger configuration corresponding to the coupling of a single resonator to a transmission line can be schematised like this :

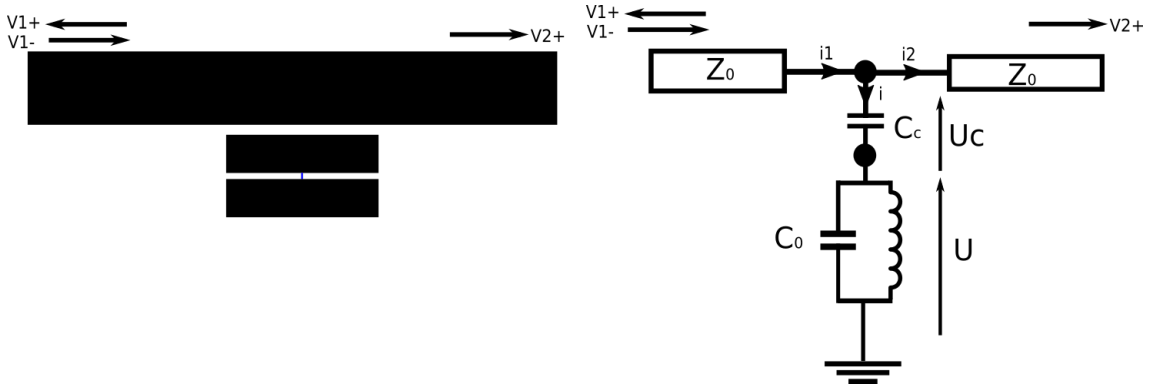

Figure 2.13: Design pattern of one of the MF47 resonator (left) and a first order scheme of the equivalent Electrical circuit

In such a configuration the incident microwave signal and the reflexion from the LC resonator account for a drop of the transmission around the resonator frequency.

Starting from the hanger equivalent circuit we calculated the transmission S_{12} for the lossless resonator in the appendix 4.4.3 giving:

$$|Sij| = |1 - \frac{\kappa_c e^{i\phi_s}}{(\kappa_c + \kappa_i + i(\omega - \omega_0)}|^2 \tag{2.3.1}$$

where $\omega_0 = \frac{1}{\sqrt{(L(C_0+Cc)}}$ is the resonator frequency, κ_c is the coupling rate of the circuit given by $Z\omega_0^4 C_c^2 L/4$, κ_i is the internal loss rate of the resonator and ϕ is the skewing angle given by $\phi \approx -ZC_c\omega_0/2$. This Lorentzian shape is a general response function for resonators coupled either capacitively and inductively to a transmission line as is shown in the references [65] and [66].

Two more parameters have to be taken out of the data or added to the fitting function: the delay and the amplitude variation of the line. The delay offset of the line will create a phase $d\phi * f$ that will continuously change the angle of the measurement which can easily be subtracted from the data. Amplitude variation of the line can be supposed slow in frequency and just add a linear shift with frequency.

As shown in the figure 2.14, the skewed Lorentzian function goes around a resonant circle in the complex space. We fit the center of the resonant circle in complex space. It is centered around z such that

$$z = e^{i\phi}\frac{\kappa_c + 2\kappa_i}{\kappa_c + \kappa_i} \tag{2.3.2}$$

where ϕ is the angle of the line at the resonance of the resonator. The norm of z gives the radius of the resonant circle.

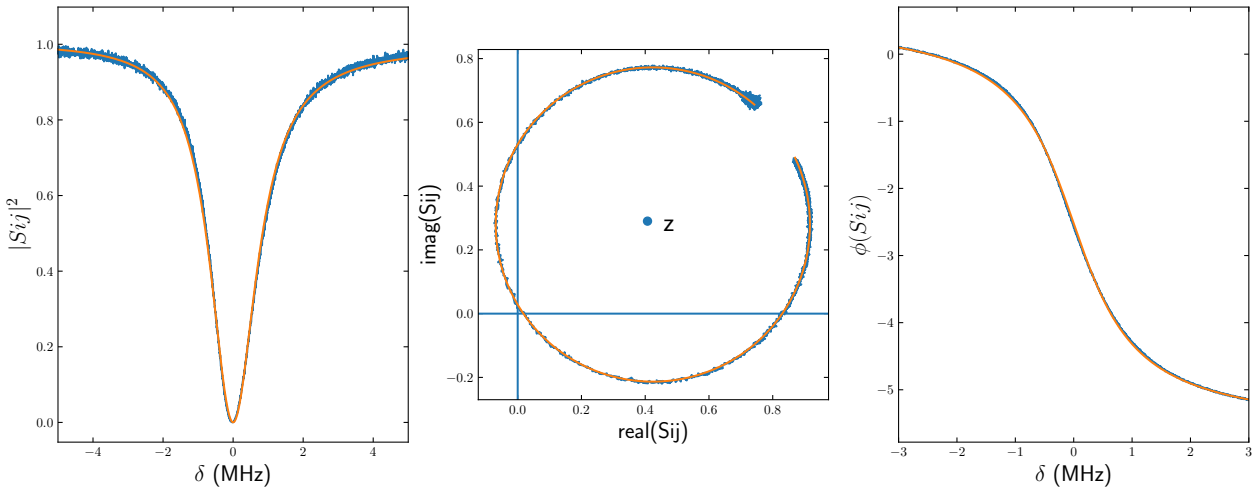

Figure 2.14: Resonance of the MF 46 sample 2.18 (in blue) with fit (orange) , resonance in linear units (left) complex resonance circle (center) and argument of S12 - z (right).

In the example 2.14 we have divided the transmission S_{12} by its maximum value.Because from 2.3.1 we know the maximum tranmission is 1, we use the measured maximum value of the tranmission to calibrate the amplitude of transmission of the line and calculate the input power that the resonator sees. From this procedure we can fit the frequency, the internal and external loss rate, the skewing angle of all of our resonators and the maximum transmission amplitude.

2.3.2 Non linear resonator resonance and fit

After fitting the linear response we need to fit the non-linear response. To do so, we come back to the dynamics of the resonator using the hamiltonian formalism. The Hamiltonian of the cavity can be written as

$$H = \hbar\omega a a^\dagger - \hbar U a^2 (a^\dagger)^2 \tag{2.3.3}$$

In the rotating frame at the frequency ω of the source the Hamiltonian becomes:

$$H = -\hbar(\omega - \omega_0) a a^\dagger - \hbar U a^2 (a^\dagger)^2 \tag{2.3.4}$$

By driving the cavity at the frequency ω with a force η and the losses $\kappa = \kappa_i + \kappa_c$ of the resonator we write the equation of motion of the field α inside the cavity as:

$$\dot{\alpha} = i\delta\alpha + i2U|\alpha|^2\alpha - i\eta - \kappa\alpha \tag{2.3.5}$$

with $\delta = (\omega - \omega_0)$. Thus in the steady state:

$$\delta\alpha + 2U|\alpha|^2\alpha - i\kappa\alpha = i\eta \tag{2.3.6}$$

$$\alpha(\delta + 2U|\alpha|^2 + i\kappa) = \eta \tag{2.3.7}$$

By multiplying with the conjugate we find:

$$|\alpha|^2((\delta + 2U|\alpha|^2)^2 + \kappa^2) = \eta^2 \tag{2.3.8}$$

From this equation we get a non-linear equilibrium point for $|\alpha|$:

$$4U^2|\alpha|^6 - 4U\delta|\alpha|^4 + (\delta^2 + \kappa^2)|\alpha|^2 = \eta^2 \tag{2.3.9}$$

We can solve this equation numerically to find $|\alpha|^2$ and use the equation 2.3.7 to give α as

$$\alpha = \frac{\eta}{\delta + 2U|\alpha|^2 + i\kappa} \tag{2.3.10}$$

The output power of the cavity in the line at a rate κ_c interferes with an angle given by the skewing angle ϕ with the power input the line and creates a dip in the amplitude:

$$Sij = 1 - i\frac{\kappa_c e^{i\phi}}{\eta}\,\alpha \tag{2.3.11}$$

If we use 2.3.10 and 2.3.7 we get :

$$Sij = 1 - i\frac{\kappa_c e^{i\phi}}{\eta}\,\alpha = 1 - \frac{\kappa_c e^{i\phi}}{\kappa - i(\delta + 2U|\alpha|^2)} \tag{2.3.12}$$

For U = 0, we recognize the equation 2.3.1 where $\kappa = \kappa_i + \kappa_c$.

For each power amplitude P_in that goes into the sample, we measure the transmission and we fit by fixing the value of η to $\eta = \sqrt{\kappa_c Pin/e_{photon}}/2/\pi$ as shown in figure 2.15

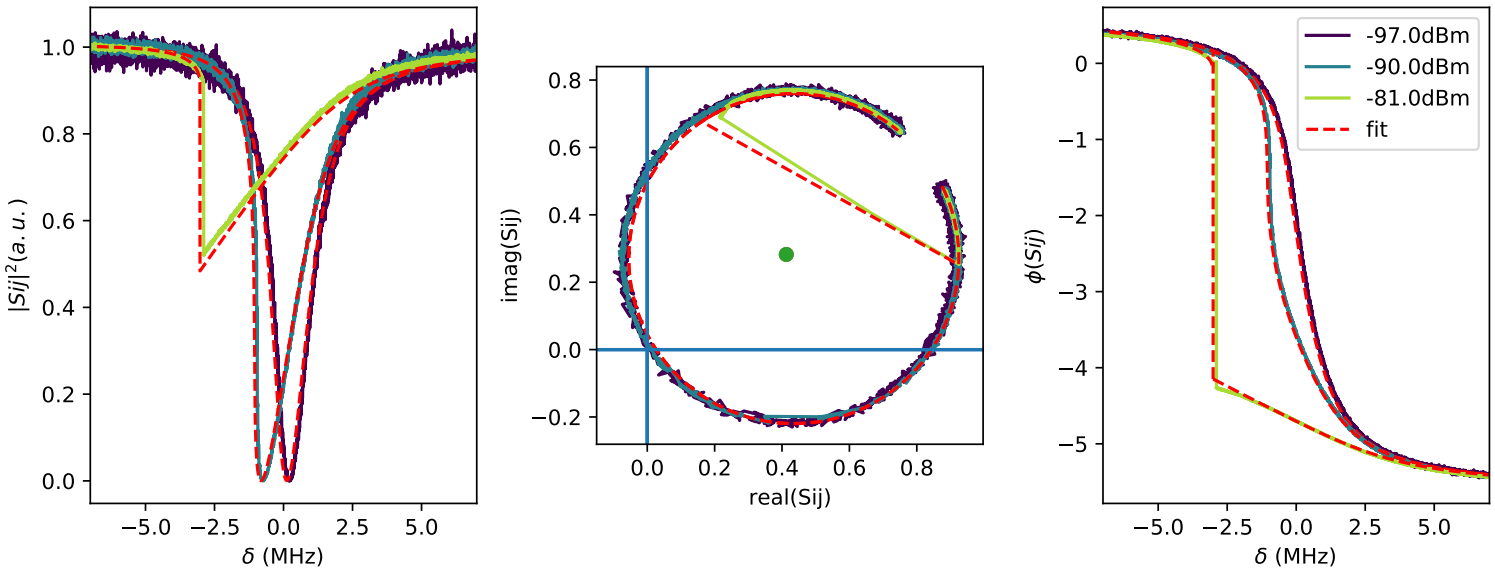

Figure 2.15: linear (red) and non linear fit (yellow) of data from the MF46 sample in the linear regime and in the non linear and bistable regime at input power -35, -30 and -22 dBm of the VNA and with 63 dB of attenuation from the output of the VNA to the sample input.

For resonators for which the internal and coupling Q factor stays constant with power the circle in complex space stays constant with power and only the angle function around the circle

changes. This function of angle becomes multivalued above the bistability and we measure a jump in the angle while the circle still indicates the value of coupling and internal factors.

We only measured with increasing frequency so we only have access to one of the two stable branch in bistability.

Non-linearity of the resonator from the inductance From the current dependence of the inductance shown in the previous section, we calculate the non linear term U so that the frequency shift of the LC resonator per photon is U:

$$\omega = \frac{1}{\sqrt{L(I)C}} \approx \frac{1}{\sqrt{L(0)C}} \left(1 + \frac{I^2}{2I_*^2}\right) \tag{2.3.13}$$

By rewriting the frequency ω_0 using the non-linear inductance we directly get to the non-linear term. You can write $\phi = I/L_0$ and with $\omega = 1/\sqrt{LC}$ we find :

$$\delta\omega = \frac{\omega_0}{2}\frac{I^2}{2I_*^2} = \frac{\omega_0}{2L_0^2 I_*^2}\phi^2 \tag{2.3.14}$$

using $\phi = i\sqrt{\frac{\hbar Z}{2}}(a + a^\dagger)$ we get:

$$-U = \frac{\hbar Z}{4}\frac{\omega_0}{L_0^2 I_*^2} = \frac{\hbar}{4}\frac{\omega_0^2}{L_0 I_*^2} \tag{2.3.15}$$

We will use this equation to extract from each resonator the j_* current density from its frequency and non linearity.

It is interesting to mention that, as seen in the model given by [46], you can also directly model the granular media as a series of Josephson junction and calculate directly the total non-linearity to get the same value for the non linearity of the total inductance by assuming $\mathbf{j}_c \propto 1/\rho_n$. This relationship is linked to the Ambegaokar-Baratoff equation which applies for Josephson junction but in the case of GrAl applied to an array of grain coupled by Josephson junctions.

Current density We measured 3 samples of different width and length, MF46, MF 47 and MF 49 , in order to measure the change induced by the width in inductance and the non-linearity. We expect from the equation 2.3.15:

$$-U = \frac{\hbar}{4}\frac{\omega_0^2}{L_0 I_*^2} \tag{2.3.16}$$

We can also write I^* :

$$I^* = \sqrt{\frac{\hbar\omega_0^2}{-U4L_0}} \tag{2.3.17}$$

With a constant resistivity we expect a constant current density over all the samples. We will calculate j_* for each sample.

2.3.3 Measurements

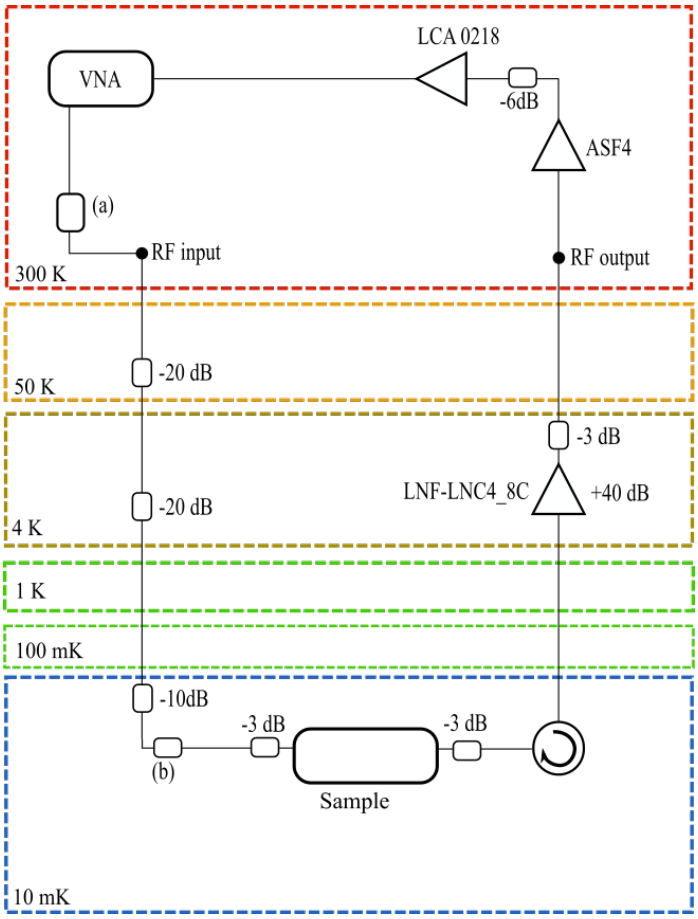

Figure 2.16: Setup for the resonator measurements. The attenuator (a) and (b) where changed between the MF 46 and MF 47/MF49 sample. (a) and (b) where set at 0 dB for MF 46 and 20 dB for the newt two.

Setup A picture of the setup inside of the fridge can be seen in figure 4.5. We changed attenuation before the input of the sample between the three measurement to accommodate the variation of non-linearity . At the measurement of MF46 there was no attenuator A and B and then two -20 dB attenuator was added for the next two measurement. We knew the total attenuation of the input and measurement line. For all of the measurement there was a direct 50 Ω line between the the input and measurement line and by measuring the amplitude of the transmission outside of the resonance we could measure the total attenuation through the setup. By calculating the difference between the expected attenuation and the measured one we where able to measure the attenuation from the cables at 16 dB through the entire setup and assumed that half (8 dB) of this attenuation was from the input line. From this we could calculate the power input of the sample.

MF 46 This sample was made using only optical lithography. There where 2 resonators on each 50 Ω line. On each line one of the resonator had a 170 μm long wire and the other a 60 μm, the wire was 5 μm wide. The 10 nm thick wires had a resistance per square of 600 Ω/□ which leads to a inductance per square of 0.410 nH /□.

Contrary to the discussion about admittance in 1.2, here the inductance wire has a surface (5*160 μm^2 and 5*60 μm^2) comparable to the surface of the resonator. Thus the simulations had include the inductive wire surface in order to compute the total capacitance of the resonator. Doing so is necessary to find an agreement on the value of the current I_* between the two types of resonators that have the same cross section of their inductive wire. The total attenuation of the input line was 63 dB.

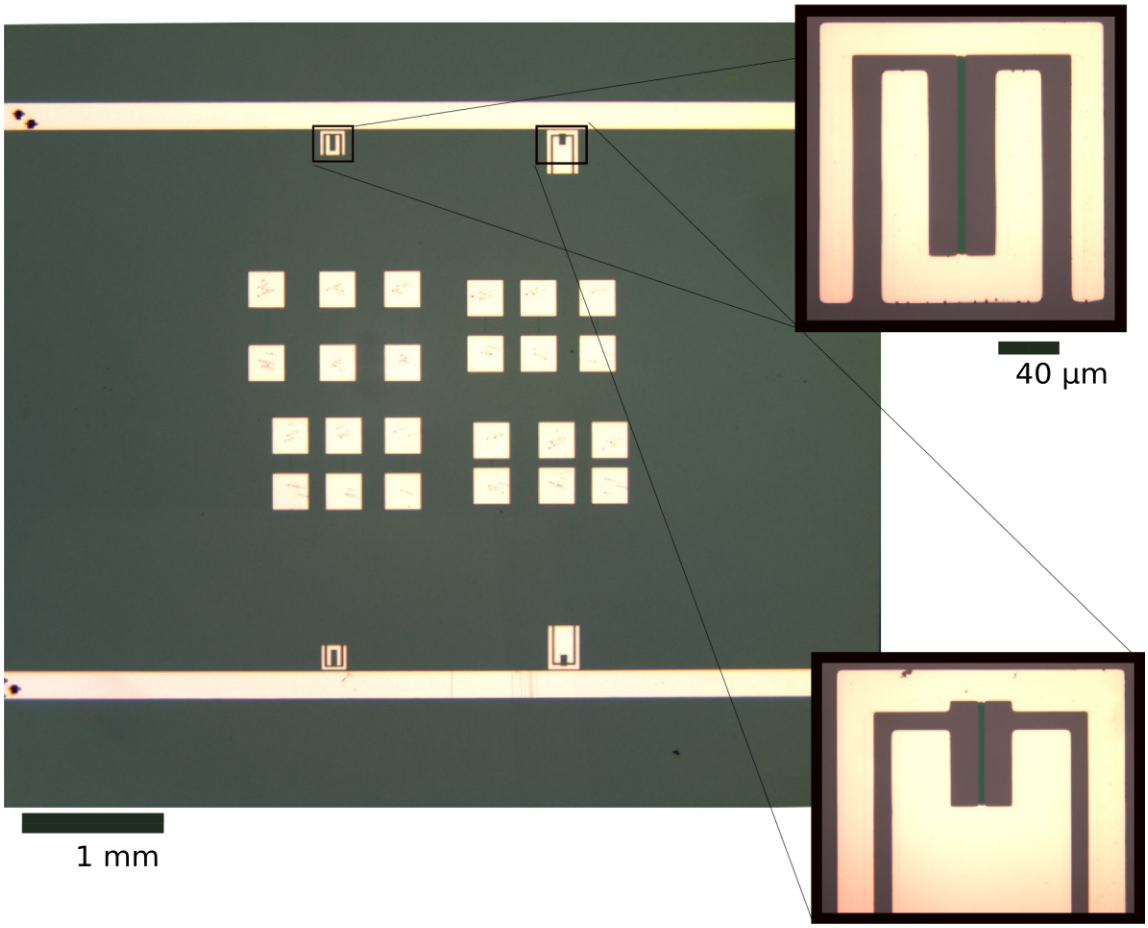

Figure 2.17: Image of the MF46 Sample with zoom on the 2 Granular Aluminium Wires. The sample is 8 mm by 8 mm.

The sample was glued inside a copper box in which it was bonded to a PCB that was connected to the outside with SMA cables using the same box as shown in figure 4.10 in the last chapter.

The examples in figure 2.15 and figure 2.14 given in the model for linear and non-linear fits are from this sample. The resonator with a longer wire has a low value of C_0 with respect to C_c which creates a lot of skewedness of the resonance as explained by our calculation in 4.4.3 and [65]. The skewing angle ϕ_s of the resonance is -0.046 rad in the simulation and coherent with the measured value of 0.05 rad.

	f_0(GHz)	L (nH)	Q_i	Q_c	U (kHz)	$I_*(\mu A)$	$R_\square$ $(k\Omega/\square)$
1	5.03	4.642	1.9 1^5	6358.0	-10.0	119	552
2	5.04	4.63	1.85 1^5	6066.0	-10.0	120	551
3	5.73	14.5	1.0 1^5	1225	-5.1	125	630
4	5.774	14.44	8.5 1^4	1146	-4.43	110	625

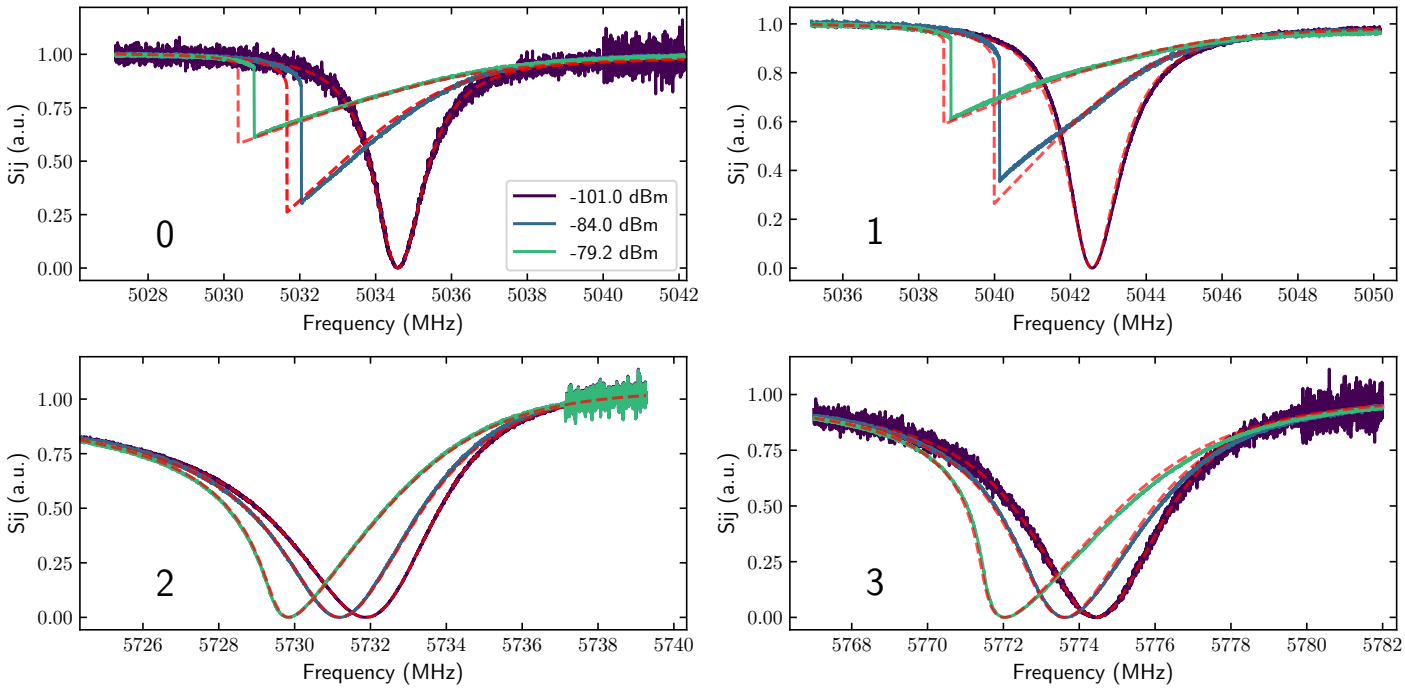

Figure 2.18: Resonances of the 4 resonators on the sample MF46. The numbers correspond to the table 2.3.3 . The increased noise seen on the high frequencies of each resonance was due to a problem of averaging. This noise did not impact the fitting of the parameters.

MF 47 The MF47 Sample had two 50 Ω lines with 4 samples each 4 resonators. The wire is 400 nm wide which is close to the reproducibility limit for the electron microscope lithography technique. Close to this limit of the lithography technique, the width varies between the resonator and within each wires which explain the variation of I_* observed. The resistance per square from the test pad on the sample was 2300 Ω/□. This sample was made using the two lithography processes mentioned before. The electronic lithography was used to make the wires and small 20 μm pads. Then we evaporated the granular aluminium and evaporated Aluminium into the pads , as well as 5 nm of palladium to prevent oxydation of the connection pads as well as chemical attack during the TMAH revelation of the second lithography. Wider test pads where lithographied in order to be able to measure the square resistance between the two steps of the process and thus adapt the design of the capacitance to the measured resistance value. Then a second optical lithography was used for the rest of the design. The sample is then argon milled for 2 minutes to insure contact with the pads before the second aluminium evaporation. The resulting resonator is showed in figure 2.19 with enhanced colors for each depositions We used this technique for these resonators because it enabled us to design the size of the capacitance after a measurement of the resistance per square of the GrAl in order to keep the frequency in our measurable range. The total attenuation of the input line was 103 dB.

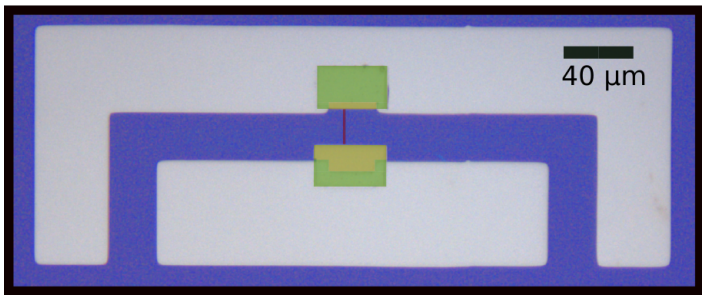

Figure 2.19: MF47 Resonator optical picture. The GrAl Wire is in red. The Aliminium + Palladium layer pads are in light yellow and light green where the second aluminium layer overlaps with it. The second aluminium layer after the optical lithography is in white.

The sample was the same layout as the precedent with 2 lines coupled to 4 resonators each . The distance to the line was of 40 mum the 8 resonators much more compact as the measured pads indicated a resistance per square value of around 2 k Ω/□ .

	f_0(GHz)	L (nH)	Q_i	Q_c	U (kHz)	$I_*(\mu A)$	$R_\square$ $(k\Omega/\square)$
1	4.89	40.1	19988.0	4837.0	-7.59	3.56	2.3
2	4.96	38.96	69115.0	4099.0	-1.41	4.23	2.3
3	5.02	38.08	74414.0	4265.0	-2.65	2.55	2.3
4	5.12	36.63	26118.0	4526.0	-3.56	2.29	2.3
5	5.15	36.08	108074.0	5076.0	-0.99	10.85	2.3
6	5.16	35.94	40820.0	4441.0	-2.11	2.85	2.3
7	5.22	35.13	47741.0	4386.0	-0.32	10.39	2.3
8	5.23	35.01	77002.0	4159.0	-1.31	4.15	2.3

Unfortunately the argon milling step used for these resonators was done at a step where the most surface of silicon is exposed. Aggressive ion milling on silicon creates a lossy interface [67] which adds to the loss of our resonator.

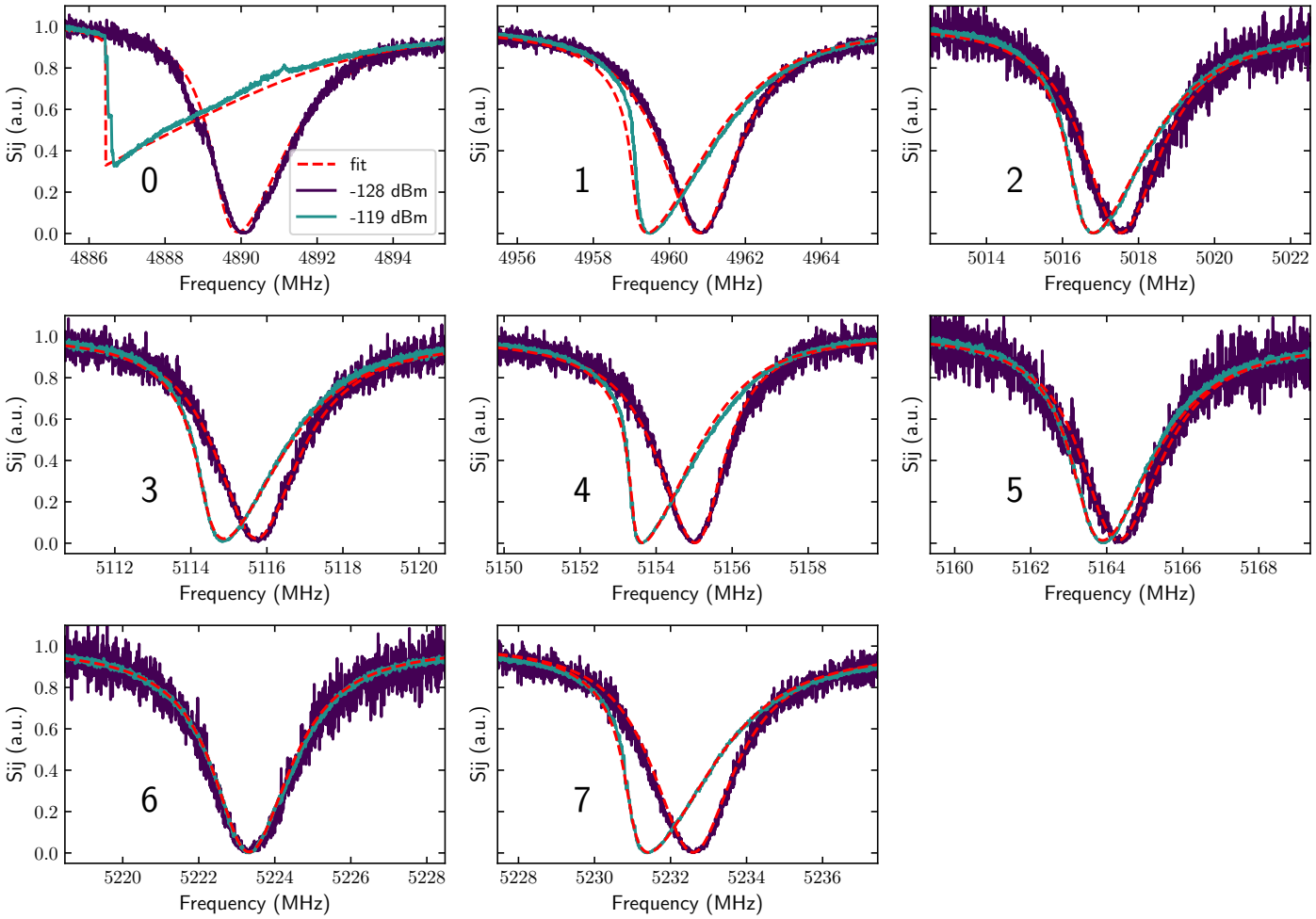

Figure 2.20: Resonances of the sample MF47 at two input power of the vna -129 and -119 dBm. The numbers correspond to the table 2.3.3.

TLS on MF47 We measured the power dependance at low power of the MF47 8 resonances and used the TLS power function shown in 2.1.14 to fit this dependance. We plot the inverse of the quality factor $\delta = 1/Q$ in figure 2.21 and summarize the fitting results for each resonance in 2.3.3.

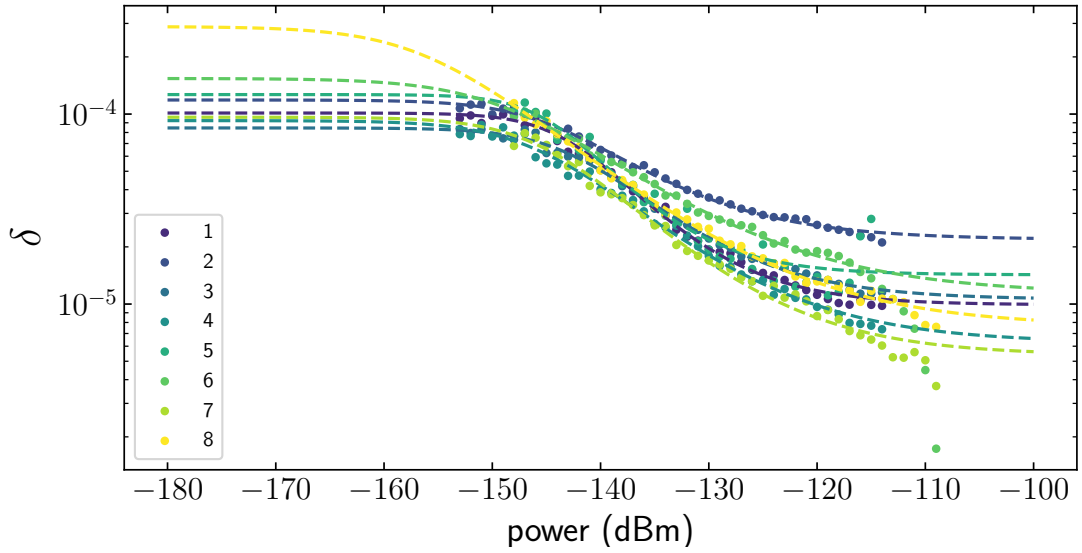

Figure 2.21: Variation of the inverse of the quality factor δ with power. The numbers correspond to the table 2.3.3.

	P_0 (dBm)	$1/\delta_{TLS}$	Q_0	β
0	-145.07	8.9 10^3	7 10^4	1.5
1	-149.6	7 10^3	0.9 10^5	0.9
3	-143.5	1.09 10^4	1.0 10^5	1.4
4	-145.2	1.03 10^4	4.5 10^4	1.1
5	-142.4	6.2 10^3	6 10^4	0.6
6	-143.2	1.35 10^4	0.9 10^4	1.2
7	-146.5	1.16 10^4	1.6 10^5	1.0
8	-156.6	3.5 10^3	1.3 10^5	0.9

We find an average saturation power P_0 equivalent to 2 photons in the resonator.

MF 49 This last sample was done with the same technique as the MF47 sample.With this sample the wires where larger ($\approx$ 800 nm) and less resistant at 940 $\Omega/\square$. The total attenuation of the input line was 103 dB. When the internal loss rate is negligible compared to the coupling rate the shape of the resonance is not impacted by changes of the internal loss rate. The internal loss rate changes with power because the internal loss rate and coupling loss rate are of the same order of magnitude.

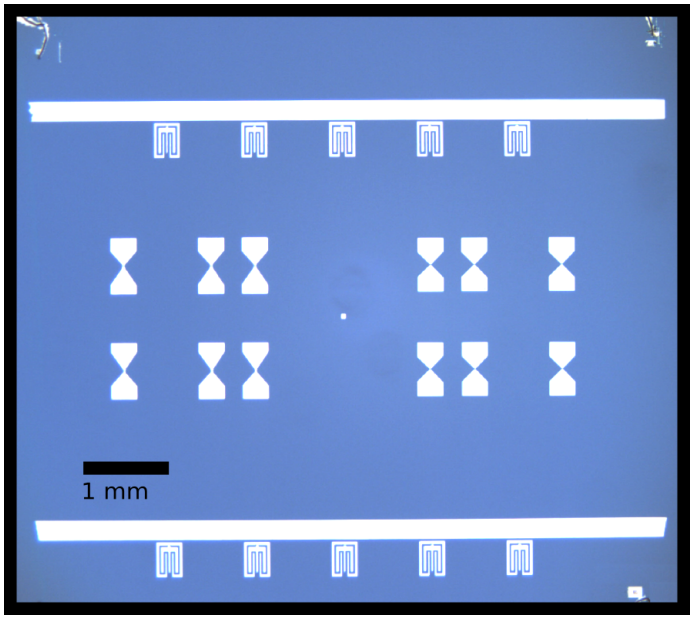

Figure 2.22: Sample Optical picture.

	f_0(GHz)	L (nH)	Q_i	Q_c	U (kHz)	$I_*(\mu A)$	$R_\square$ $(k\Omega/\square)$	width (nm)
1	6.55	4.74	15 10^3	3.2 10^4	-1.65	12.03	940	800
2	6.57	4.71	14 10^3	3.1 10^4	-1.61	12.39	940	800
3	6.65	4.59	15 10^3	3.7 10^4	-1.41	13.43	940	800
4	6.82	4.37	11 10^3	2.9 10^4	-1.10	17.21	940	800

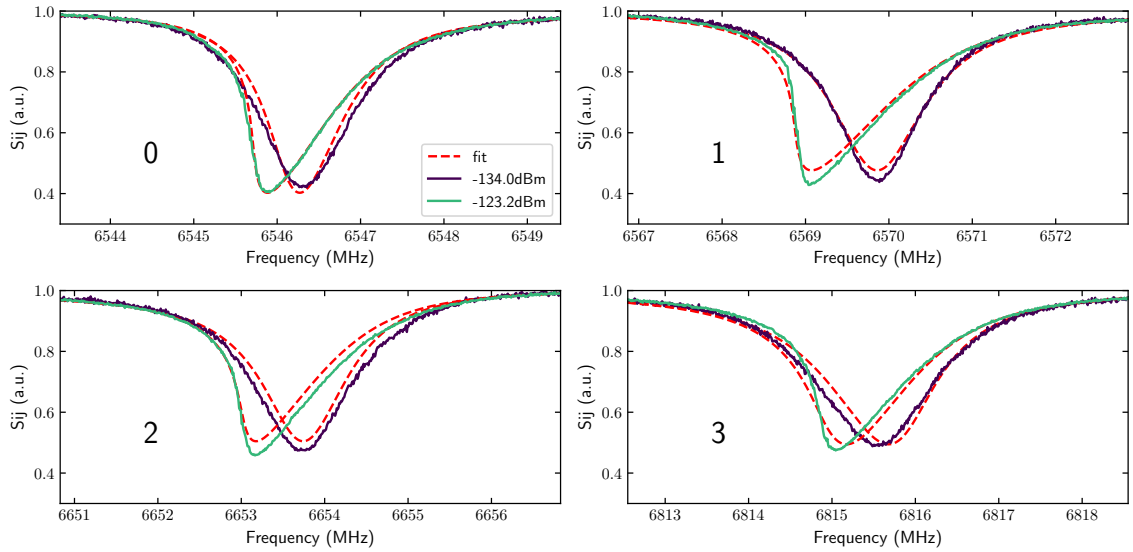

Figure 2.23: Resonances of the sample MF49 at two input power of the vna -134 and -123.2 dBm. The numbers correspond to the table 2.3.3 .

2.3.4 Comparison of the samples

The resonators non-linearity span multiple order of magnitude going from 5 Hz to 10 kHz that we resume here.

The sample from the MF46 sample had two different designs which explains their difference of non-linearity. The variation of the non-linearity for the resonators of the MF47 sample can be explained by the fact that the fabrication width was 400 nm which is the minimum size that we could do . At this size the sizes are not reproducible and could have constrictions that change the non-linearity..

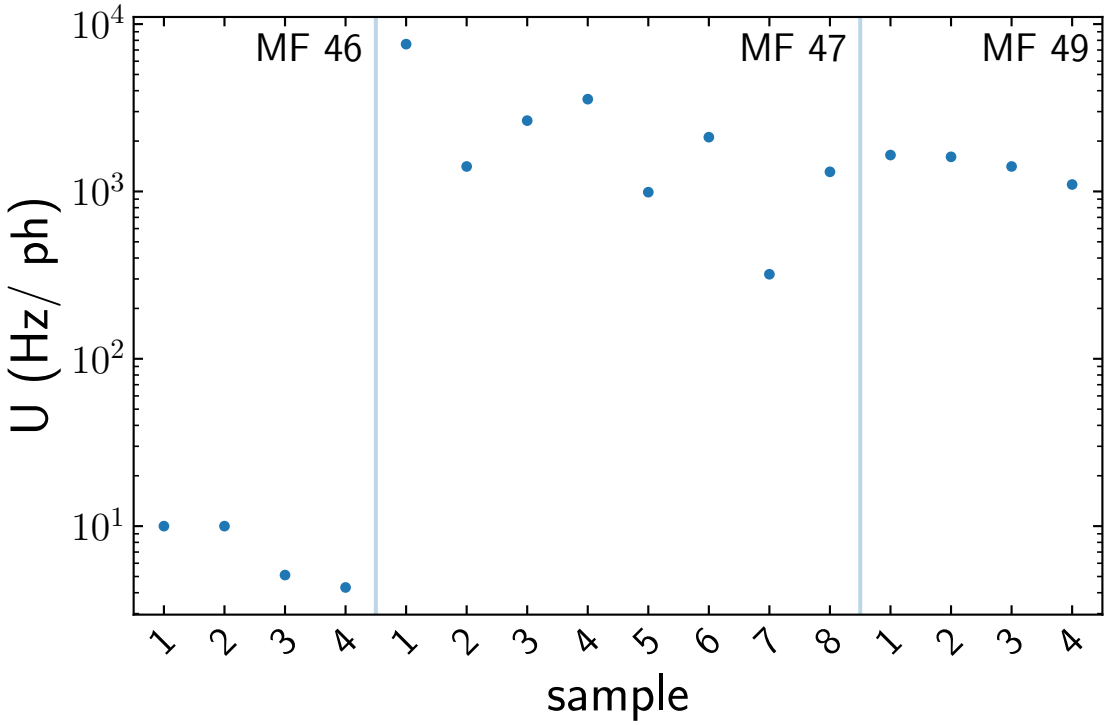

Figure 2.24: Non-linearity of each sample presented before. The plot is divided in three section for each sample. The number corresponds to the tables for each sample.

From the equation 2.3.18 we know that with the section S:

$$-\frac{4L_0U}{\hbar\omega_0^2} = \frac{1}{j_*^2 S^2} \tag{2.3.18}$$

where S is the cross section of the wire. We show in figure 2.25 the values of $\frac{-4L_0U}{\hbar\omega_0^2}$ compared to $\frac{1}{S^2}$ for each sample. The curve for the average critical current density over all of the resonators of 1.45 $mA/\mu m^2$ is shown with the dashed line.

In this first comparison, we have simply used an average of critical current density over all the sample but have not taken into account the change of resistivity between the samples. We expect that the GrAl aluminium follows the rule $j_* \approx 1/\rho$ and thus that the product $j_*\rho$ stays constant throughout all Granular Aluminium samples. We show in figure 2.26 the product ρj_* for all of the samples and compare it to the expected value from DC measurement of ρj_c.With the DC measurement, we measured a product $j_c\rho$ of 8.7 kV/m in DC and thus expect $j_*\rho$ at 28.5 kV/m using the calculations shown in 2.1.2.

We find a good agreement between the samples to the expected $j_*\rho$ product for the 14 resonators over the 3 samples ranging from U = 12 Hz to U = 3 kHz. Those variation could come from the measurement setup calibration and variation of the input amplitude between the frequency. The measured value of the non-linearity is dependent on the attenuation of the input line. Because this calibration is the main source of uncertainty of the measurement, the error corresponding to a 3 dB attenuation variation of the input line is shown with the red area.

Variation between the resonators of each samples could also be explained by the presence of geometry defects in the thickness or the width. Such variation could cause tightening where the critical current would be lowered. This effect is consistent with the values slightly lower than the expected j_* .

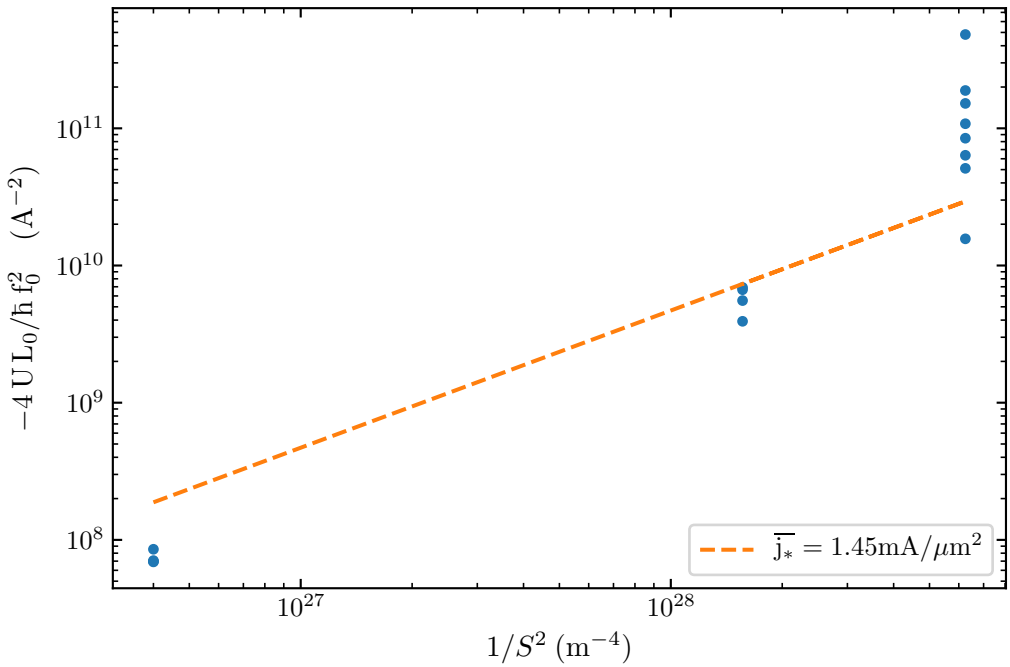

Figure 2.25: Variation of the term $-\frac{4L_0U}{\hbar\omega_0^2}$ with respect to $1/S^2$ for each of the sample. The curve for the average critical current of 1.45 $mA/\mu m^2$ is shown in dashed orange.

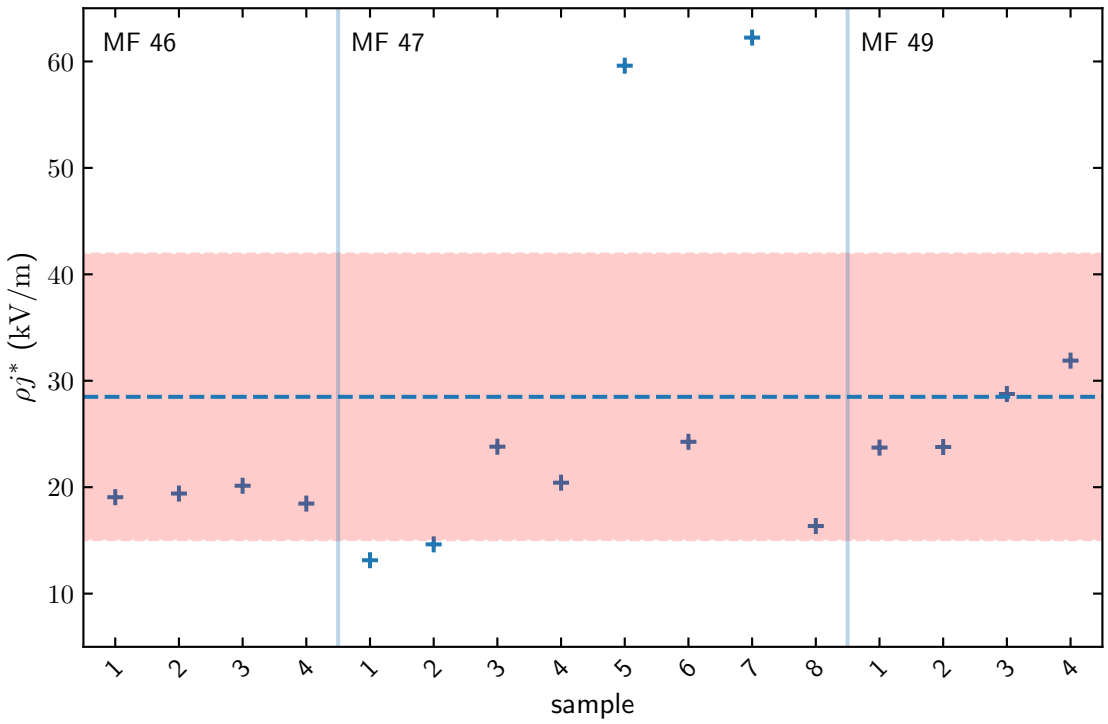

Figure 2.26: Current density j_* multiplied by their resistivity ρ for each resonator. The dashed line corresponds to the expectation of the product $j_*\rho$ from the DC measurement of 28.5 kV/m. The red area correspond to an error of 3dB of the calibration of the input line around this expectation.

Conclusion

In this chapter we introduced the main theoretical results needed to explain the inductive and non-linear behavior of Granular Aluminium. We presented the techniques we used to produce thin layers of such material and we reported on the spectroscopy of non-linear LC resonators and compare their non-linearity. In conclusion, we verified the link between the room temperature resistance and the zero temperature inductance, we measured the non-linearity of different samples over 5 order of magnitude and verified the scaling law with the critical current density. Finally, we fabricated non-linear resonators whose non-linearity is about 10 kHz that we can use as a basis for the experiments on lattices .

Chapter 3

Thermalization and condensation in finite lattices of transmon like resonator

Contents

In this chapter, we discuss the thermal equilibrium of a a photon gas in a two dimensional lattice as the one described in the first chapter and experimentally studied in chapter four. We will consider a description in the micro-canonical ensemble, where the total energy E and the total number of particles N is fixed. This is an unusual description for a photon gas, for which one normally considers the grand canonical ensemble with temperature T and chemical potential μ, leading to the Planck's law of blackbody radiation. However, in the case of a Kerr medium, the Hamiltonian conserves both energy and photon number, which justifies a micro-canonical approach. As this is often the case in this situation, we will consider an equivalent grand canonical distribution. In the regime of large temperature $k_B T \gg \mu$, the resulting distribution corresponds to the Rayleigh-Jeans distribution, which is the limiting case of the Bose-Einstein distribution in the classical limit. This thermal equilibrium of classical waves has been studied in various non-linear wave media [68, 69].

One important aspect of these two distributions is that they both predict a condensation at sufficiently low temperature or large density. In the quantum regime, this condensation corresponds to the well-known phenomenon of Bose-Einstein condensation. But the phenomenon persists in the classical regime, and has been given the name of «classical wave condensation» [41, 70]. This wave condensation at thermal equilibrium has only been observed very recently in a multimode optical fiber [36]. In two dimensions, both the Bose-Einstein and the wave condensation do not exist at the thermodynamic limit but result of finite size effects. We will discuss in details the predictions for this condensation in the MF56 square lattice designed in the first chapter.

A major question in our experiment is to know whether the photons injected in the lattice have time to thermalize (and eventually condense) before the system relaxes towards vacuum because of losses. In classical non-linear wave media, the time evolution of the system towards equilibrium is well understood in the case of weak non-linearity, for which the theory of weak turbulence applies [68, 69]. This theory describes the evolution of the waves by a kinetic equation, which admits the Rayleigh-Jeans distribution as steady state. It is well adapted to the description of continuous systems. In our case, the number of modes is small and it is possible to numerically obtain the time evolution for the amplitude of each mode. We will derive the equations of motion for the mode amplitudes, including the non-linearity, and present the result of numerical simulations. We will show that relaxation towards thermal equilibrium is recovered, and that we numerically observe the phenomenon of wave condensation.

3.1 Thermal equilibrium of photons in a lattice

A key feature of the Kerr interaction is that the corresponding Hamiltonian not only conserves the energy but also the number of photons, or in classical language the total intensity. In the first chapter, we have seen how to obtain the normal modes of a lattice, which leads to the following second quantized Hamiltonian

$$H = \sum_m \hbar \Omega_m a_m^\dagger a_m \tag{3.1.1}$$

where Ω_m is the frequency of the m-th normal mode and a_m the associated bosonic operator. Here, we use a quantum description, but the same calculation could be done using classical wave amplitudes α_m. In the presence of Kerr interactions between the mode, the Hamiltonian becomes

$$H = \sum_m \hbar \Omega_m a_m^\dagger a_m + \sum_{mnpq} \hbar U_{mnpq} a_m^\dagger a_n^\dagger a_p a_q \tag{3.1.2}$$

We will see in the next section how to derive the expression of the U_{mnpq} tensor starting from the non-linear inductance of the transmons building the lattice. A straightforward calculation

then gives

$$\left[a_m^\dagger a_n^\dagger a_p a_q, a_r^\dagger a_r\right] = -\delta_{mr}\, a_r^\dagger a_n^\dagger a_p a_q - \delta_{nr}\, a_m^\dagger a_r^\dagger a_p a_q + \delta_{pr}\, a_m^\dagger a_n^\dagger a_r a_q + \delta_{qr}\, a_m^\dagger a_n^\dagger a_p a_r \tag{3.1.3}$$

from which we obtain

$$[H, N] = 0 \quad \text{with} \quad N = \sum_r a_r^\dagger a_r \tag{3.1.4}$$

Therefore, in a lossless Kerr lattice, both H and N are constant of motions. If light is injected into the lattice and the system reaches equilibrium, the final state of the system must be described by the micro-canonical ensemble. As usual, it is more convenient to work in the grand canonical ensemble and find the corresponding temperature T and chemical potential μ such that $\langle H\rangle$ and $\langle N\rangle$ coincide with H and N.

If we include losses, the time evolution of the lattice is governed by the master equation

$$\frac{d\rho}{dt} = -\frac{i}{\hbar}[H, \rho] + \sum_m \kappa_m (a_m \rho a_m^\dagger - \frac{1}{2}\{a_m^\dagger a_m, \rho\}) \tag{3.1.5}$$

The evolution of $\langle N\rangle$ is then given by

$$\sum_m \frac{d\langle a_m^\dagger a_m\rangle}{dt} = -\sum_m \kappa_m \langle a_m^\dagger a_m\rangle \tag{3.1.6}$$

and, neglecting the contribution of the non-linear term, the mean energy $\langle H\rangle$ evolves as

$$\sum_m \hbar\Omega_m \frac{d\langle a_m a_m\rangle}{dt} = -\sum_m \kappa_m\, \hbar\Omega_m\, \langle a_m^\dagger a_m\rangle \tag{3.1.7}$$

If the loss rates κ_m of the different modes are all equal to κ, then $\langle N\rangle$ and $\langle H\rangle$ simply evolve as $N_0 e^{-\kappa t}$ and $H_0 e^{-\kappa t}$, where N_0 is the initial photon number and H_0 is the initial energy. If the decay time $1/\kappa$ is sufficiently large compared to the thermalization time, we may assume that the system stays at equilibrium with a distribution that follows a deterministic evolution due to losses. Of course, at times $t \gg 1/\kappa$, the number of photons become too small for collisions to thermalize the system, and the quasi-equilibrium approximation breaks down.

3.1.1 Bose-Einstein and Rayleigh-Jeans distributions

If the non-linearity is sufficient to bring the system to equilibrium, but weak enough so that an ideal gas description is still valid, we expect that the photon populations in the normal modes follow the Bose-Einstein distribution

$$n_m = \frac{1}{e^{\beta(\hbar\Omega_m - \mu)} - 1} \tag{3.1.8}$$

where $\beta = 1/(k_B T)$ is the inverse temperature. As justified in the previous section, even though the particles are photons, we do not expect a zero chemical potential because of the conservation of the total photon number by the Kerr term. In the limit of large temperature, $\exp\beta(\hbar\Omega_m - \mu) \approx 1 + \beta(\hbar\Omega_m - \mu)$, and the Bose-Einstein distribution can be approximated by the Rayleigh-Jeans distribution

$$n_m \approx \frac{k_B T}{\hbar\Omega_m - \mu} \tag{3.1.9}$$

This distribution, without the chemical potential μ, was introduced in 1900 by Rayleigh and corrected by Jeans to describe the blackbody spectrum at low frequency $\hbar\Omega \ll k_B T$. The same name was used later to describe the equilibrium distribution of classical waves that thermalize in a Kerr medium.

In order to clarify the physical origin of these two distributions, and in particular to justify the Rayleigh-Jeans distribution for classical waves, we reproduce the detailed balance argument that is often used to derive these distributions. If the non-linearity is not too strong, we can suppose that only quadruplet of modes such that $\Omega_1 + \Omega_2 = \Omega_3 + \Omega_4$ are coupled by the Kerr term. Detailed balance imposes that the collision rate for the process $1, 2 \to 3, 4$ is equal to the one of the reverse process $3, 4 \to 1, 2$ for all quadruplets that fulfill the frequency matching condition. This leads to the following detailed balance condition

$$n_1 n_2 (n_3 + 1)(n_4 + 1) = (n_1 + 1)(n_2 + 1) n_3 n_4 \quad \text{if} \quad \Omega_1 + \Omega_2 = \Omega_3 + \Omega_4 \tag{3.1.10}$$

where n_i is the population or intensity of mode i. The $(n_i + 1)$ term accounts for simulated emission in the final mode, if it is already populated. Introducing $f_i = n_i/(n_i + 1)$, we obtain $f_1 f_2 = f_3 f_4$. Supposing that f_i is only a function of Ω_i, such that $f_i = f(\Omega_i)$, we obtain that f must be an exponential function and we arrive at

$$\frac{n_i}{n_i + 1} = e^{-\tilde{\beta}(\Omega_i + \tilde{\mu})} \tag{3.1.11}$$

where $\tilde{\beta}$ and $\tilde{\mu}$ are constants that can be later identified to the inverse temperature and the chemical potential in frequency units. Inverting the equation to obtain n_i leads to the Bose-Einstein distribution (3.1.8). In the limit of small occupation number $n_i \ll 1$, one obtains the Boltzmann distribution $n_i = \exp -\tilde{\beta}(\Omega_i + \tilde{\mu})$.

The other limit $n_i \gg 1$ is considered less often and corresponds to the classical wave limit. The detailed balance (3.1.10) becomes

$$n_1 n_2 n_3 + n_1 n_2 n_4 = n_1 n_3 n_4 + n_2 n_3 n_4 \tag{3.1.12}$$

where we have neglected quadratic terms in comparison to cubic terms. This condition can be rewritten

$$n_4^{-1} + n_3^{-1} = n_2^{-1} + n_1^{-1} \tag{3.1.13}$$

Again, if we suppose that n_i is only a function of Ω_i, we obtain that

$$n_i^{-1} = \tilde{\beta}(\Omega_i + \tilde{\mu}) \tag{3.1.14}$$

This corresponds to the Rayleigh-Jeans distribution given in (3.1.9). A more rigorous derivation can be found, for example, in [68], where it is shown that, under the random phase approximation, classical waves in a Kerr medium admit this distribution as equilibrium distribution. This is expected because quantum bosonic modes in the large occupation limit are equivalent to classical harmonic modes.

Comparison of the two distributions

We now consider the predictions for the spectrum of photons in our lattice comparing the two distributions. In order to obtain more general and simple results, we consider in this paragraph a square lattice described by a tight-binding model with the same hopping rate J in the x and y directions. The dispersion of the band is given by

$$\Omega(k) = \omega_0 - J(\cos k_x a + \cos k_y a) \tag{3.1.15}$$

where a is the distance between the sites. In the first chapter, we have seen that the dispersion of our square transmon lattice is well approximated by this model. The density of states $\rho(\omega)$ can be obtained from the following formula

$$\rho(\omega) = \frac{1}{\pi} \sum_k \mathrm{Im} \frac{1}{\omega - \Omega(k) - i\kappa} \tag{3.1.16}$$

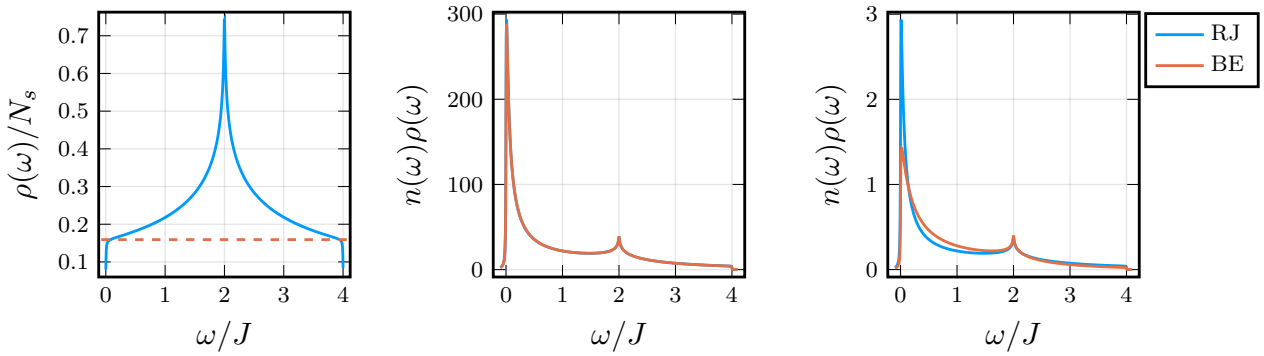

Figure 3.1: Left: Density of states of a square lattice with $Ns = 10^6$ sites. The dashed line shows the constant value for massive 2D particles. Center: Lattice photon spectral density in the classical regime. The spectrum is normalized to the number of sites. The mean photon density is 100 per site (it corresponds to the integrated spectrum), and the mean energy per photon is $\hbar J$. Right: Photon spectrum in the quantum regime. The mean photon density is one per site and the mean energy per photon is $\hbar J$. The Rayleigh-Jeans and Bose-Einstein distributions predict different spectra only in the quantum regime.

where κ is a small positive frequency which accounts for the finite width of the lattice modes. The sum over k goes over N_s values in the first Brillouin zone, where N_s is the number of sites in the lattice. The left plot in figure 3.1 shows the DOS for a large lattice with $N_s = 10^6$ sites. At the bottom of the band, the DOS is approximately constant, as expected for massive particles in two dimensions, and equal to $N_s/(2\pi J)$.

The resulting photon spectra $n(\omega)\rho(\omega)$ are shown in the central and right plots in figure 3.1, considering both the Bose-Einstein and Rayleigh-Jeans distributions. The central plot corresponds to the classical regime, while the right plot corresponds to the quantum regime, where we see a clear difference between the two distributions. For each plot, the parameters T and μ of the distributions are adjusted to describe the same micro-canonical ensemble defined by the values of H and N. The mean photon density is 100 photons per sites in the classical case, and one per site in the quantum case. The mean energy per photon is $\hbar J$ in both cases. In the classical case, we obtain that the temperature for both distributions are almost identical and close to $k_B T \approx 100\,\hbar J$. In the quantum case, the temperature of the two distributions are quite different: we obtain $k_B T \approx 2\,\hbar J$ for the Bose-Einstein distribution, and $k_B T \approx \hbar J$ for the Rayleigh-Jeans one.

The Bose-Einstein distribution leads to a wider distribution, because collisions to empty modes are more favored than with the Rayleigh-Jeans distribution. This is due to the presence of vacuum fluctuations, which are taken into account only by the Bose-Einstein distribution.

3.1.2 Wave and Bose-Einstein condensation in 3D

Before considering the 2D situation that applies to our lattice, we consider the 3D case in order to discuss the difference between the two phenomena of wave and Bose-Einstein condensation in a situation where a «true» condensation occurs, in the sense that it happens at the thermodynamic limit. In 3D, the density of states per unit volume for free massive particles grows as $m/(2\pi^2\hbar^3)\sqrt{2m\epsilon}$ with the energy ϵ, where m is the mass of the particles. As a result, the density of particles in an ideal Bose gas can be computed as

$$n = \int_0^\infty \frac{m}{2\pi^2\hbar^3}\frac{\sqrt{2m\epsilon}}{e^{\beta(\epsilon-\mu)}-1}\,d\epsilon \xrightarrow[\mu\to 0]{} n_c^{\text{3D BE}} = \lambda_{\text{th}}^{-3} \times 2.612\ldots \tag{3.1.17}$$

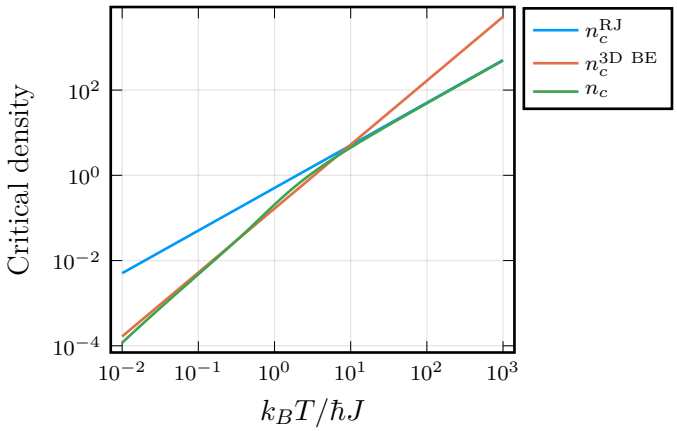

Figure 3.2: Crossover between Bose-Einstein and classical wave condensation in a 3D photonic cubic lattice. We plot the critical density above which the condensate appears as a function of temperature. The numerical simulation of the critical density interpolates between a quantum regime where the critical density (number of photons per site) corresponds to the one of Bose-Einstein condensation in a 3D uniform gas and a classical regime where the critical density for condensation can be explained by considering the Rayleigh-Jeans distribution and the lattice dispersion. This condensation at high temperature is a classical wave effect.

where $\lambda_{\mathrm{th}} = \sqrt{2\pi\beta\hbar^2/m}$ is the thermal de Broglie wavelength. At a given temperature, the density of the gas saturates to a finite value when μ increases. This saturation density corresponds to a mean distance between particles of the order of the thermal de Broglie wavelength. The particles in excess condense in the ground state, whose population was neglected in the integral formula. This corresponds to the phenomenon of Bose-Einstein condensation, which is a quantum effect due to the quantum statistics of bosons.

However, a similar phenomenon can be observed with classical waves and was given the name of wave condensation. If we replace the Bose-Einstein distribution by the Rayleigh-Jeans one, we obtain a divergent integral at high frequency. This is the famous «ultraviolet catastrophe», which was solved by Planck. In the theory of classical weakly non-linear waves, where the Rayleigh-Jeans distribution is expected to be valid, one introduces a cutoff at large k whose physical justification depends on the considered type of waves. With the cutoff, the integral for the total intensity saturates as in the quantum case. For example, if we consider waves with a linear dispersion $\Omega = kc$, we obtain for the density

$$n = \int_0^{k_{\max}} \frac{4\pi k^2}{\beta(ck-\mu)}\,dk \xrightarrow[\mu\to 0]{} \frac{2\pi k_{\max}^2}{\beta c} \tag{3.1.18}$$

where $k_{\max}$ sets the cutoff. Once this maximal density is reached, the remaining intensity goes into the lowest energy mode [41]. This equilibrium condensation phenomenon has been observed only recently in a pumped multimode fiber [36]. As discussed in this reference, related non-linear phenomena leading to the accumulation of energy in the lowest energy mode have been observed before but in out-of-equilibrium situations.

In the case of a photonic lattice, the lattice spacing introduces a natural cutoff $k_{\max} \approx 1/a$ in the system. We thus expect that both classical wave and Bose-Einstein condensation can be observed in such systems. If we suppose that the lattice dispersion is $\Omega(k) = \omega_0 - J(\cos k_x a + \cos k_y a + \cos k_z a)$, we obtain that, with the Rayleigh-Jeans distribution, the photon density is

$$n = \frac{1}{(2\pi)^3}\iiint_{-\pi/a}^{\pi/a} \frac{k_BT}{\hbar\Omega(k)-\mu}\,d^3k \xrightarrow[\mu\to\omega_0-3J]{} n_c^{\mathrm{RJ}} = \frac{k_BT}{\hbar J} \times 0.505\ldots \tag{3.1.19}$$

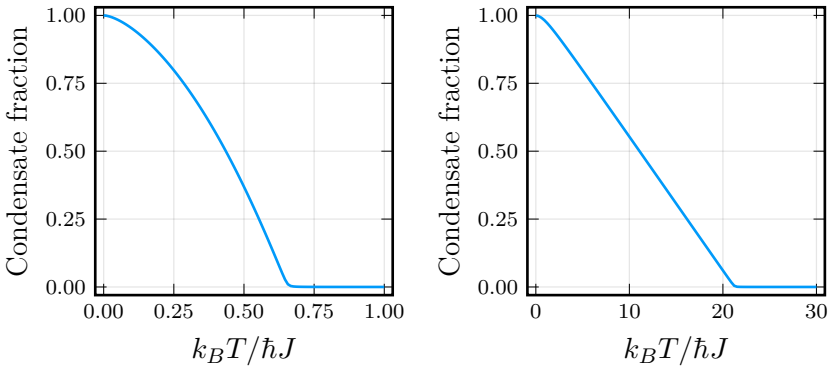

Figure 3.3: Evolution of the condensate fraction as a function of temperature for a Bose-Einstein condensate (left) and a classical wave condensate (right) in a 3D lattice. In the first case, the mean photon density is 0.1, while the second case corresponds to a density of 10 photons per site.

The last expression sets the expression for the critical density in units of number of photons per site, above which wave condensation occurs. The cutoff does not appear explicitly and we obtain a universal expression, which is valid at the thermodynamic limit. We have derived this result for a cubic lattice, but we expect that this expression remains correct for other types of lattices, except for the precise value of the numerical constant that depends on the details of the considered lattice.

We now derive the expected critical density for Bose-Einstein condensation in the same lattice. If the temperature is sufficiently small, which is the regime where the Bose-Einstein distribution is expected to be valid, we can consider the lattice dispersion to be well approximated by $\hbar J k^2 a^2/2$. This corresponds to an effective mass $m = \hbar/(Ja^2)$ and the thermal de Broglie wavelength in the lattice can be written as $\lambda_{\text{th}} = a\sqrt{2\pi\beta\hbar J}$. The condensation threshold (3.1.17) then becomes

$$n_c^{\text{3D BE}} = \left(\frac{k_BT}{2\pi\hbar J}\right)^{3/2} \times 2.612\ldots \tag{3.1.20}$$

In figure 3.2, we plot the two critical densities n_c^{RJ} and $n_c^{\text{3D BE}}$ as a function of $k_BT/\hbar J$. We compare them to a numerical calculation of the exact critical density using the Bose-Einstein distribution and making no approximation about the lattice dispersion, in which case we obtain

$$n_c = \frac{a^3}{(2\pi)^3}\iiint_{-\pi/a}^{\pi/a} \frac{1}{e^{\beta\hbar J(3-\cos k_x a-\cos k_y a-\cos k_z a)}-1}\,dk_x\,dk_y\,dk_z \tag{3.1.21}$$

We observe the expected crossover between a low temperature regime where the condensation corresponds to Bose-Einstein condensation, with a critical density increasing as $T^{3/2}$, and a high temperature regime, where the condensation is a classical wave condensation due to the lattice cutoff. In this case, the critical density increases as T. The crossover happens when the mean number of photon per site is on the order of unity, or equivalently when $k_BT \sim \hbar J$, which is also equivalent to $\lambda_{\text{th}} \sim a$.

In an experiment, the distinction between the two phenomena could be clearly established by measuring the condensate fraction as a function of temperature as shown in figure 3.3. In the quantum regime, the condensate fraction follows the well known $1-(T/T_c)^{3/2}$ behavior [71], while, in the classical case, the condensate fraction varies almost linearly as $1-(T/T_c)$. This linear behavior comes from the linear dependence of the occupation number with temperature in

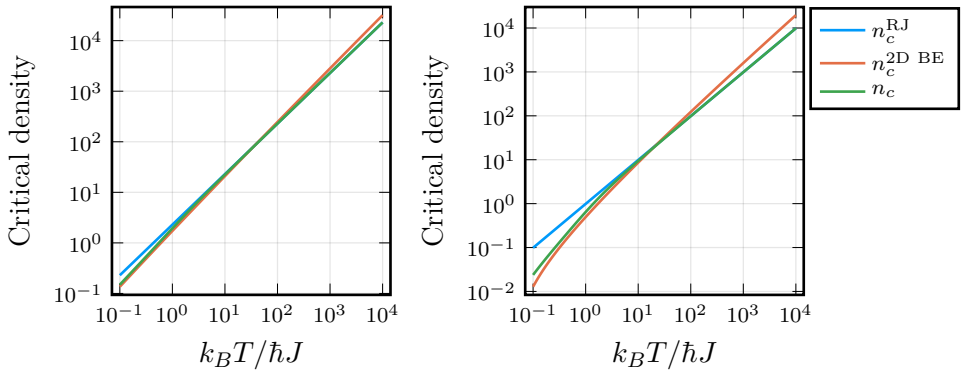

Figure 3.4: Crossover between Bose-Einstein and classical wave condensation in a 2D photonic square lattice. As in 3D (see figure 3.2), the critical density interpolates between two limiting cases: Bose-Einstein condensation at low temperature and classical wave condensation at high temperature. The left plot corresponds to a large lattice (1001×1001 sites) and the right plot to a small lattice (21×21 sites), similar to the one realized in our experiment.

the Rayleigh-Jeans distribution. Using the Rayleigh-Jeans distribution, the density or intensity of the waves can be written as

$$n = n_0 + Tf(\mu) \tag{3.1.22}$$

where n_0 is the condensate density and f is a function that depends on the dispersion of the considered waves. When μ tends to zero, the function $f(\mu)$ saturates to a finite value $f(0)$, which defines the critical temperature $T_c = n/f(0)$. The previous equation can then be rewritten

$$\frac{n_0}{n} = 1 - \frac{T}{T_c} \tag{3.1.23}$$

3.1.3 Wave and Bose-Einstein condensation in 2D

We now turn to the case of a 2D lattice, which corresponds to our experiment. It is well known that there is no Bose-Einstein condensation at the thermodynamic limit in a 2D system [71]. But condensation may still occur as a finite size effect. This is the same for classical wave condensation. In a 2D square lattice, the density in the classical limit can be computed analytically with the Rayleigh-Jeans distribution, one obtains

$$n = \frac{a^2}{(2\pi)^2} \iint_{-\pi/a}^{\pi/a} \frac{1}{\beta\hbar J(2 - \cos k_x a - \cos k_y a) - \mu}\, dk_x\, dk_y = \frac{8\pi}{\mu - 2} K\left(\frac{4}{(\mu-2)^2}\right) \tag{3.1.24}$$

where we have shifted the origin of energy to the bottom of the band and K is the complete elliptic integral of the first kind. The K function diverges when its argument tends to one from below, confirming that there is no wave condensation in 2D at the thermodynamic limit.

In order to take into account the finite size of the system, we introduce the small frequency $\delta = J(2\pi)^2/N_s$ which is the frequency difference between the ground state and the first excited state with $\delta k = 2\pi/(\sqrt{N_s}a)$. We now repeat the same reasoning as in the 3D case. We first consider a Bose gas with particles having a mass $m = \hbar/(Ja^2)$, which corresponds to the effective mass in the lattice. Taking into account all states except the ground state, the density saturates, when μ reaches zero, to

$$n_c^{\mathrm{2D\ BE}} = \frac{1}{2\pi\hbar J} \int_\delta^\infty \frac{1}{e^{\beta\epsilon} - 1}\, d\epsilon \tag{3.1.25}$$

$$\approx -\frac{k_B T}{2\pi\hbar J} \ln \frac{\hbar\delta}{k_B T} \tag{3.1.26}$$

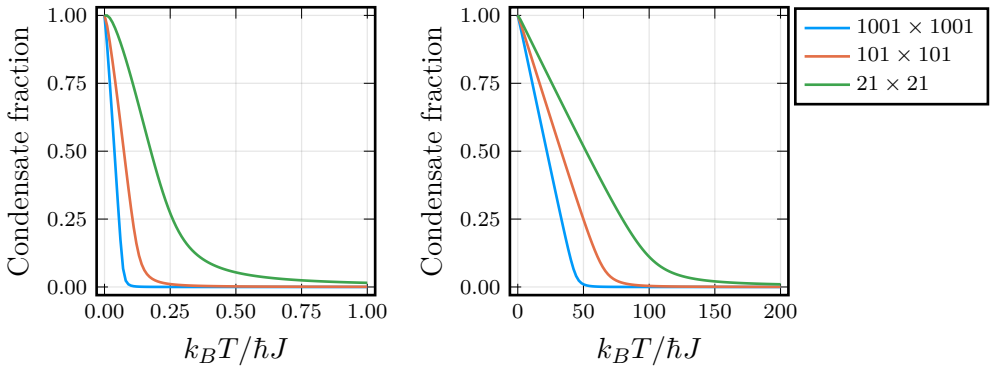

Figure 3.5: Evolution of the condensate fraction as a function of temperature for a Bose-Einstein condensate (left) and a classical wave condensate (right) in a 2D square lattice. The mean photon density is 0.1 in the first case and 100 in the second case. In each plot, the different curves correspond to different lattice sizes, showing the weak dependence of the critical temperature with the system size.

where we have supposed that $\beta\hbar\delta \ll 1$ to obtain the final expression. We now consider the Rayleigh-Jeans distribution and include the band structure of the lattice to introduce a high energy cutoff. The critical density for condensation is given by

$$n_c^{\mathrm{RJ}} = \frac{1}{N_s}\sum_{k\neq 0}\frac{1}{\beta\hbar J(2-\cos k_x a-\cos k_y a)} \tag{3.1.27}$$

where the sum goes over $Ns-1$ values in the Brillouin zone, excluding $k_x = k_y = 0$. In order to obtain an analytical expression, we approximate the sum by an integral and we replace the lattice dispersion $\Omega(k)$ by its quadratic expansion. This leads to the following approximate expression

$$n_c^{\mathrm{RJ}} \approx \frac{a^2}{(2\pi)^2}\int_{\delta k}^{\pi/a}\frac{2k_BT}{\hbar J k^2a^2}\,2\pi k\,dk = -\frac{k_BT}{2\pi\hbar J}\ln\frac{\delta k^2a^2}{\pi^2} \tag{3.1.28}$$

Finally, we compare these expressions to the exact critical density that we numerically compute through

$$n_c = \frac{1}{N_s}\sum_{k\neq 0}\frac{1}{e^{\beta\hbar J(2-\cos k_x a-\cos k_y a)}} \tag{3.1.29}$$

Figure 3.4 compares the predictions of equation (3.1.26), (3.1.27) and (3.1.29) for two different lattice sizes. We observe the same behavior than in the 3D case, but the difference between the classical and quantum regime is less pronounced. Finally, we show in figure 3.5 the evolution of the condensate fraction in the case of Bose-Einstein condensation (left plot) and classical wave condensation (right plot). As in the 3D case, the classical wave condensation shows a characteristic linear dependence of the condensate fraction with temperature. Because the condensation is a finite size effect, the critical temperature at a given density depends on the lattice size. But the dependence is only logarithmic, when the number of sites increases by a factor 100, the critical temperature decreases by less than a factor two as can be seen in the figure.

3.1.4 Wave and Bose-Einstein condensation in MF56 lattice

We now apply the calculations of the previous section to the specific case of the MF56 square lattice that is described in the first chapter. In this chapter, we assume that the inductance of each granular Aluminum wire in the lattice is 17 nH. Figure 3.6 shows the critical density as a

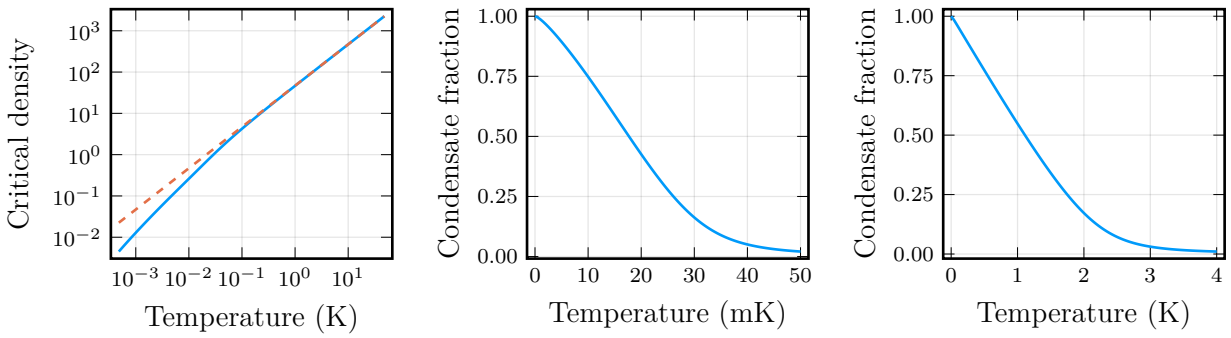

Figure 3.6: Bose-Einstein and classical wave condensation in a square lattice corresponding to the MF56 sample. Left: Evolution of the critical density for condensation. The solid blue line is the prediction using the Bose-Einstein distribution. At high temperature, the curve coincides with the critical density predicted from the Rayleigh-Jeans distribution shown by the dashed red line. Center and right: Evolution of the condensate fraction as a function of temperature in the Bose-Einstein condensation and classical wave condensation regimes. The mean photon density is one for the central plot, and 100 for the right one.

function of temperature, as well as the evolution of the condensate fraction in the Bose-Einstein and classical wave condensation regimes. One should note that, because the effective mass in the lattice is negative, the temperature is also negative, while the chemical potential is always above the highest frequency in the spectrum. For convenience, the different curves are plotted with a positive temperature, which is the opposite of the actual temperature appearing in the distribution functions.

Finally, we show in figure 3.7 the evolution of the photon spectrum in the lattice, when the temperature is decreased below the critical temperature for classical wave condensation. The mean density is fixed to 100 photons per site as in the right plot of figure 3.6. Because the effective mass is negative, the condensate corresponds to a macroscopic population of the highest frequency mode.

3.2 Numerical simulation of thermalization in a 2D lattice

In the previous section, we have studied the equilibrium properties of photons in a lattice. One important question is whether this thermalization may occur before losses empty the lattice. In this section, we study a scenario where the lattice modes are initially populated, evolve with a Kerr Hamiltonian and eventually reach thermal equilibrium. We start by deriving the equations governing the time evolution of the mode amplitudes and then show the results of numerical simulations. Here, we treat the mode amplitudes as classical degree of freedom. We thus expect that the system should relax towards an equilibrium given by the Rayleigh-Jeans distribution.

3.2.1 Non-linear Kerr tensor

In the first chapter, we have derived the Hamiltonian of a lattice of transmons in the linear regime and obtained

$$H_{\text{lin}} = \frac{1}{2}\sum_{ij} C_{ij}^{-1} q_i q_j + K_{ij}\phi_i\phi_j = \sum_m \Omega_m \, \alpha_m^* \alpha_m \tag{3.2.1}$$

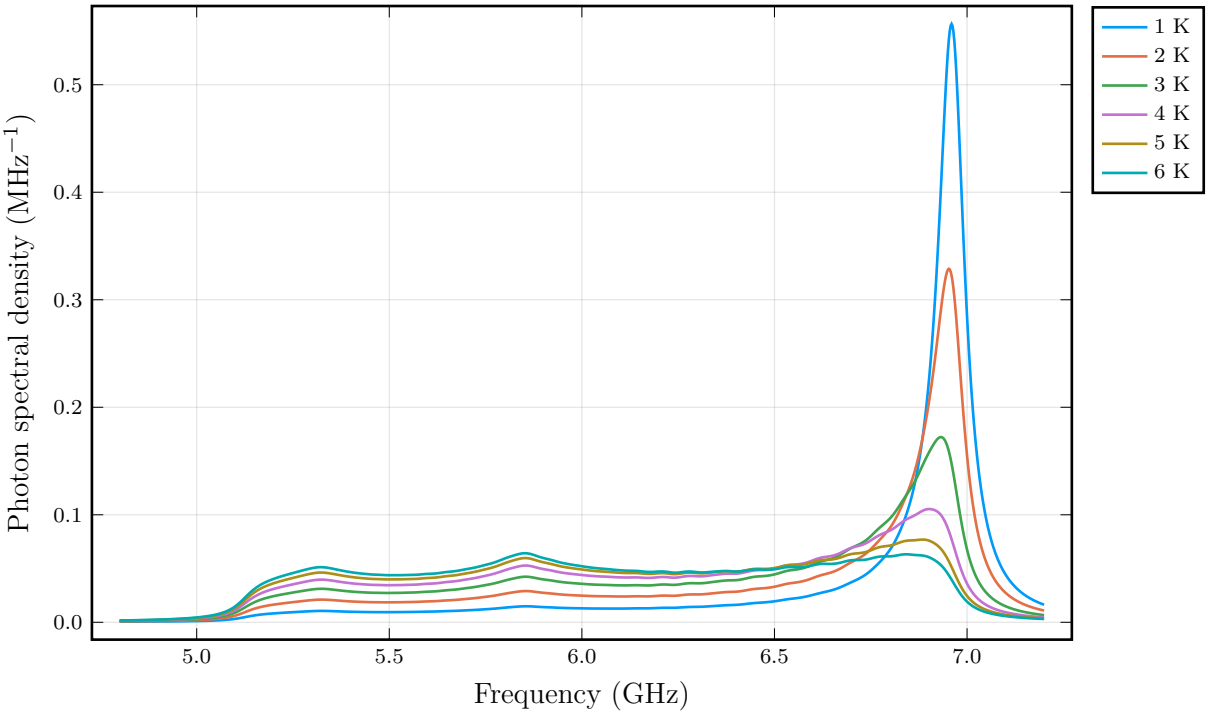

Figure 3.7: Evolution of the photon spectrum as a function of temperature in the MF56 lattice for a mean density of 100 photons per site. The critical temperature for wave condensation is approximately 2.3 K. The condensate appears as a growing peak at the upper end of the spectrum. The spectrum is computed using a 40 MHz wide lorentzian response function to obtain a smooth function.

where Ω_m are the frequencies of the normal modes, which correspond to the diagonal elements of the Ω matrix obtained in 1.2.13. As derived in 2.1.2, if two nodes i and j are connected by a HKIS wire of inductance L_0, the non-linearity of the inductance adds a term $(\phi_i - \phi_j)^4/(2L_0^3 I_*^2)$ to the potential energy. The Kerr term in the Hamiltonian can thus be written as

$$H_{\text{Kerr}} = -\sum_{\langle ij \rangle} \frac{(\phi_i - \phi_j)^4}{2L_0^3 I_*^2} \tag{3.2.2}$$

where the sum goes over all pairs of nodes connected by a wire. We now rewrite this term in the normal mode basis in order to obtain the non-linear tensor introduced at the beginning of this chapter. We have seen that the flux at node i may be written as $\phi_i = \sum_m T_{\phi,im}(\alpha_m + \alpha_m^*)/\sqrt{2}$, from which we obtain

$$H_{\text{Kerr}} = -\frac{1}{4L_0^3 I_*^2} \sum_{\langle ij \rangle} \left[\sum_m (T_{\phi,im} - T_{\phi,jm})(\alpha_m + \alpha_m^*) \right]^4 \tag{3.2.3}$$

We label the pairs of connected nodes with a single index $k = \langle i, j \rangle$, and introduce the matrix $A_{km} = T_{\phi,im} - T_{\phi,jm}$, from which we obtain

$$H_{\text{Kerr}} = -\frac{1}{4L_0^3 I_*^2} \sum_{kmnpq} A_{km} A_{kn} A_{kp} A_{kq} \, (\alpha_m + \alpha_m^*)(\alpha_n + \alpha_n^*)(\alpha_p + \alpha_p^*)(\alpha_q + \alpha_q^*) \tag{3.2.4}$$

Performing a rotating wave approximation, we only retain terms involving the product of two mode amplitudes and two conjugate mode amplitudes, and finally obtain

$$H_{\text{Kerr}} = -\frac{3}{2L_0^3 I_*^2} \sum_{kmnpq} A_{km} A_{kn} A_{kp} A_{kq} \, \alpha_m^* \alpha_n^* \alpha_p \alpha_q \tag{3.2.5}$$

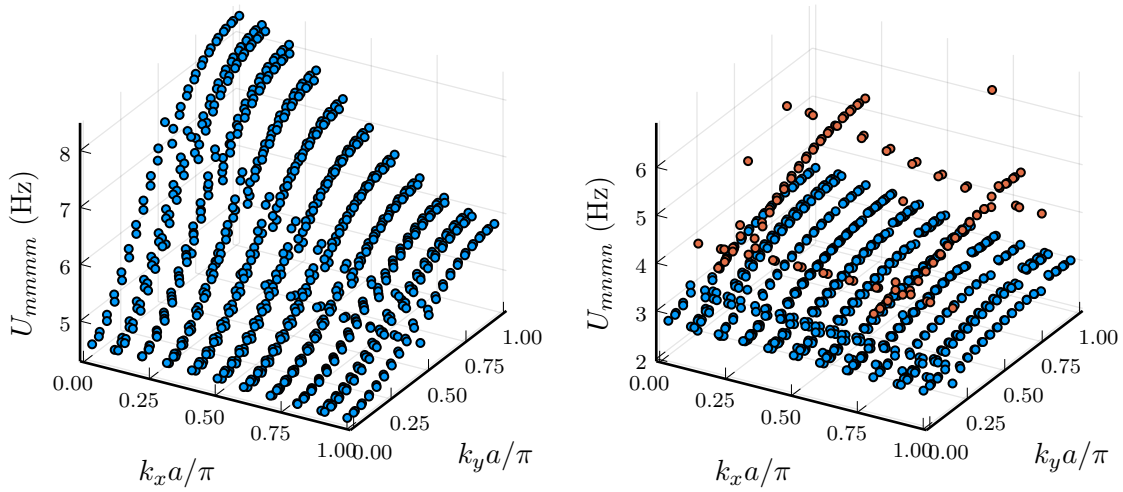

Figure 3.8: Variation of the self Kerr tensor (left) and cross Kerr tensor (right) for the MF56 lattice with parameters $L_0 = 17\,\mathrm{nH}$ and $I_* = 30\,\mu\mathrm{A}$. The left plot shows the variation of the self Kerr term in the reduced Brillouin zone. To a good approximation, it is proportional to the mode frequency. The right plot shows the variation of the cross Kerr term between the mode at $k_x a = k_y a = 0.2\,\pi$ and all the other modes. The cross Kerr is efficient if the wave-vector of the second mode lies on one of the four lines defined in the main text. The orange points correspond to the values of efficient cross Kerr ($> 0.5\,\mathrm{Hz}$), they effectively align on two horizontal and two vertical lines.

which conserves the number of photons, as shown in the beginning of the chapter. Here, we have supposed that the mode amplitudes α_m are classical variables that commute. In the quantum case, extra terms proportional to $\alpha_m^\dagger \alpha_n$ appear because of the commutation rules.

We now briefly look at the properties of the Kerr tensor $U_{mnpq} = 3\hbar/(2L_0^3 I_*^2) \sum_k A_{km} A_{kn} A_{kp} A_{kq}$. One usually classify the different processes depending on the number of modes involved in the non-linear process:

Self Kerr processes These processes correspond to terms proportional to U_{mmmm}. The effect of these terms is to shift the mode frequency from the value Ω_m as a function of the mode intensity. The dependence of U_{mmmm} as a function of the mode wave-vector is shown in the left plot of the figure 3.8. We observe that U_{mmmm} is approximately proportional to Ω_m. The order of magnitude for the self Kerr effect is given by $U_{mmmm} \sim U/N_s$, where $U = (3\hbar Z^2)/(2L_0^3 I_*^2)$ is the non-linearity of a single site. With the parameters chosen here ($L_0 = 17\,\mathrm{nH}$, $I_* = 30\,\mu\mathrm{A}$), we obtain a non-linearity per site $U = 2\pi \times 2.2\,\mathrm{Hz}$ per photon. The values of U_{mmmm} are slightly larger, because the density of photon in one mode is not uniform over the lattice, which enhances the non-linearity.

Cross Kerr processes These processes correspond to terms proportional to U_{mnmn}. They also create frequency shifts: the frequency of the m mode is shifted as a function of the intensity in the n mode. In the left plot of the figure 3.8, we plot the dependence of U_{mnmn} for a given m as a function of the wave-vector of the other mode. We observe that the cross-Kerr is large with modes that are distributed along two horizontal and two vertical lines in the reduced Brillouin zone. This corresponds to modes with a wave-vector such that

$$k_{\alpha n} = \begin{cases} k_{\alpha m} \\ \pi/a - k_{\alpha m} \end{cases} \tag{3.2.6}$$

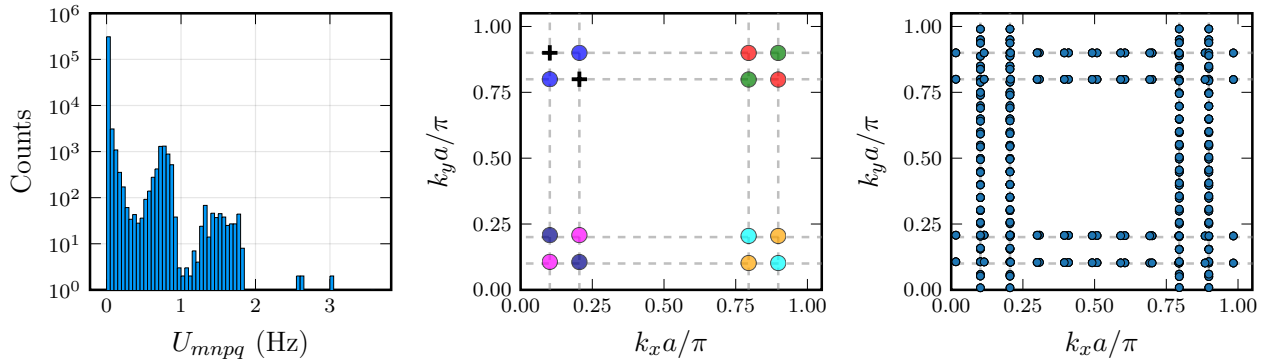

Figure 3.9: Variation of the four wave mixing tensor in the MF56 lattice. We choose one pair of modes with $k_{xm}a = k_{ym}a = 0.2\,\pi$ and $k_{xn}a = k_{yn}a = 0.1\,\pi$ and compute U_{mnpq} for all the other pairs (p, q). The left plot shows the repartition of the values of U_{mnpq}. The central plot shows the location in the reduced Brillouin zone of the seven pairs which give the largest U_{mnpq}, each pair is identified with a different color. The two crosses correspond to the position of the (m, n) pair. The dashed lines corresponds to $k_\alpha = k_{\alpha i}$ and $k_\alpha = \pi/a - k_{\alpha i}$ with $\alpha = x, y$ and $i = m, n$. The right plot shows the positions of the modes (p, q), for which the value of U_{mnpq} is more than $2\pi \times 1\,\mathrm{Hz}$.

where $\alpha = x, y$. This condition can be explained by supposing that the spatial dependence of the modes can be approximated by the product of two standing waves, one for each direction. The overlap of modes that appear in the tensor can then be separated into the product of two independent contributions for each axis. For each axis, one easily shows that the overlap is maximum for the conditions given above.

Three and four wave mixing processes These processes correspond to terms proportional to U_{mnmp} and U_{mnpq}. They can be interpreted as collisions between photons that redistribute the energy in the lattice. In free space, the tensor U_{mnpq} is non zero only for pairs of states such that the total momentum is conserved during the collision. Figure 3.9 shows the distribution of the values U_{mnpq} for a given pair (m, n) and the location in the reduced Brillouin zone of the states that efficiently collide with this pair. These modes are located along four horizontal and four vertical lines, for the same reasons as the cross Kerr terms are maximal along two horizontal and two vertical lines.

3.2.2 Equation of motions for the normal mode amplitudes

The equations of motion for the amplitudes of the normal modes are

$$\frac{d\alpha_m}{dt} = i\Omega_m\alpha_m - \frac{\kappa_m}{2}\alpha_m + i\frac{\partial H_{\mathrm{Kerr}}}{\partial \alpha_m^*} \tag{3.2.7}$$

$$= i\Omega_m\alpha_m - \frac{\kappa_m}{2}\alpha_m - i\frac{3}{L_0^3 I_*^2}\sum_{knpq} A_{km}A_{kn}A_{kp}A_{kq}\,\alpha_n^*\alpha_p\alpha_q \tag{3.2.8}$$

where we include a damping rate κ_m for each mode. For numerical efficiency, it is advantageous to move to the rotating frame for each mode. We thus define $\alpha_m(t) = \sqrt{\hbar}\,\tilde{\alpha}_m(t)\exp i\Omega_m t$ and look for the evolution of the $\tilde{\alpha}_m$ amplitudes. The scaling by $\sqrt{\hbar}$ makes the $\tilde{\alpha}_m$ dimensionless, and $|\tilde{\alpha}_m|^2$ corresponds to the number of photons in the mode m. The equations of motion become

$$\frac{d\tilde{\alpha}_m}{dt} = -\frac{\kappa_m}{2}\tilde{\alpha}_m + i\frac{3\hbar}{L_0^3 I_*^2}\sum_{knpq} A_{km}A_{kn}A_{kp}A_{kq}\,e^{-i(\Omega_m+\Omega_n-\Omega_p-\Omega_q)t}\,\tilde{\alpha}_n^*\tilde{\alpha}_p\tilde{\alpha}_q \tag{3.2.9}$$

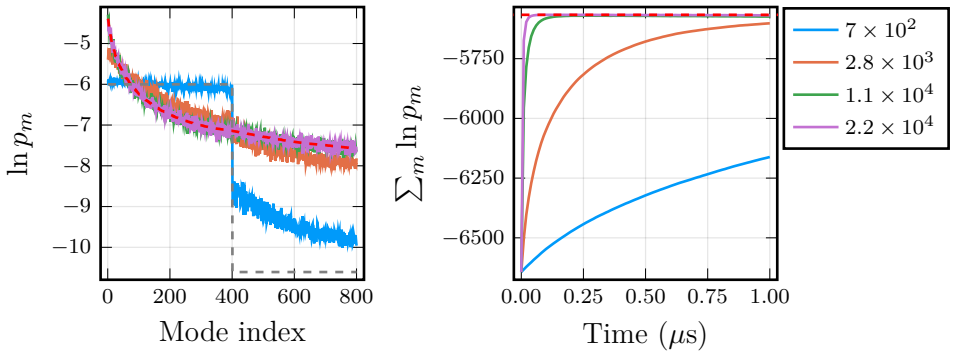

Figure 3.10: Thermalization in the MF56 sample for different initial populations in the lattice. The initial distribution is the steplike function shown by the black dashed line, multiplied by a number of photons n_0 indicated in the legend. The left plot shows the final distributions after one microsecond of evolution. When n_0 increases, the distributions tend to the equilibrium distribution shown by the red dashed curve. The right plot shows the growth of entropy with time for the different initial populations.

We numerically solve this set of coupled non-linear ordinary differential equations using an open source explicit Runge-Kutta algorithm [72]. The precision of the algorithm is adjusted by checking that the number of photons and the energy are conserved during evolution. In the numerical code, we evaluate the non-linear term by rewriting it as

$$\sum_{knpq} A_{km} A_{kn} A_{kp} A_{kq}\, e^{-i(\Omega_n - \Omega_p - \Omega_q)t}\, \tilde{\alpha}_n^* \tilde{\alpha}_p \tilde{\alpha}_q = \sum_k A_{mk}^T |\beta_k|^2 \beta_k \tag{3.2.10}$$

with $\beta_k = \sum_m A_{km}\, \tilde{\alpha}_m \exp(i\Omega_m t)$. We first evaluate the vector β, which can be computed as a matrix product, and then compute $\sum_k A_{mk}^T |\beta_k|^2 \beta_k$, which is also a matrix product. We find that this is the fastest way to contract the non-linear tensor.

In the simulations shown below, we adjust the initial population in each mode and draw random phases to obtain the initial values $\alpha_m(0)$. The simulation is repeated 128 times with different initial random phases. We then average over the different realizations to obtain the evolution of the average mode population $n_m(t) = \langle |\alpha_m(t)|^2 \rangle$.

3.2.3 Thermalization rate

The process of thermalization can be monitored by looking at the evolution of the entropy in the lattice. During thermalization, one expects that the entropy increases and then reaches a maximum, which signals thermal equilibrium. The entropy of an ideal Bose gas writes

$$\frac{S}{k_B} = \sum_m \ln(1 + n_m) + n_m \ln(1 + n_m) \tag{3.2.11}$$

The first term is often called «wave entropy» and the second term «particle entropy» [73]. In the regime of validity of the Rayleigh-Jeans distribution, the wave entropy term dominates and we obtain

$$\frac{S}{k_B} = \sum_m \ln n_m \tag{3.2.12}$$

One easily checks that maximizing $S/k_B - \beta(H - \mu N)$ with $N = \sum_m n_m$ and $H = \sum n_m \hbar\Omega_m$ gives back the Rayleigh-Jeans distribution $n_m^{-1} = \beta(\Omega_m - \mu)$, showing that (4.4.2) is indeed the correct entropy in the classical wave regime. The entropy can be rewritten

$$\frac{S}{k_B} = \ln N + \sum_m \ln p_m \tag{3.2.13}$$

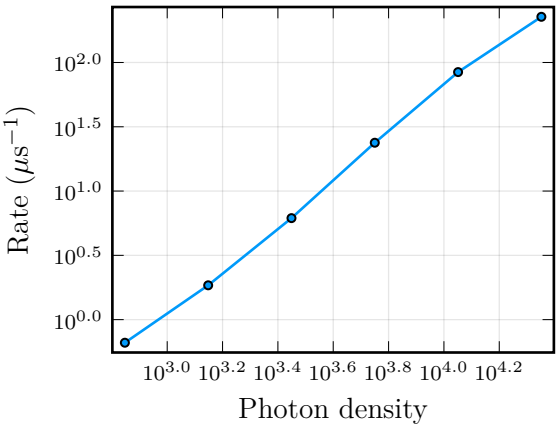

Figure 3.11: Thermalization rate as a function of the initial population per mode, which is also the mean photon density, in the MF56 sample. The rates are extracted by fitting the growth of entropy shown in figure 3.10 to an exponential function.

where $p_m = n_m/N$ is the probability for a photon to be in mode m. The second term is a normalized entropy that only depends on the shape of the distribution of populations. This quantity is easier to obtain experimentally than the absolute value of entropy.

In the numerical experiment shown in figure 3.10, the 400 modes with highest frequency are initially populated with a population n_0, while the 400 lowest frequency modes have a population set to $n_0/100$. The different initial distributions have the same shape and only differ by a global scaling factor, therefore the ratio H/N is the same for all the distributions. The system is then evolved for one microsecond without losses ($\kappa_m = 0$). The left plot of figure 3.10 shows the probabilities of mode occupation p_m at the end of the evolution. The modes are indexed from high to low frequency. We observe that, when n_0 is increased, the final distribution tends to a limit distribution. The existence of this limit distribution comes from the fact that the populations predicted by the Rayleigh-Jeans distribution are proportional to T. This has two consequences, first the probabilities p_m at equilibrium only depend on μ, and second the value of μ for the equilibrium distribution can be calculated by only considering the ratio H/N of the initial distribution. Because this ratio is the same for all the initial distributions, the distribution of p_m converges to a unique equilibrium distribution. The initial population n_0 only changes the timescale over which thermalization occurs.

The growth of the normalized entropy $\sum_m \ln p_m(t)$ is shown in the right plot of figure 3.10. We observe that thermal equilibrium is reached in less than one microsecond if $n_0 \gtrsim 3 \times 10^3$ photons. The growth of entropy is close to exponential. By adjusting the curves with an exponential, we obtain the thermalization rates shown in figure 3.11. This curve shows that thermal equilibrium can only be reached deep in the classical regime with the MF56 sample. In order to reach the quantum regime with $n_0 \approx 1$, the non-linearity should be increased by a factor 10^3.

3.2.4 Dynamic of wave condensation

We have seen in in the previous paragraph, that scaling the initial distribution leads to the same normalized distribution at thermal equilibrium. In terms of thermodynamic parameters, both the final density and the temperature at equilibrium are proportional to the initial density. Therefore, one cannot cross the critical line for condensation in this way. The figures 3.12 and 3.13 show the results of a different numerical experiment, where we keep the total number of photons constant but change the number of initially populated modes. The average density of

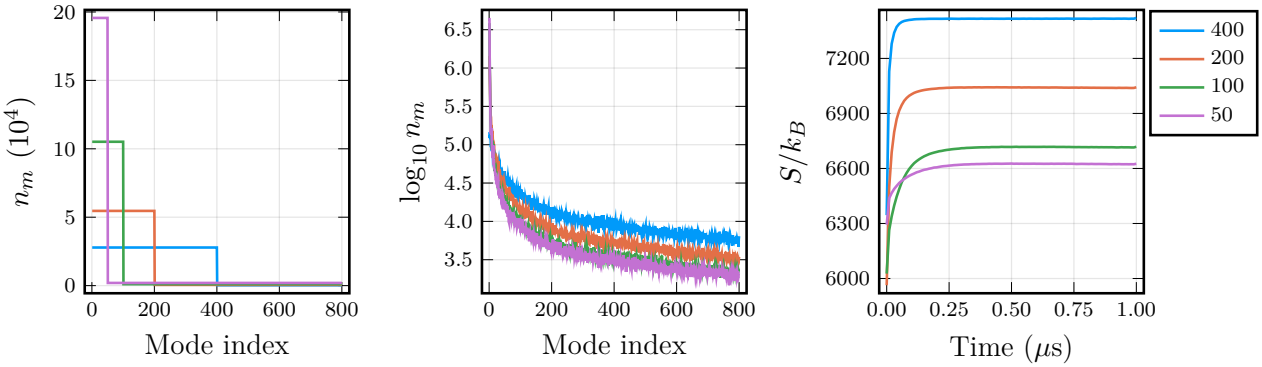

Figure 3.12: Crossing the transition for wave condensation in the MF56 sample. The left plot shows the initial distributions, which all contain the same number of photons ($1.4 \times 10^4 \times 800$), but spread over a different number of modes. The central plot shows the final populations after one microsecond of evolution. The right plot shows the growth of entropy with time for the different number of initially populated modes indicated in the legend.

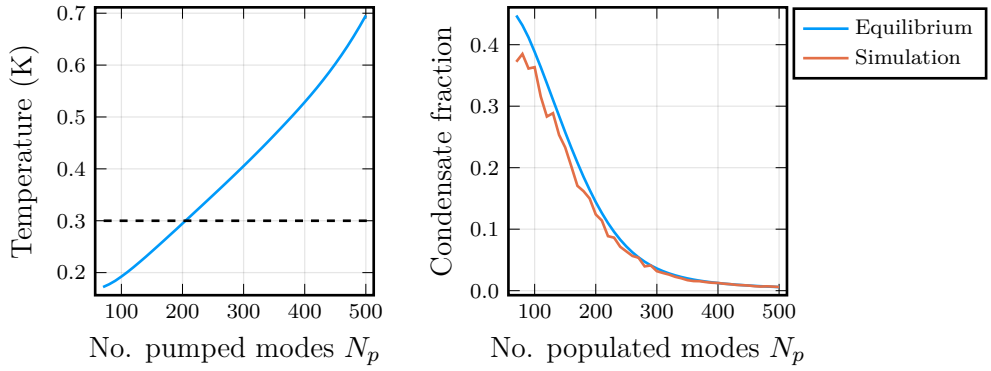

Figure 3.13: Evolution of the expected temperature (left) and condensate fraction (right) at equilibrium as a function of the number of initially populated modes. Reducing the number of modes N_p reduces the temperature of the equilibrium distribution. When the temperature is below the critical temperature for wave condensation (black line in the left plot), we observe that the condensate fraction increases in the simulation as predicted by the ideal gas theory.

photon per mode or per site is 1.4×10^4 for all the curves shown in the two figures. The figure 3.12 shows the initial and final mode populations in log scale and the growth of entropy with time, which shows that the system reaches equilibrium in less than one microsecond.

We observe that the temperature associated to the final distribution decreases with the number of initially populated modes as the final distributions become more and more peaked. We compute the expected final temperature as a function of the number of initially populated modes N_p by first finding μ from the ratio H/N of the initial distribution and then obtain T by adjusting the number of photons to be equal to N. The left plot in figure 3.13 shows the decrease of the expected temperature when N_p decreases. We choose the photon density to be 4×10^4, such that the temperature goes below the critical temperature when reducing N_p. The right plot in figure 3.13 shows that the condensate fraction as a function of N_p obtained in the simulation is in good agreement with the expected equilibrium value. This simulation also indicates that the condensate is stable, even though the interactions between the photons are attractive. Because the mass in the lattice is negative, the sign of the interaction must be reversed before making a comparison with the usual case of massive particles. In our lattice, the condensate thus behaves as the usual repulsive condensate, which is known to be stable

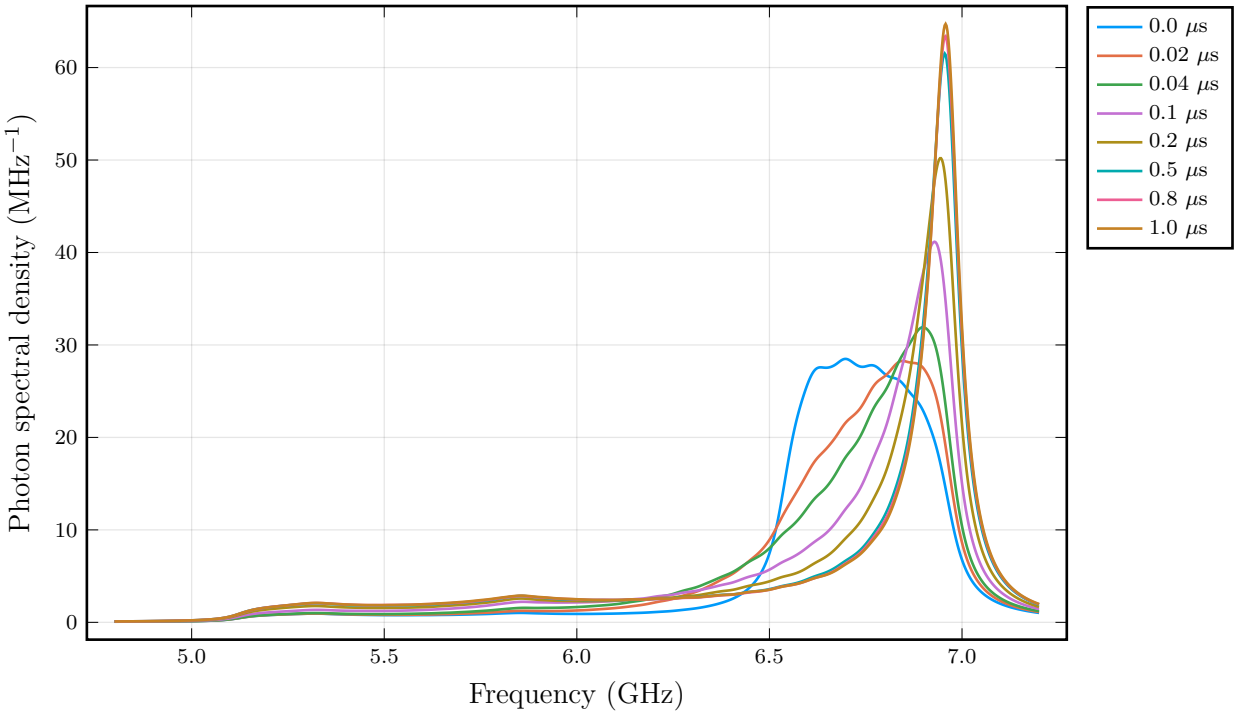

Figure 3.14: Evolution of the photon spectrum as a function of time in the MF56 lattice for a mean density of 5×10^3 photons per site initially spread over $N_p = 100$ modes (green curves in figure 3.12). At the end of the evolution, the condensate fraction is approximately 0.1. The spectrum is computed using a lorentzian response function of width 40 MHz to obtain a smooth function.

[71]. We finish this section by showing in figure 3.14 the time evolution of the lattice spectrum, as could be measured in an experiment, for the case of $N_p = 100$ initially populated modes. We observe the apparition of the condensate as thermalization occurs in the lattice.

Chapter 4

Experimental Characterization of lattices of transmon like resonator

Contents

In this chapter we present the measurements on the Lieb and square lattice that follow the design shown in figure 1.13 and figure 1.21. We first present each sample and the measurement of the transmission and reflexion of both lattices. We compare those transmission to the expected frequency of their modes, which in the case of the square sample is directly related to the measured resistance of each site's wire. To complete our understanding of the low power characteristics of the square lattice, we show one example of the power dependence of one of the modes of the square lattice and compare it to single resonator measurement.

In the second part we present the measurement of the non-linearity of the square sample. The non-linear term is characterized through the measurement of the self and cross Kerr processes on the square lattice. The self Kerr is measured using the frequency shift of each mode and the cross Kerr using the frequency shift induced by photon amplitude in other modes. We compare those values to the expected non-linearity calculated previously. Then, in order to complete the measurement of the non linear term of the square lattice, we present the measurement of the four wave mixing between four different modes of the square lattice.

In the last part, we show pulsed excitation measurement of the square sample. We present the setup used to send pulse frequency combs. We show the impact of the loss on the transient response of the lattice. We then show the lattice dynamics of single modes. We then show the measured dynamics of the lattice in response to a pulsed frequency comb.

4.1 Linear Regime

4.1.1 Square Lattice Sample

The square lattice was made using the design shown in figure 1.13 and the electron microscope fabrication technique showed in 2.2. We fabricate the resonator lattice of the sample on a 2 times 1.5 cm silicon slab that we cut to 1 by 2 cm before gluing the sample to the box in order to clamp safely the silicon. We then measure each resistances using the automatic probe shown in figure 2.10 to make sure that the resistances of each resonator both have a low dispersion and also that the expected frequencies of the lattice are in the measurable bandwidth of 4 to 8 GHz. We then use a lift off technique with a thin optical resist S1805 and an evaporation of 40 nm of aluminium for the lines and ground planes around the lattice. We then evaporated a back plane of 40 nm of aluminium over the entire back of the sample before gluing and bonding the sample.

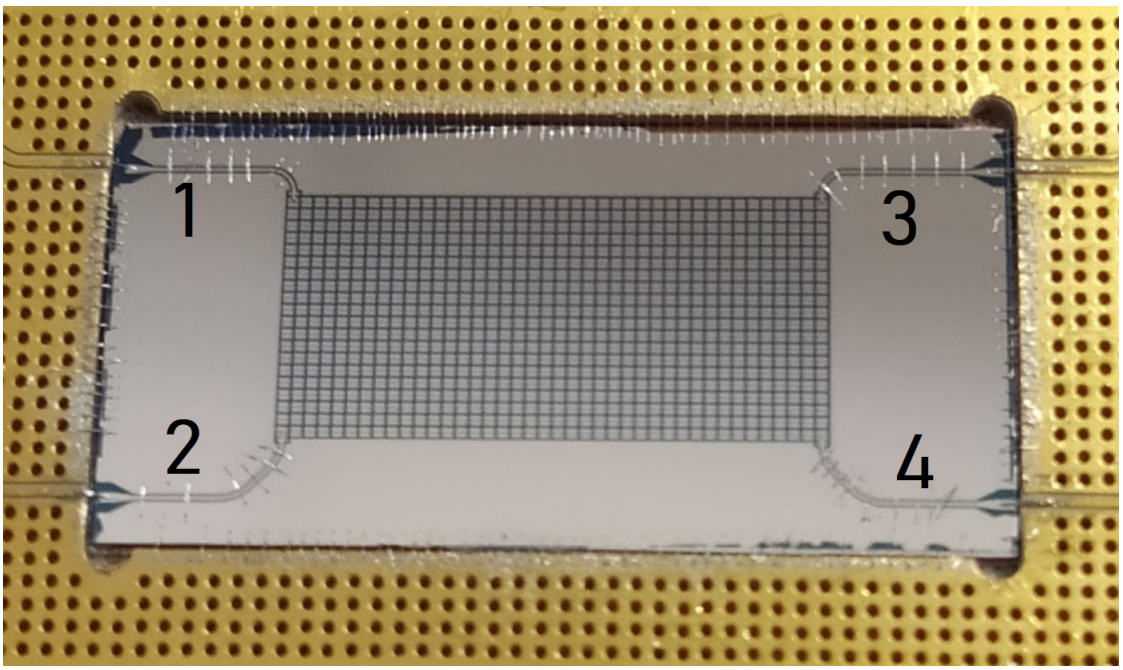

Figure 4.1: Photo of the bonded final sample. The grounds around the 50 Ω line input ports on the wafer are bonded in order to ensure the ground over the whole surface. At the end the 50 Ω lines are designed to accomodate the bounding and are bounded to the the 50 Ohm line of the box.

The wires are 40 nm thick, and 1 μm wide. Each line has a constant length which varies in the y direction from 17.4 to 20 μm to compensate a gradient of the resistance of 5 %. As shown in figure 4.2,the average resistance of the wires is 19.3 kΩ giving a resistivity of 3867 $\mu\Omega$cm. From a value of ρj_* of 28.5 kV/m we expect an average critical current of the wires of 30 μA The value of gradient was higher than the 5 % expected thus the lattice has a total deviation of its resistances of 10 %. If we substract the gradient along the y axis the values are within a 3.1 % deviation. Three of the resistance values indicate very high resistance values. We consider them as open for the computation of the frequencies and modes.

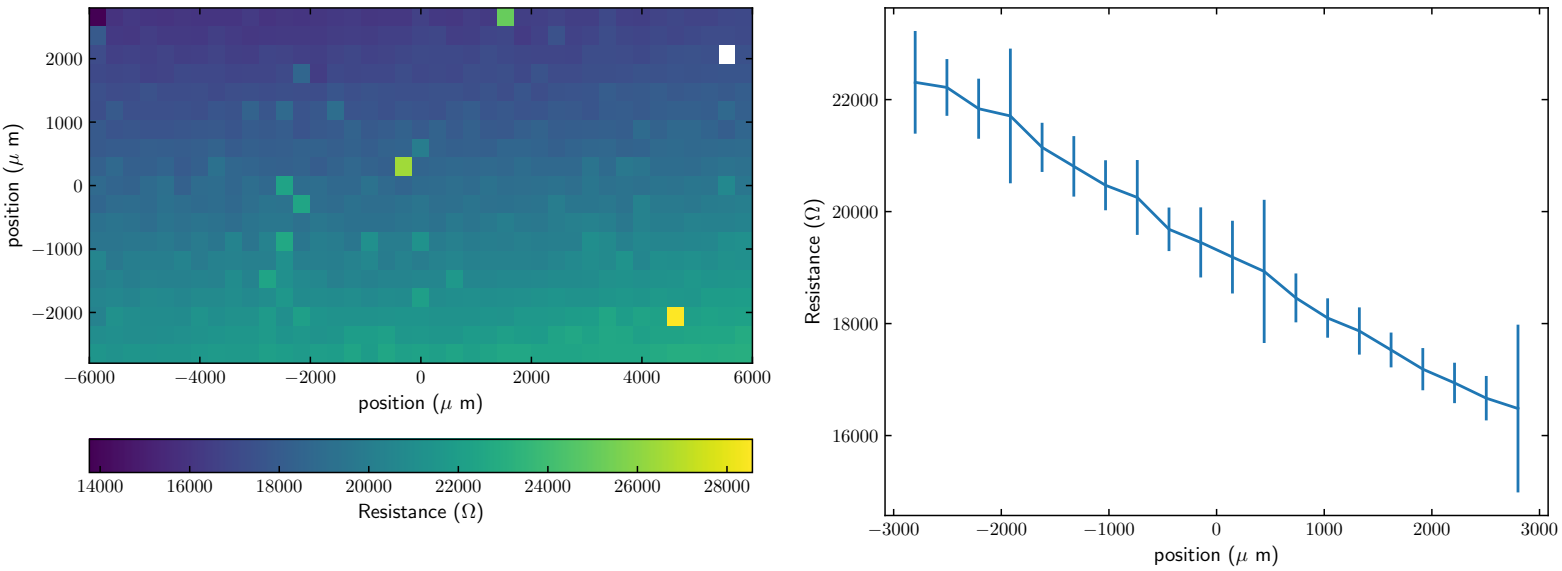

Figure 4.2: Resistances of the GrAl wires measured with the automatic probe shown in 2.10(left) Average resistance per line as a function of the position on the y axis (right)

The frequencies are widened by the gradient over the sample bringing the total band size from a theoretical 1.7 GHz band to a 2.8GHz band. We show in figure 4.3 the comparison between the two calculation. The resistance of the theoretical map is chosen to match the average frequency of the entire lattice.

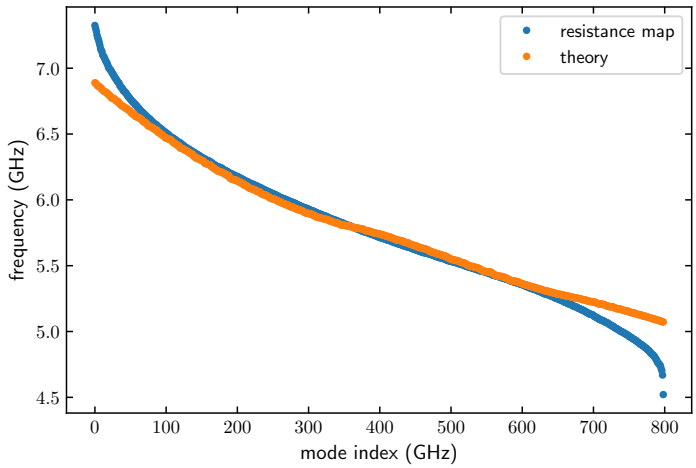

Figure 4.3: Comparison of the mode frequencies between the theoretical 40 by 20 resonators with no variation of resistance (orange) and the calculation using the resistance map (blue)

The mod at high frequencies are pushed toward the low resistance side of the sample. We show the current amplitude of the four highest frequency modes in figure 4.4

Transmission and reflexion The setup inside of the fridge for this sample used for this sample is shown in figure 4.5. The room temperature setup is shown in figure 4.6. We show

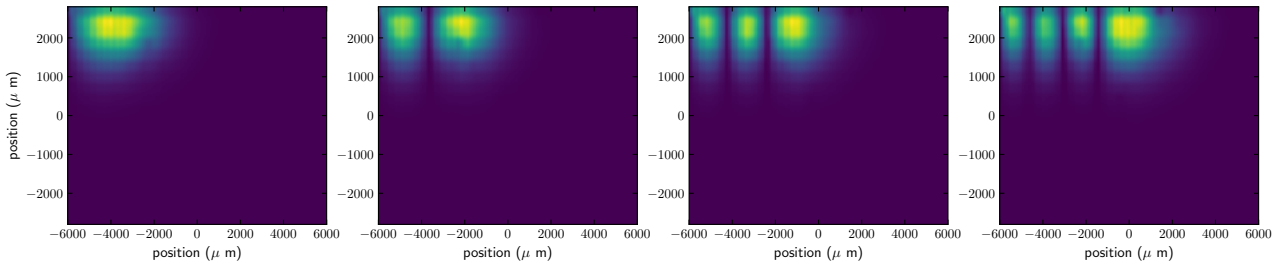

Figure 4.4: Four highest frequency modes of the lattice calculated from the resistance map

the transmission through the port 1 to 3,1 to 2 and 2 to 3 as well as the reflexion on the port 3 in the figure 4.7 . The left line without attenuation shown in the setup was used on the first cool down to measure the transmissions but was removed for the next experiments.

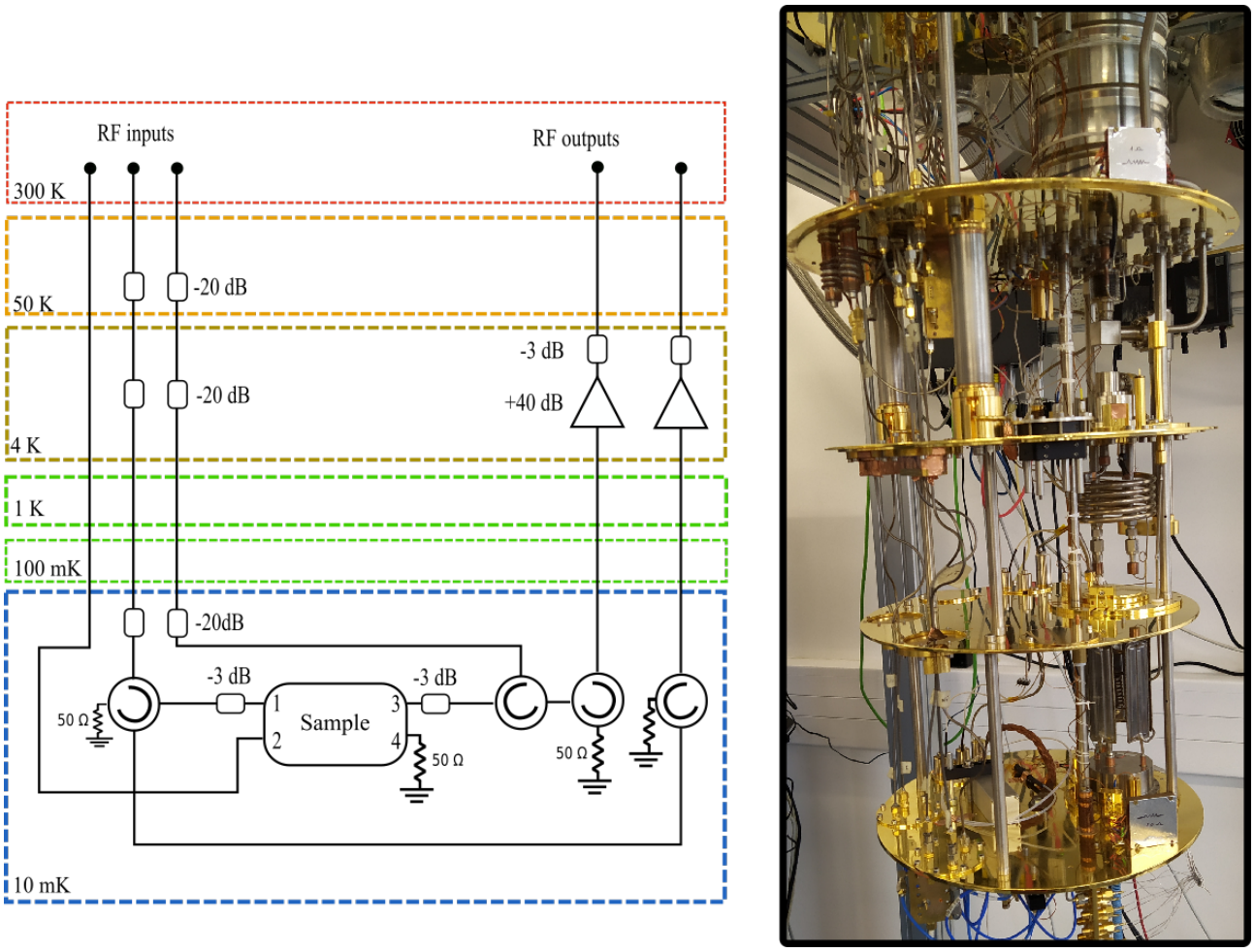

Figure 4.5: RF setup inside the fridge for the square sample. Two input lines with 60 dB of attenuation are plugged into circulators . One line of each circulator goes into the sample ports. The signal from those circulator goes back with two amplified line with 6 dB of attenuation and each a cryogenic amplifier(LNF LNC4 8C).

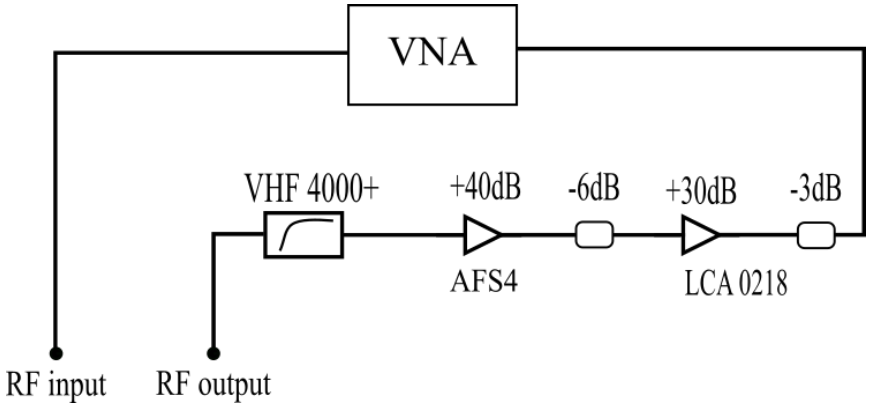

Figure 4.6: RF setup outside the fridge for the transmission measurement.

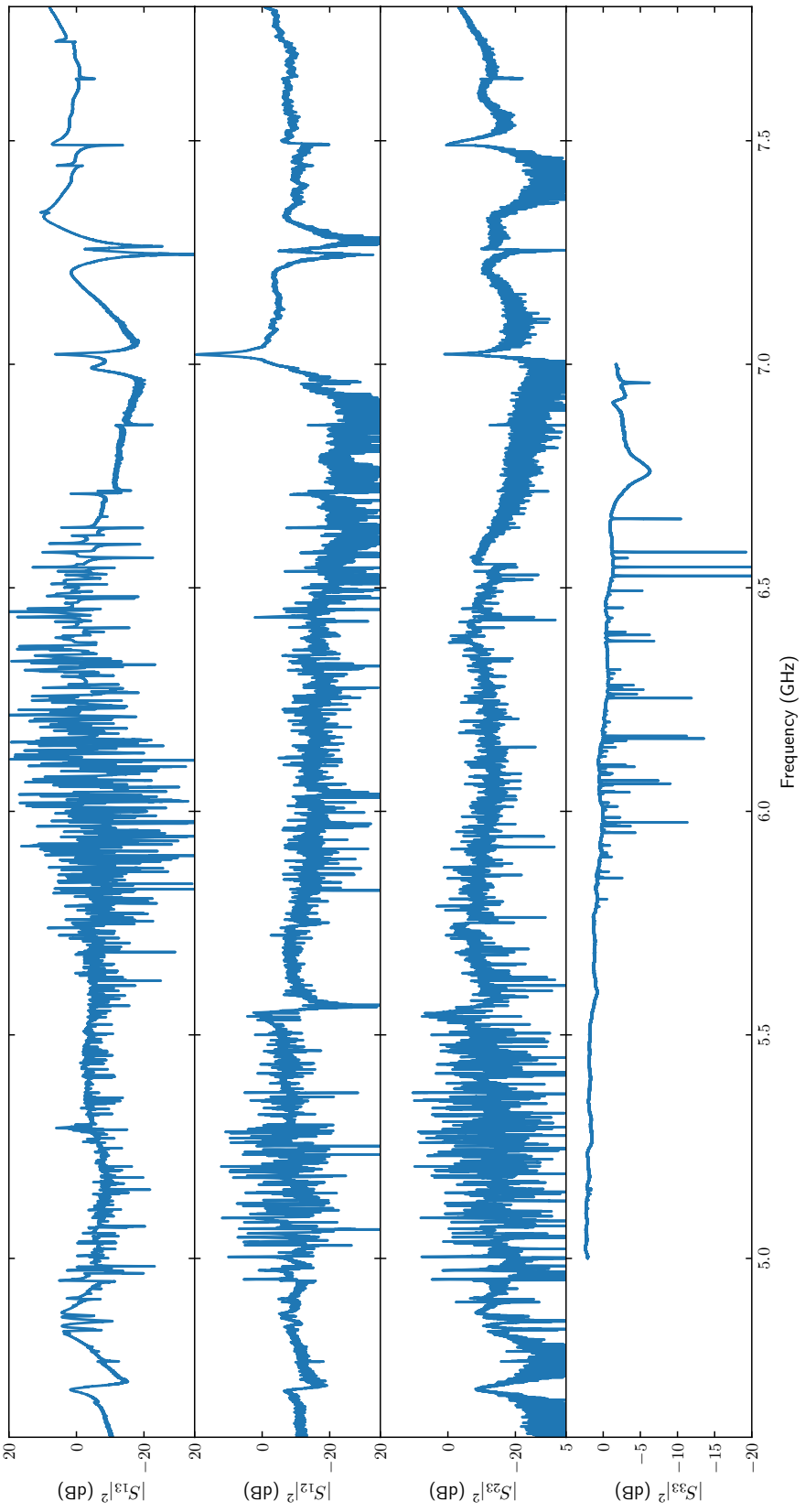

Figure 4.7: Transmission S_{12} , S_{13} and S_{23} of the square sample using the setup shown in figure 4.6

Using the resistance map showed in figure 4.2 we compute the frequencies and the coupling rate using 1.3.12. We use those values to compare the theoretical values to the measured transmission and reflexion. For each transmission we run a peak finding algorithm We dismiss multiple occurrences of the frequencies at less than 1 MHz and compute the density of mode per MHz. We find 448 single frequencies out of the expected 800. In figure 4.8 we show the comparison of mode density. For the purpose of this comparison, we assumed that the modes that we cannot measure are equally distributed thus we readjust the measured density by the ratio of number of measured modes to the number of expected theoretical modes. Dismissal of degenerate modes (less than 1 MHz) in the theoretical expectations leads to overlooking 133 modes.

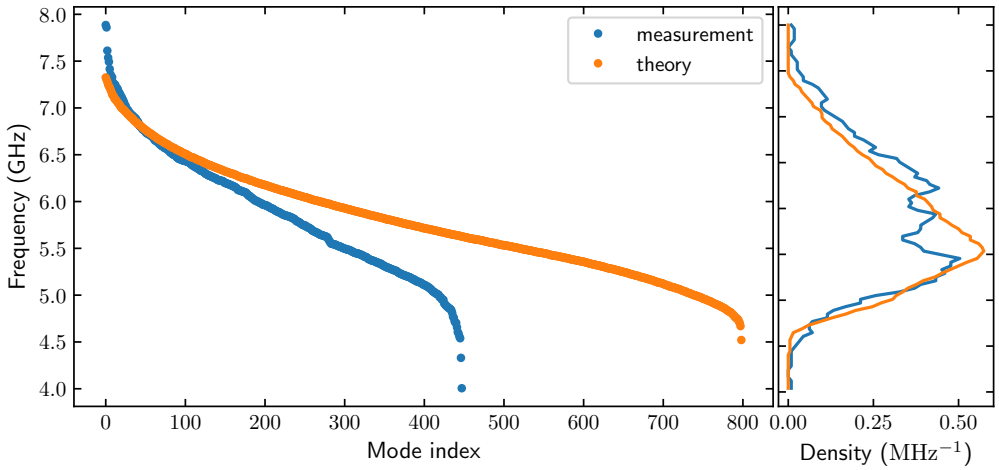

Figure 4.8: Single frequencies measured using the 3 transmissions (blue) and theoretical expectations (orange) (left) Experimental density reajusted to the number of frequencies(blue) and theoretical mode density (right)

The lattice frequencies are lower than the expected values from the resistances. The comparison showed in figure 4.8 used values of the inductance calculated from the resistance map that where multiplied with a ratio of 1.38. For the inductance calculation we used gap values measured at resistivities of 500 $\mu\Omega cm$ which is expected to be lower at 3500 $\mu\Omega cm$ and thus an increase of the inductance. This does not explain entirely the measured ratio of inductance that also could have been due to aging between the time of the measurement of the resistances measurement of the sample in the fridge. We also compare the densities of measured modes of each port measurement as shown in figure 4.9 For this comparison, we assumed a constant internal loss rate $\mathbf{k}_i$ of 1kHz and calculate the height of the theoretical modes given $\kappa_i/(\kappa_i+\kappa_c)$ with the coupling loss rate κ_c. We calibrated the threshold of measurement so that the number of total modes measured above this threshold matches the experiment.

The mode densities for the transmission from the 1 to 3 ports fits well the theoretical expectations. We do not observe a good agreement of the other transmission and reflexion. A variation of the TLS loss threshold between modes would impact the transmission density and measured mode density. The short measured on the resistance map shown in figure 4.2 was not measured with a different sensitivity. It is possible that its inductance was higher but in the same range as the other ones which could explain changes to the mode transmission density as well as the high frequency modes above the band structure as seen in figure 4.8.

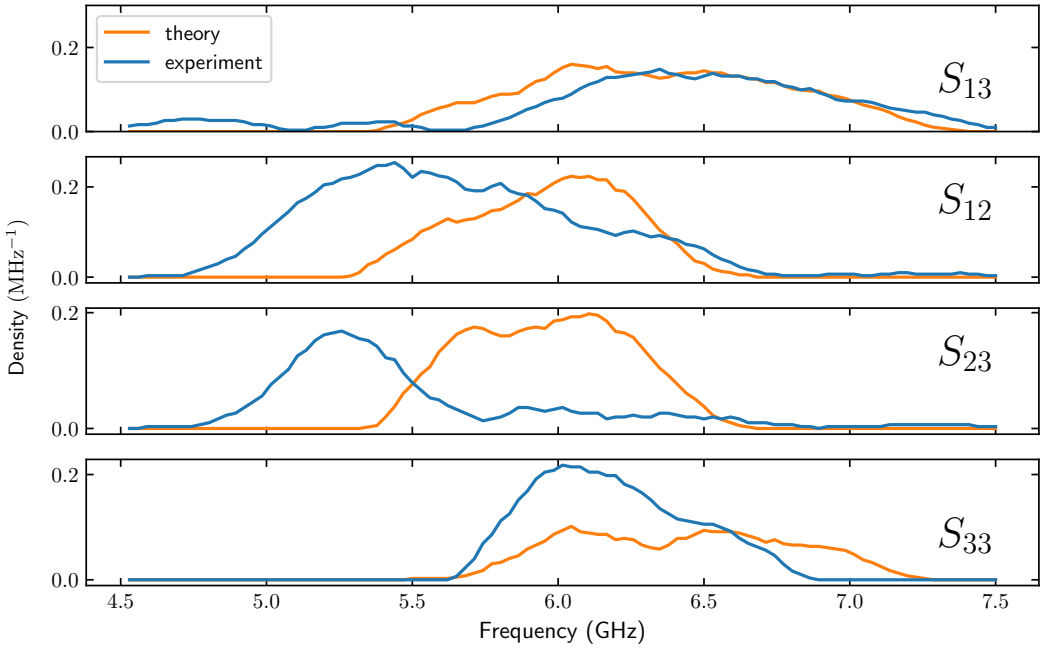

Figure 4.9: Single frequencies measured for each of the 3 transmissions (blue) and theoretical density expectations (orange)

4.1.2 Lieb Lattice

The Lieb lattice follows the design showed in figure 1.21. The fabrication followed the technique showed in 2.2. A wafer of 2 inches was patterned with 16 identical samples. Each sample was surrounded by 8 test wires. Each of the 8 test wires around the sample are 100 from 300 μm long and 4.5 μm wide. The test wire of the measured sample had a resistance per square of 970 $\Omega/\square$ and the 8 test values had a dispersion of 3.5 %. From the average resistance per square of the test wires we expect an average inductance of 8.2 nH in the sample.

Transmission measurement The setup inside of the fridge is shown in figure 4.11. For the transmission measurement of this Lieb lattice, the room temperature setup consists only of the VNA directly connected to the inputs and outputs of the fridge as shown in figure 4.11.

We compare the mode density of the transmissions to a computation of the modes with a realization of disorder of the resistances of 4 % of deviation. The mode density computation is done on a 51 by 51 lattice in order to average out the realizations of disorder. The average frequency that corresponds to the measured frequency band of the sample points to an inductance of 7.5 nH instead of 8.2 nH. The measured size of the flat band fits the 4 % deviation of the inductances.

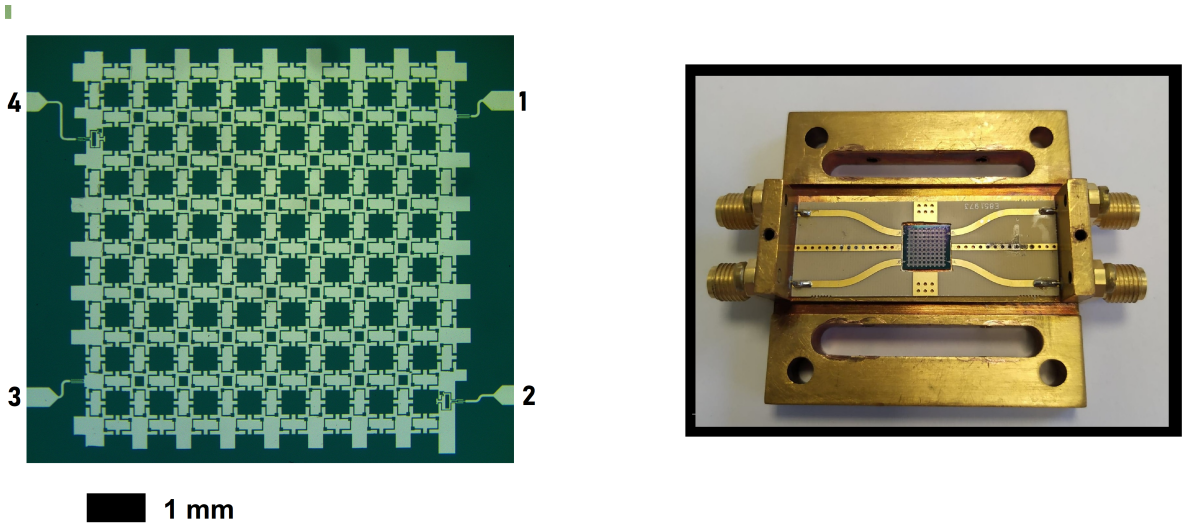

Figure 4.10: Microscope image of the Lieb lattice. The line 1 and 4 are connected on A nodes while the line 2 and 3 are connected on B nodes. (left) Measurement box used for the Lieb sample (also used for the single resonator experiments). The sample is glued with conductive glue to the copper bottom then micro-bonded to the PCB which is connected to two SMA connectors. (right)

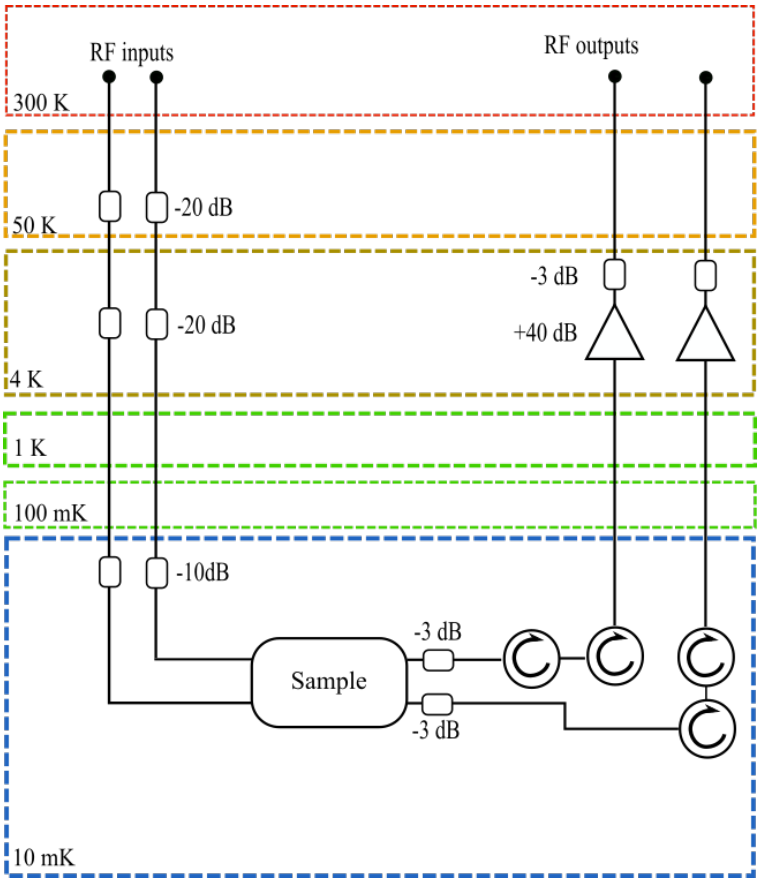

Figure 4.11: RF setup inside the fridge for the Lieb sample. The input lines 3 and 4 have 50 dB of attenuation and are connected to the left of the sample as shown in figure 4.10. The measuring lines 1 and 2 have 40 dB of amplification with the amplifier (LNF LNC4 8C) and 6 dB of attenuation.

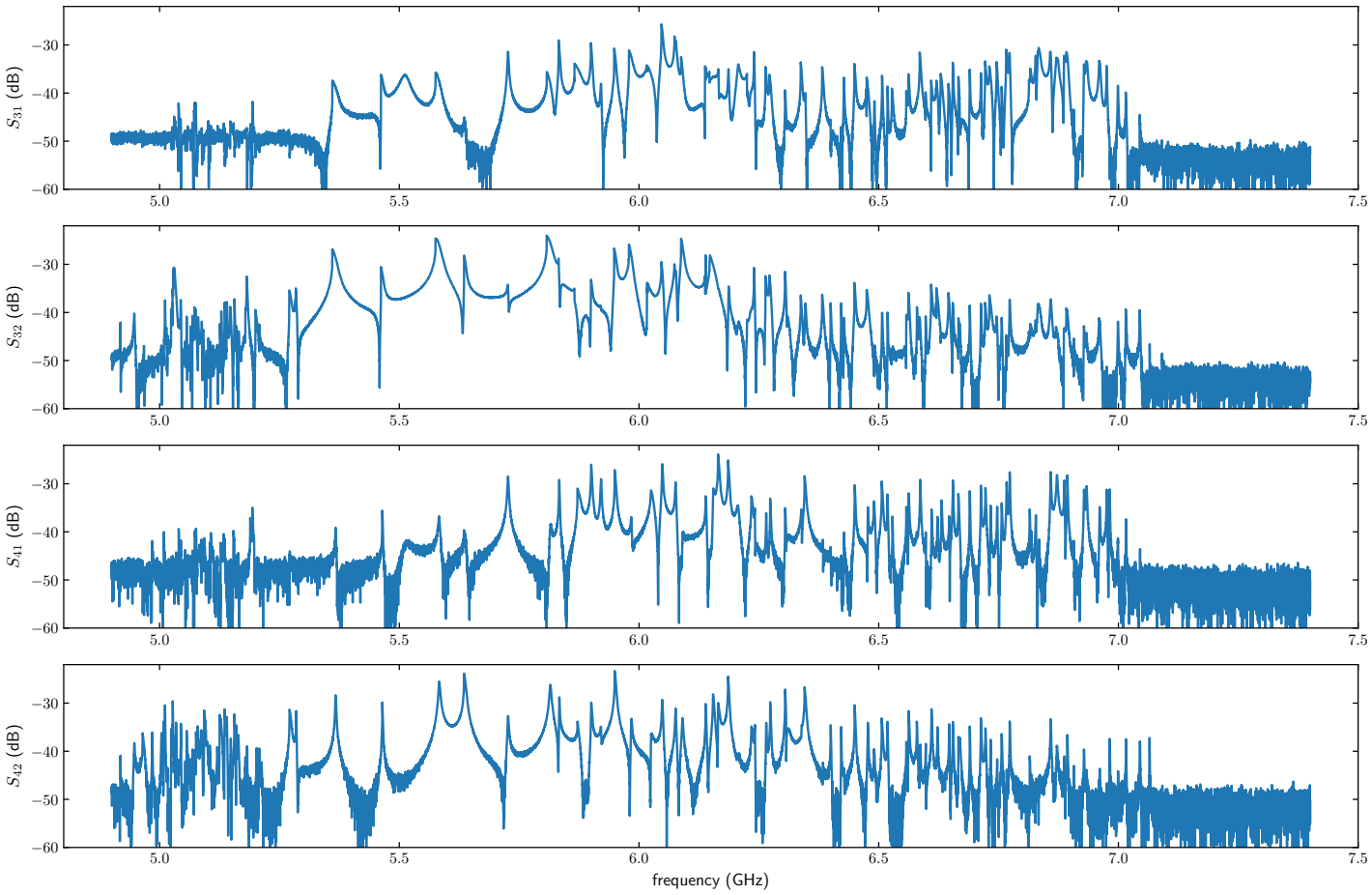

Figure 4.12: Plot of the transmission from the Lieb lattice through the ports 2 to 3 measured at -45 dB. We measure two separate frequency bands (Top) Plot of the expected frequency with an inductance of 7.5 nH with a dispersion of 4.5 %

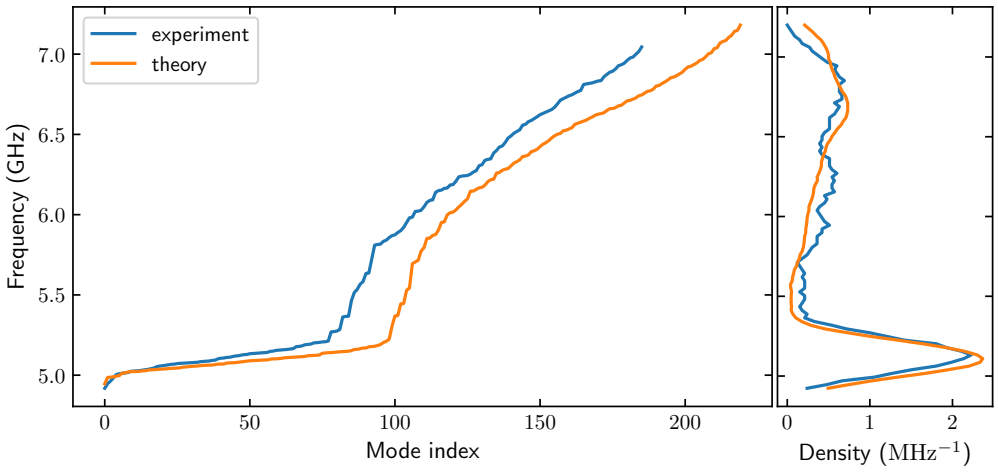

Figure 4.13: Single frequencies measured using the 4 transmissions (blue) and theoretical expectations (orange) (left) Experimental density (blue) and theoretical mode density (right)

There is a good agreement of the experiment and theoretical expectations. The precise variations of amplitudes between the transmissions can not be accounted for because we do not have access to the values of each resistances in the sample.

4.1.3 Evolution of the resonance width with power

We measured the width and ringdown of the mode at 6.104 GHz in order to quantify the losses. We use the same setup as shown in figure 4.36 where the signal generator denoted by "setup 1" is replaced by an RF source (agilent E8257D). We did two different measurement. First we make a homodyne measurement of the source output with the spectrometer and measure at each frequency and power from -55 dBm to -35 dBm from the source. The result is shown in the left part in figure 4.14 . We observe the duffing shift and a widening of the peak at lower power. The power amplitude of the source is adjusted using the known attenuation of the line to show the amplitude input at the sample. We fit the resonance below the duffing using the lorentzian equation 4.1.1 giving us the full width at half maximum γ.

$$S = \frac{\frac{\gamma}{2}}{(f - f_0)^2 + (\frac{\gamma}{2})^2} \tag{4.1.1}$$

At higher power we measure the ringdown of the cavity after the pulse. We show in the center of figure 4.14 the ringdown in time after the pulse. We measured with pulses of 20 μs with a bandwidth of 128 MHz. The amplitude shown is divided by the plateau amplitude during the pulse. We fit the decay with $e^{t/\tau}$

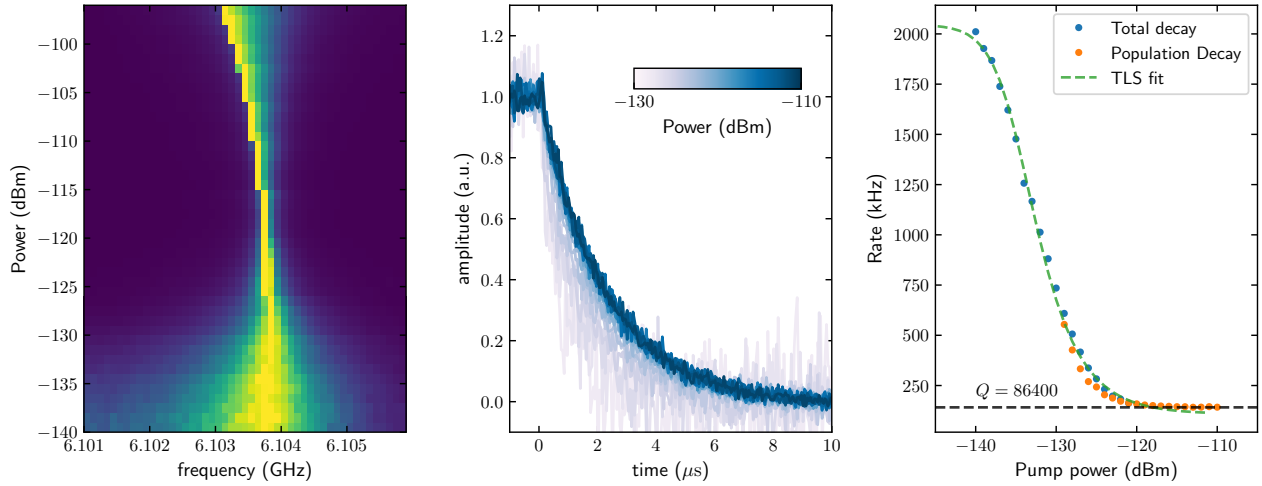

Figure 4.14: Measure of one resonance with power. The amplitude of each line is normalized to 1 to show the variation of width of the resonance. The power shown is the input power at the input of the sample. (left)Ringdown measurement from -130 tto -110 dBm input power (center) Width of the mode with power taken from the reflexion measurement shown left(blue) and ringdown time of the population (orange). We can fit the measure width using 4.1.2 with $Q_0 = 1/\delta_0 = 2807$,P_c = -130 dBm and $\beta = 3.3$. The high intensity quality factor cannot be measured with this fit.(right)

Assuming that the loss of the lattice comes from coupling to TLS systems, the quality factor varies with the power inside the resonator P following the equation shown in 2.1.14:

$$\kappa(P) = \kappa_{TLS} \frac{1}{\sqrt{1 + (P/P_s)^{\beta/2}}} + \kappa_0 \tag{4.1.2}$$

In the measurement of the single resonators we where able to determine average parameters for the resonators of the MF47 sample of P_s = -149 dBm, κ_{TLS} = 3.31 MHz, κ_0 = 3.4 10^{-4} MHz ,$\beta \approx 1$. The exact values of κ_{TLS} and κ_0 are difficult to compare to values extracted from

single resonators but we can compare the saturation power P_s in terms of numbers of photons. For the MF47 sample we found a saturation power P_s of 2.0 photons. The saturation power for the mode of the lattice corresponds to 430 photons. This is compatible with a scaling of this power with the total electrical surface amplitude of the mode.

4.2 Self and Cross Kerr Processes

In this section we show the measurement of the non linear tensor of the square lattice. We first show the diagonal term ,or self Kerr term, involving only one mode by measuring nonlinear shift of each resonator with power. We then measure the non diagonal terms involving only two modes,or cross Kerr term, by measuring the linear frequency shift of each mode with power in other modes. We will focus on a set of four modes and will extract the self and cross Kerr matrix U_{mmnn} over these four frequencies

4.2.1 Matching frequencies in the square lattice

The square lattice has transmission in the higher frequencies between the ports 1 and 3. We chose to focus on this transmission to measure phase matching as well as pulse experiment showed in the last section. We show a frequency section of the S_{13} transmission in 4.15. We selected transmission resonances within the 5.7 -6.6 GHz shown with a red dashed line doing an automatic peak finding algorithm and selecting the ones that fitted best to a Lorentzian fit.

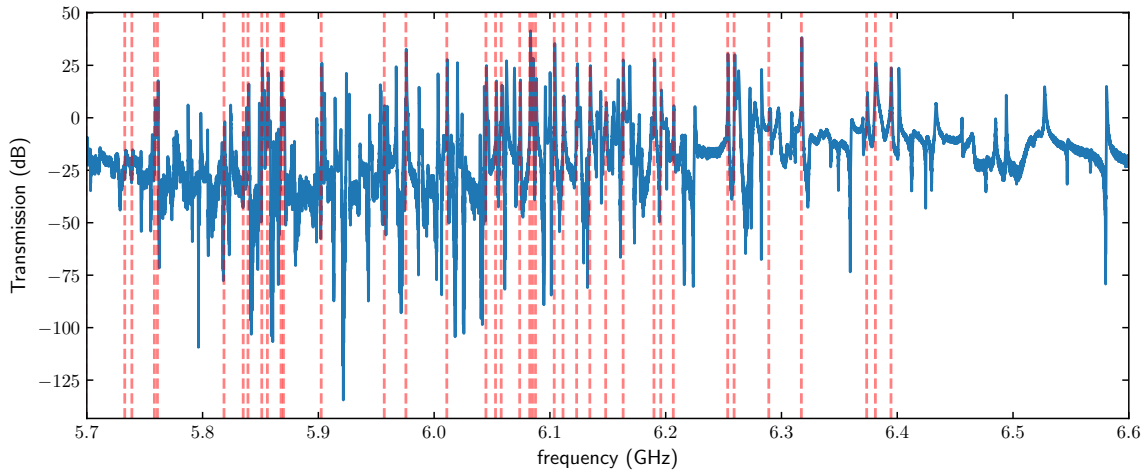

Figure 4.15: High frequencies in the 5.7 -6.4 GHz band of the transmission from port 1 to 3

From the frequencies of the fit, we compute each possible quartet of four within these 40 frequencies and calculate the distance to exact phase matching δf such that $f_1+f_2-f_3-f_4 = \delta f$.

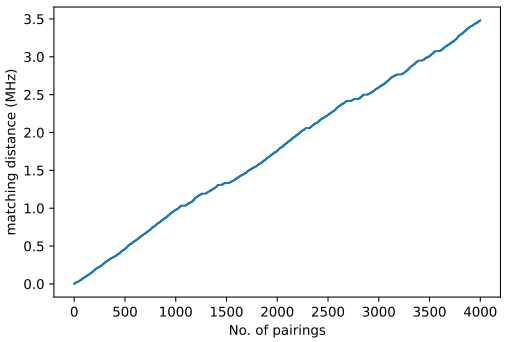

Figure 4.16: Frequency distance to perfect frequency matching $\delta f = f_1 + f_2 - f_3 - f_4$ for each of the quartets within the frequencies highlined in figure 4.15

The phase matching necessary for four wave interaction does not need to be exact if the frequencies fluctuate with a rate Γ higher than δf. As is discussed in the resarch by Zakharov,[74], it is possible to distinguish three cases for finite systems with a frequency spacing Δf that fluctuate at a rate Γ. If $\Delta f >> \Gamma$ then the system is "frozen" and only the exact quartet resonances interact. Inversely if $\Delta f << \Gamma$ the interacting sets of four modes trace a continuous three dimension surface within all of the quartet of modes and the system can approach the parameters of continuous media. The case where both values are in the same range is called "mesoscopic". The set of 40 frequencies shown in figure 4.16 has an average frequency spacing higher that the full lattice but of the same order of magnitude. We compute 256 10^4 possible quartets that we sort by δf in figure 4.16. We find 500 pairings below 0.5 MHz.

In order to characterize the non-linear interaction beween the modes we chose to measure the full matrix of interaction of the self, cross Kerr and four wave mixing on one of the best matched pairing. We chose the pairing with frequencies $f_1 = 5.758$ GHz,$f_2 = 5.850$ GHz,$f_3 = 6.011$GHz and $f_4 = 6.10369$ GHz shown in 4.17 :

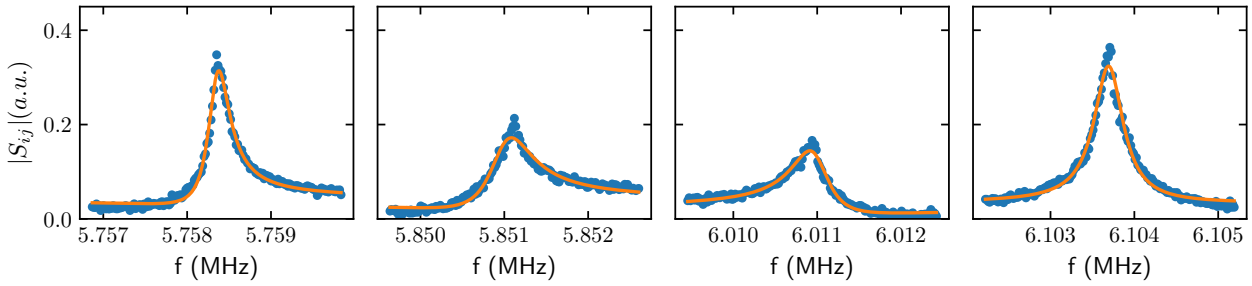

Figure 4.17: Example of choice of matching frequencies measured with the VNA (blue)and fitted woth a lorentzian fit(orange).

We measure in the rest of this section the non-linear interaction between those four modes of the lattice.

4.2.2 Self Kerr

To measure the non-linearity of the lattice, we characterize the non linear tensor U_{mnpq} using the resonant modes shown in 4.17. The first step is to measure the self-Kerr of each of these modes. We use the same room temperature setup as shown in 4.6 connected to the fridge setup shown in 4.5. We sweep the power input with the VNA and measure the duffing frequency shift and bistability. We suppose that the 1 and 2 microwave lines are coupled to the mode by the coupling rates κ_1 and κ_2. We rewrite the equation 2.3.5 of the field of the mode α adding the coupling to the lines denoted by the field $b_{1\,in}/b_{1\,out}$ and $b_{2\,in}/b_{2\,out}$ we can write the mode equation of motion:

$$\dot{\alpha} = i\delta\alpha + i2U|\alpha|^2\alpha - i\eta - \kappa\alpha - \sqrt{\kappa_1}b_{1\,in} - \sqrt{\kappa_2}b_{2\,in} \tag{4.2.1}$$

and for each field $b_{i\,in}$:

$$b_{i\,out} = b_{i\,in} + \sqrt{\kappa_i}\alpha \tag{4.2.2}$$

Considering $b_{2\,in} = 0$, we obtain a transmission S_{12} with :

$$S_{12} = \frac{b_{2\,out}}{b_{1\,in}} = i\frac{\kappa_c}{\eta}\,\alpha \tag{4.2.3}$$

where $\kappa_c = \sqrt{\kappa_1\kappa_2}$ and the term . This equation is similar to the equation 2.3.11 in the hanger configuration where the signal of the transmission line does not interfere with the signal. The same method as in 2.3.2 applies to the field inside of the cavity and allows us to compute the non-linear response for each mode. Contrary to the hanger coupling used in the one resonator measurement we have no direct measurement of the amplitude of the full transmission which is added as a fitting parameter. Also, the transmission input amplitude η depends on the power given by:

$$\eta = \sqrt{\frac{\kappa_1 P_1}{\hbar\omega}} \tag{4.2.4}$$

We measure the rate κ_1 and κ_2 by fitting the resonance in reflexion on the port 1 and 2. We show in figure 4.18 the transmissions for power from -110 dBm to -95 dBm of power input for the sample. The results of the fit are shown in the table 4.2.2. The values of Q_i vary with power for each mode thus the highest value is given in the table.

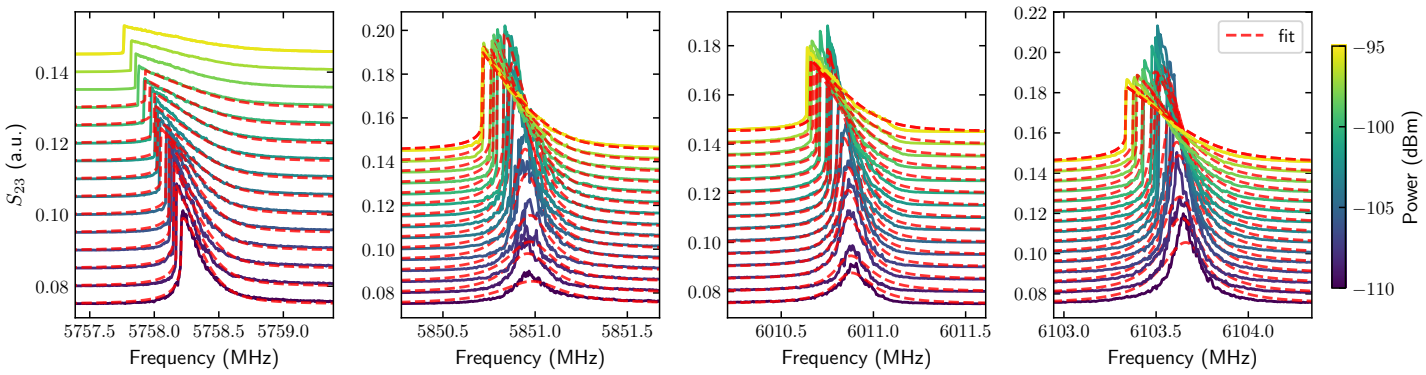

Figure 4.18: Transmission from port 1 to 3 around each of the for the 4 resonances shown in 4.17 shown for power varying from -110 to -96 dBm. Each transmission is shifted for clarity. The non-linear fit is shown is dashed red.

	f_0 (GHz)	Q_i	Q_c	U (kHz)
1	5.75	$4.2 \cdot 10^4$	$5 \cdot 10^5$	-0.9
2	5.85	$1.4 \cdot 10^5$	$5 \cdot 10^5$	-0.31
3	6.01	$1.01 \cdot 10^5$	$6 \cdot 10^5$	-0.38
4	6.10	$8.6 \cdot 10^4$	$3.9 \cdot 10^5$	-0.47

4.2.3 Cross-Kerr experiment

Now that we have measured the non-linearity of each mode we measure the nonlinear interaction between two modes. The Hamiltonian between two modes is :

$$H = U_{mmnn}\alpha_m\alpha_m^*\alpha_n\alpha_n^* = UA_{km}^2A_{kn}^2\alpha_m\alpha_m^*\alpha_n\alpha_n^* = (\omega_{n0} + UA_{km}^2A_{kn}^2\alpha_m\alpha_m^*)\alpha_n\alpha_n^* \quad (4.2.5)$$

We can measure the frequency shift of the mode with respect to the number of photon in other modes which gives directly the value of U_{mmnn}. For this measurement, we use the same setup as shown in figure 4.36 where the signal generator denoted by "setup 1" is replaced by an RF source (agilent E8257D) and the amplifier that follows it has been removed.

Cross-Kerr measurement for all the lattice modes Before measuring quantitatively the non-linear interaction between specific modes we qualitatively measure the presence of the non-linear interaction in the lattice. We measure the transmission from port 1 to 3 while sweeping the frequency of an RF signal at -20 dBm sent by the source. Each driven mode i shifts any selected other mode j by $U_{iijj}n_j$ with n_j the number of photons in j. We show in figure 4.19 transmission of multiple modes as well as the fitted variation of frequency for each of them. We show the result between 5.2 and 6.5 GHz as well as between 6.15 and 6.25 GHz.

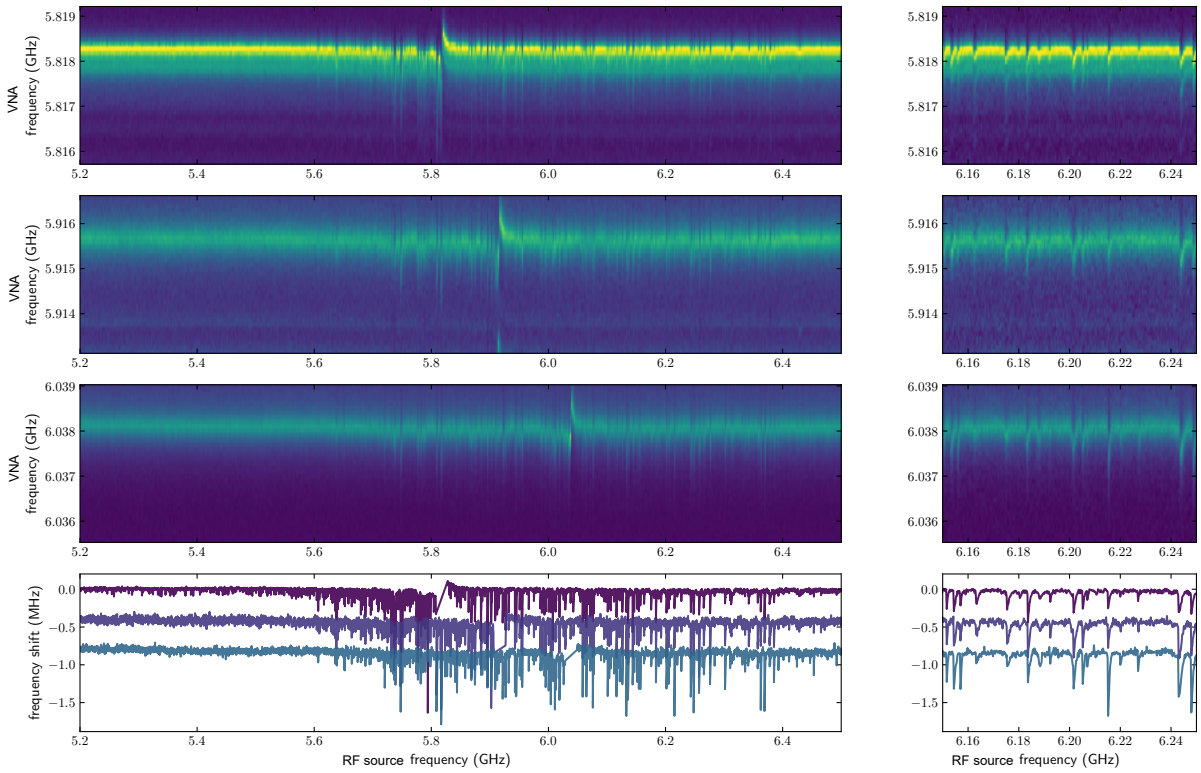

Figure 4.19: VNA measurement around 5.817, 5.915 and 6.037 GHz with a sweep of the source frequency at -20 dBm between 5.2 and 6.5 GHz.(top left) Selection of the same sweep between 6.16 and 6.25 GHz (top right) Average frequency shift for a selection of mode with frequency of the source for the 5.2 and 6.5 GHz frequency span of the source. An added shift is added between the three plots for clarity(bottom left) Same frequency shift measurement of the three modes for the 6.16 and 6.25 GHz span (bottom right)

We shown in figure 4.19 the transmission measured with the VNA around the resonant frequency of one mode of the lattice while sweeping the source frequency. When we observe each mode shift with respect to the source frequency we observe the photon amplitude in each mode pumped by the source modulated by the amplitude of the cross Kerr interaction. At -20 dB most resonances are above bistability. We do observe non continuous shifts of the mode with the frequency of the pump as can be seen on the zoom in on the bottom right of figure 4.19. We have also observed hysteresis when sweeping manually the pump in the opposite direction. The visible positive frequency shift around the source frequency is an artifact of the measurement and has been canceled out in the plot of the frequency fit.

Quantitative measurement In order to quantify the number of photon in the driven mode, we measure its output power on port 1 directly with a spectrum analyzer and relate that value with respect to the measured shift on mode n for each power. As shown by equation 4.3.1 we expect a linear relation between the shift and the photon amplitude which we observe as shown in 4.20.

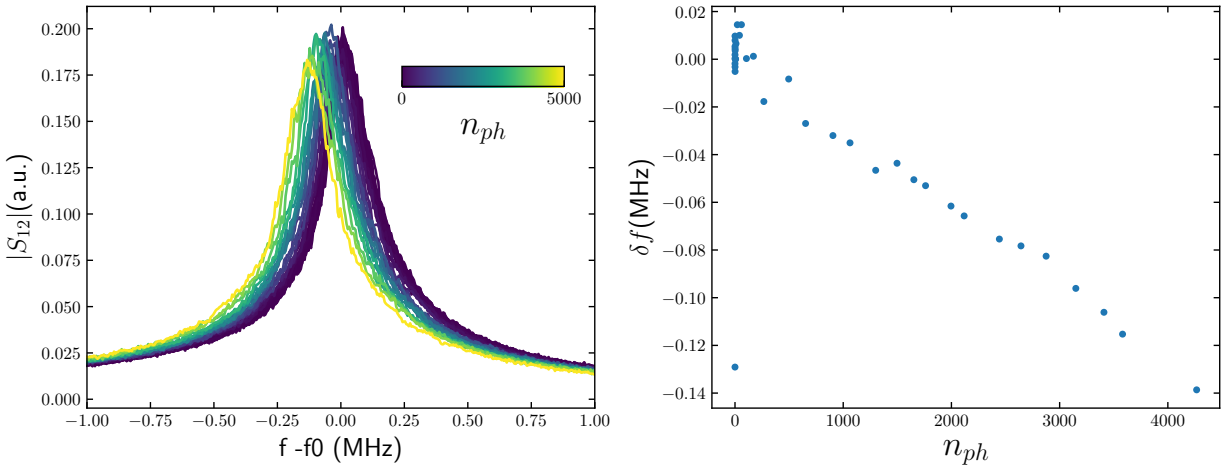

Figure 4.20: Example of the frequency shift of mode at frequency 6.104 GHz with power sent by the source into the mode at 5.85 GHz. The transmission for varying powers of the source sent at 5.85 GHz (left) Frequency variation of the resonance with power in mW (right)

We know the relation between the power output at the source frequency of mode m and the shift of the other mode n.We compute the number of photon $n_{ph\,m}$ of mode m knowing the output power P given by :

$$P = \kappa_{c\,m} n_{ph\,m} \hbar \omega_m \tag{4.2.6}$$

where $\kappa_{c\,m}$ is the coupling rate to the measuring line of the mode m and ω_m the pulsation of this mode. Knowing the amplification of the line we compute the number of photon inside the resonator m from the measured power. We measure that the deviation is linear with the cavity photon number from which we calculate U_{mmnn} between each two modes as shown in figure 4.21 with values summarized in the table 4.2.3 .

U_{ij} (Hz)	mode 0	mode 1	mode 2	mode 3
mode 0	- 900	-8	- 24	- 10
mode 1	- 40	-310	- 30	- 12
mode 2	- 38	- 15	-380	- 14
mode 3	- 28	- 13	- 57	-470

We were able to quantify the non-linear self and cross Kerr effect on a set of 4 modes in the same order of magnitude as the interactions expected for the lattice.

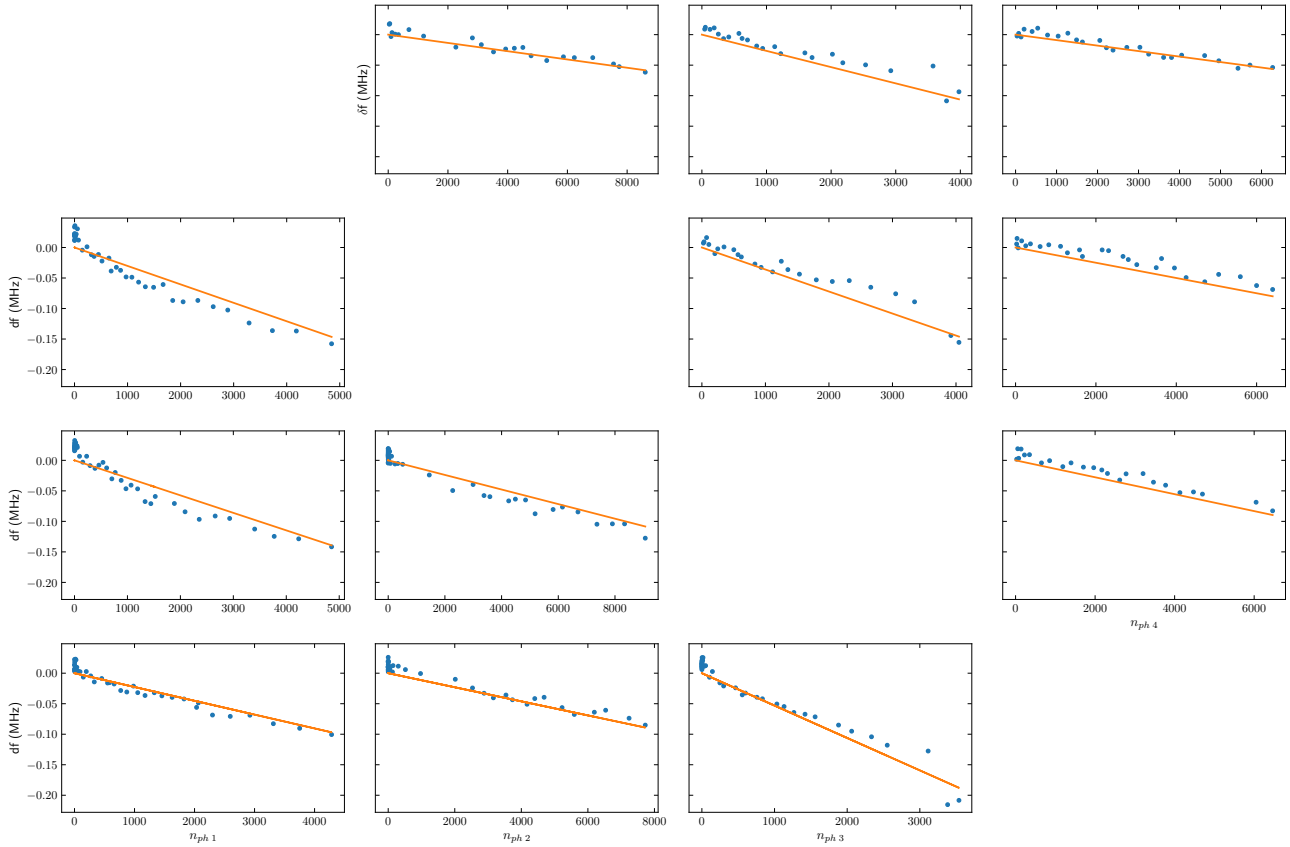

Figure 4.21: Measured frequency shift δf for each of the 4 mode with respect to the number of photons $n_{ph\ i}$ measured coming out of the pumped mode i

4.3 Four Wave Mixing Processes

Four wave mixing processes are at the core of the thermalization process described in the previous chapter. They are at the source of multiple phenomenon observable in both the Lieb and the Square lattice. We will show processes measured with a single pump and a spectrometer . We will then quantify this process on the set of four modes used previously.

4.3.1 Single Pump Sweep

Using the setup shown in figure 4.28 we send a high power source signal and measure the output of the lattice caused by this high intensity signal over a wide span of frequency. We show in figure 4.27 an example of measured spectrum on the Lieb sample at high intensity. The non-linear interaction in the lattice scatters the input signal over the frequency span of the lattice.

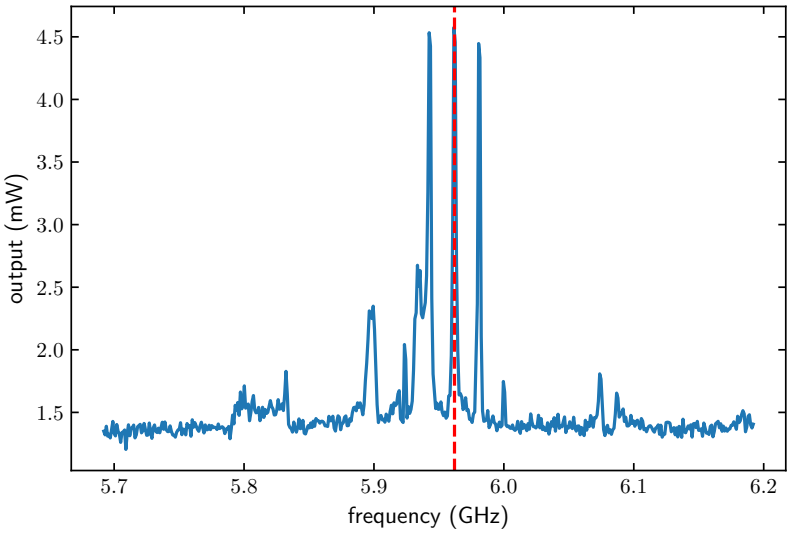

Figure 4.22: Spectrum output of the Lieb lattice pumped by a 20 dBm source at 5.962 GHz

We measured this heterodyne output at each input frequency for both samples by sending a -20 dBm signal on the Lieb sample and -80 dBm on the rectangle sample. We show in figures 4.23 and 4.24 the spectrum output with frequency centered around the source frequency

We observe multiple types of non-linear phenomena for both samples. The Lieb example is measured at 22 dBm from the source and the rectangle sample at 15 dB. We observe many different phenomena around the pump frequency as shown in 4.23.

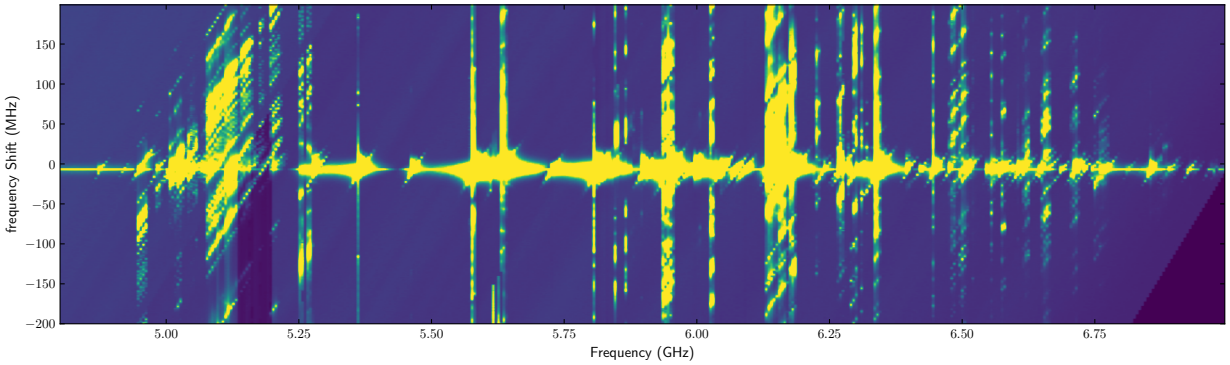

Figure 4.23: Output of the Lieb sample at 22 dBm of input power.

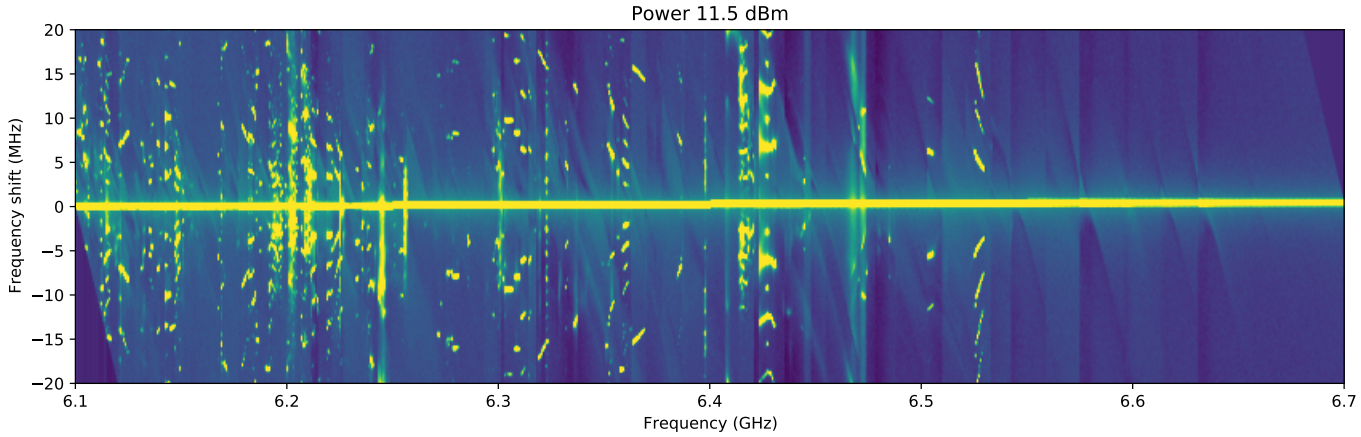

Figure 4.24: Output of the square sample at 15 dBm of input power from the source.

This broad heterodyne measurement points to typical non-linear patterns that point to non-linear interactions in both lattices.

4.3.2 Kerr frequency combs

Continuous pumping of modes with a Kerr non-linearity can create evenly spaced frequency pattern also known as Kerr frequency combs . Those pattern emerge from cascaded parametric interactions through four wave interaction between the pump, the mode. The first measurement of such patterns was made in optical micro-resonators [75, 76] and since have been a focus in circuit QED [77, 78].

In typical Kerr experiments those excitations arise from pumping a multimode system. The output frequency spacing of the comb then relates to both the frequency spacing between the modes, with the pump as well as the detuning of the cavity due to the pump strengh. For certain values of detuning and power the equations become unstable and the system goes into limit cycles creating multiple frequency spectra. The distance between the modes of the cavity is called the free spectral range (FSR) which, in micro-resonator, is fixed the modes are evenly spaced. In both samples, many modes and different frequency spacing are present. The patterns emerging from continuous pumping of our lattice are thus extremely sensitive to the pump power and frequency.

The frequency dependence showed in 4.24 as well as the zoom showed in 4.25 show this dependence of the output comb with frequency. The power dependence at a fixed frequency showed in 4.25 also show the presence of threshold powers characteristics of non-linear processes.

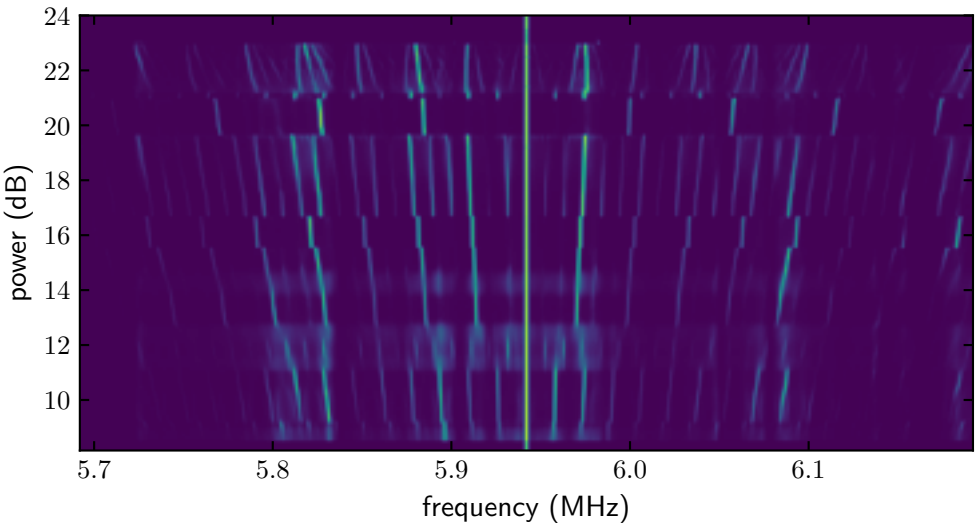

Figure 4.25: Output of the Lieb sample at 15 dBm of input power from the source. we observe a transition from a type I Kerr comb to a type II.

Two types of combs are referenced in the literature. Type 1 are combs that come from the interaction of evenly spaced modes which creates combs of multiples of the modes spacing. Type 2 combs are when ratios of these multiple occur and sub-comb lines appear. We show in 4.26 two power cuts of 4.25 that exemplify this pattern formation. The presence of many different frequency spacings in our lattice yields the possibility that changes of the comb spacing originate from a different set of modes. Though the division occurring with power seen on 4.25 strongly indicates the type 2 comb process.

At higher power, the limit cycles can break and the dynamic creates a continuous band of frequencies typical of chaotic behavior. The figure 4.27 shows a frequency sweep and a cut at 5.955 GHz showing a chaotic continuous frequency output

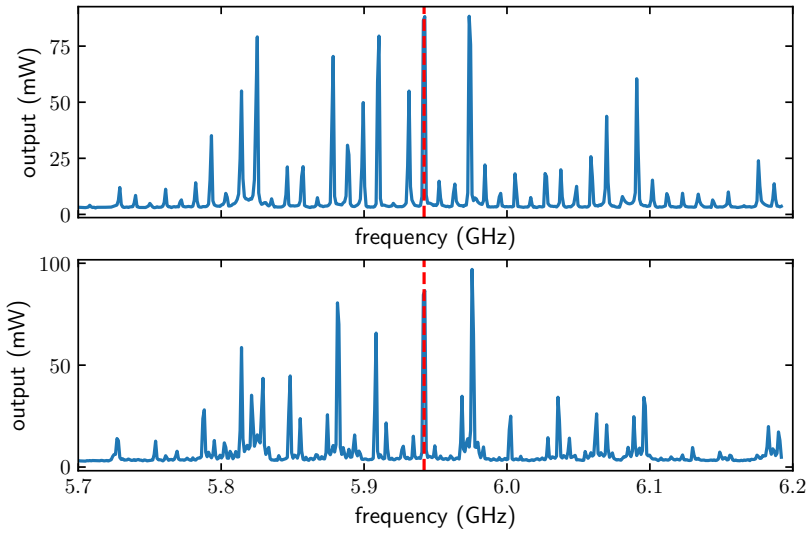

Figure 4.26: Example of type I (top) and type II (bottom) Kerr frequency Comb taken at 18 dBm of power with a source at 5.942 GHz. The measured spacing of 10 MHz in the type I comb is of the same order of magnitude as the average distance between the modes of the lattice.

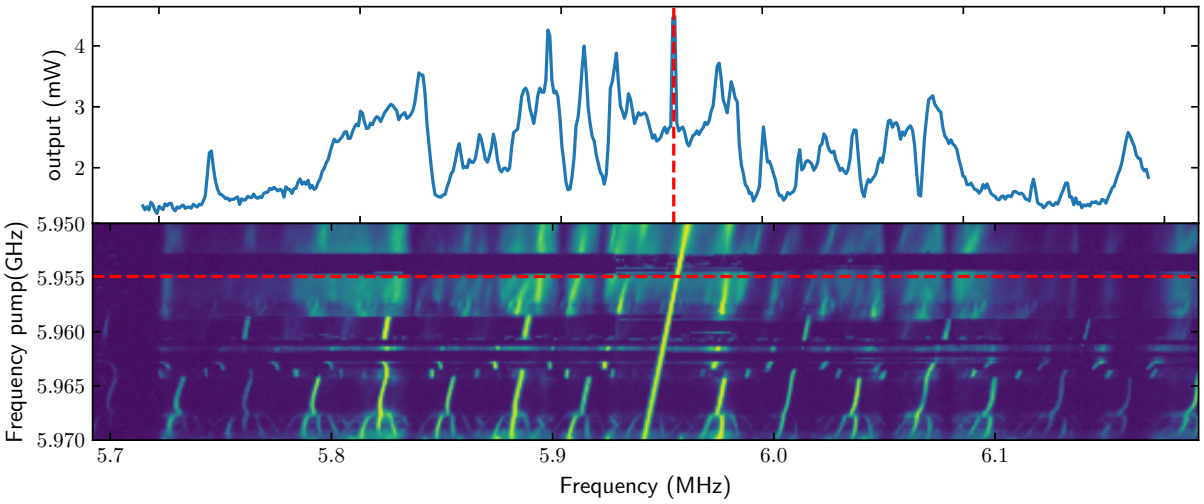

Figure 4.27: Output from a frequency sweep of a high power source at -20 dBm on the lieb sample (bottom) with a cut at 5.955 GHz (top)

4.3.3 Four wave mixing processes

The presence of four wave mixing processes in the lattice is exemplified by the various effects shown in the previous section and we now can quantify the amplitude of this effect using the set of frequency matching modes shown in 4.17

The Hamiltonian between four modes is :

$$H_{nl} = U_{mmnn}\alpha_m\alpha_m^*\alpha_n\alpha_n^* = UA_{km}^2A_{kn}^2\alpha_m\alpha_m^*\alpha_n\alpha_n^* \tag{4.3.1}$$

Classically we expect a number of photon n in the resonator such that

$$n = |a_i|^2 = \frac{\eta^2}{\kappa^2} = \frac{(Ua_j^*a_ka_l)^2}{\kappa_i^2} \tag{4.3.2}$$

We measure the number of photon in each of the driven cavities and we can calculate the non-linear term U_{ijkl} following:

$$\frac{\kappa_i\sqrt{n_i}}{\sqrt{n_j}\sqrt{n_k}\sqrt{n_l}} = \frac{\kappa_i|a_i|}{|a_j||a_k||a_l|} = \frac{\kappa_iU_{ijkl}|a_j||a_k||a_l|}{\kappa_i|a_j||a_k||a_l|} = U_{ijkl} \tag{4.3.3}$$

We can measure the output from three input cavities separately. For a term U_{mnpq} of 10 Hz per photon a loss rate κ_i of 3 MHz and 10^5 photons in each j, k and l modes we expect a number of photons output of only 0.1 photons. The value of κ_i used to calculate the term U_{ijkl} is taken from the fully unsaturated TLS loss rate factor shown in 4.14 at 3 MHz.

We have used the setup as shown in figure 4.28.

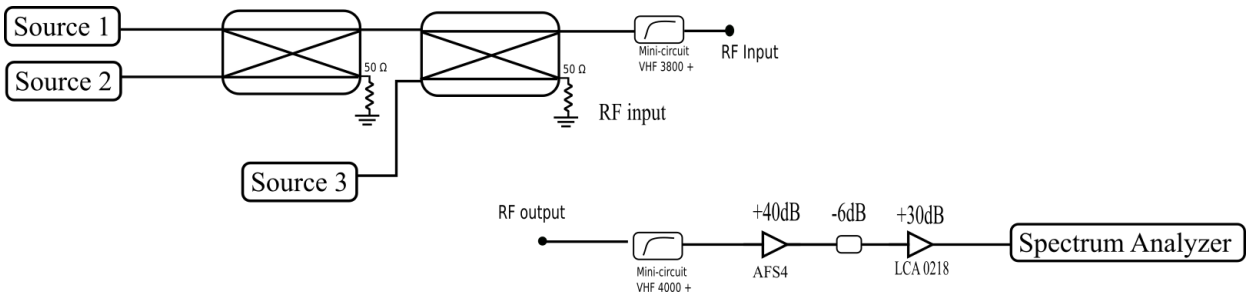

Figure 4.28: Setup for the four wave interaction measurement We used 2 network analyzer (ZVA AVB Rhode& Schwarz) and a RF source (agilent E8257D) for the three sources. We used one spectrum analyzer that we centered consecutively around each frequency

We measure an output power p_i coming from each frequency. We compute the number of photon in each of the driving modes knowing their coupling rates from the reflexion port from the fit of the reflexion shown in figure 4.31. The input modes are measured with a resolution bandwidth of 50 kHz of bandwidth while the output mode is measure with a resolution bandwidth of 10 Hz . The self and cross Kerr changes the frequencies of each mode thus there is no linear relationship between the source power and the number of photon in each driven mode. Thus, we measure the output for each of the configuration. We show in figure 4.29 the power measured at the first mode frequency and the amplitude fit with a Gaussian fit. We also show the power measured at the output mode.

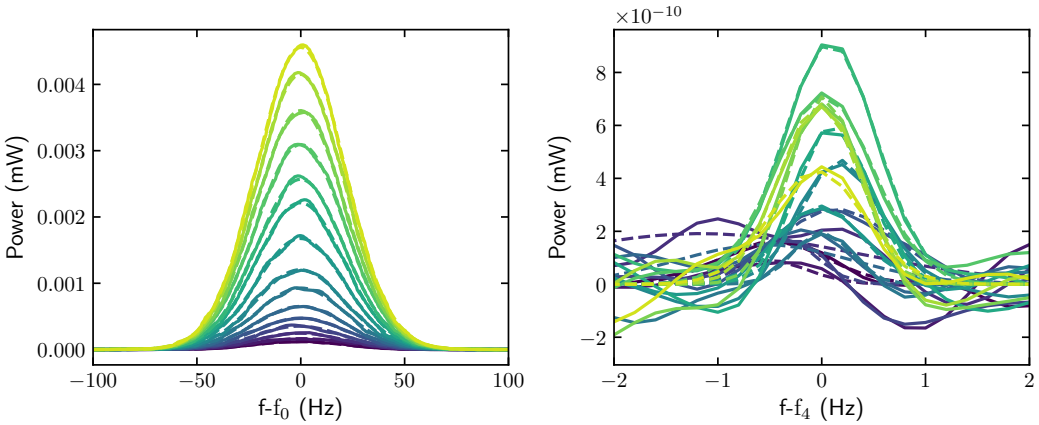

Figure 4.29: Power measured on mode 1 at 5.732 GHz with 50kHz bandwidth for varying source power from -30 to -15 dBm from the source.(left) Power measured on mode 1 at 6.1037 GHz with 10Hz of bandwidth for the varying power on the first source and constant power of the source 2 and 3 on mode 2 and 3 at -30 dBm.(left)

We relate the output power with the power of the first mode which is only pumped by the three others. We plot in figure 4.30 the output number of photons $sqrt(n_4)$ with the product of the square root of the input $\sqrt{n_0}\sqrt{n_1}\sqrt{n_2}$ in logarithm scale. We measure a 1.6 power law at odds with the expectation of a linear relationship between the two.

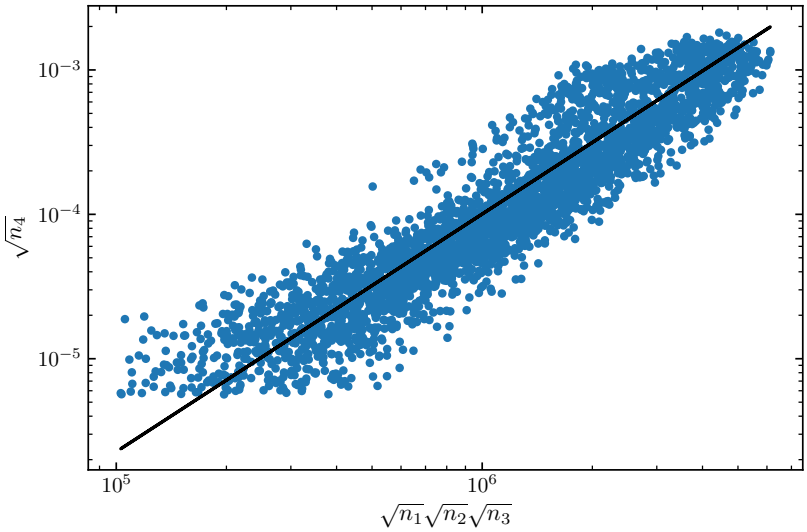

Figure 4.30: Square root of the output number of photons in mode 4 with the product of the square root of the number of photons of the input modes.

One possible origin of the problem with this first measurement is that the third mode is close to degenerate with another mode as is seen in the measure in reflexion in figure 4.31 . We do not have a way to explain the different power law taking into account the two modes close in frequency.

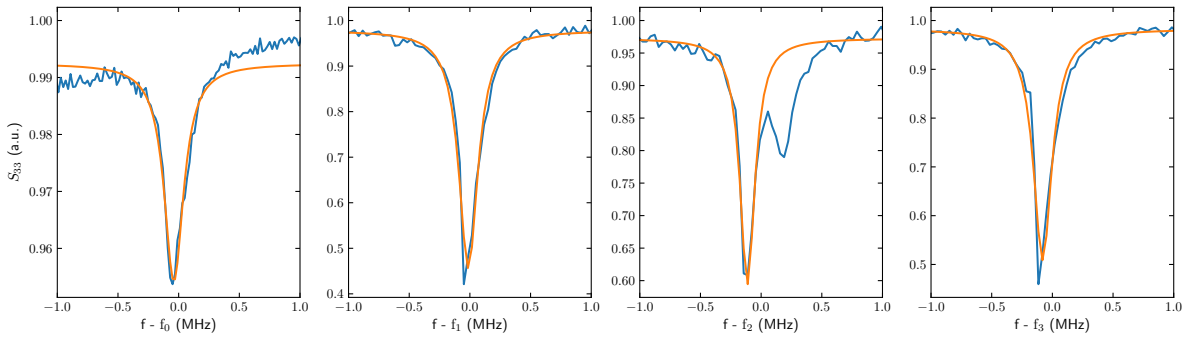

Figure 4.31: Modes at 5.758, 5.851, 6.011 and 6.104 GHz shown in reflexion along with a Lorentzian fit.

We performed the same measurement on another set of modes at frequencies 5.733 , 5.835 , 6.087 and 6.190 GHz shown in reflexion in figure 4.32.

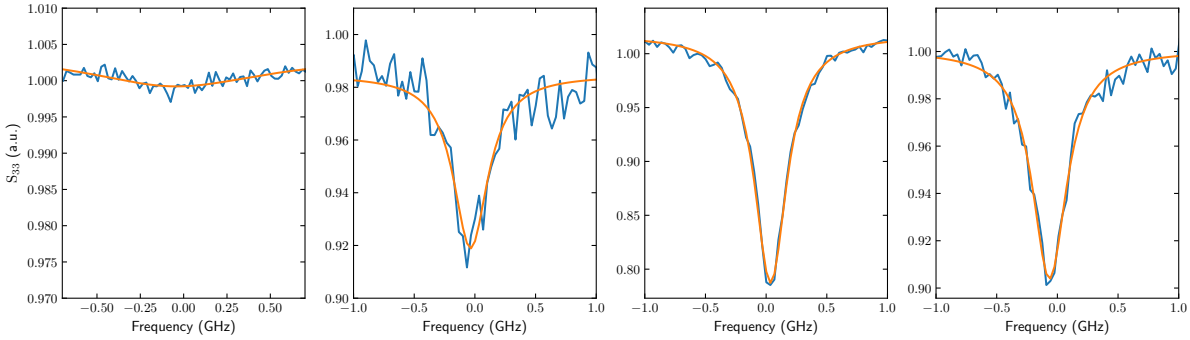

Figure 4.32: Modes at 5.733, 5.835, 6.087 and 6.190 GHz shown in reflexion along with a lorentzian fit.

Using this set of four modes we verified the expected linear relationship law between $\sqrt{n_4}$ and $\sqrt{n_1}\sqrt{n_2}\sqrt{n_3}$ as shown in figure 4.33 and find an average four-wave mixing amplitude of 5.3 ± 0.7 Hz /ph.

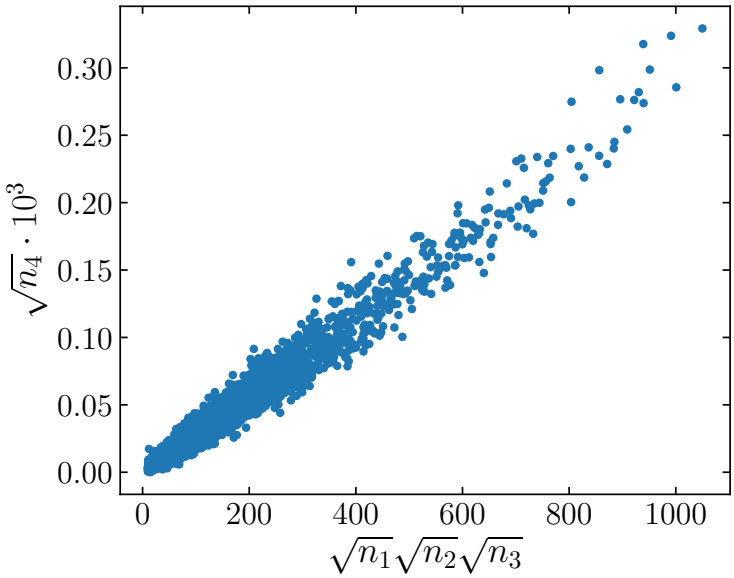

Figure 4.33: Square root of the output number of photons in mode 4 at 6.190 GHz with the product of the square root of the number of photons of the input modes at 5.733 , 5.835 and 6.087 GHz.

4.4 Pulsed Experiments

In this section we will show the measurements of the transient response of the square lattice. We show the setup used for this experiment and the generation of a pulsed frequency comb . We then discuss the problem induced by the TLS losses when measuring dynamical properties of the mode amplitudes. We then present the output of the measurement for a set of 5 different input amplitudes. We conclude this section by extracting the number of photons in time

We aim to measure dynamics of the lattice by setting multiple modes at a high number of photons and analyze the ring down of the entire lattice. Following the simulations shown in 3.2, the goal is to measure population variation between modes due to non-linear interaction between them. By driving at high amplitudes a set of modes and letting the system relax toward vacuum we aimed to measure such interaction by measuring exchanges of energy within the modes.

4.4.1 Setup to generate a pulsed frequency comb at GHz frequencies

In order to send a frequency comb where each of the peak of the comb is pulsed, we use the setup shown in 4.34.

The Texas Instrument DAC board (TSW14J56+DAC38RF82EVM) has a controllable bandwidth of 1GHz with an added local oscillator that brings the entire possible bandwith to 0-4GHz . We chose to a 1GHz frequency band around 750 MHz and mix it with a source (Agilent E8257D) at 7.05 GHz that is pulsed at the desired rate. The amplitude of the source is set at 7dBm below the saturation of the mixer. The mixer has a bandwidth of 1.5 GHz. The mixer bandwidth leads to variations of output amplitude thus we perform a calibration procedure to flatten the output in the 5.8 -6.8 GHz band. We send 100 peaks equally distributed with the TI DAC and measure the output of the full setup with the spectrometer. We then reverse the amplitudes sent from the TI DAC to calibrate as shown in 4.35. We perform that calibration multiple times to obtain a flat output within one %. We amplify with an amplifier (Minicircuit ZX60-53LN+) that signal to reach amplitudes up to -15 dB. We then control the output am-

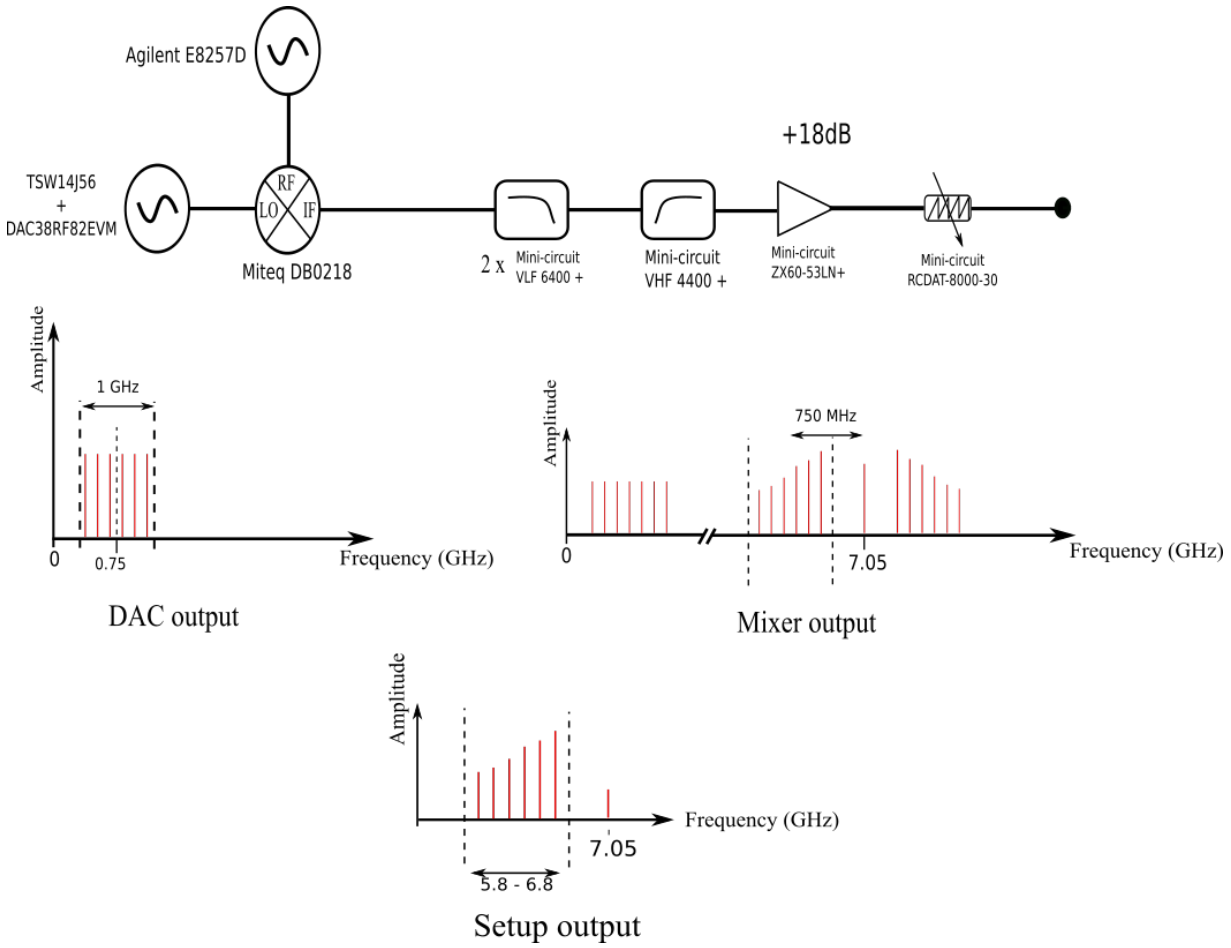

Figure 4.34: Setup for the pulse experiment.(top) Schematics of the RF signal through each stage of the setup.(right)

plitude after the amplifier with a controllable attenuator (Minicircuit RCDAT-8000-30). We control better the amplitude with the attenuator than changing the amplitude of the source or the TI DAC which leads to many non-linear effects in both the mixer and amplifier.

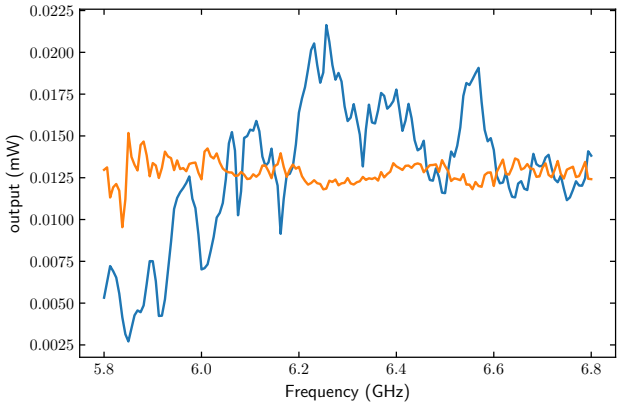

Figure 4.35: Measurement of the amplitude of 100 peaks sent at the same amplitude from the TI DAC measured at the output of the setup. (blue) Same measurement after one calibration (orange)

We then use the rest of the room temperature setup shown in 4.36 towards the fridge input. We added 28 dB of amplification (LCA 0218). We send a maximum of -15 dB well below the saturation of this amplifier. We use two relays to measure the comb before the fridge in order to do the calibration. The VNA was setup in order to check the transmission of specific modes during this pulse experiment.

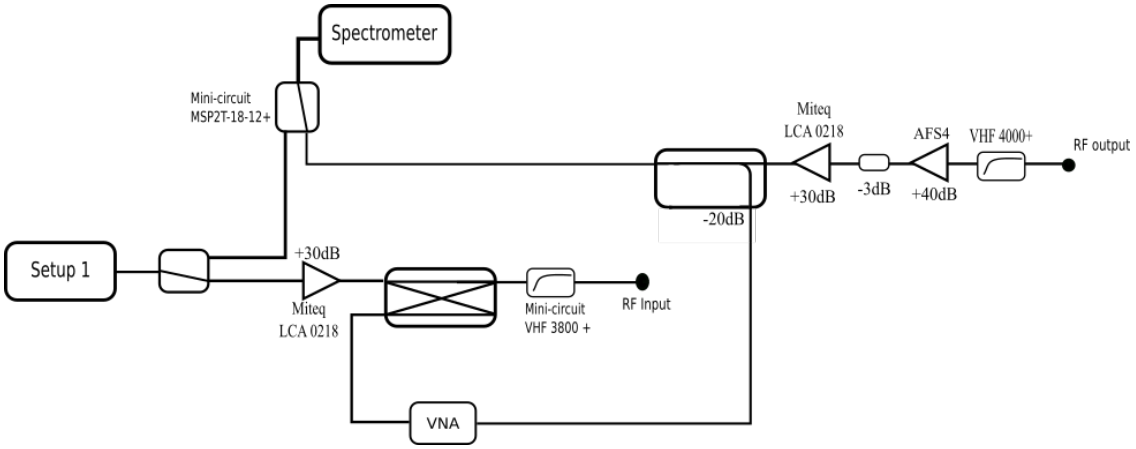

Figure 4.36: Setup at room temperature. The setup 1 used for this experiment is the DAC setup shown in figure 4.34. We measure the output of setup 1 directly through the relay for calibration

This setup allows us to create any pulsed signal within the 5.8 -6.8 GHz band.

4.4.2 TLS dynamics

During the start of each pulse our expectations was that the TLS would not be saturated and impact the dynamical features of the lattice. Multiple measurements point to dynamical properties of the modes . As an example of this dynamic we measured the dynamics of two separate pulses with a delay from 0 to 10 ms between the two. The setup used for this experiment is

the same as the one shown in 4.28 using the source 1 and 2 with a delay on the source 2. The source 1 was set at -35 dBm of output power and the source 2 at -38 dBm. The lattice mode for this example is at 5.835 GHz. Both sources are sending power for which the mode is is the linear regime with respect to the self-Kerr non-linearity. An example of measurement is shown in 4.37

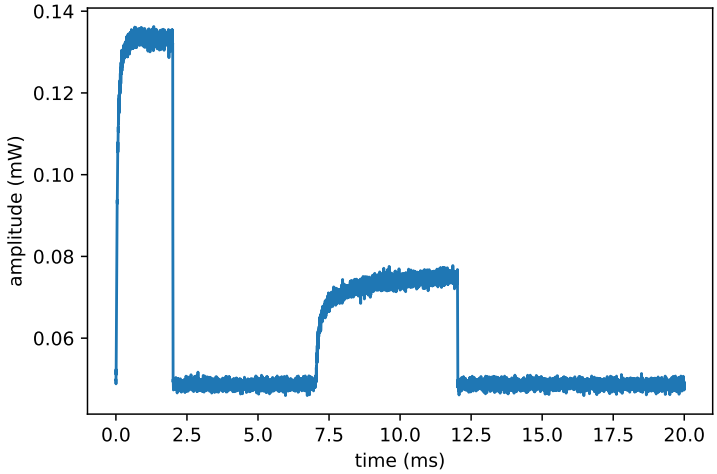

Figure 4.37: Example of measurement of two pulse experiment

The rate at which the second pulse reaches the steady state with respect to the delay is shown in 4.38

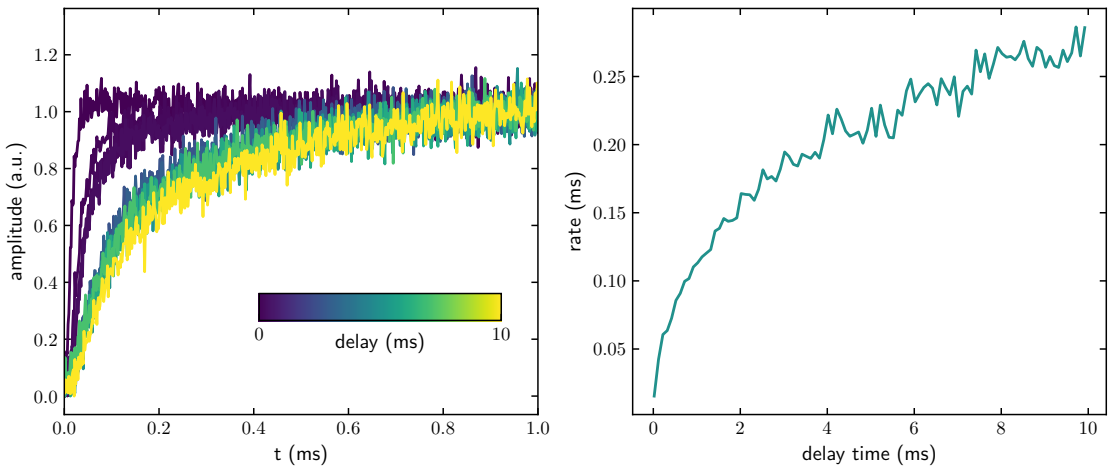

Figure 4.38: Transient response of the cavity for varying delays(left). Rate of the cavity with delay between the pulses (right)

The time to reach a steady state from an input power is greatly reduced by a high power pulse before the second pulse on short timescales. The timescale of dynamics in the millisecond points toward dynamics of the TLS systems around the lattice. We decided to focus on the dynamics after the pulse at high power in a regime for which the modes that have been pumped have a lower loss rate. Nonetheless such effects does show some limitations of the experimental setup. Especially, the modes that have a very low coupling with the lines can not be pumped to lower their losses.

4.4.3 Measurement

Driving combs We sent combs consisting of 48 frequencies with power outputs ranging from -35 to -20 dB for each peaks at the output of the DAC setup. The total output power over the whole band did not exceed the saturation power of the LCA amplifier after the DAC setup. With the attenuation in the setup and the expected attenuation of the line the amplitude of the comb at the sample input ranges from -105 to -90 dBm this puts it far into the duffing regime for each mode as shown with the VNA measurement shown in 4.18.

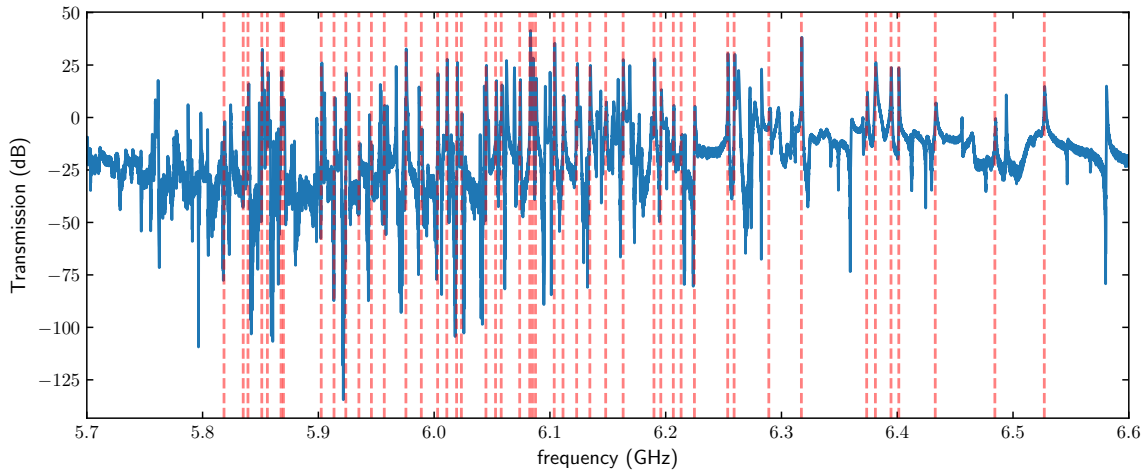

Figure 4.39: Chosen frequencies in the 5.7 -6.4 GHz band of the transmission from port 1 to 3 to drive the lattice.

We setup the source to pulse the output every millisecond for 10 μs and then measure with the spectrometer at each frequencies with a bandwidth of 28 MHz and sample the output every MHz. Each data measurement is averaged 1000 times and an example output is shown in 4.40.

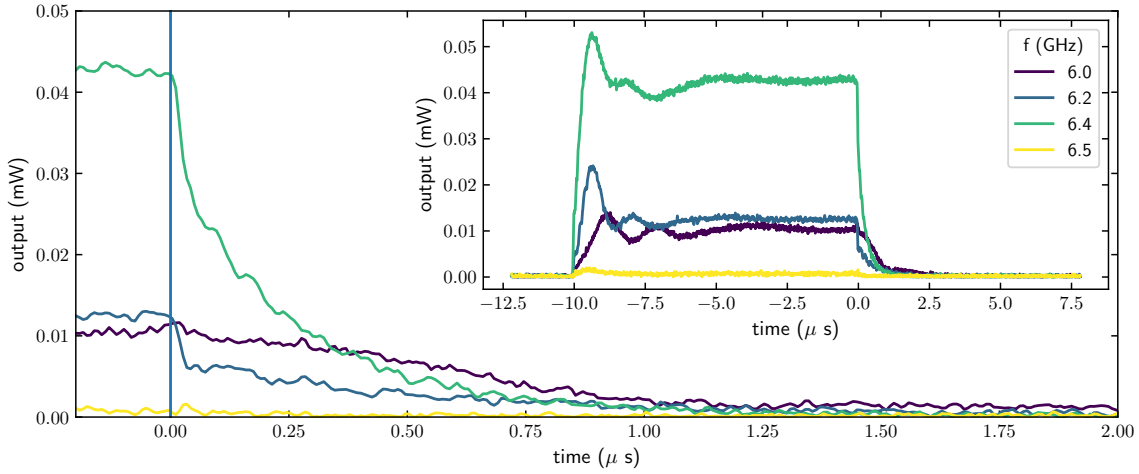

Figure 4.40: Output of the lattice at the frequencies 6,6.2 6.4 and 6.5 GHz.The noise level of 0.0458 mW has been substracted

By slicing each of those time evolution in time we can show the frequency output at each time. In 4.41 we show the output at 10.1 μs after a pulse at -25 dB output from the DAC setup. We observe that the response of the lattice as seen from the spectrometer is step-like

corresponding to the bandwidth of the spectrometer. The frequency output is a convolution of the lattice output and the response function of the spectrometer set at 28 MHz of bandwidth.

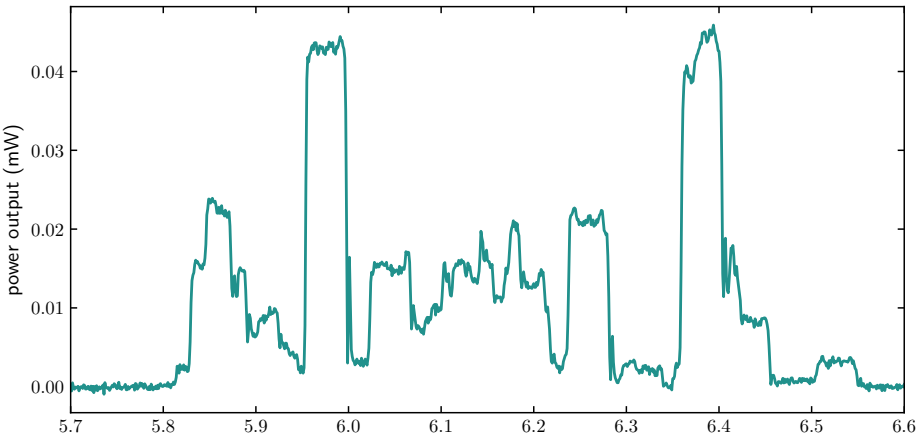

Figure 4.41: Output of the lattice with frequency at time 0.1 μs. The noise level of 0.0458 mW has been substracted.

Total power output Before analyzing frequency dependent characteristics of the response we observe the different regimes that we observe for the total power output of the lattice. We plot in 4.42, for the 5 comb amplitudes, the total power output over the whole spectrum.

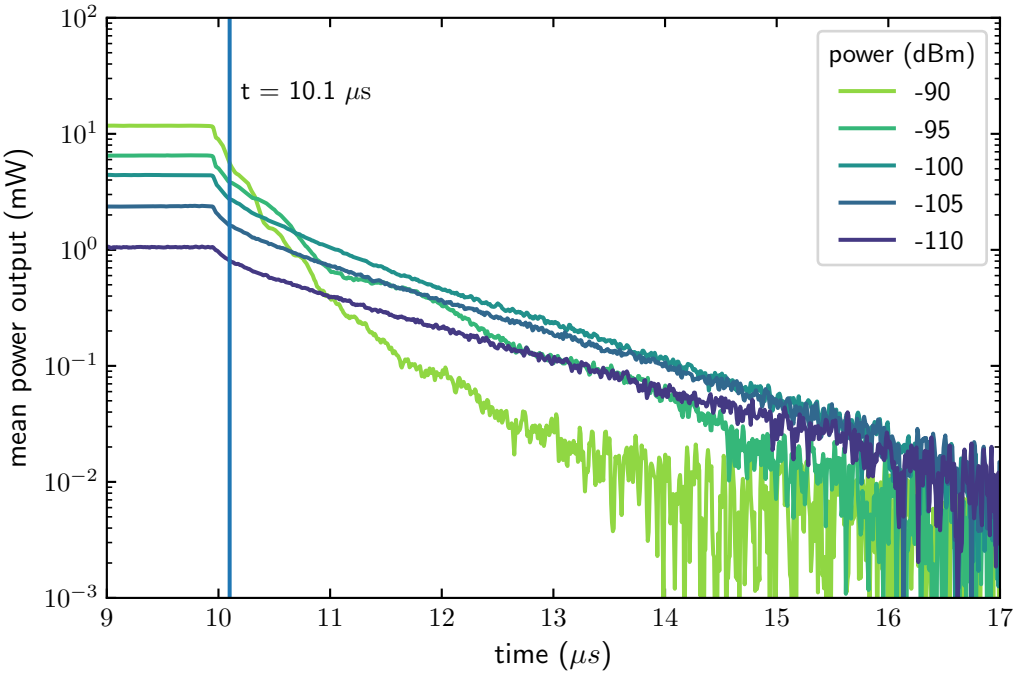

Figure 4.42: Variation of the integrated power output after a pulse for different pump pulse power .

We observe a change of behaviour starting -100 dBm. Below this value, the total output follows a logarithmic ring down. This is compatible with an ensemble of resonators that are driven higher or lower on the TLS scale and have different losses but all ringdown without interaction. We observe already that the power loss rate already lowers with power. This is in opposition with the behaviour on one resonator showed in 4.14 where the power saturates the loss of the resonator. The behavior accentuates at higher power. The power output does not decay exponentially and the power loss rate keeps increasing. This could be explained in multiples ways. One possibility is that the power into the lattice spreading over multiple modes could create hot spots at specific points of the lattice and increase the losses of superconductor. Another explanation also could point towards thermalization of the lattice towards higher frequencies as expected from the simulation. In this second case the amplitude thermalizes to modes uncoupled to the measuring line.

As we also observe, even at lower power and just after the end of the pulse (between 10 and 10.1 μs), the amplitude does does not follow a logarithmic variation. This is due to a part of the pulse amplitude that we see directly through the sample. Thus the plateau amplitude during the pulse does not correspond to the lattice output amplitude. In the rest of this section we analyze amplitude after the 10.1 μs mark.

Frequency output distribution with time We expect variation of total population between the frequencies. We show in 4.43 the output divided by the total measured output after 10.1 μs.

At low power, we observe that the higher frequency decay faster which is coherent with the high loss rate modes measured in this bandwidth. We observe this trends at every power thus we observe the lower frequency increase with respect to the higher frequencies even if no energy transfer is taking place. At the highest power the loss rate over the entire frequency span is too high and most of the information is lost. We observe that at the highest power input, the high frequency modes have saturated due to the non-linear self-Kerr, changing the starting energy repartition towards the low frequencies. This is coherent with lower coupling rate for the high frequency modes and thus higher number of photon inside the mode. Specifically at -95 dB we do observe a change of the amplitude distribution in the 5.8-6.2 band.

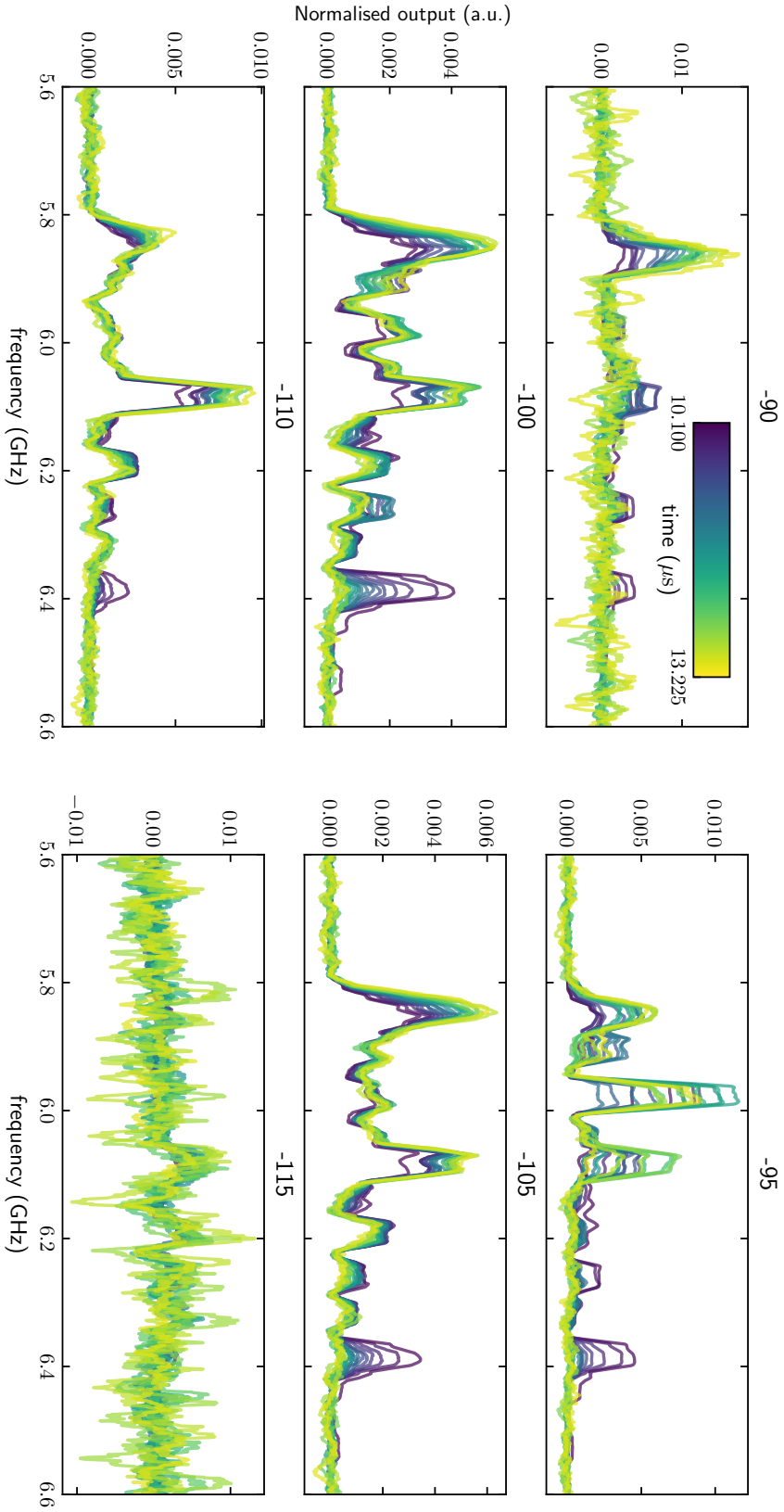
Normalised output (a.u.)
frequency (GHz)
time (μs)
10.100
13.225
-90
-95
-100
-105
-110
-115

Figure 4.43

Mode population reconstruction From the measurement of the reflexion shown in 4.7 we fitted the coupling rates of the 148 measured resonances coupled with the output port 3. We assume that each modes of the lattice i containing an amplitude P_i outputs a power $P = P_i * \kappa_c$. We measured the response function of the spectrometer to an input directly from the RF source at f_0 and power P with the 28 MHz bandwidth that we define as $F(f, f_0)$ as shown in figure 4.44.

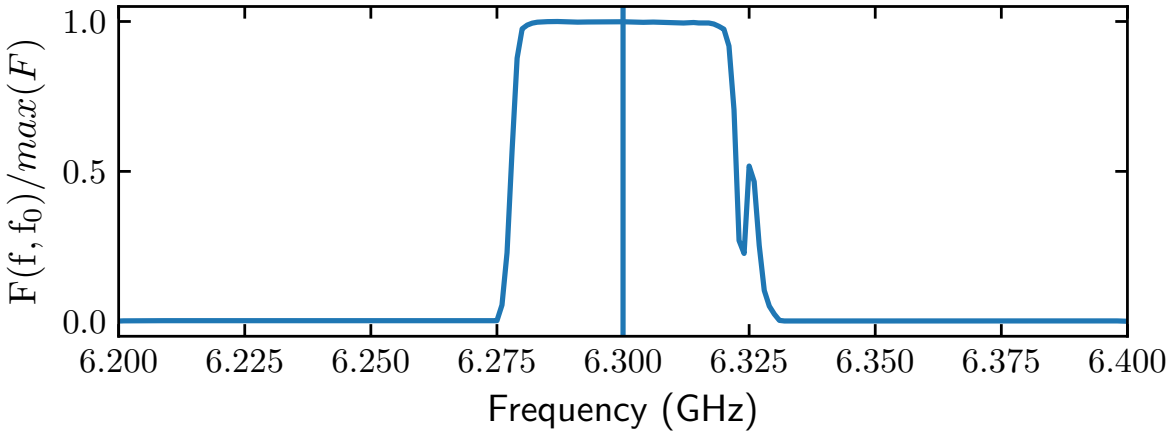

Figure 4.44: Normalized output of one pumped mode seen by the spectrometer at a bandwidth of 50 MHz.

The bandwidth of the spectrometer is of 28 MHz and we assume that each of the modes will output an amplitude $\kappa_c(i)P_i$ and that the total output measured with the spectrometer is a sum of those responses for each mode i given by:

$$P = \sum_i \kappa_c(i) P_i F(f, f_i) \tag{4.4.1}$$

Knowing the frequencies, loss rate and response function the output is the linear combination of the one photon response function of each mode and the number of photon in each mode. For a set of N_m modes and an spectrum that we measure in N_f frequencies we can create a matrix A of size $N_m \cdot N_m$ where each line n corresponds to the spectrum output of one photon in the mode n. For each spectrum that is a vector B of size N_m we compute the photon amplitude n_{ph} vector in each mode as a the solution of $A \cdot n_p h = B$ using a non-negative least square solver. As an example we show the reconstruction for an output in figure 4.45

We analyzed each time cut and get time evolution of each modes as shown in 4.46. We analyzed using the 110 highest coupling rates from the reflexion measurement and for clarity we plot only the 15 highest number of photons in time for each power pulse amplitude.

We can confirm that we have an exponential ring down from multiple modes at low power. Above -110 dBm we observe mode amplitude variation and non exponential variations, coherent with the integrated output shown in figure 4.42 .

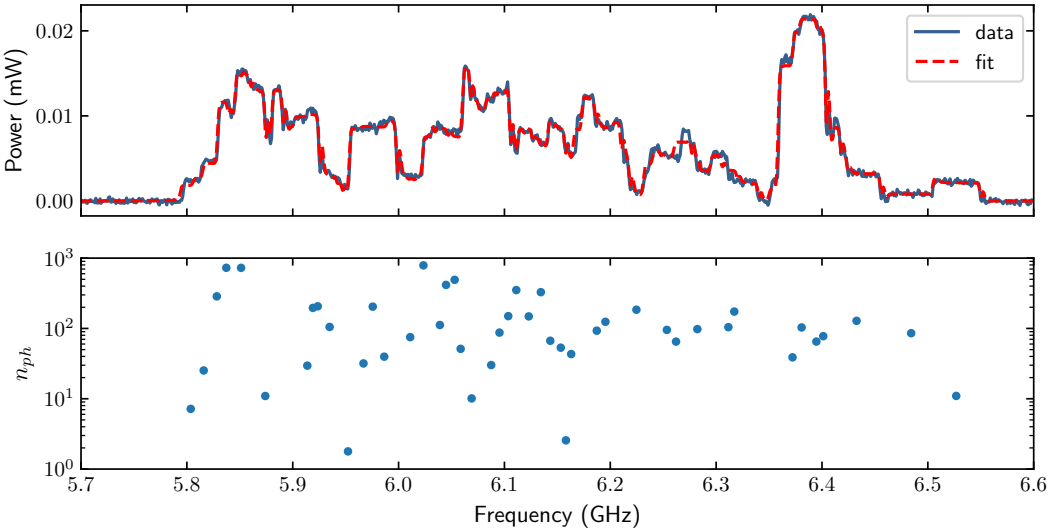

Figure 4.45: Spectrum measured at 0.1 μs after the pulse at -95 dBm (blue) and reconstruction in red using the method described in this section (top) Photon amplitudes found for the reconstruction (red)

Reliability of the reconstruction Two main issues arise with the reconstruction technique that hinder its reliability. The first one is the fact that it is possible that the modes shift slightly of up to 5 MHz at high power . In order to match the measure shifted output the algorithm might enhance modes close to the shifting mode. By doing this it creates variation of mode amplitudes as well as oscillations between modes otherwise non present. The second problem has to do with the number of modes needed for a full reconstruction. we show in figure 4.47 an example of output reconstruction using from one to 45 modes taken. This example shows that a set of 45 modes can reconstruct most of the signal power output. This is not enough to reliably make assessment on the dynamics in the lattice. Moreover even if the amplitude reconstruction used the 140 modes fitted for the reconstruction we still do not have a good quantitative picture of amplitude dynamics in the lattice. This points to the need for a lattice coupling scheme that can provide constant coupling on a band of frequencies.

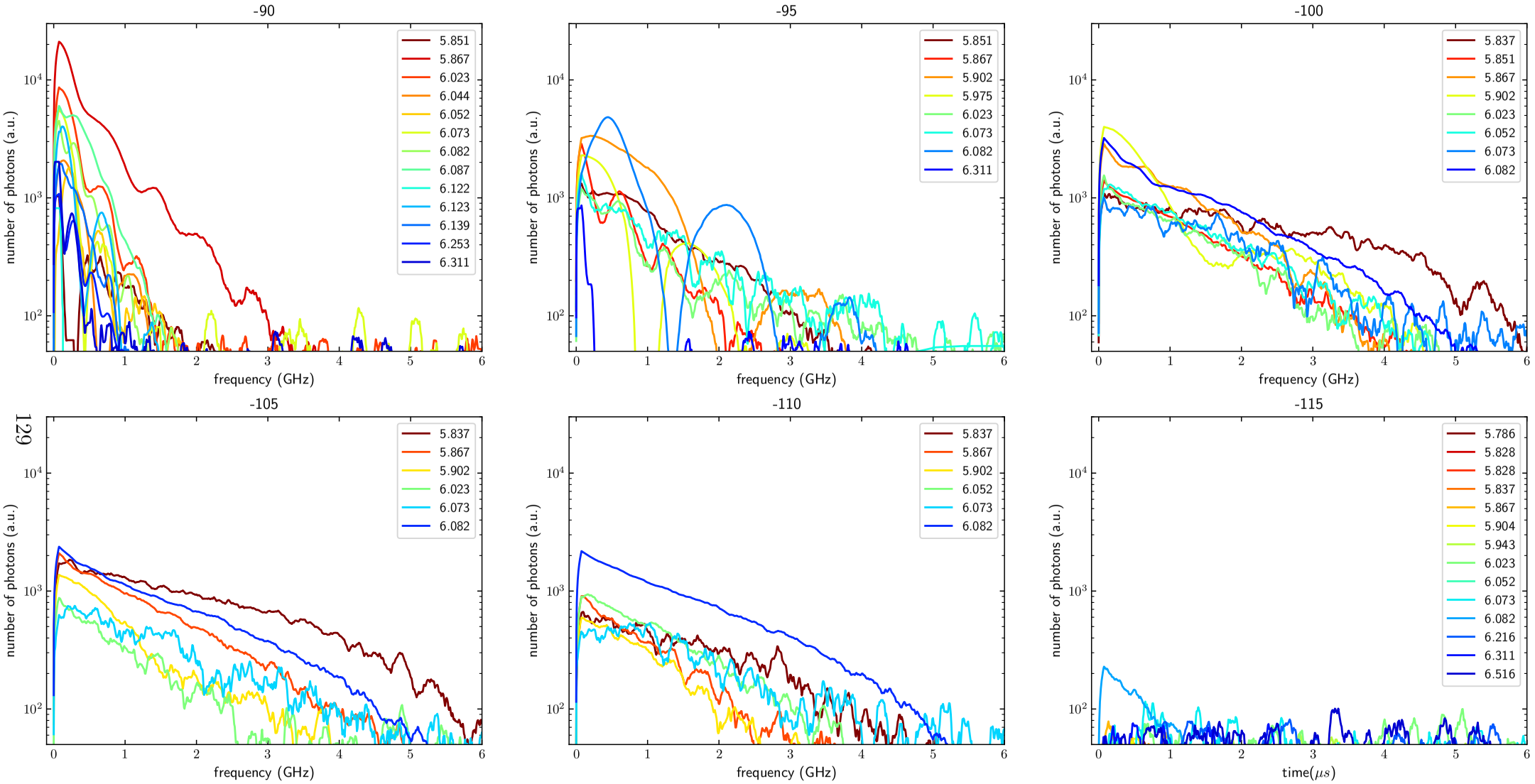

Figure 4.46: Pulse in time at each amplitude of the driving pulse from minimum to maximum attenuation. Only the highest significant modes are shown with a threshold above the noise of the measurement.

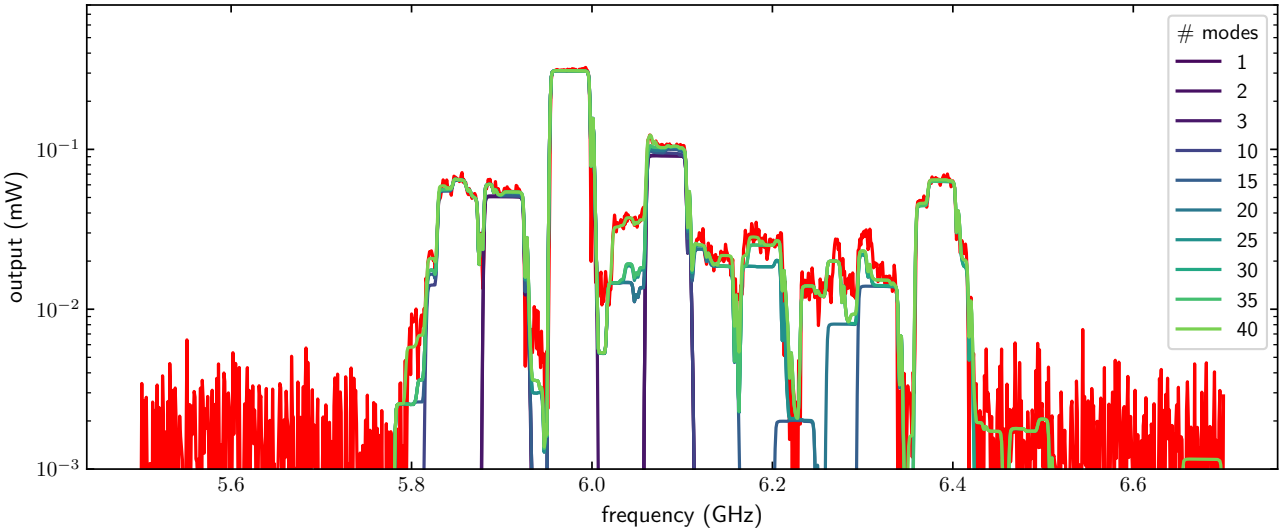

Figure 4.47: Example of reconstruction using different number of mode from 1 to 40. In red is shown the output after the -90 dBm comb pulse at 10.15 μs .

Entropy of the lattice Using those measured photon numbers we can compute the statistical variation of the population from those measured modes of the lattice. We compute the entropy at each time from the mode populations $n_{ph\,i}$ measured as:

$$S = \sum_i log(p_i) \tag{4.4.2}$$

where $p_i = \frac{n_i}{N}$. We show in 4.48 the entropy computation for each of the comb amplitude using the reconstruction of the mode using 110 modes. As the amplitude of the signal lowers, the signal to noise ratio goes down thus at higher times we measure the noise of the signal at every mode which is coherent with an increase of the measured entropy. But for the comb of power -90 and -95 we again observe signal consistent to the amplitude movement shown previously.

Again most of the signal comes from the amplitude of a few modes. We show in figure 4.49 the same entropy calculation for varying number of modes used in the reconstruction. We retain most of the features from 60 to 110 modes used in the calculation.

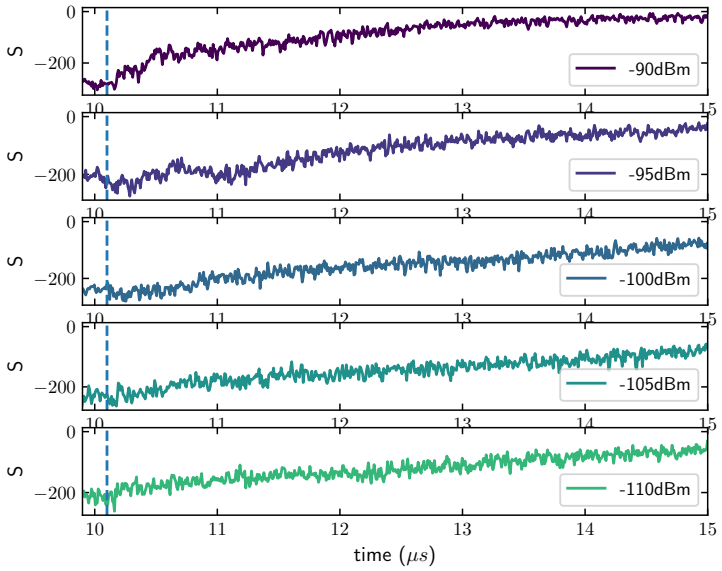

Figure 4.48: Entropy variation measured using the population showed in 4.46 for each of the 5 amplitude of pulse using the reconstruction technique with 110 modes.

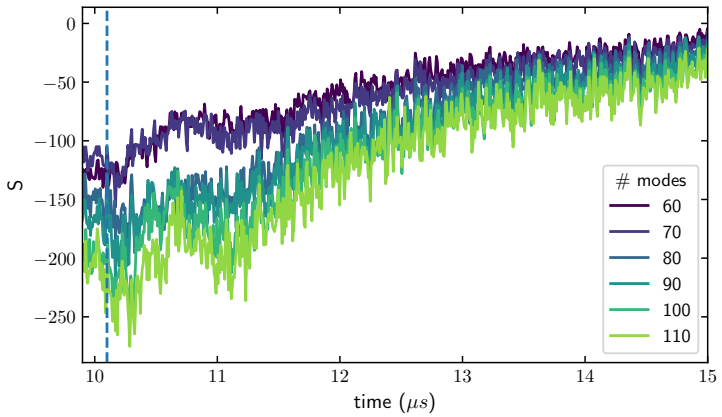

Figure 4.49: Entropy variation using the population reconstruction with varying number of modes from 60 to 110 modes using the measurement from the -95dBm amplitude comb.

Conclusion

In this chapter we presented both the rectangular lattice sample (MF56) and Lieb lattice sample (MF45). We showed measurements of the transmission through their ports and confirmed the theoretical expectations from the design. We measured and quantified the TLS losses on one mode of the MF56 sample and compared it to losses of the single resonators. We observed the Duffing effect due to the self Kerr on a set of four frequencies of the rectangular lattice sample. We measured the cross Kerr effect on all of the modes of the rectangle lattice and quantified it on the same set of four frequencies. We presented effects of four wave mixing in the MF56 sample and the presence of Kerr frequency combs . We quantified the FWM on the same set of four phase matching frequencies. We finally present preliminary data on the measurement of dynamical excitation of the lattice . We show the setup allowing creation of pulsed frequency combs in the 5 to 7 GHz band and show the response of the lattice for different amplitude of the comb.

Conclusion and perspectives

This thesis work aimed to study the fabrication, design and analysis of many non-linear microwave resonators. We harvested the non-linearity of High kinetic inductance superconducting wires made of granular aluminium to create non-linear resonators and chose to design a rectangle geometry as well as a Lieb geometry.

We have presented a description of lattices of transmon-like resonators and showed how to use their design to predict their properties. We showed how to compute the band structure of infinite lattice as well as the normal modes of finite size ones. We showed how to obtain input output relations for a microwave guide coupled to a finite lattice. We then presented the two sampled designed using those methods. We showed the parameters of the rectangular lattice and how to avoid variations on the edges. We then developed a lattice with a flat band by analogy with the Lieb tight binding lattice (Chapter 1) An improvement of design of the sample would be to change the coupling to the line in order to have a constant coupling over the top frequencies which are of interest for the thermalization process.

We discussed the theory for the source of kinetic inductance and its non-linearity. We presented the in lab techniques that allowed us to fabricate and control the parameter of granular aluminium wires. We then observed the non-linear resonance of different resonators which spans multiple orders of magnitude of non-linearity and were able to explain their scaling from measured parameter. (Chapter 2) The fabrication process for granular aluminium was started during the course of this thesis in the lab and thus some improvements could be made. One of them is increasing the resistivity at which there is a superconducting to insulator transition of the granular aluminium by implementing a liquid nitrogen cooling of the evaporation target [79]. Increasing the resistivity could help enhance the non-linearity of each resonator. We also could change the resonator geometry and reduce the electric intensity in the substrate and TLS losses. Higher resistivities could help change the geometry in that direction without changing the non-linear and frequency parameters. Another fabrication improvement would be to reduce the gradient of resistance on the sample during the evaporation. Also there are still questions around the properties of the material. A better characterization of the loss of the granular material could help reducing them in the lattice. Characterizing the link between the non-linearity with the thickness as well as the coherence length of the material is also of interest.

We showed how thermal equilibrium could apply to the rectangle lattice we fabricated and performed simulations of the equation of motion of the lattice we fabricated exhibiting both thermalization and wave-condensation. (Chapter 3)

We measured the transmission of both rectangle and Lieb lattice. Both samples confirmed the expectations given from the design and resistance values. We measured the non-linear parameters of the rectangle lattice by observing the self and cross Kerr as well as the four wave mixing processes in the lattice. We presented measurements of the dynamical response of the rectangular lattice. We observed that non-linear processes did take place even if we could not observe thermal equilibrium. (Chapter 4)

The main challenge for this project is to effectively measure the thermalization process and characterize it and further along to heighten the non linearity to probe the classical to quantum transition.

In a broader perspective, this thesis work confirms the possibilities of high kinetic inductance superconductors for the realization of simulations.

Appendices

Transmission of hanger resonator

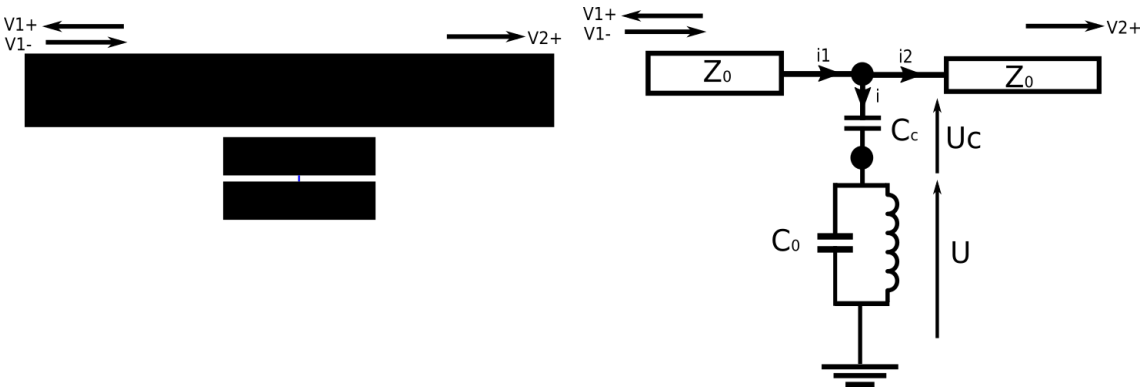

Figure 50: Design pattern of one of the MF47 resonator (left) and a first order scheme of the equivalent Electrical circuit

$$\begin{aligned} V_1^+ + V_1^- = V_2^+ * &= U + U_c \\ \frac{1}{Z_0}(V_1^+ + V_1^-) &= i_1 \\ i &= iC_c c\omega U_c \\ i &= iC\omega U + \frac{U}{iL\omega} \end{aligned} \tag{.0.3}$$

$$\begin{aligned} V_1^+ + V_1^- &= \left(\frac{1}{iC_c\omega} + \frac{1}{iC\omega + \frac{1}{iL\omega}}\right)\frac{2}{Z_0}V_1^- \\ V_2^+ &= V_1^+ + V_1^- \end{aligned} \tag{.0.4}$$

$$S_{21} = \frac{V_2^+}{V_1^+} = 1 + \frac{C_c\omega(1 - CL\omega^2)Z_0}{-2i + C_c\omega(2iL\omega - Z_0) + CL\omega^2(2i + C_c\omega Z_0)} \tag{.0.5}$$

let's define ω_{LC} and ω_0 as $\omega_{LC} = \sqrt{\frac{1}{LC}}$ and $\omega_0 = \sqrt{\frac{1}{L(C+C_c)}}$

$$S_{21} = 1 + \frac{Z_0 C_c\omega(1 - \frac{\omega^2}{\omega_{LC}^2})}{2i(\frac{\omega^2}{\omega_0^2} - 1) - Z_0 C_c\omega(1 - \frac{\omega^2}{\omega_{LC}^2})} \tag{.0.6}$$

now we can use $\frac{1}{\omega_{LC}^2} = \frac{1}{\omega_0^2} - LC_c\omega^2$ and get :

$$S_{21} = 1 + \frac{Z_0 C_c \omega (1 - \frac{\omega^2}{\omega_0^2} - L C_c \frac{\omega^2}{\omega_0^2})}{i(\frac{\omega^2}{\omega_0^2} - 1) - Z_0 C_c \omega (1 - \frac{\omega^2}{\omega_0^2} - L C_c \frac{\omega^2}{\omega_0^2})} \tag{.0.7}$$

Now we can define $\delta\omega$ as $\omega - \omega_0$ and if we reduce to the first order in δ in the denominator we find:

$$S_{21} = 1 + \frac{Z_0 C_c^2 L \omega_0^5}{Z_0 C_c^2 L \omega_0^5 + i\delta(4\omega_0 - 2iZ_0\omega_0^2 C_c)} \tag{.0.8}$$

We define κ_c as $Z\omega_0^4 C_c^2 L/4$ and find:

$$S_{21} = 1 + \frac{\kappa_c \frac{1}{1 - iZC_c\omega_0/2}}{\kappa_c + i\delta} \tag{.0.9}$$

which leads to the Lorentzian form :

$$S_{21} = 1 + \frac{\kappa_c e^{i\phi}}{\kappa_c + i\delta} \tag{.0.10}$$

with $\phi \approx -ZC_c\omega_0/2$.

We can include internal losses by adding a resistance in series with the inductance and then get a set of equation that follows .0.3 :

$$\begin{aligned} V_1^+ + V_1^- = V_2^+ * &= U + U_c \\ \frac{1}{Z_0}(V_1^+ + V_1^-) &= i_1 \\ i &= iC_c c\omega U_c \\ i &= iC\omega U + \frac{U}{iL\omega + R} \end{aligned} \tag{.0.11}$$

Using the same steps as the previous calculation we obtain the same Lorentzian form but with an added internal loss parameter κ_i:

$$S_{21} = 1 + \frac{\kappa_c e^{i\phi}}{\kappa_c + \kappa_i + i\delta} \tag{.0.12}$$

where $\kappa_i = \frac{R\omega_0^2(C+C_c)}{2}$ and $\kappa_c = Z\omega_0^4 C_c^2 L/4 - \kappa_i$.

Calculations found in [65] and [66] show that .0.12 is the general response function of a resonator with both inductive and capacitive coupling to a transmission line.

Bibliography

[1] R. P. Feynman, "Simulating Physics with Computers", International Journal of Theoretical Physics **21**, 467–488 (1982).

[2] A. Trabesinger, "Quantum simulation", Nature Publishing Group, 2012 (2012).

[3] V. Bouchiat, D. Vion, P. Joyez, D. Esteve, and M. Devoret, "Quantum Coherence with a Single Cooper Pair", **165** (1998).

[4] Y. Nakamura, Y. Pashkin, and J. . Tsai, "Coherent control of macroscopic quantum states in a single-Cooper-pair box", Nature, `https://doi.org/10.1038/19718` (1999).

[5] A. Blais, J. Gambetta, A. Wallraff, D. I. Schuster, S. M. Girvin, M. H. Devoret, and R. J. Schoelkopf, "Quantum-information processing with circuit quantum electrodynamics", Phys. Rev. A **75**, 032329 (2007).

[6] J. Koch, T. M. Yu, J. Gambetta, A. A. Houck, D. I. Schuster, J. Majer, A. Blais, M. H. Devoret, S. M. Girvin, and R. J. Schoelkopf, "Charge-insensitive qubit design derived from the cooper pair box", Phys. Rev. A **76**, 042319 (2007).

[7] V. E. Manucharyan, J. Koch, L. I. Glazman, and M. H. Devoret, "Fluxonium: single cooper-pair circuit free of charge offsets", Science **326**, 113–116 (2009).

[8] J. Jin, D. Rossini, R. Fazio, M. Leib, and M. J. Hartmann, "Photon solid phases in driven arrays of nonlinearly coupled cavities", Phys. Rev. Lett. **110**, 163605 (2013).

[9] M. J. Hartmann, "Polariton crystallization in driven arrays of lossy nonlinear resonators", Phys. Rev. Lett. **104**, 113601 (2010).

[10] T. Grujic, S. R. Clark, D. Jaksch, and D. G. Angelakis, "Non-equilibrium many-body effects in driven nonlinear resonator arrays", New J. Phys. **14**.

[11] I. Carusotto, A. A. Houck, A. J. Kollar, P. Roushan, D. I. Schuster, and J. Simon, "Photonic materials in circuit quantum electrodynamics", Nature Physics, `10.1038/s41567-020-0815-y` (2020).

[12] S. Hacohen-Gourgy, V. V. Ramasesh, C. De Grandi, I. Siddiqi, and S. M. Girvin, "Cooling and autonomous feedback in a bose-hubbard chain with attractive interactions", Phys. Rev. Lett. **115**, 240501 (2015).

[13] R. Ma, B. Saxberg, C. Owens, N. Leung, Y. Lu, J. Simon, and D. I. Schuster, "A dissipatively stabilized Mott insulator of photons", Nature, 0–6.

[14] N. M. Sundaresan, R. Lundgren, G. Zhu, A. V. Gorshkov, and A. A. Houck, "Interacting qubit-photon bound states with superconducting circuits", Phys. Rev. X **9**, 011021 (2019).

[15] M. Fitzpatrick, N. M. Sundaresan, A. C. Y. Li, J. Koch, and A. A. Houck, "Observation of a dissipative phase transition in a one-dimensional circuit qed lattice", Phys. Rev. X **7**, 011016 (2017).

[16] J. M. Fink, A. Dombi, A. Vukics, A. Wallraff, and P. Domokos, "Observation of the photon-blockade breakdown phase transition", Phys. Rev. X **7**, 011012 (2017).

[17] J. J. Mazo and T. P. Orlando, "Discrete breathers in nonlinear lattices: Experimental detection in a Josephson array", (2018).

[18] J. Pfeiffer, M. Schuster, A. A. Abdumalikov, and A. V. Ustinov, "Observation of Soliton Fusion in a Josephson Array", **034103**, 1–4 (2006).

[19] D. Abraimov, P. Caputo, G. Filatrella, M. V. Fistul, and A. V. Ustinov, "Broken symmetry of row switching in 2D Josephson junction arrays", 1–5 (2018).

[20] M. Trepanier, D. Zhang, O. Mukhanov, V. P. Koshelets, P. Jung, S. Butz, E. Ott, T. M. Antonsen, A. V. Ustinov, and S. M. Anlage, "Coherent oscillations of driven rf SQUID metamaterials", **050201**, 1–5 (2017).

[21] R. Cosmic, K. Kawabata, Y. Ashida, H. Ikegami, S. Furukawa, P. Patil, J. M. Taylor, and Y. Nakamura, "Probing XY phase transitions in a Josephson junction array with tunable frustration", 1–10 (2020).

[22] A. Morvan, "Honeycomb lattices of superconducting microwave resonators: Observation of topological Semenoff edge states", (2019).

[23] D. L. Underwood, W. E. Shanks, A. C. Y. Li, L. Ateshian, J. Koch, and A. A. Houck, "Imaging photon lattice states by scanning defect microscopy", Phys. Rev. X **6**, 021044 (2016).

[24] G. Kollár, M. Fitzpatrick, and A. A. Houck, "Hyperbolic lattices in circuit quantum electrodynamics", Nature, `10.1038/s41586-019-1348-3`.

[25] I. M. Pop, K. Geerlings, G. Catelani, R. J. Schoelkopf, L. I. Glazman, and M. H. Devoret, "Coherent suppression of electromagnetic dissipation due to superconducting quasiparticles", Nature **508**, 369–372 (2014).

[26] A.Kher, "Superconducting Nonlinear Kinetic Inductance Devices. Dissertation (Ph.D.)", `10.7907/Z9JQ0Z1F` (2017).

[27] P. K. Day, H. G. Leduc, B. A. Mazin, A. Vayonakis, and J. Zmuidzinas, "A broadband superconducting detector suitable for use in large arrays", Nature **425**, 12–14 (2003).

[28] G. Deutscher, H. Fenichel, M. Gershenson, E. Griinbaum, and Z. Ovadyahu, "Transition to Zero Dimensionality in Granular Aluminum Superconducting Films", Journal of Low Temperature Physics, 231–243 (1973).

[29] A. J. Kerman, "Metastable Superconducting Qubit", Physical Review Letters **027002**, 1–4 (2010).

[30] L. Grunhaupt, N. Maleeva, S. T. Skacel, M. Calvo, F. Levy-bertrand, A. V. Ustinov, H. Rotzinger, A. Monfardini, G. Catelani, and I. M. Pop, "Loss Mechanisms and Quasiparticle Dynamics in Superconducting Microwave Resonators Made of Thin-Film Granular Aluminum", Physical Review Letters, `10.1103/PhysRevLett.121.117001` (2018).

[31] L. Grunhaupt, M. Spiecker, D. Gusenkova, N. Maleeva, S. T. Skacel, I. Takmakov, F. Valenti, P. Winkel, H. Rotzinger, W. Wernsdorfer, A. V. Ustinov, and I. M. Pop, "Granular aluminium as a superconducting material for high-impedance quantum circuits", Nat Mater., 816–819 (2019).

[32] H. Rotzinger, S. Skacel, M. Pfirmann, J. Voss, J. Münzberg, S. Probst, P. Bushev, M. Weides, A. Ustinov, and J. Mooij, "Aluminium-oxide wires for superconducting high kinetic inductance circuits", Superconductor Science and Technology (2016).

[33] P. Winkel, K. Borisov, L. Grunhaupt, D. Rieger, M. Spiecker, F. Valenti, A. V. Ustinov, W. Wernsdorfer, and I. M. Pop, "Implementation of a Transmon Qubit Using Superconducting Granular Aluminum", Physical Review X **10**, 31032 (2020).

[34] D. Leykam, A. Andreanov, and S. Flach, "Artificial flat band systems : from lattice models to experiments", Advances in Physics: X, 10.1080/23746149.2018.1473052 (2018).

[35] S. Nazarenko, *Wave Turbulence* (2011).

[36] K. Baudin, A. Fusaro, K. Krupa, J. Garnier, S. Rica, G. Millot, and A. Picozzi, "Rayleigh-Jeans condensation of classical light: Observation and thermodynamic characterization", Physical Review Letter, 42–44.

[37] M. Zhurahov, A. Bekker, B. Levit, R. Weill, and B. Fischer, "CW laser light condensation", Opt Express. **24**, 1022–1024 (2016).

[38] E. Monsalve, M. Brunet, B. Gallet, and P.-p. Cortet, "Quantitative Experimental Observation of Weak Inertial-Wave Turbulence", Physical Review Letters **125**, 254502 (2020).

[39] A. Ruckriegel and P. Kopietz, "Rayleigh-Jeans Condensation of Pumped Magnons in Thin-Film Ferromagnets", **157203**, 1–5 (2015).

[40] C. Sun, S. Jia, C. Barsi, S. Rica, A. Picozzi, and J. W. Fleischer, "Observation of the kinetic condensation of classical waves", Nature Physics **8**, 470–474 (2012).

[41] C. Connaughton, C. Josserand, A. Picozzi, Y. Pomeau, and S. Rica, "Condensation of classical nonlinear waves", Phys. Rev. Lett. **95**, 263901 (2005).

[42] J. A. Schreier, A. A. Houck, J. Koch, D. I. Schuster, B. R. Johnson, J. M. Chow, J. M. Gambetta, J. Majer, L. Frunzio, M. H. Devoret, S. M. Girvin, and R. J. Schoelkopf, "Suppressing charge noise decoherence in superconducting charge qubits", Physical Review B **77**, 10.1103/PhysRevB.77.180502 (2008).

[43] T. Weisl, B. Küng, E. Dumur, A. K. Feofanov, I. Matei, C. Naud, O. Buisson, F. W. J. Hekking, and W. Guichard, "Kerr coefficients of plasma resonances in Josephson junction chains", Physical Review B **92**, Publisher: American Physical Society, 104508 (2015).

[44] A. J. Annunziata, D. F. Santavicca, L. Frunzio, G. Catelani, M. J. Rooks, and A. Frydman, "Tunable superconducting nanoinductors", Nanotechnology **21**, 10.1088/0957-4484/21/44/445202 (2010).

[45] H. Greenhouse, "Design of planar rectangular microelectronic inductors", IEEE Transactions on Parts, Hybrids, and Packaging **10**, 101–109 (1974).

[46] I. M. P. N. Maleeva L. Grünhaupt, "Circuit quantum electrodynamics of granular aluminum resonators", Nat Commun **9**, 10.1038/s41467-018-06386-9 (2018).

[47] A. Glezer Moshe, E. Farber, and G. Deutscher, "Granular superconductors for high kinetic inductance and low loss quantum devices", Applied Physics Letters **117**, Publisher: AIP Publishing LLC, 062601 (2020).

[48] C. Gardiner and M. Collett, "Input and output in damped quantum systems: Quantum stochastic differential equations and the master equation Physics", Physical Review A (1985).

[49] D. Leykam, S. Flach, O. Bahat-Treidel, and A. S. Desyatnikov, "Flat band states: disorder and nonlinearity", Phys. Rev. B **88**, 224203 (2013).

[50] N. Lazarides and G. P. Tsironis, "Squid metamaterials on a lieb lattice: from flat-band to nonlinear localization", Phys. Rev. B **96**, 054305 (2017).

[51] J. D. Bodyfelt, D. Leykam, C. Danieli, X. Yu, and S. Flach, "Flatbands under correlated perturbations", Phys. Rev. Lett. **113**, 236403 (2014).

[52] J. M. Kreikebaum, A. Morvan, and I. Siddiqi, "Improving wafer-scale Josephson junction resistance variation in superconducting quantum coherent circuits", (2020).

[53] D. Niepce, "Fabrication and Characterisation of Thin-Film Superconducting Nanowire Superinductors for Novel Quantum Devices", (2014).

[54] J. I.-j. Wang and W. D. Oliver, "An aluminium superinductor", Nature Materials **18**, 775–776 (2019).

[55] A. Anthore, H. Pothier, and D. Esteve, "Density of states in a superconductor carrying a supercurrent", Phys. Rev. Lett. **90**, 127001 (2003).

[56] M. Tinkham, *Introduction to superconductivity.*

[57] K. E. et al., "Current-dependent kinetic inductance of superconducting ybacuo thin films", Jpn. J. Appl. Phys. **34** (1995).

[58] C. McRae, H. Wang, J. Gao, M. Vissers, T. Brecht, A. Dunsworth, D. Pappas, and J. Mutus, "Materials loss measurements using superconducting microwave resonators", Review of Scientific Instruments **091101**, 10.1063/5.0017378 (2020).

[59] J. Goetz, F. Deppe, M. Haeberlein, F. Wulschner, C. W. Zollitsch, S. Meier, M. Fischer, P. Eder, E. Xie, K. G. Fedorov, E. P. Menzel, A. Marx, and R. Gross, "Loss mechanisms in superconducting thin film microwave resonators", Journal of Applied Physics **119** (2016).

[60] L. Faoro and L. B. Ioffe, "Interacting tunneling model for two-level systems in amorphous materials and its predictions for their dephasing and noise in superconducting microresonators", Phys. Rev. B **91**, 014201 (2015).

[61] H. Le Sueur, A. Svilans, N. Bourlet, L. Berg, A. Murani, L. Bergé, L. Dumoulin, and P. Joyez, "Microscopic charged fluctuators as a limit to the coherence of disordered superconductor devices",

[62] L. Cardani, N. Casali, G. Catelani, T. Charpentier, M. Clemenza, I. Colantoni, A. Cruciani, L. Gironi, L. Gruenhaupt, D. Gusenkova, F. Henriques, M. Lagoin, M. Martinez, S. Pirro, I. M. Pop, C. Rusconi, A. Ustinov, F. Valenti, M. Vignati, and W. Wernsdorfer, "Suppression of the Relaxation Induced by Radioactivity in Superconducting Qubits", Journal of Low Temperature Physics, 10.1007/s10909-019-02265-9 (2019).

[63] E. N. Coker, "The oxidation of aluminum at high temperature studied by thermogravimetric analysis and differential scanning calorimetry.", 10.2172/1096501 (2013).

[64] F. Levy-Bertrand, T. Klein, T. Grenet, O. Dupré, A. Benoit, A. Bideaud, O. Bourrion, M. Calvo, A. Catalano, A. Gomez, J. Goupy, L. Grünhaupt, U. v. Luepke, N. Maleeva, F. Valenti, I. M. Pop, and A. Monfardini, "Electrodynamics of granular aluminum from superconductor to insulator: observation of collective superconducting modes", Phys. Rev. B **99**, 094506 (2019).

[65] "An analysis method for asymmetric resonator transmission applied to superconducting devices ", Journal of Applied Physics **111** (2012).

[66] K. L. Geerlings, "Improving Coherence of Superconducting Qubits and Resonators", Yale University, ProQuest Dissertations Publishing (2013).

[67] A. Dunsworth, A. Megrant, C. Quintana, Z. Chen, R. Barends, B. Burkett, B. Foxen, Y. Chen, B. Chiaro, A. Fowler, R. Graff, E. Jeffrey, J. Kelly, E. Lucero, J. Y. Mutus, M. Neeley, C. Neill, D. Sank, A. Vainsencher, J. Wenner, T. C. White, and J. M. Martinis, "Characterization and Reduction of Capacitive Loss Induced by Sub-Micron", Appl. Phys. Lett. **111** (2017).

[68] A. C. Newell and B. Rumpf, "Wave turbulence", Annual Review of Fluid Mechanics **43**, 59–78 (2011).

[69] A. C. Newell, S. Nazarenko, and L. Biven, "Wave turbulence and intermittency", Physica D: Nonlinear Phenomena **152-153**, Advances in Nonlinear Mathematics and Science: A Special Issue to Honor Vladimir Zakharov, 520–550 (2001).

[70] S. Dyachenko, A. C. Newell, A. Pushkarev, and V. E. Zakharov, "Optical turbulence : weak turbulence , condensates and collapsing filaments in the nonlinear Schrodinger equation", Physica D **57**, 96–160 (1992).

[71] L. Pitaevskii and S. Stringari, *Bose-Einstein Condensation and Superfluidity* (2016).

[72] C. Rackauckas, "A Comparison Between Differential Equation Solver Suites In MATLAB, R, Julia, Python, C, Mathematica, Maple, and Fortran", 1–13 (2018).

[73] Y. Yamamoto and H. A. Haus, "Preparation, measurement and information capacity of optical quantum states", Rev. Mod. Phys. **58**, 1001–1020 (1986).

[74] V. E. Zakharov, A. O. Korotkevich, A. N. Pushkarev, and A. I. Dyachenko, "Mesoscopic Wave Turbulence", J.E.T.P. **82**, 487–491 (2005).

[75] A. Schliesser, O. Arcizet, T. Wilken, R. Holzwarth, and T. J. Kippenberg, "Optical frequency comb generation from a monolithic microresonator", Nature **450**, 1214–1217 (2007).

[76] M. L. Gorodetsky and T. J. Kippenberg, "Kerr-frequency combs in microresonators", Nature Photonics, `10.1038/nphoton.2012.127` (2012).

[77] P. Lu, S. Khan, T.-C. Chien, X. Cao, O. Lanes, C. Zhou, H. Türeci, and M. Hatridge, "Nearly quantum-limited josephson-junction frequency comb synthesizer", (2020).

[78] S. Khan and H. E. Tureci, "Frequency combs in a lumped-element josephson-junction circuit", Phys. Rev. Lett. **120**, 153601 (2018).

[79] A. G. Moshe1, E. Farber, and G. Deutscher, "Granular superconductors for high kinetic inductance and low loss quantum devices", Appl. Phys. Lett. **117**, `https://doi.org/10.1063/5.0017749` (2020).

[80] I.-c. Hoi, C. M. Wilson, T. Palomaki, T. M. Stace, B. Fan, and P. Delsing, "Giant Cross Kerr Effect for Propagating Microwaves Induced by an Artificial Atom", (2018).

[81] N. M. Sundaresan, A. V. Gorshkov, and A. A. Houck, "Interacting Qubit-Photon Bound States with Superconducting Circuits", Physical Review X **9**, `10.1103/PhysRevX.9.011021` (2019).

[82] S. T. Skacel, C. Kaiser, S. Wuensch, H. Rotzinger, A. Lukashenko, M. Jerger, G. Weiss, M. Siegel, and A. V. Ustinov, "Probing the TLS Density of States in SiO Films using Superconducting Lumped Element Resonators", 3–6 (2018).

[83] J. Zmuidzinas, "Superconducting microresonators: physics and applications", Annual Review of Condensed Matter Physics **3**, 169–214 (2012).

[84] U. Vool and M. Devoret, "Introduction to quantum electromagnetic circuits", International Journal of Circuit Theory and Applications **45**, 897–934.

[85] "NANO PMMA and Copolymer Product Information", (2014).

[86] D. Marcos, A. Tomadin, S. Diehl, and P. Rabl, "Photon condensation in circuit quantum electrodynamics by engineered dissipation", New Journal of Physics **14**, 055005 (2012).

[87] A. Fusaro, "Auto-organisation d'ondes optiques incohérentes: Condensation, thermalisation et repolarisation", (2019).

[88] G. Deutscher, "Critical current of granular superconductors ", Rev. Phys. Appl. **8**, 127–129 (1973).

[89] S. K. Remillard, "The effects of granularity on the microwave surface impedance of high kappa superconductors", 10.21220/s2-gwc0-2s71 (1993).

[90] A. P. Sears, "Extending Coherence in Superconducting Qubits : from microseconds to milliseconds ", (2013).

[91] F. R. Ong, M. Boissonneault, F. Mallet, A. Palacios-Laloy, A. Dewes, A. C. Doherty, A. Blais, P. Bertet, D. Vion, and D. Esteve, "Circuit qed with a nonlinear resonator: ac-stark shift and dephasing", Phys. Rev. Lett. **106**, 167002 (2011).

[92] V. Lahtinen and M. Mottonen, "Effects of device geometry and material properties on dielectric losses in superconducting coplanar-waveguide", **32** (2020).

[93] U. S. Pracht, N. Bachar, L. Benfatto, G. Deutscher, E. Farber, M. Dressel, and M. Scheffler, "Enhanced cooper pairing versus suppressed phase coherence shaping the superconducting dome in coupled aluminum nanograins", Phys. Rev. B **93**, 100503 (2016).

[94] H. T., H. K., R. J., and al., "Universal formation dynamics and noise of Kerr-frequency combs in microresonators", Nature Photon. **6**, 480–487 (2012).

[95] W. R., B. A., L. B., and al., "Bose–Einstein condensation of photons in an erbium–ytterbium co-doped fiber cavity", Nat Commun **10**, https://doi.org/10.1038/s41467-019-08527-0 (2019).

[96] F. Ferdous1, H. Miao, D. E. Leaird1, K. Srinivasan, J. Wang, L. Chen, L. T. Varghese, and A. M. Weiner, "Spectral line-by-line pulse shaping of on-chip microresonator frequency combs", Nature Photonics **5**, 770–776.

[97] V. S. L'vov and S. Nazarenko, "Discrete and mesoscopic regimes of finite-size wave turbulence", Phys. Rev. E **82**, 056322 (2010).

[98] A. Picozzi, J. Garnier, T. Hansson, P. Suret, S. Randoux, G. Millot, and D. N. Christodoulides, "Optical wave turbulence : Towards a unified nonequilibrium thermodynamic formulation of statistical nonlinear optics", Physics Reports, 1–132 (2014).

[99] M. Leib, F. Deppe, A. Marx, R. Gross, and M. J. Hartmann, "Networks of nonlinear superconducting transmission line resonators", New Journal of Physics **14**.

[100] R. Ma, B. Saxberg, C. Owens, N. Leung, and Y. L. J. S. D. I. Schuster, "A dissipatively stabilized Mott insulator of photons", Nature **566**, 51–57 (2019).

[101] S. Schmidt and G. Blatter, "Phase Diagram and Excitations of the Jaynes-Cummings-Hubbard Model", (2017).

[102] R. Ma, B. Saxberg, C. Owens, N. Leung, Y. Lu, J. Simon, and D. I. Schuster, "A dissipatively stabilized Mott insulator of photons", Nature, 10.1038/s41586-019-0897-9.

[103] M. S. Khalil, M. J. A. Stoutimore, F. C. Wellstood, and K. D. Osborn, "An analysis method for asymmetric resonator transmission applied to superconducting devices", (2012).

[104] A. A. Clerk, M. H. Devoret, S. M. Girvin, F. Marquardt, and R. J. Schoelkopf, "Introduction to Quantum Noise , Measurement and Amplification : Online Appendices",

[105] C. Gardiner and P. Zoller, *Quantum noise: a handbook of Markovian and Non-Markovian Quantum Stochastic Methods with Applications to Quantum Optics*, 1991.

[106] C. M. Caves, "Quantum limits on noise in linear amplifiers", Physical Review D (1982).

[107] T. Jacqmin, I. Carusotto, I. Sagnes, M. Abbarchi, D. D. Solnyshkov, G. Malpuech, E. Galopin, A. Lemaitre, J. Bloch, and A. Amo, "Direct observation of dirac cones and a flatband in a honeycomb lattice for polaritons", Phys. Rev. Lett. **112**, 116402 (2014).

[108] T. Boulier, M. J. Jacquet, A. Maître, G. Lerario, F. Claude, S. Pigeon, Q. Glorieux, A. Amo, J. Bloch, A. Bramati, and E. Giacobino, "Microcavity polaritons for quantum simulation", Advanced Quantum Technologies **3**, 2000052.

[109] S. Léger, J. Puertas-martínez, K. Bharadwaj, R. Dassonneville, J. Delaforce, F. Foroughi, V. Milchakov, L. Planat, O. Buisson, C. Naud, W. Hasch-guichard, S. Florens, I. Snyman, and N. Roch, "Observation of quantum many-body effects due to zero point fluctuations in superconducting circuits", Nature Communications **10**, 1–23.

[110] F. Valenti, F. Henriques, G. Catelani, N. Maleeva, L. Grunhaupt, U. von Lupke, S. T. Skacel, P. Winkel, A. Bilmes, A. V. Ustinov, J. Goupy, M. Calvo, A. Benoit, F. Levy-Bertrand, A. Monfardini, and I. M. Pop, "Interplay between kinetic inductance, nonlinearity, and quasiparticle dynamics in granular aluminum microwave kinetic inductance detectors", Phys. Rev. Applied **11**, 054087 (2019).

université PARIS-SACLAY

ÉCOLE DOCTORALE
Physique en l'Île-de-France (PIF)

Titre: Réseaux Non-linéaire de Résonateurs Supraconducteurs en Aluminium Granulaire

Mots clés: Interations, Cavités micro-ondes,Quantique

Résumé: Le but de cette thèse est d'étudier les propriétés des réseaux non-linéaires de résonateurs micro-ondes. Les résonateurs ont été réalisés en aluminium granulaire, un supraconducteur désordonné à forte inductance cinétique, ce qui nous a permis d'obtenir des résonateurs avec un facteur de qualité élevé (jusqu'à 3 10^5) et des non-linéarités jusqu'à 10 kHz. Nous avons développé un cadre pour calculer les paramètres de réseaux avec couplage capacitif et l'avons utilisé pour concevoir deux échantillons. Un échantillon comprenant une géométrie rectangle ainsi qu'un deuxième échantillon présentant une géométrie Lieb conduisant à une bande plate. Nous avons présenté la théorie du supraconducteur désordonné et plus particulièrement de l'aluminium granulaire. Nous avons mesuré un résonateur unique non-linéaire fabriqué à l'aide d'inductances granulaires en aluminium et vérifié la loi d'échelle de leur non-linéarité sur plusieurs ordres de grandeur. Nous discutons des processus de thermalisation dans les systèmes avec interaction de Kerr et avons présenté le principe de la condensation d'onde classique dans les réseaux 3D et 2D. Nous avons calculé le tenseur de Kerr pour l'échantillon de réseau rectangle conçu dans le premier chapitre. Nous avons simulé. l'équation de mouvement de l'amplitude de ses modes et a montré que l'équation conduit à un processus de condensation. Nous mesurons la transmission de l'échantillon de Lieb et du rectangle. Nous quantifions ensuite les processus non linéaires dans le réseau en mesurant les interactions de Kerr ainsi que les processus de mélange d'ondes dans le réseau rectangle. Nous présentons des résultats préliminaires sur la réponse dynamique du réseau rectangle et sa thermalisation. Ces résultats soulignent le potentiel des réseaux de résonateurs supraconducteurs pour simuler des systèmes non-linéaire à nombreux dégrés de liberté.

Title: Non-linear Lattices of Granular Aluminium Resonators

Keywords: Interaction, micro-wave cavities, quantum

Abstract: The purpose of this thesis is to investigate the properties of non-linear lattices of microwave resonators. The resonators where realized in granular Aluminum, a disordered superconductor with high kinetic inductance, which allowed us to obtain modes with a high quality factor (up to 3 10^5) and non-linearities in the 10 kHz range. We develloped a framework to compute parameters of lattices with capacitive coupling and used it to design two samples. One sample with a rectangle geometry as well as a second sample with a Lieb geometry leading to a flat band. We presented the theory of disordered superconductor and specifically of granular aluminium. We measured non-linear single resonator made using granular aluminium inductances and verified the scaling law of their non-linearity over multiple orders of magnitude. We discuss the thermalization processes in systems with Kerr interaction and presented the priniciple of classical wave condensation in 3D and 2D lattices. We computed the Kerr tensor for the rectangle lattice sample designed in the first chapter. We simulated the equation of motion of the amplitude of its modes and showed that the equation leads to a condensation process. We measure the transmission of both the Lieb and rectangle sample. We then quantify the nonlinear processes in the lattice by measuring the self and cross Kerr interaction as well as four wave mixing processes in the rectange lattice. We present preliminary results on the dynamical response of the rectangle lattice towards thermalization . These results underline the potential of lattices of many superconducting resonators to simulate non-linear Hamiltonians with many degrees of freedom.